Optical Method for Antenna Near-Field Sensing

by

Shuyu Ding

A thesis
presented to the University of Waterloo
in fufilment of the
thesis requirement for the degree of
Doctor of Philosophy
in
Electrical and Computer Engineering

Waterloo, Ontario, Canada, 2024

Examining Committee Membership

The following served on the Examining Committee for this thesis. The decision of the Examining Committee is by majority vote.

Supervisor(s):	Hamed Majedi Professor, Dept. of Electrical and Computer Engineering, University of Waterloo
External Examiner:	Li Wei Professor, Dept. of Physics and Computer Science, Wilfrid Laurier University
Internal Member:	Dayan Ban Professor, Dept. of Electrical and Computer Engineering, University of Waterloo
Internal Member:	Raafat Mansour Professor, Dept. of Electrical and Computer Engineering, University of Waterloo
Internal-External Member:	Brenda Lee Lecturer, Dept. of Physics and Astronomy, University of Waterloo

Author's Declaration

I hereby declare that I am the sole author of this thesis. This is a true copy of the thesis, including any required final revisions, as accepted by my examiners.

I understand that my thesis may be made electronically available to the public.

Abstract

This thesis explores the application of Thin Film Lithium Niobate (TFLN) in advancing the fabrication of optical devices for electric field (E-field) sensing within phased-array antenna systems. The research primarily focuses on the deployment of fully dielectric TFLN-based Mach-Zehnder Interferometer (MZI) waveguides to detect E-field variations, representing a shift from conventional metallic-based sensing approaches. By leveraging the electro-optic (EO) effect inherent in TFLN, this study assesses the capability of these waveguides to passively modulate the power of an optical signal in response to E-field alterations, with the goal to contribute to the enhancement of E-field sensing technology.

The methodology incorporated a comprehensive phase of design, simulation, fabrication, and experimental validation. Simulations were conducted using HFSS for analyzing antenna performance and Lumerical to measure optical device behaviour, establishing the fundamental groundwork for device optimization. The fabrication stage was elaborately engineered, utilizing electron beam lithography with HSQ, ZEP, and SiO_2 processing techniques, among which the ZEP process method was identified as providing optimal outcomes in producing precise optical device structures with minimal surface defects. The experimental component was operated in the Advanced Optical Lab at University of Waterloo, validated the responsiveness of the TFLN waveguide to E-field variations emitted by antenna elements. Notable experimental findings included a recorded 2% reduction in the waveguide's output power following antenna E-field activation, which was slightly lower than the 5% decrease predicted by simulation models.

This 3% difference illustrates the challenges associated with applying theoretical models to practical implementations, highlighting the necessity for rigorous experimental validation. Further observations revealed that when the input power of antennas was maintained below 10 dBm, the power variance at the waveguide's output was less than 1%. This sensitivity to E-field fluctuations suggests that TFLN-MZI waveguides could effectively function as detectors for electromagnetic field variations, potentially serving as a valuable tool for synchronous diagnostics and calibration of antenna arrays.

In conclusion, this thesis proposes an innovative approach for E-field sensing with TFLN-based optical devices, specifically in the context of phased-array antennas. Through a synthesis of theoretical analysis, fabrication techniques, and empirical validation, the study advances the knowledge of integrating TFLN waveguides into antenna systems for enhanced diagnostics and calibration. The findings suggest paths for further research, particularly in optimizing the sensitivity and integration efficiency of TFLN-based optical devices for telecommunications and sensing applications.

Acknowledgements

I wish to begin by expressing my profound sorrow and respect for my late supervisor, Prof. Safieddin Safavi-Naeini, who passed away unexpectedly in October 2021. His support, both professionally and personally, was a cornerstone of my journey, and his absence is deeply felt. His invaluable guidance and wisdom significantly contributed to my academic progress, and though he is no longer with us, his legacy continues to persist. His contributions to science and technology remain a beacon of inspiration for scholars and practitioners alike.

Heartfelt gratitude is extended to Prof. Hamed Majedi, whose exceptional intellect and innovative thinking have been instrumental in guiding this work. His patience and inspirational professional demeanor have been invaluable. Being under his tutelage is among the greatest fortunes of my life, offering both academic enlightenment and personal growth over the past years.

My deepest appreciation goes to Prof. Sujeet K. Chaudhuri, whose expertise and insights have been fundamental to the success of my research. His support, especially the financial backing for the QNC fabrication project, played a vital role in advancing my research pursuits.

I am also thankful to my thesis committee members, Prof. Li Wei, Prof. Daya Ban, Prof. Raafat Mansour, and Prof. Brenda Lee, for their invaluable suggestions and insights on my thesis, which have significantly contributed to its refinement.

I am profoundly grateful to Dr. Arash Rohani for his vast knowledge, boundless enthusiasm, and unwavering support. His encouragement has been a source of inspiration not only to me but also to all his colleagues and friends, past and present. Our numerous discussions have been both enjoyable and enlightening, and I cherish his friendship and look forward to our future scientific collaboration.

Additionally, my sincere thanks go to my colleagues at the Centre for Intelligent Antenna and Radio Systems (CIARS)—particularly Dr. Naime Ghafarian and Dr. Aidin Taeb. Their assistance in the laboratory, readiness to share their knowledge, and spirit of collaboration have significantly contributed to the richness of my research experience.

Dedication

For my wife Xiaoge and children, Adina, and Winston.

Table of Contents

List of Figures

List of Tables

Chapter 1

Introduction and Research Goals

1.1 Research Motivation

As the technology roadmap for satellite telecommunications, high-resolution radar, and the advent of 5G/6G technologies is progressively expanding, the development of next-generation high-frequency communication and radar/imager antenna systems faces a multitude of significant challenges. This evolution is propelled by the relentless quest for higher transmission data rates and a burgeoning interest in exploiting higher frequency spectrums for cutting-edge applications in high-resolution imaging and spectroscopy. Consequently, the operational frequencies of radio frequency (RF) and antenna systems are experiencing a steady uptrend. While this shift to higher frequencies presents a strategic advantage of substantially miniaturizing antenna dimensions, it simultaneously imposes stringent requirements on maintaining the quality of the radiation beam [1]. This beam quality is critically reliant on the precise control over the amplitude and phase distribution across the radiating aperture, a task that grows increasingly complex and challenging at elevated frequencies.

Phased-array antenna systems, renowned for their unique beam-forming flexibility and highly adaptable structures, have emerged as exemplary solutions to address these burgeoning challenges in the field. They are particularly indispensable in applications ranging from high throughput satellite (HTS) communication services and high-resolution radars/imagers to the evolving sectors of 5G/6G telecommunications, particularly where mobility is required at one or both ends of the radio link. The imperative for high-performance systems necessitates the deployment of large-scale phased-array systems, which boast an extensive array of antenna elements with programmable polarization capabilities.

These sophisticated, reconfigurable, and software-defined radiating architectures are now at the epicentre of intensive research and development efforts. Such efforts are directed towards a new era of communication and sensing systems, capable of satisfying the escalated demands for data throughput, resolution, and flexibility across a broad spectrum of commercial, military, and scientific applications. The pursuit of these advanced systems underlines the critical role of innovation and research in overcoming the technical challenges posed by the next frontier in antenna and RF system design. Figure 1.1 showcases a phased-array antenna system along with its characterization setup, providing a visual insight into the complexity and capability of these cutting-edge systems [2].

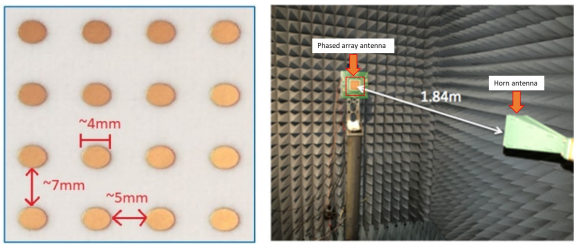

Figure 1.1: Antenna System Comparison. Left: A commercial phased array antenna operating at 30 GHz with 16 elements. Right: Characterization of a phased array antenna within an antenna chamber.

A paramount challenge within high-end applications, such as mobile Satellite Communication (SatCom), is fulfilling the stringent demands for antenna gain pattern, polarization quality, and beam-pointing accuracy. These elements are essential for the reliability and efficiency of communication systems, especially concerning Effective Isotropically Radiated Power (EIRP), the product derived from Antenna Gain and total radiated power. Additionally, the stability of EIPR is directly influenced by these factors, as a function of scan angle on the transmit side. Similarly, on the receiving side, the Gain-to-Noise Temperature ratio (G/T) stands as a fundamental performance metric for phased-array systems. Both EIRP and G/T are significantly dependent on the antenna system's gain and radiation pattern, emphasizing the critical role of precise calibration in securing optimal system performance.

In the context of phased-array systems, the quality of radiation pattern and gain is largely determined by the accuracy and effectiveness use of the calibration method. Such methods are essential for identifying and rectifying any phase/amplitude imbalances between the array's input (or output) and each individual antenna element. This level of precision is critical not only at the point of factory calibration but also throughout the operational lifespan of high-performance, large-scale phased arrays. As a result, these sys-

tems frequently incorporate an internal or on-board calibration mechanism to sustain their performance over time.

The methodology for on-board or internal calibration typically entails measuring the signal sample in close proximity to the antenna or the radiated electromagnetic field in the vicinity of, or at, the radiating aperture [3]. This task becomes notably challenging at microwave/millimetre-wave frequencies, or higher, where rapid and non-intrusive measurement of the antenna near-field is indispensable yet difficult to achieve. While lower frequencies have allowed for simpler near-field measurement techniques, the complexity multiplies as the increased frequency, highlighting the need for innovative solutions in calibration technology. Near-field measurement yields essential data on antenna performance, extending beyond calibration to enhance the functionality of tunable engineered surfaces, such as meta-surfaces, and assisting in the diagnosis of potential malfunctions. These capabilities are fundamental for optimization and troubleshooting within advanced high-frequency antenna systems.

Traditionally, employing small test antennas, including horn antennas, open waveguides, or small dipoles (or loops), has been a standard practice in near-field measurement systems. However, these methods typically require expensive, complex, and bulky equipment, such as precision scanners and millimetre-wave up-converter/down-converter heads, to capture the field close to the antenna and analyze it. The impracticality of these approaches for the online calibration of phased-array systems has spurred the exploration of more feasible alternatives [3]. Over the last few decades, a variety of antenna calibration methods have been developed and explored. Among these, capturing signals from the antenna under test (AUT) with a receiving antenna for subsequent signal processing has been widely adopted. Furthermore, the application of electro-optical (EO) materials for electric field mapping and sensing has demonstrated promising results. Techniques utilizing EO material probes for E-field mapping, EO material ring resonators, and receiver antennas equipped with EO material devices for E-field measurement exemplify the diverse strategies employed to address the calibration challenges faced by modern antenna systems.

In the realm of calibration techniques, a prominent method involves placing a bulk lithium niobate (LN) layer atop the probe, strategically positioned between the optical signal generator and a total reflection layer. This configuration enables a laser beam to penetrate the EO material, facilitating entry and exit due to reflection, therefore permitting precise measurement of the field's intensity and distribution. Another innovative approach involves the use of a silicon-on-insulator (SOI) strip waveguide ring resonator, characterized by its non-metallic structures for the side cladding layer, with bulk LN serving as the top cladding layer. This design has demonstrated effective in E-field sensing at specific frequencies, revealing the potential of integrated photonic structures to deliver sensitive,

localized electromagnetic fields measurements.

Moreover, metal-based sensing methodologies constitute an integral component of the calibration toolkit. These methods utilize various receiving antenna structures that incorporate metallic elements to amplify the received electric field intensity. By harnessing metallic structures, these techniques exploit the conductive properties of metals to concentrate and guide electromagnetic fields, thus facilitating enhanced accuracy and efficiency in the sensing of fields proximal to the antenna. Such metal-based methods are particularly valuable in scenarios where strong signal detection and calibration capabilities are required, underlining the versatility and adaptability of calibration strategies in meeting the multifaceted demands of contemporary antenna systems.

In an effort to elucidate the landscape of current research and development within this field, the introduction chapter includes a table detailing recent advancements in EO devices for E-field sensing applications. This table, serving as an essential reference point, not only illustrates the innovative strides in EO technology but also contextualizes metal-based approaches within a range of calibration techniques. It accentuates their ongoing significance and the broadening opportunities presented by optical solutions in the realm of antenna system calibration. Overall, this comparative analysis highlights the evolving nature of calibration strategies, emphasizing the complementary contributions of both metal-based and optical methodologies to the advancement of antenna calibration technology.

A significant limitation of metal-based sensing techniques, particularly noticeable when the measurement point is in close proximity to each antenna element, is their substantial footprint [7]. This characteristic frequently causes intense interactions between the test probe's receiver and the emitting device, resulting in severe perturbation of the antenna element's near-field. Such disturbances can profoundly impact the precision of field measurements and, consequently, the entire calibration procedure. Figure 1.2 displays two kinds of antenna characterization tools: a horn antenna designed for transmit/receive antenna measurements [2], and a handheld RF probe utilized for mapping the EM field of an antenna [8]. These instruments illustrate the diverse methodologies applied in antenna characterization, highlighting the balance between comprehensive field mapping and the need to minimize interaction effects on antenna performance.

In response to the challenges faced, especially in high-frequency antenna EM field sensing, a variety of technologies have been proposed. Among them, optical techniques are distinguished for their unique potential to overcome the constraints associated with traditional metal-based methods. Optical EM field sensors, in particular, capitalizing on the minimal interference and compact size characteristics inherent to optical systems, have demonstrated considerable potential. These sensors are advantageous in that they sig-

Table 1.1: EO Devices for E-field Sensing Applications Reported in Recent Years

Ref.	Picture	Function of EO Device	Design Features	Disadvantages
[4]	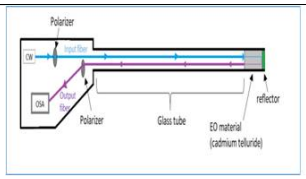	E-field measurement	Dielectric material, up to 1.8 GHz.	Prone to inaccuracies, limited to low frequencies.
[5]	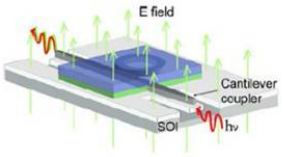	E-field measurement	Entirely dielectric, up to 1.8 GHz.	Restricted to low frequencies.
[6]	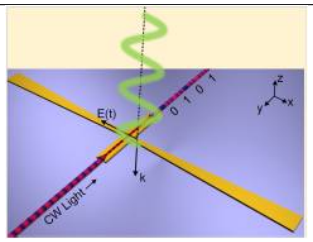	E-field enhancement and measurement	E-field boost of 35,000, up to 60 GHz.	Uses conductive materials, affecting E-field purity.

nificantly reduce electromagnetic interference with the antenna's near-field and radiation pattern, hence facilitating more accurate and less disruptive measurements. The adoption of optical technologies in constructing EM sensors not only addresses the critical issue of perturbation linked to metal-based sensing approaches but also paves new pathways for innovative advancements in antenna calibration, as evidenced by recent research findings [9].

Over the past decades, there has been a significant shift in antenna operating frequencies, with a notable increase prompting a gradual integration of photonics technology into higher frequency ranges [10]. Optical sensing technologies, characterized by their high bandwidth, compact footprint, and reduced EM interference- attributable to the use of fibre or dielectric waveguide (non-metallic) components- have emerged as valuable tools in this domain [11]. These features make optical sensing methods particularly adaptable for high-frequency EM field applications. In contrast to traditional electronic-based sensors, an optical-based sensor, which depends on metallic parts, electrical wires, and connectors, provides substantially lower loss and dispersion [12]. Additionally, recent progress in the

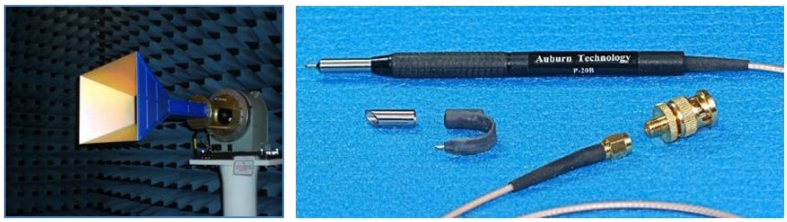

Figure 1.2: Antenna Characterization Equipment. Left: A metal-based horn antenna in the electromagnetic radiation lab. Right: A 12 GHz hand-held RF probe with connector.

fabrication of thin-film lithium niobate (TFLN) has further advanced this field, facilitating the creation of devices with smaller sizes and enhanced performance. As a result, optical sensors that utilize the electro-optic (EO) effect represent a highly promising direction for millimeter-wave EM field sensing. This is due to the superior efficiency and minimal physical intrusion they offer [13].

Despite the progress and potential of these EM field sensing techniques, literature reviews reveal that none fully meet the comprehensive needs of an internal calibration system for compact phased-array satellite antennas operating at millimetre-wave frequencies. Traditional EM-field sensing approaches, for instance, often struggle with the constraint of system size, typically being too bulky compared to the millimetre-wave antenna unit of a phased-array [3]. Furthermore, the interference caused by the metal or non-metallic structures of such EM field sensors presents a considerable challenge in the complex configurations of intricate millimetre-wave antenna arrays.

Therefore, the pursuit of advanced EM field sensing methods that offer both a minimal footprint and reduced EM field interference to the antenna under test (AUT), especially those utilizing dielectric materials, remains a central and unresolved area of research in the realm of high-frequency phased-array antenna systems.

1.2 Thesis Objective

The escalating demand for high-frequency phased-array antenna systems underlines the necessity for advanced near-field E-field sensing techniques. These techniques are critical for the internal calibration of complex antenna arrays, hence attracting considerable attention from RF researchers worldwide. This Ph.D. research introduces and validates an innovative approach for near-field sensing in phased-array antennae, utilizing TFLN material waveguides positioned in close proximity to the antenna units within the array. The

insulating property of TFLN waveguides allows their placement adjacent to antenna units without adversely affecting antenna radiation patterns. Moreover, the capability of TFLN waveguides to operate at higher frequencies presents the benefit of a minimized footprint, which is essential for their incorporation into the complex, multi-layered architecture of phased-array antenna systems [14].

Central to this research is the innovative application of TFLN waveguides for near-field E-field sensing within phased-array antennas. By capitalizing on the non-conductive attributes of TFLN, these waveguides can be positioned exceptionally close to individual antenna units without impacting the antennas' radiation patterns. This proximity is crucial, enabling the accurate sensing of electromagnetic fields with minimal interference, a challenge that escalates with the increase in frequency. The compact nature of TFLN waveguides offers a significant advantage for their integration into the densely packed, multilayered structures characteristic of phased-array systems.

The extensive adoption of TFLN in telecommunications and optical signal processing, attributed to its low loss, high bandwidth, and minimal dispersion characteristics, demonstrates the material's aptness for high-frequency E-field sensing tasks. Recent technological advancements in TFLN have addressed previous constraints, broadening its applicability across various settings and markedly improving the efficacy of optical sensors. As a result, TFLN has emerged as a forefront optical technology in telecommunications and sensing, signifying a critical evolution in the development of E-field sensing methodologies for the internal calibration of phased-array antennas. This advancement not only promises to refine the precision of phased-array systems but also paves the way for future innovations in antenna technology.

This research aims to tackle the challenge of internal (online) near-field E-field sensing in high-performance, high-frequency phased-array antennas. It investigates the application of TFLN waveguides for E-field sensing in close proximity to radiating structures, encompassing the proposal, design, fabrication, and measurement phases documented within this thesis. The exploration of optical methods for near-field E-field sensing is thoroughly articulated from multiple perspectives throughout this work.

The thesis engages in the design, theoretical analysis, simulation, optimization, fabrication, and measurement of TFLN waveguide structures and a patch antenna representing the phased-array system. Optical devices based on TFLN Mach-Zehnder Interferometer (MZI) waveguides have been rigorously designed and assessed for optical parameters. Meanwhile, the antenna unit, referred to as AUT, has been subjected to a comprehensive process of design, simulation, fabrication, and E-field parameter measurement processes. Hybrid experiments that integrate TFLN waveguide structures with the AUT have been

conducted to demonstrate and substantiate the core concept of the thesis. This work seeks to validate the efficacy of TFLN waveguides for real-time near-field E-field sensing within antenna systems, enabling the determination of antenna operational status (e.g., on or off) by analyzing the output of TFLN waveguide devices during antenna transmission, all without disrupting the radiated RF signal. This approach promises to offer an insightful method for enhancing the calibration and operational monitoring of advanced antenna systems, potentially leading to significant improvements in their performance and reliability.

1.3 Thesis Outline

This thesis introduces the integration of TFLN-MZI waveguide structures, employing TFLN grating couplers for effective optical coupling from fibre to waveguide, as a pioneering approach for near-field E-field sensing within phased-array antennas. The fabrication methodologies of these TFLN waveguide structures are elaborated, accompanied by an analytical examination of an antenna unit within a phased-array system, designated as the AUT. The research culminates in a comprehensive experiment that demonstrates the capability of the TFLN waveguide to perform antenna E-field sensing, thus validating the proposed concept.

This report undertakes an in-depth exploration of optical methods for E-field sensing, beginning with a foundational design and theoretical study that lays the groundwork for this research. Fundamental theories are elucidated in the study, with a particular focus on the EO effect and various EO modulators, setting the stage for the subsequent investigation. Following this introductory overview, the thesis progresses to detail into optical waveguide theory, with special emphasis on the MZI waveguide structure. The design process of the TFLN waveguide, specifically tailored for close proximity to the radiation edge of a patch antenna to capture a more potent E-field, is comprehensively outlined. Enhancements in measurement accuracy are achieved through the incorporation of MZI structures, which convert phase variations into discernible differences in optical signal power.

Computer simulations aimed at optimizing the optical parameters of the TFLN MZI waveguide and the grating coupler (GC) are presented, highlighting the significant role of simulations in refining the design. The simulations, conducted using HFSS for antenna and RF aspects and Lumerical simulation package for optical components, provide comprehensive insights into the EO effect and its optimization within the TFLN waveguide. The detailed simulation process not only aids in the fine-tuning of the waveguide and grating coupler designs but also in understanding the complicated interactions between the

electromagnetic fields and the EO materials. This approach ensures that the final design is not only theoretically sound but also practically viable, paving the way for the successful implementation of TFLN waveguides in E-field sensing applications within phased-array antennas.

The "Fabrication" chapter thoroughly details the processes executed in constructing the patch antenna and TFLN waveguide structures, emphasizing the technical path towards realizing a 30 GHz frequency aperture-coupled patch antenna and the integration of a TFLN waveguide with a GC. This exploration provides an in-depth analysis of various fabrication techniques, including the HSQ negative resist process, ZEP positive resist process, and SiO_2 hard mask process, ultimately identifying the ZEP resist process as the most effective in GC structure formation and waveguide endpoint precision. The chapter emphasizes the indispensable role of microscopic and Scanning Electron Microscopy (SEM) imaging techniques in verifying the accuracy of the fabrication process. These imaging modalities are highlighted for their critical contribution to confirming the structural integrity and precision of the fabricated components. Through detailed SEM analysis, it demonstrates how these imaging techniques provide essential validation of the fabrication efforts, ensuring that the physical realization of the patch antenna and TFLN waveguide structures aligns with the theoretical and design specifications. This rigorous examination and validation process is also crucial as it sets a foundation for the subsequent experimental investigations and applications in E-field sensing within phased-array antennas.

The primary object of this research is to validate the effectiveness of the TFLN waveguide in sensing the E-field emanating from the near-field of an antenna, a crucial component of the experimental phase. Optical measurements were precisely established in the Advanced Optical Lab at the University of Waterloo campus lab, alongside the antenna radiation measurement setup located in the Microwave Lab on the same floor. For these optical experiments, a laser emitting at a wavelength of 1550 nm was utilized. This particular wavelength is favoured in telecommunications for its optimal balance of low optical loss and minimal dispersion in fibre optics, rendering it especially competent for the requirements of this study. The laser signal was transmitted through a tapered fibre, which facilitated its coupling into the waveguide via the GC structure. In parallel, the antenna unit, engineered to function at a 30 GHz frequency within the phased-array antenna system, was analyzed in the Advanced Antenna Lab to assess its near-field radiation pattern. This assessment was conducted using vector network analyzers, with the setup encircled by absorbing materials to significantly reduce external interference. This experimental setup takes a comprehensive approach to investigate the interaction between the TFLN waveguide and the antenna's E-field, aiming to demonstrate the waveguide's potential as a sensitive and accurate E-field sensor within complex antenna systems.

After completing the optical and RF measurements independently, the apparatus for RF measurement was relocated to the Advanced Optical Lab for integration with the existing optical measurement setup. This hybrid experiment was designed to observe variations in optical signal power intensity correlated with the transmitting state of the antenna, during which the antenna's E-field exerted influences on the sensing waveguide within the TFLN MZI waveguide structure. This methodology not only substantiates the concept of employing TFLN waveguides in antenna E-field sensing applications but also illustrates the potential of incorporating optical devices into high-frequency phased-array antenna systems. This integration facilitates real-time calibration and characterization, significantly enhancing functionality without disrupting the continuity of the radiated RF signal.

In concluding the innovative experiment, this thesis represents a significant milestone in the exploration of TFLN waveguides for E-field sensing, while laying the groundwork for a transformative era in phased-array antenna sensing and calibration systems. The successful application of TFLN waveguides to detect the E-field radiated from an antenna's near-field is merely the initial step. With a 30 GHz antenna as the focal point and the precision usage of a 1550 nm wavelength laser, which is widely recognized in telecommunications, this study has ventured into previously unexplored domains of optical measurements and antenna calibration. Overall, it has not only validated the conceptual framework but also shed light on potential avenues for further research.

The integration of optical devices within phased-array systems, as demonstrated by the experiments, provides a compelling preview of a future where antenna calibration and characterization are seamlessly incorporated, while enhancing system performance without interfering with the emitted RF signals. Thus, this thesis does not merely conduct a research project; rather, it signals the commencement of an exhilarating progression toward the incorporation of optical technologies in antenna systems, which poises to transformative advancements in telecommunications and sensing applications. To project forward, the potential applications of TFLN waveguides in antenna E-field sensing are extensive and multifaceted, inviting continued exploration and innovation. Despite the obstacles encountered, the insights garnered from this research have been indispensable, establishing a foundation for subsequent studies that will undoubtedly expand the horizons of technological capabilities. The journey of discovery is far from complete; it has only just begun, heralding a future where the integration of optical devices within phased-array antenna systems will revolutionize the discipline.

Chapter 2

Theory and Project Design

2.1 Overview of Electro-Optical Sensing Application

Electro-optic (EO) materials are important in enabling a myriad of optoelectronic applications, encompassing EO modulators [15], photodetectors [16], terahertz spectroscopy [17], and photonics computing [18], in addition to their critical roles in global telecommunications [19]. Among these applications, EO modulators, known for their extensive bandwidth and high-speed capabilities, have emerged as a significant research direction, underpinned by their indispensable role in telecommunication networks. This field has garnered substantial interest from research groups globally, resulting in a wealth of contributions to the academic literature. A primary function of the EO effect is facilitating the conversion of data between electrical and optical signals. While electrical signals offer numerous advantages for data transmission within integrated circuits, their efficacy diminishes over long distances due to increased signal propagation loss, a limitation not encountered with optical signals. Nonetheless, optical signals often face compatibility issues with prevailing digital and analog systems [9]. EO modulators, utilizing the EO effect, serve as critical devices in bridging these two signal formats.

Over the years, Lithium Niobate (LN) has solidified its position as the preferred EO material for EO modulators and a variety of integrated optical devices. Its remarkable EO coefficients and the stability of its crystal structure set it apart from other EO materials, such as potassium dihydrogen phosphate (KDP) and its derivatives, making LN an ideal candidate for both design verification processes and widespread commercial deployment. The exploration of modulators crafted from EO materials has been an extensive and global pursuit, with researchers dedicating attention to critical attributes like the modulator's di-

mensions and its capacity to handle varying data bit rates. Highlighting this advancement, Figure 2.1 showcases a schematic diagram of EO modulators that employ annealed proton exchange (APE) waveguides within LN crystals, presenting a visual representation of the cutting-edge developments in this field [20].

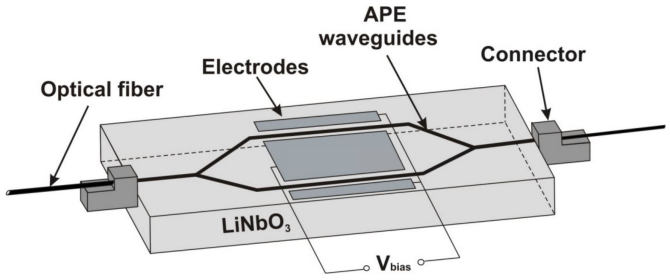

Figure 2.1: Schematic of the EO Modulator Based on Annealed Proton Exchange (APE) Waveguide in LN.

In this EO modulator setup, the optical signal is directed from an optical fiber through an APE waveguide embedded in a LN crystal. The APE process is specifically leveraged to achieve a homogeneous waveguide structure within the LN crystal's near-field by facilitating a proton exchange mechanism. Post-treatment, the waveguide region of the LN crystal exhibits a distinct refractive index, setting it apart from the rest of the crystal matrix.

To enable modulation, electrodes are designated as V (voltage) and ground, each connected to the respective positive and negative terminals of an electrical power source. As the optical signal traverses the LN waveguide beneath these electrodes, it undergoes modulation due to the E-field emanating from both sides. Nonetheless, the strength of the radio frequency (RF) drive signal, especially from lower frequency antennas, typically falls short of inducing adequate modulation within the bulk LN waveguide. The effectiveness of the EO effect is closely tied to the EO material's length within the waveguide, suggesting that reliance purely on the RF signal would demand an impractically extended length of the EO material waveguide. Addressing this limitation requires the addition of a DC bias voltage, enhancing the electric field (E-field) intensity to a level sufficient for activating the EO effect within the waveguide. This strategic integration not only compensates for the shortfall in RF drive signal intensity but also optimizes the modulator's functionality, ensuring efficient modulation of the optical signal in line with the desired EO dynamics.

A crucial challenge for EO modulators is the inadequacy of the RF signal's intensity to initiate the EO effect for optical signal modulation, necessitating a direct current (DC) bias voltage source to amplify the RF signal's intensity. This standard EO modulator

configuration is unsuitable for antenna near-field sensing applications for several reasons. Primarily, the antenna near-field lacks sufficient field intensity to provoke the EO effect, compounded by E-field interference from the electrical connections to the DC bias voltage source with antenna radiation. The direct conversion of E-fields from radiated electrical signals to optical signals has been a subject of significant interest, given the myriad advantages optical methods offer in the RF domain.

This research efforts to harness the E-field from high-frequency phased-array antennas for optical signal modulation within the EO material waveguide, with the antenna unit's RF signal intensity being a crucial determinant of the resultant EO effect. However, the radiated E-field's intensity from the antenna unit significantly diminishes due to energy dispersion in free space, making it substantially weaker than that from direct electrical connections. While escalating the RF device's frequency may enhance the E-field's intensity, it remains inferior to the electrical signal from wired connections at lower frequencies. The efficacy of the EO effect in modulating the optical signal is inherently tied to the E-field's intensity, analogous to the significance of the energy bandgap in semiconductor materials.

Addressing the challenge of efficiently capturing or collecting open space's E-field to modulate the optical signal constitutes the research project's initial hurdle. A comprehensive review of pertinent literature has been conducted to deepen understanding of this challenge, with a summary of recent research findings to follow in subsequent sections.

2.2 Optical Method for E-field Sensing

Considerable advancements have been achieved by the global research community in the quest to either directly or indirectly transform a free space E-field into an optical signal within the realm of EO material applications. The predominant approach involves the use of receiving antennas to capture and sense E-fields from open space. A notable contribution to this field is the work of Yannick et al. [6], who delineated their findings in the study titled "Direct conversion of free space millimeter waves to optical domain by plasmonic modulator antenna." This research presents a novel design for modulating optical signals by leveraging a RF source operating at 60 GHz [6]. The study introduces the concept of a plasmonic phase modulator (PPM), a groundbreaking innovation depicted in Figure 2.2, emphasizing its potential in enhancing the efficacy of EO material applications.

The innovative design commences with the antenna arms acting as receivers, tasked with capturing the free space E-field and directing it towards the central gap. These E-field waves are then confined along the surfaces of the antenna arms, leading to the amplification

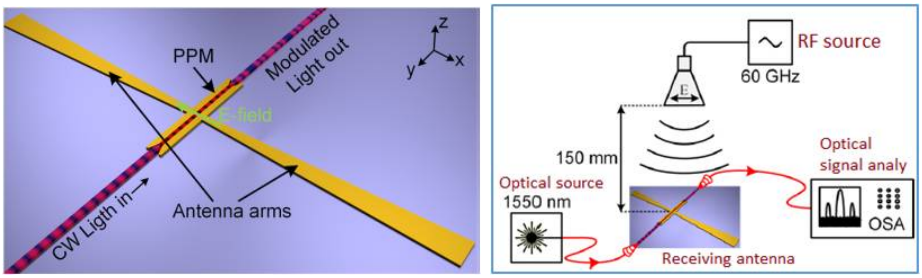

Figure 2.2: Modulator Comparison. Left: Schematic view of the plasmonic modulator antenna. Right: Experimental testing setup.

of the E-field intensity at the juncture where the antenna's metallic structure meets the central gap. This gap is filled with EO materials, specifically focusing on non-linear optical (NLO) materials, which are distinguished by their superior EO coefficients compared to conventional EO materials. The modulation mechanism is based on the principle that the refractive index of EO materials changes in proportion to the induced E-field intensity, resulting in a phase shift of the optical signal as it passes through the gap. Consequently, the optical signal is directly modulated by the stronger E-field induced on the plasmonic phase modulator (PPM), showcasing the capability of using excited EM waves at 60 GHz frequency and 20 V/m power to modulate the optical signal through NLO material [6].

A significant advantage of this approach is the use of a bowtie antenna to create a high E-field intensity region in the center. With the sidewalls of the middle gap being merely 75 nm apart, the E-field intensity in this confined area is amplified to 35,000 times that of the ambient E-field [6]. This enhancement is crucial for the EO effect, allowing for a reduction in the EO material length to just 50 µm. The experimental setup, illustrated in Figure 2.2, right side, demonstrates a 1,550 nm optical signal being modulated by a 60 GHz antenna source located 150 mm away. An optical signal analyzer (OSA) connected to the EO modulator measures the modulated optical signal, highlighting the system's effectiveness.

However, the project faces challenges with traditional calibration methods due to the metal material in the signal-receiving structure and the instability of the EO polymer over time and under varying temperatures. The objective is to devise a method for sensing the electrical near-field from the phased-array antenna that minimizes interference with the antenna's radiation pattern. Metal receiver antennas near the phased-array antenna units can adversely affect antenna performance, indicating that conventional receiver antennas are not suitable for this task. Additionally, the compact arrangement of phased-array antennas generates heat during operation, which could affect the optical sensing structure

if placed too closely, emphasizing the importance of EO material stability.

A promising approach is the creation of an EO material structure designed to accurately sense the near-field E-field intensity emanating directly from the antenna unit, all while avoiding disruptions from metallic components. The adoption of dielectric materials in the fabrication of the EO structure promises to mitigate E-field interference, facilitating a seamless integration with the phased-array antenna assembly. Besides NLO polymers, LN has been significantly investigated for its potential in E-field sensing applications. This includes its use in LN Mach-Zehnder Interferometers (MZI) [21] and the employment of thin-film LN (TFLN) probes for precise field mapping [22]. This section introduces a discussion on recent advancements in EO materials and their fabrication techniques, highlighting the dynamic research efforts dedicated to addressing the challenges outlined earlier.

2.3 Lithium Niobate for Electrical Field Sensing

Lithium niobate has been a cornerstone in the field of telecommunications, serving as a preferred material for optical signal modulation for decades. Recently, the scope of research has expanded, exploring the application of LN devices in innovative, electrode-less E-field sensing technologies geared towards next-generation applications. This shift towards an all-optical sensor framework is driven by its inherent advantage: the absence of metallic structures eliminates the risk of interference with the precise measurement and characterization of targeted E-field environments.

A significant study by a team from SRICO, Inc. has introduced a groundbreaking electrode-less, all-optical E-field sensor, employing LN as the core material [23]. At the heart of this innovative sensor lies an integrated optic MZI waveguide, ingeniously designed to harness the inherent properties of LN for phase modulation. This MZI waveguide effectively translates phase changes induced by the E-field into intensity modulation, which can be readily observed at the interferometer's output. Illustrative of this cutting-edge sensor, a photograph within the publication, showcased in Figure 2.3, provides a visual testament to the technology's capabilities and the versatile applications of LN in E-field sensing [23]. This breakthrough underlines the significant potential of LN in advancing the field of E-field sensing, highlighting its effectiveness and the transformative impact of integrating optic components for precise measurement and analysis.

During its application, the LN based MZI E-field sensor is placed within the testing E-field environment. The E-field induces phase shifts in the optical signals traveling through

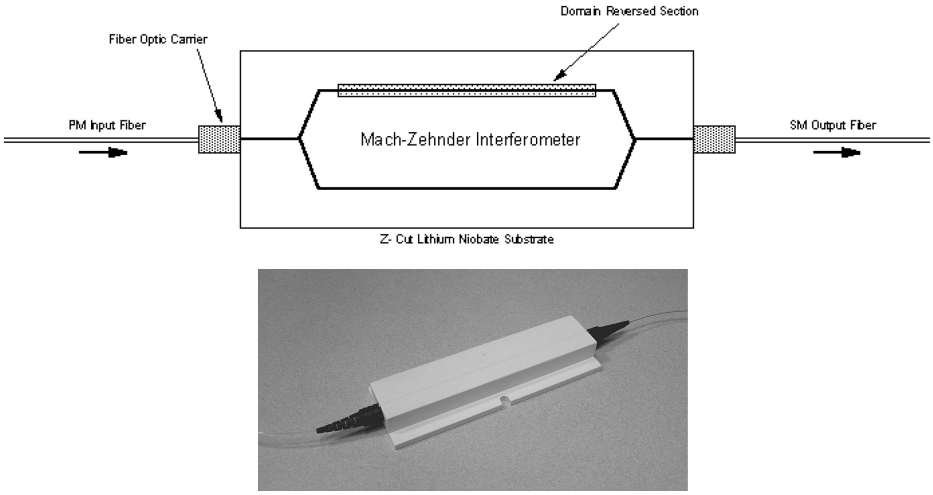

Figure 2.3: E-Field Sensor. Top: Schematic of the sensor. Bottom: Photograph of the LN E-field sensor.

the two arms of the MZI, which, due to the negligible distance between the arms, are initially equal. To create a phase difference, one arm of the interferometer is designed with a series of reverse-poled regions, allowing it to experience the E-field's opposite polarity. As a result, a phase shift difference is established between the two MZI arms, translating into an intensity difference at the interferometer's output. However, a significant drawback of this E-field sensor is its geometry. The size of the LN material necessitates a substantially large enclosure for packaging compared to the fiber connector, with the long edge exceeding 100 mm as indicated in the figure.

For several decades, the development of LN based E-field sensing applications progressed slowly due to the limitations imposed by the geometry of bulk LN. This changed with the advent of TFLN on the market. Traditional diffusion-based photonic devices in bulk LN faced several challenges, such as high drive voltage requirements and the inability to facilitate tight waveguide bends, hindering the development of integrated and efficient optical devices. The introduction of thin-film Lithium Niobate on Insulator (LNOI) wafers aimed to overcome these challenges by enabling the integration of various functionalities on a single LN chip. Initial attempts to create high-quality TFLN through deposition and growth techniques, such as chemical vapor deposition [24] and molecular beam epitaxy [25], faced difficulties in achieving high crystallinity and substrate compatibility. The breakthrough came with the adoption of the Smart-Cut technology, which emerged as the leading method for fabricating high-quality LN thin films [26]. This technique, developed

in the late 1990s and early 2000s, involves ion slicing a high-quality bulk substrate and bonding it to an insulating substrate, with options for adhesive and direct wafer bonding. Direct wafer bonding is often preferred for its potential to restore the ion-sliced material's nonlinear and electro-optic properties via higher annealing temperatures. The Smart-Cut process defines a cleavage plane in the LN substrate through ion implantation, followed by wafer bonding and thermal annealing to establish the thin film. Additional annealing steps are employed to diminish defects from ion implantation, and surface smoothness is improved through polishing. The commercialization and growing interest in TFLN among research groups worldwide were significantly boosted after the ion slicing technology's patent expired in 2018 [27].

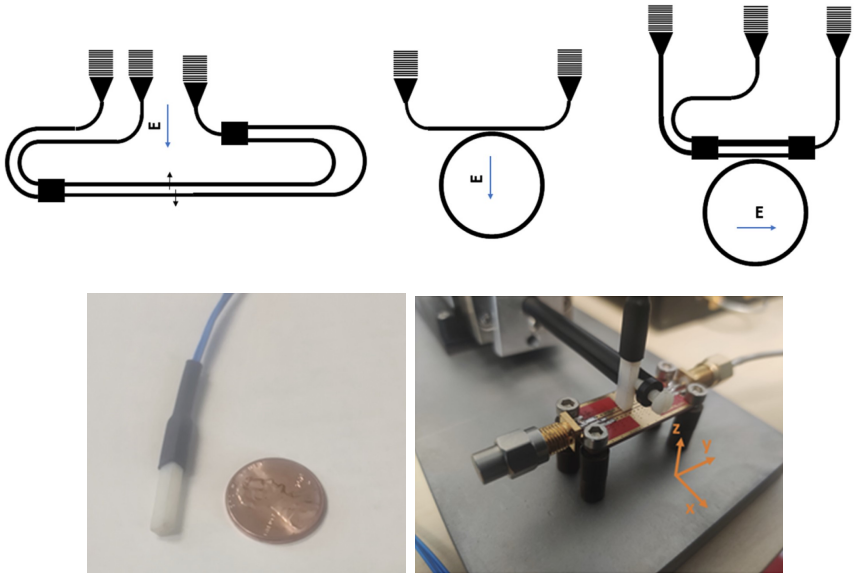

Figure 2.4: Sensor Design and Characterization. Top (left to right): Schematics of MZI E-field sensor, micro-ring resonator sensor, and MZI coupled with micro-ring resonator. Bottom Left: Packaged E-field sensor head. Bottom Right: Measurement setup for sensor characterization.

In recent years, TFLN devices have showcased their potential in a myriad of applications, including optical modulators, microwave frequency shifters, and various optical device functions across numerous domains [28]. In 2022, Partow Technologies LLC, based in the USA, unveiled their groundbreaking results utilizing TFLN micro-ring modulators and MZI modulators for E-field sensing applications. The micro-ring sensor, illustrated in Figure 2.4, is capable of sensing E-field frequencies up to several GHz and features a

compact size of just 300 µm. Meanwhile, the MZI EO E-field sensor offers E-field sensing capabilities extending to several THz, with an interaction length of 600 µm [22]. Illustrations within the publication depict the schematics of each sensor and the packaged E-field sensor head. From the images of the packaged sensor, it is evident that the EO structure is meticulously integrated within the sensor head, complete with a protective layer encapsulating it. When positioned within an E-field environment subject to analysis, the induced E-field on the EO devices alters the optical signal phase in the MZI sensing arm or the micro-ring waveguide, leading to a discernible intensity difference at the EO device's output.

However, the EO E-field sensor discussed in Zhu's paper functions primarily as a field mapping device, rendering it unsuitable for the objectives of this project [28]. The optical sensing device required for this initiative must be fabricated entirely from non-electrical materials and possess a small footprint to facilitate seamless integration with the antenna system. Following this, a comprehensive exploration of antenna theory and the EO effect is provided to enhance understanding of the project's foundational concepts. Ultimately, the design process of the antenna unit, as part of the phased array antenna system, alongside the EO E-field sensing device, is detailed and introduced as a key component of this project.

2.4 Background: Electro-Optic Effect

At its core, EO effect manifests as a change in a material's optical properties, directly proportional to the presence of an E-field. This phenomenon can lead to two distinct types of modifications: alterations in the material's absorption characteristics and shifts in its refractive index. Among these, the alteration in absorption is typically less pronounced than the change in refractive index, to the extent that it often becomes negligible under many conditions. Within the realm of optical E-field sensing, the focus is predominantly on leveraging the EO effect to detect external E-fields varying in intensity, frequency, and phase. The modification of the refractive index attributed to the EO effect emerges as the fundamental aspect of interest and is set to undergo extensive examination throughout this project. To provide a visual representation of this phenomenon, an illustrative image depicting the EO effect in action is showcased in Figure 2.5 [29].

The EO effect encompasses a range of physical interactions between electrical signals and optical properties, though many of these interactions manifest weakly and thus fall outside the primary focus of this project. Fundamentally, the EO effect can be categorized into two principal phenomena based on the nature of the induced E-field's influence on the optical signal: the Pockels effect and the Kerr effect.

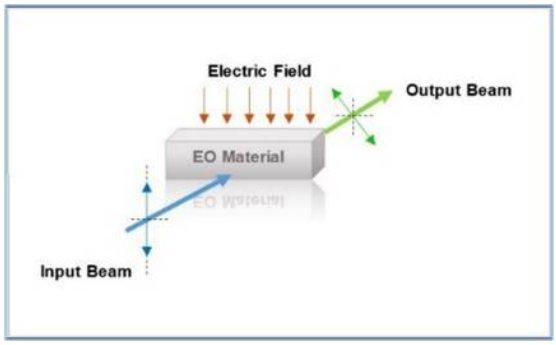

Figure 2.5: EO Effect Impact. Illustration of refractive index changes in EO material due to the EO effect.l

The Pockels effect, also known as the linear EO effect, results in a change in the material's refractive index (ΔK_{ij}) that is linearly proportional to the magnitude of the applied E-field (F_k), represented by the equation 2.1 [29]:

$$\varepsilon_0 \Delta K_{ij} = \sum_{k=1}^{3} r_{ijk} F_K \tag{2.1}$$

This effect is notable for its occurrence exclusively in EO materials that lack centrosymmetry in their lattice structures, rendering such materials as Pockels materials. This distinction is significant, as materials exhibiting the Pockels effect—such as LN and certain EO polymers—are among the most widely used EO materials globally due to their efficient and predictable response to E-field stimulation.

Conversely, the Kerr effect, also referred to as the quadratic EO effect, modifies the refractive index (ΔK_{ij}) of a material in proportion to the square of the excited E-field (F_k), as described by the following relationship:

$$\varepsilon_0 \Delta K_{ij} = \sum_{k=1}^{3} r_{ijk} F_K + \sum_{k,l=1}^{3} S_{ijk} F_K F_l \tag{2.2}$$

The Kerr effect notably occurs in EO materials characterized by centrosymmetric lattice structures. This architectural feature means that if an EO material displays a centrosymmetric lattice, it inherently lacks the capability to demonstrate the Pockels effect; instead, it exhibits the Kerr effect, with its influence rendered null [30]. When comparing the mathematical expressions governing both the Pockels and Kerr effects, it becomes evident

that the Pockels effect entails a simpler interaction of parameters and considerations. This simplicity largely accounts for the preference for Pockels materials in many applications, especially since most organic EO polymers fall into this category. In contrast, materials exhibiting the Kerr effect necessitate third-order nonlinearity, a complexity that presents synthesis challenges in laboratory settings. Furthermore, the nonlinear relationship between the induced E-field and phase delay restricts the utility of Kerr materials relative to their Pockels counterparts.

Given these considerations, this research project will primarily concentrate on the linear EO effects, specifically the Pockels effects, due to their numerous outlined advantages. The unique symmetry properties of the crystals enable the application of a three-by-three matrix, commonly referred to as the engineering notation, within the EO material structure. This matrix facilitates a direct correlation between the EO coefficients (r_{ijK}) and the crystal lattice numbers, offering a streamlined approach to understanding and manipulating the Pockels effect [29]. As such, the formulation for the Pockels effect is given clarity and specificity within the context of this project, leveraging the intrinsic symmetry properties of the crystals to elucidate the interaction between the optical signal and the E-field.

$$\varepsilon_0 \begin{bmatrix} \Delta K_1 \\ \Delta K_2 \\ \Delta K_3 \\ \Delta K_4 \\ \Delta K_5 \\ \Delta K_6 \end{bmatrix} = \begin{bmatrix} r_{11} & r_{12} & r_{13} \\ r_{21} & r_{22} & r_{23} \\ r_{31} & r_{32} & r_{33} \\ r_{41} & r_{42} & r_{43} \\ r_{51} & r_{52} & r_{53} \\ r_{61} & r_{62} & r_{63} \end{bmatrix} \begin{bmatrix} F_x \\ F_y \\ F_z \end{bmatrix} \tag{2.3}$$

The classification of EO modulators is fundamentally determined by the alignment of the input optical signal's propagation direction with that of the E-field. This delineation gives rise to two distinct modulator types: the longitudinal amplitude modulator and the transverse amplitude modulator. The longitudinal amplitude modulator is characterized by its application of an E-field that propagates in parallel to the optical wave, effectively aligning the electric and optical fields in the same direction. This modulator configuration is visually represented in Figure 2.6, top, providing a clear schematic of its operational principle.

Conversely, the transverse amplitude modulator operates under a different paradigm, where the applied E-field is oriented perpendicular to the optical signal's propagation direction. This orthogonal arrangement allows for a different modulation mechanism, as depicted in the lower section of Figure 2.6 [9]. The schematic illustrates the fundamental design and operational approach of the transverse amplitude modulator, offering insight

into its functionality and application within EO systems [29].

This distinction between longitudinal and transverse modulators highlights the versatility and adaptability of EO technologies in manipulating optical signals through precise control of the E-field's orientation relative to the optical wave propagation. Such understanding is crucial for the design and implementation of advanced EO devices within various optical communication and sensing applications.

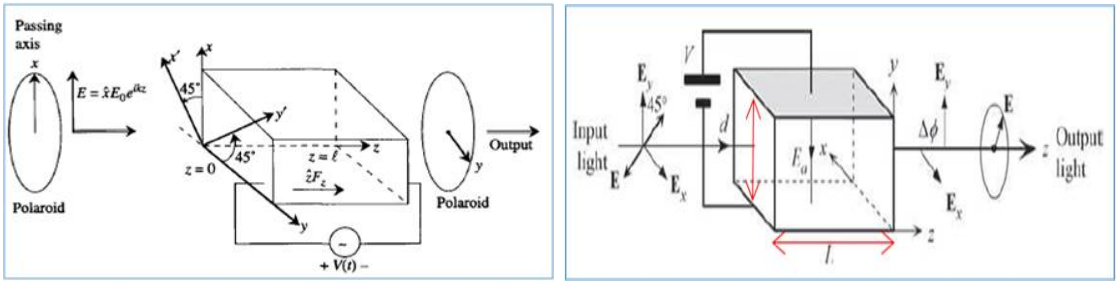

Figure 2.6: Optical Amplitude Modulator Schematics. Left: Longitudinal amplitude modulator. Right: Transverse amplitude modulator.

Leveraging the benefits of TFLN, this project selects TFLN as the EO material of choice. A key property of EO materials is their ability to alter refractive indices in response to external E-fields, especially when the material's guest polarization aligns with the polarization of the induced E-field. This alignment results in a change in the refractive index, which can be quantitatively described by the following equation:

$$\begin{aligned} \Delta n_x &= n_x - \frac{1}{2}\, n_0^3 r_{1j} F_k \\ \Delta n_y &= n_y - \frac{1}{2}\, n_0^3 r_{2j} F_k \\ \Delta n_z &= n_z - \frac{1}{2}\, n_0^3 r_{3j} F_k \end{aligned} \tag{2.4}$$

Given the alignment of polarizations, the refractive index change (Δn) in the material can be modeled accurately, allowing for precise manipulation of optical signals within the EO device. This capability underpins the utility of TFLN in this project, offering a sophisticated method to modulate light based on E-field interactions.

The refractive index variations induced by the Pockels EO effect manifest distinctly along the XYZ axes, with the coefficients r_{1j}, r_{2j}, and r_{3j} embodying the Pockels EO coefficients. These coefficients are closely tied to the crystal's symmetry, which in turn is

determined by the EO material's intrinsic properties. Notably, several matrix elements, referred to as r_{jk}, may be rendered null due to the crystal's unique symmetry features. This variability in Pockels coefficients (r_{ij}) across different axes necessitates consulting a crystal material data book for accurate identification and application [31]. The equations specifically formulated to compute the phase change resulting from the EO effect in LN material will be elaborated upon in the subsequent "Project Design Process" section, providing a deeper insight into the mathematical underpinnings essential for understanding and leveraging the EO effect in practical applications.

2.5 Background: Antenna

This research venture intersects the realms of optical and RF technologies, embarking on a cross-disciplinary inquiry that merges foundational theories from both the optical and RF domains. At the heart of this exploration is the EO sensing of E-fields in free space, a concept fundamentally reliant on the EO effect. The EO effect, arising from EO materials, enables the modulation of optical signals through variations in the material's refractive index induced by external E-field sources.

A key challenge addressed in this project is the measurement of the electrical near-field emanating from phased-array antenna units without distorting the antenna's radiation pattern. The solution entails devising a sensing device whose geometric design and integration with the antenna unit are meticulously planned to ensure minimal E-field interference. To conduct a thorough investigation into the behaviours of both the phased-array antenna unit and the tailored EO material device, an aperture-coupled patch antenna operating at 30 GHz has been selected as the antenna under test (AUT). Illustrative of the project's analytical depth, Figure 2.7 showcases two schematic diagrams: the left diagram provides a comprehensive view of a 64-element Active Phased-Array Antenna (A-PAA) [32], illustrating the array's overarching structure, while the right diagram zooms into an individual antenna element, highlighting the aperture-coupled feeding technique employed.

An A-PAA represents a sophisticated blend of multiple antenna elements, orchestrating a radio wave beam that can be electronically directed towards various orientations without necessitating any physical adjustment to the antenna itself. This capability to steer beams electronically is important, allowing for dynamic targeting and coverage adjustments. The A-PAA architecture comprises numerous antenna elements, each functioning akin to an individual patch antenna. The scale and complexity of an A-PAA can significantly vary, ranging from arrays with as few as four elements to configurations featuring thousands of elements, tailored to meet specific application needs [32].

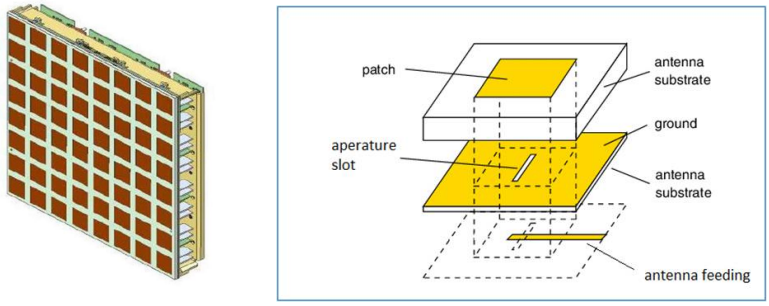

Figure 2.7: Active Phased Antenna Design. Left: Schematic of a 64-element active phased antenna. Right: Schematic diagram of an aperture-coupled patch antenna element in the A-PAA.

Several compelling reasons guided the selection of an aperture-coupled patch antenna as the target antenna for this project. A important factor is the configuration of the antenna patch, which is mounted atop the substrate layer, isolated from any surrounding materials. This distinctive setup allows for the strategic placement of optical sensing devices in areas where the E-field intensity is markedly strong, without the concern of causing interference with the antenna's top-mounted components. The use of this antenna type is prevalent in phased-array antenna designs due to its conducive surface condition that facilitates the capture of intensified E-field regions around the patch, making it an exemplary choice for this project [33].

The AUT is engineered to operate at 30 GHz, benefiting from a broad bandwidth attributed to its three-layer substrate design. The construction materials include copper for the patch, ground, and feeding mechanisms, while the substrate is composed of Rogers material, selected for its varying dielectric constants. These material choices and design considerations not only enhance the antenna's performance but also align with the project's objectives of E-field sensing. Further elaboration on the AUT, including in-depth discussions and analyses, is reserved for the simulation chapter, where these aspects will be explored comprehensively.

2.6 Project Design Process

Drawing insights from the comprehensive literature review, it's established that EO materials possess the capability for E-field sensing. Nonetheless, the structures outlined in

existing literature come with limitations that render them incompatible with the specific design requirements of this project. The ultimate goal here is to formulate an optical measurement methodology tailored for high-frequency phased-array antenna near-field assessments. This approach is distinct in its passivity, reliance on all-dielectric components, and immunity to electromagnetic interference, setting a high bar for the project's objectives.

Thus, the sensing structure to be designed is tasked with a critical function: it must accurately relay information regarding the E-field's strength, frequency, and phase as emanating from the antenna. This requirement not only emphasizes the need for precision in the sensing mechanism but also underlines the importance of integrating the EO material in a manner that complements the phased-array antenna's operational dynamics. The challenge lies in navigating the complexities of high-frequency electromagnetic fields while ensuring that the sensing structure remains non-intrusive and effectively immune to external electromagnetic disturbances.

The design process, therefore, revolves around innovating a solution that aligns with these stringent criteria, facilitating a seamless integration of EO materials into a sensing architecture capable of delivering precise, reliable measurements. This pursuit involves iterative design iterations, simulations, and testing to refine the sensing structure, ensuring it meets the project's unique requirements for high-frequency E-field measurement in phased-array antenna systems. For the purpose of this project, the focal point is a compact two by two phased-array antenna system, meticulously designed to operate at the 30 GHz frequency range. Each antenna element within this A-PAA is an aperture-coupled patch antenna, characterized by a flat metallic patch situated atop the substrate surface, ensuring uniformity in design across all array elements. To facilitate a detailed analysis and evaluation, one of these homogeneously designed elements is designated as the AUT. This detailed schematic representation serves as a foundational reference, aiding in the visualization and understanding of the A-PAA's configuration and the intrinsic design principles of its constituent antenna elements.

Drawing on antenna theory, it's understood that a patch antenna generates a significant electrical near-field in the space between the patch atop the substrate and the metallic ground plane beneath it. This near-field phenomenon is crucial for understanding and harnessing the antenna's operational characteristics, especially in the context of EO sensing. Figure 2.8 vividly illustrates this concept: the left image showcases the distribution of the E-field between the patch and the ground [34], while the right image highlights the intensified E-field present near the patch's edges. The pronounced E-field at the edges of the patch represents a critical zone of the near-field that necessitates precise measurement due to its substantial impact on the antenna's performance and the accuracy of field sensing.

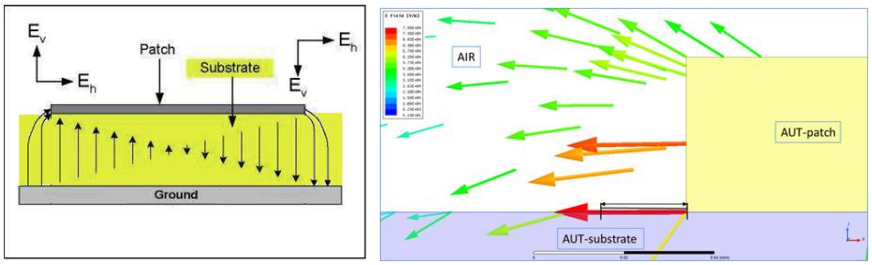

Figure 2.8: Antenna Field Distribution. Left: E-field distribution diagram of a patch antenna (side view). Right: Simulation of the E-field near the interface between the patch sidewall and the substrate.

At the commencement of this project, the design included a waveguide structure specifically engineered to encompass the antenna patch, strategically to harness the intensified E-field prevalent in this area. Simultaneously, TFLN was selected as the preferred material for constructing the optical sensor, designated to measure the E-field in the near-field region of the AUT. This selection was driven by LN's established effectiveness and reliability in EO applications, especially attributed to the Pockels effect. LN's distinguished performance in optical and sensing device applications underlines its suitability for capturing nuanced E-field variations, making it an optimal choice for achieving precise and stable near-field measurements within the project's scope.

The Pockels EO effect articulates that the refractive index of an EO material adjusts linearly in response to the intensity of the induced E-field, as encapsulated by the following equation [35]. This linear relationship between the E-field intensity and the refractive index change underpins the optical sensor's mechanism, enabling it to translate variations in the near-field E-field into measurable optical signals. Such a method promises not only to enhance the fidelity of E-field measurements but also to explore new avenues in the precise characterization and optimization of phased-array antennas.

$$\Delta n_e = -\frac{1}{2}\, n_e^3 r_{33} E_z \tag{2.5}$$

In this equation 2.5, n_e is the extraordinary refractive index of LN, serving as a critical factor in the EO response. r_{33} represents the primary EO coefficient of LN, crucial for modulating the material's optical properties under E-fields. E_z refers to the uniform E-field directed along the Z-axis, produced by the antenna, which facilitates the interaction between the antenna's electromagnetic output and the EO material. The refractive index alteration within the TFLN waveguide, resulting from the antenna's E-field, is described by

this equation. It illustrates the role of the induced Ez in modulating the TFLN's refractive index, employing LN's unique EO properties.

Subsequently, the phase change experienced by an optical beam as it travels through the TFLN waveguide is a direct consequence of the refractive index alteration induced by the antenna's E-field. This phase change is fundamental to understanding how E-fields affect light propagation within EO materials, providing a basis for designing optical sensing mechanisms that can accurately measure E-field strengths and patterns in the vicinity of antennas. The precise calculation of this phase change involves applying the modified refractive index values to the optical beam's propagation equations, enabling the determination of how the E-field influences the optical signal's phase as it traverses the EO waveguide.

$$\Delta\phi = -\frac{2\pi}{\lambda}\, n_e^3 r_{33} E_z L \tag{2.6}$$

Where λ denotes the wavelength of the optical beam navigating through the TFLN waveguide, n_e represents the effective refractive index of the LN waveguide, and L represents the length of the TFLN waveguide that is subjected to the E-field. This contextual setting lays the groundwork for understanding the interaction between the optical signal and the E-field within the confines of the waveguide.

Based on the aforementioned equation, it becomes evident that the phase change induced by the EO effect within the TFLN waveguide exhibits a direct linear relationship with both the intensity of the induced E-field and the waveguide's length. The intensified E-field, particularly pronounced at the edges of the antenna patch, enables the TFLN waveguide to be strategically positioned in areas where the E-field intensity is at its peak. This positioning is critical for maximizing the EO effect's influence on the optical signal. However, a significant consideration in this setup is the constraint imposed on the TFLN waveguide's length by the E-field's distribution characteristics. Specifically, the optimal length of the waveguide is dictated to align with the length of the antenna patch, ensuring that the waveguide is fully encompassed by the strong E-field generated at the patch's edge. Adhering to this parameter ensures that the TFLN waveguide, when influenced by the strong E-field emanating from the patch, can efficiently induce a phase difference in the optical signal as it propagates through the waveguide.

This precise manipulation of the optical signal's phase, driven by the controlled interaction with the E-field, underlines the potential of TFLN waveguides in EO sensing applications. By carefully designing the waveguide's dimensions and positioning relative to the antenna patch, it is possible to harness the EO effect for detailed and accurate

measurements of the E-field characteristics, contributing significantly to the field of optical sensing technology.

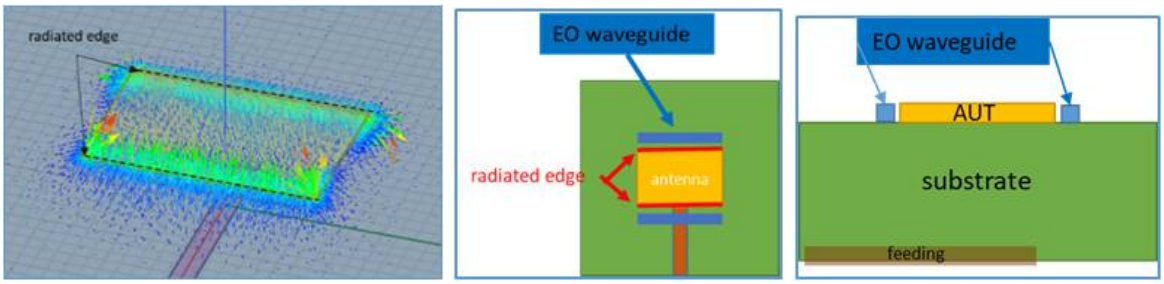

Figure 2.9: E-Field Distribution and EO Waveguide Design. Left: Simulation of E-field distribution from the edge of the AUT patch. Middle: Top view schematic diagram of two EO waveguides adjacent to the radiated edge. Right: Side view of the two EO waveguides alongside the radiated edge, on the same plane as the patch.

A distinctive characteristic of the aperture-coupled patch antenna is its design, where the two longer edges above the feeding stub act as the radiating edges. These radiated edges are crucial as they generate an E-field along their entire length, facilitating the EO effect across different points. Consequently, to harness the EO effect efficiently, the EO waveguide needs to be positioned adjacent to these radiated edges, where the E-field presence is most significant. The non-radiated edges, in contrast, do not emit an E-field and, thus, do not contribute to the generation of the EO effect, rendering them less pertinent for this purpose.

Illustrated in Figure 2.9, the left image showcases the simulation results highlighting the E-field distribution emanating from the patch's radiated edge. These results reveal a conspicuous absence of E-field activity at the center of the non-radiated edges, highlighting the targeted nature of E-field generation in this antenna design. Additionally, the middle figure provides a top view of two EO waveguides strategically positioned near the radiated edge to optimize E-field reception. The right figure offers a side view, presenting the EO waveguides adjacent to the radiated edge and aligned on the same plane as the patch. This configuration is designed to maximize the interaction between the EO waveguides and the E-field, thereby enhancing the sensing capabilities of the EO material.

Given that the phase delay induced by the EO effect is directly proportional to the EO coefficient r_{ij}, the utilization of LN material, recognized for its high EO coefficient relative to other EO materials, serves to significantly amplify the EO effect. This strategic choice of material not only optimizes the waveguides' sensitivity to the E-field but also leverages

the inherent properties of LN to facilitate a more pronounced and measurable phase shift in the optical signal. Such an approach emphasizes the meticulous consideration of material properties and antenna design in enhancing the efficiency and effectiveness of EO sensing applications.

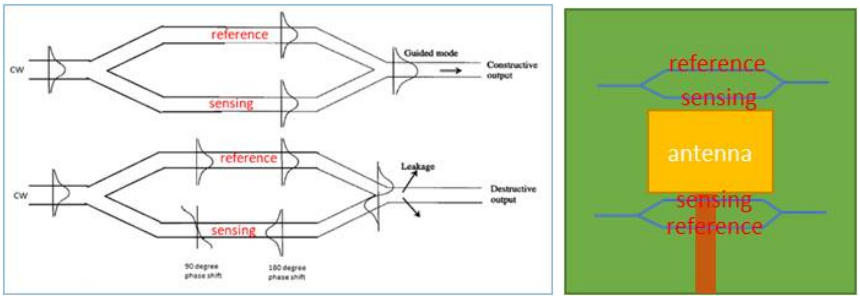

Figure 2.10: MZI Waveguide Structures. Left: Illustration of an MZI waveguide structure. Right: Schematic diagram of two TFLN-MZI waveguides adjacent to the antenna patch's radiated edge.

Given the distinct discrepancy between optical frequencies utilized within waveguides and the frequencies emitted by antennas, accurately analyzing phase differences in the optical signal traversing the waveguide can present complexities, potentially impacting the precision of experimental measurements. To mitigate these challenges and enhance measurement accuracy, the project has adopted the use of a MZI waveguide structure fabricated from TFLN material. This strategic choice allows for the conversion of phase differences, induced by the EO effect, into variations in signal intensity at the MZI output, offering a more straightforward and precise analysis method.

According to MZI theory, when the sensing waveguide and the reference waveguide within the MZI structure exhibit different phases, the optical signal recombined at the MZI waveguide's output is characterized by reduced signal intensity relative to that of the input signal. This phenomenon is attributed to the interference pattern resulting from the phase disparity between the two waveguide paths. In this setup, the sensing waveguide is strategically positioned close to the patch edge—where the E-field intensity is strongest—while the reference waveguide is placed farther away from this edge. Due to the rapid decrease in e-field intensity with increased distance from the patch edge, the E-field impact on the reference waveguide is significantly weaker in comparison to that on the sensing waveguide, to the extent that the EO effect on the reference waveguide becomes negligible.

This design ensures that the phase shift induced by the E-field in the TFLN waveg-

uide—corresponding to the sensing path—is effectively transformed into an intensity modulation observable at the MZI waveguide's output. The power of this modulated signal can be quantified by employing Equation 2.7 that account for the intensity modulation induced by the differential phase shift between the sensing and reference paths [29]. Through this approach, the project leverages the inherent advantages of the MZI structure, combined with the EO properties of TFLN, to achieve a sensitive and accurate method for measuring the E-field's influence on the optical signal, facilitating precise near-field measurements in experimental setups.

$$P_{out} = P_{in}\frac{1 + \cos\Delta\phi}{2} \tag{2.7}$$

Where P_{in} is the input power fed into the interferometer, $\Delta\phi$ symbolizes the phase difference encountered along the two paths within the MZI. This functional relationship elucidates how the output optical power from the MZI is linearly related to the phase shift engendered by the EO effect within the TFLN waveguide.

Leveraging the MZI waveguide structure facilitates the transformation of the phase shift into a discernible change in power, which can subsequently be captured and quantitatively assessed using an optical power meter. This conversion principle is critical, as it provides a direct method for measuring the impact of the EO effect on the optical signal's phase, translating it into a measurable power variation at the MZI waveguide's output. Such a mechanism highlights the MZI waveguide's utility across a spectrum of applications, encompassing optical switching, modulation, and sensing. By meticulously adjusting the phase difference between the two waveguide paths, the MZI enables precise control over the output power, showcasing its versatility and effectiveness in various optical systems. This ability to directly relate phase changes to power variations offers a robust method for exploring the EO effect's nuances, particularly in contexts requiring high precision and sensitivity in optical signal manipulation and measurement.

Choosing the right coupling method to integrate an optical signal from a laser source into a waveguide is a crucial decision that demands comprehensive analysis. Various coupling strategies have been investigated for their efficacy and suitability for different applications. These include the end-fire coupling method, which aligns the fiber directly with the waveguide's end facet to facilitate the direct entry of the optical mode from the fiber into the waveguide [36]; the grating coupling (GC) method, which employs a periodic structure etched onto the waveguide's surface to diffract light from the fiber into the waveguide [37]; and the tapered coupling method, which uses tapered sections in the waveguide to gradually match the waveguide's mode size with that of the fiber [38]. Each of these methods comes with its unique set of benefits and limitations.

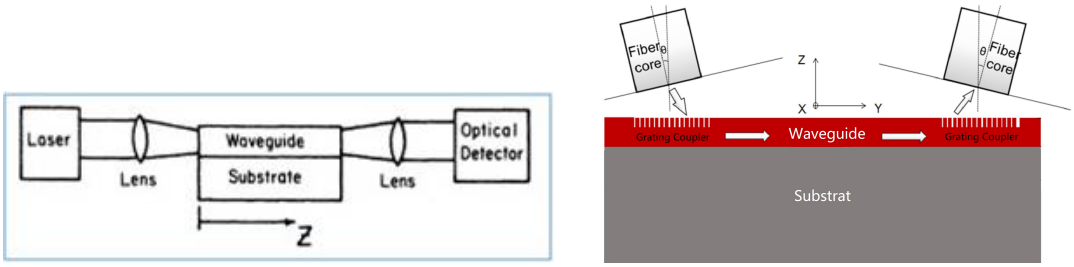

Figure 2.11: Coupling Methods Schematic. Left: Schematic diagram of the end-fire coupling method. Right: Schematic diagram of a grating coupler in the waveguide.

Illustrating these methods, Figure 2.11 on the left displays a schematic diagram of the end-fire coupling method [36], showcasing how the laser signal is coupled into and out of the waveguide. On the right side of Figure 2.11, a schematic diagram highlights how a GC is implemented within the waveguide setup [37]. These visual representations serve as invaluable references for understanding the practical application of each coupling method, offering insights into their operational principles and potential impact on the efficiency of light coupling in waveguide-based systems.

The end-fire coupling approach entails a direct alignment of the optical fiber with the waveguide's end facet, facilitating a direct transition of the optical mode from the fiber into the waveguide. This method necessitates precise alignment both laterally and longitudinally to ensure maximal coupling efficiency. Meanwhile, GC introduce light into the waveguide via a periodic structure etched onto the waveguide's surface, allowing for top-side coupling and potentially simplifying the alignment process. The tapered coupling method, on the other hand, employs tapered sections within the waveguide to gradually adapt the mode size, ensuring compatibility with the fiber's mode.

For this project, the GC method emerges as the optimal choice, particularly because the TFLN waveguide is positioned atop the antenna substrate. This positioning makes the GC's top-side coupling capability highly advantageous, enhancing efficiency and facilitating the experimental process. In contrast, for the transmission of the optical signal from the TFLN waveguide to the optical signal detector, the end-fire coupling method is preferred. This preference is due to its minimal fabrication requirements and the reduced need for extensive measurement equipment, streamlining the experimental setup. These strategic choices in coupling methods highlight the project's nuanced approach to experimental design, balancing efficiency, precision, and practical considerations to optimize the integration of optical signals within the EO sensing apparatus.

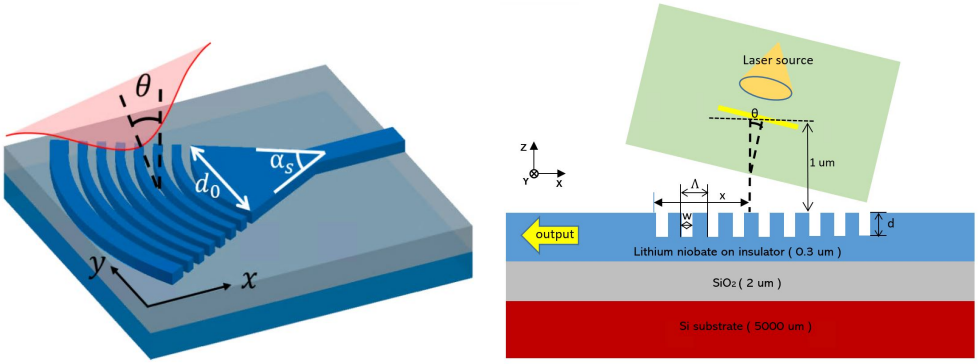

Figure 2.12: Focusing Grating Coupler Design. Left: 45-degree top view of a focusing GC. Right: Cross-sectional view of a GC with design parameters for the TFLN waveguide.

The schematic depicted in Figure 2.12 showcases a dual perspective: on the left, a 45-degree view highlights a focusing GC characterized by its curved grating lines [39] on the right, the detailed architecture of the GC, as employed in the TFLN waveguide configuration, is revealed. This illustration delineates key parameters integral to the GC's functionality: Λ represents the grating's period, Θ denotes the incident angle of the laser source relative to the surface normal, w specifies the grating's etching length, d indicates the etching depth, and x marks the laser source's incident position in relation to the GC's first pitch. Highlighted in green, the input optical laser source is strategically positioned atop the GC, while the LN waveguide, adorned with uniformly etched grating structures, is depicted in blue.

The GC stands as a cornerstone element in waveguide devices, streamlining the transition of optical signals from free space into the waveguide's confines with remarkable efficiency. The design of the GC's periodic pattern is crucial; by accurately calibrating parameters such as Λ, Θ, w, and d, the incident optical signal can be diffracted at meticulously calculated angles. This precision ensures an optimal alignment with the waveguide mode, thereby enhancing coupling efficiency. Particularly, the parameter Λ is finely adjusted to resonate with the 1550 nm wavelength of the incoming laser and the effective refractive index of the LN waveguide mode, fulfilling the phase matching conditions requisite for maximal coupling efficiency. The relationship between Λ and the laser source angle, Θ, is described by the following equation 2.8, providing an empirical foundation for estimating Λ's range to achieve optimal coupling dynamics.

$$\frac{\lambda}{n_{GC} - \sin\Theta} \leq \Lambda \leq \frac{\lambda}{n_{sub} - \sin\Theta} \tag{2.8}$$

Central to the design of the GC is the precise calculation of its period (Λ), a task guided by the equation 2.8, where λ is the wavelength of the optical signal, n_{GC} is the refractive index of the grating coupler, and n_{sub} is the refractive index of the substrate. For this project, the chosen wavelength, λ, is 1550 nm, reflecting the operational standard in optical telecommunications. The refractive index of LN at this wavelength is 2.21, showcasing its optical clarity, while that of SiO_2, the substrate, is 1.555, ensuring optimal light propagation conditions.

To circumvent high second-order reflections at the waveguide-grating interface, a critical design consideration, the laser source's incident angle, Θ, is meticulously maintained between 8-degree and 10-degree, as advised by Taillaert (2006) [40]. Following the guidance of the aforementioned equation, the grating period, Λ, is calculated to ideally span from 749 nm to 1122 nm. This range is vital for achieving efficient coupling, illustrating the complicated balance between optical physics and practical design constraints. Moreover, the grating's fill factor—the proportion of the etched versus the unetched region within one grating period—and its depth emerge as important variables. These elements not only influence the coupling strength but also dictate the operational bandwidth of the GC, emphasizing the necessity for their careful consideration during the design phase.

The exploration and optimization of these parameters continue beyond theoretical calculations, extending into the domain of simulations detailed in the subsequent chapter on simulation strategies. Through the employment of advanced simulation tools and iterative design methodologies, engineers and researchers can fine-tune the GC's characteristics. This process is instrumental in realizing high coupling efficiency, a crucial factor in minimizing signal losses within photonic integrated circuits and thus, elevating the overall performance of optical communication systems.

With the decision to utilize an aperture-coupled patch antenna for the AUT, the initial design process enables the estimation of some fundamental RF parameters based on the antenna's configuration. The electrical near-field emitted by the AUT is expected to resonate and propagate from the metallic patch situated atop to the metal ground layer beneath. Furthermore, considering the skin effect, the architecture of the feeding network below, and the orientation of the aperture slot on the ground plane, it is plausible to deduce that the patch's longer edge will serve as a hotspot for E-field emission [41].

For this project, TFLN has been selected as the EO material of choice, distinguished by its Pockels coefficient (r_{33}) of 30 pm/V, as cited in the literature. Additionally, the effective refractive index of LN waveguide is calculated to be 3.58 at a 1550 nm wavelength, aligning with the chosen wavelength for the optical sensing application. The choice of the 1550 nm wavelength is strategic, considering its widespread use in telecommunications, which

inherently enhances the project's experimental feasibility by simplifying the procurement of laser source equipment and other optical devices operating at this wavelength.

This strategic selection of materials and wavelengths highlights a meticulous approach to designing an experimental setup that is both practical and aligned with industry standards. By leveraging the prevalent 1550 nm laser technology, the project is poised to benefit from the readily available infrastructure, thereby reducing potential challenges associated with equipment compatibility and availability, and ensuring a smoother transition from theoretical design to experimental validation. In this project, the dimensional congruence of the TFLN waveguide with the antenna patch is paramount, with both featuring a length of 3 mm along the patch's long edge. This specification is critical for ensuring optimal interaction between the waveguide and the E-field radiated by the antenna patch. Notably, the E-field intensity near the patch edge reaches a significant 30,000 V/m, providing a substantial basis for the EO effect to modulate the optical signal within the TFLN waveguide.

Utilizing these parameters, the phase delay induced by the TFLN waveguide due to the EO effect can be precisely calculated. The resultant phase change is determined to be 0.502 radians. This phase shift is of particular interest as it directly translates into an intensity difference observable within the MZI waveguide structure. When the EO material's length is maintained at 3 mm and subjected to an E-field intensity of 30,000 V/m, the phase delay attributable to the EO effect is quantified at 0.502 radians, which corresponds to an intensity difference of 6.2 % according to equation 2.7. Given the experimental setup includes two MZI waveguides positioned on either side of the antenna patch's radiating edge, the cumulative theoretical power difference induced by the antenna's E-field is estimated at 12.4 %. This figure represents the calculated power difference at the output of two MZI waveguides, excluding considerations for the coupling efficiency of both the GC at the waveguide's input and the end-fire coupling at its output.

This meticulous calculation highlights the theoretical foundation for analyzing the EO effect's impact on the optical signal within the project's framework. By correlating the E-field intensity with the induced phase and intensity changes in the TFLN waveguide, the project advances towards achieving a passive, all-dielectric, and electromagnetic interference-immune method for high-frequency phased-array antenna E-field near-field measurement. The detailed approach to coupling, combined with precise calculations, lays the groundwork for subsequent experimental validation and optimization of the TFLN waveguide sensing mechanism.

2.7 Summary

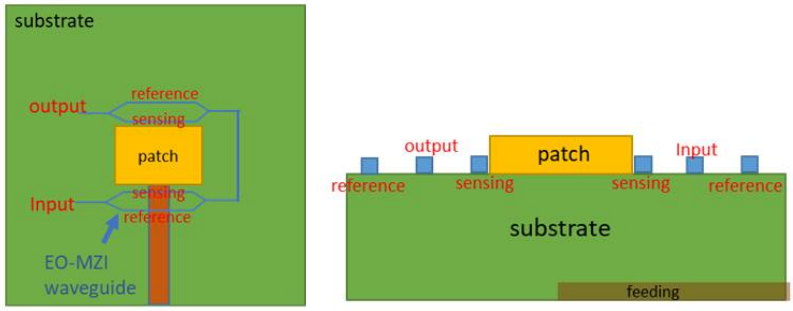

Figure 2.13: U-Shape TFLN-MZI Waveguide Configuration. Left: Top view of U-shape TFLN-MZI waveguide structures around the antenna patch. Right: Side view of the antenna patch and U-shape TFLN-MZI waveguide structures.

The novel design of the TFLN MZI waveguide structure for E-field sensing of patch antennas is elaborately depicted in Figure 2.13. This illustration provides a comprehensive view, with the left side offering a top perspective of the proposed TFLN-MZI waveguide sensing architecture, while the right side furnishes a side perspective of the same structure. Central to this design is the patch antenna characterized by two radiated edges, alongside which the sensing waveguide—comprising U-shaped TFLN waveguide structures equipped with dual MZI configurations—is strategically positioned. This precise placement ensures optimal reception of the E-field radiated by the antenna's edges.

The U-shaped configuration of the TFLN waveguide, incorporating two MZI setups, is ingeniously designed to facilitate the propagation of the modulated optical signal from the first MZI structure's output port to the second MZI structure's input port. To maintain structural and operational coherence, the connecting waveguide mirrors the TFLN-MZI waveguide's design, ensuring uniformity in signal transmission within the sensing framework.

At the waveguide's inception point, a GC, meticulously crafted from TFLN material, serves to adeptly channel the optical beam from the fiber into the waveguide, exemplifying an efficient coupling strategy that capitalizes on the material's EO properties. Conversely, at the waveguide's termination, the end-fire coupling method is employed to facilitate the egress of the optical signal from the U-shaped TFLN waveguide structure, enhancing the system's overall effectiveness in signal transmission.This carefully crafted TFLN EO E-field sensing waveguide structure is set to demonstrate a 6.2 % reduction in optical

signal intensity when subjected to an E-field intensity of 30,000 V/m originating from the antenna patch. This reduction is not observed in conditions where the antenna's E-field is absent. Such pronounced modulation, attributed to the responsiveness of the TFLN-MZI waveguide structure to an EO coefficient of 30 pm/V, highlights the structure's acute sensitivity and its capability to accurately detect and quantify changes in the optical signal induced by the E-field.

Moving forward, the next chapter will delve into simulations of the designed patch antenna and the TFLN-MZI waveguide structure. This step aims to deepen the understanding of how these devices operate and to identify avenues for enhancing their performance. Through simulation, complicated aspects of the waveguide's interaction with the E-field and its effects on the optical signal will be explored, paving the way for further optimization of this advanced EO sensing solution.

Chapter 3

Simulations for Antenna and Optical device

3.1 Introduction

This project introduces an innovative optical structure designed for electric field (E-field) sensing applications, utilizing electro-optical (EO) materials. The focus is on detecting the near-field E-field emanating from an aperture-coupled patch antenna operating at 30 GHz, referred to as the antenna under test (AUT). The optical signal within this structure is characterized by a 1,550 nm continuous-wave mode, generated by a laser source. The foundational principle of employing EO materials, such as lithium niobate (LN) with significant EO coefficients for sensing the near-field emitted by the AUT, has been elucidated in the preceding chapter. Following this, comprehensive simulations are undertaken to evaluate the functionality and performance of the designed thin-film lithium niobate (TFLN) waveguide structures in conjunction with the AUT. These simulation results are crucial for validating the design concept and for the refinement of the proposed structures. Accordingly, a variety of simulation software packages are applied in this research to address different simulation domains: HFSS for antenna performance, Lumerical for optical waveguide analysis, and Lumerical Device Simulation for hybrid simulations.

The HFSS software is utilized to simulate the performance of the AUT and to compute near-field outcomes, including the S-parameter for electromagnetic (EM) field return loss (S_{11}), the S-parameter for EM field insertion loss (S_{12}), and the E-field distribution emanating from the AUT. These simulations are conducted in three dimensions to ensure the accuracy of the results. Following this, the Lumerical software is employed to simulate the

design and optimization of the TFLN optical waveguide structure under two-dimensional conditions. This step is fundamental for minimizing optical loss within the TFLN waveguide structure, both for individual components and the structure as a whole. Additionally, the performance and optimization of the TFLN-based gating coupler (GC) are investigated using Lumerical. Next, the multiphysics capabilities of Lumerical simulation package are leveraged to simulate the hybrid scenario where the AUT in the radio frequency (RF) domain and the waveguide in the optical domain are simultaneously active, facilitating the study of EO effects. Given the disparity in wavelength scales between the optical signal (1,550 nm) and the antenna (10 mm), a comprehensive 3D simulation encompassing the entire optical waveguide structure alongside the AUT is impractical on a desktop computer. Plans were made to execute a 3D simulation of the TFLN-MZI waveguide structure at the CIARS cluster; however, the simulation was halted after 5 hours due to insufficient memory, despite an anticipated duration exceeding 1,000 hours. Subsequently, a simplified simulation incorporating only a straight TFLN waveguide with the AUT was conducted in Lumerical FDTD 3D simulation to corroborate the EO effect on the optical signal as influenced by the AUT's near-field. Finally, a device-level simulation will be conducted using Lumerical Interconnect to predict the performance of the optical measurement system and the integrated experiment. The COMSOL Multiphysics simulation package will also be used in the project to analyze the simulation results from Lumerical as a secondary tool and handle minor simulation tasks.

3.2 Simulation: Antenna

The initial simulation task within this project focuses on the analysis of an aperture-coupled patch antenna, serving as an antenna element within a phased-array antenna system. This particular patch antenna is designated as the AUT for the duration of this project. Following the preliminary design phase, the antenna's performance is simulated in HFSS to evaluate its efficacy as a transceiver antenna. Based on the design specifications, the AUT is constructed as a six-layer structure, featuring a slot on the ground layer to facilitate aperture-coupling and a copper tape at the base serving as the feeding network.

The selection of an aperture-coupled patch antenna for the AUT is justified by several design considerations. Principally, the flat rectangular patch situated at the top is physically separated from the feeding mechanism located at the bottom. This spatial separation is critical in mitigating potential E-field interference between the feeding network and the patch itself. Moreover, this antenna design is a prevalent choice for units within phased-array antenna systems, attributed to its ability to minimize interference and en-

hance performance [42]. Figure 3.1 (left) displays the simulated representation of the AUT in HFSS, while Figure 3.1 (right) provides a schematic overview of the AUT, with each layer meticulously labelled for clarity.

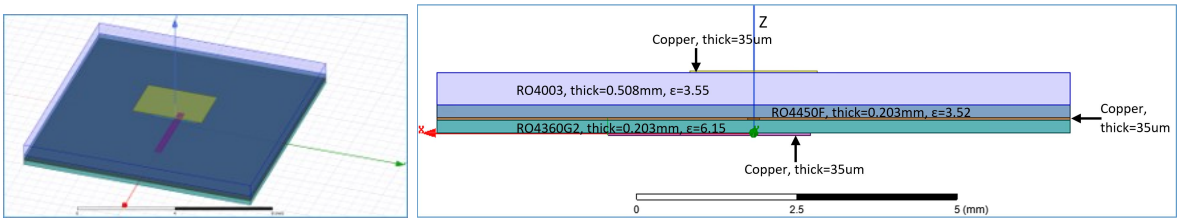

Figure 3.1: Phased-Array Antenna Unit Simulation. Left: 45-degree top-side view HFSS simulation of an aperture-coupled patch antenna. Right: Cross-sectional view of the AUT showing diameter for each layer in HFSS.

The evaluation of the AUT encompasses three critical aspects within HFSS: the S_{11} parameter, the radiation gain plot, and the radiation pattern. The S_{11} plot is instrumental in assessing not only the return loss of the antenna's feeding network but also the excitation frequency of the AUT. Examination of the S_{11} plot reveals that the operating frequency is identified at the curve's lowest point, which is determined to be 28.9 GHz. Additionally, the excitation frequency of the AUT is established at 28.9 GHz. The bandwidth of the antenna is delineated by the width of the curve falling below -10 dB, with the AUT exhibiting a 10% antenna bandwidth, as illustrated in the plot displayed in Figure 3.2. Furthermore, Figure 3.2 investigates the effects of integrating vias into the antenna structure, presenting simulated S_{11} parameters for configurations with and without vias. The inclusion of vias in the antenna design is observed to induce a slight upward frequency shift in the S_{11} pattern and a decrease in the S_{11} peak magnitude. Hence, the dimensions and positioning of these vias are identified as crucial considerations, necessitating careful attention in subsequent experimental attempts.

The radiation gain plot, as depicted in Figure 3.3 on the left side, showcases the gain of the AUT at two distinct phases. Analyzing the plot, the red curve signifies the gain at the 0-degree phase, while the purple curve corresponds to the gain at the 90-degree phase. It is observed that the maximum gain for the 0-degree phase shift approximates 6, a value that remains consistent with the maximum gain observed in the 90-degree phase shift curve. On the right side of Figure 3.1, the near-field radiation pattern of the AUT, as simulated in HFSS, is illustrated. This radiation pattern employs a rainbow-coloured bar to denote the direction of the radiated RF signal from the AUT, showcasing varying intensities. A label positioned at the top of the radiation pattern highlights that the maximum value reaches

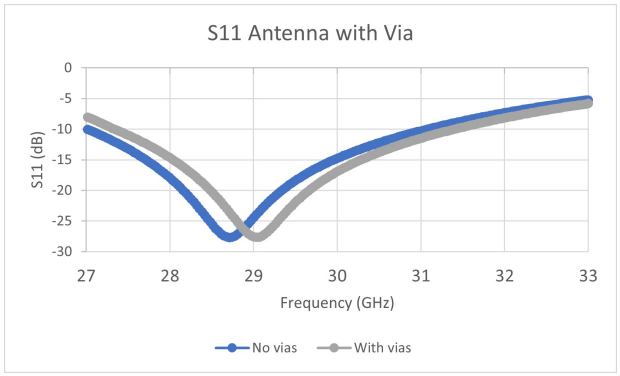

Figure 3.2: S_{11} Parameter Measurement. Plot showing S_{11} measured from the AUT with and without vias using HFSS.

6.2, corroborating the results obtained from the gain plot simulation on the left. This alignment between the gain values and the radiation pattern emphasizes the consistency and reliability of the simulation outcomes.

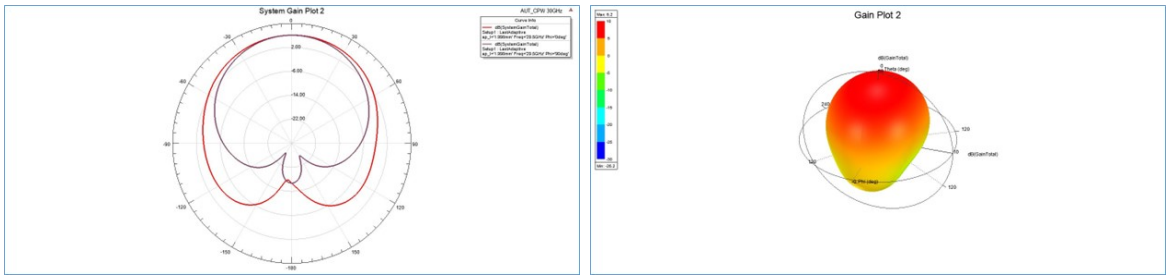

Figure 3.3: AUT Performance Plots. Left: AUT gain plot measured by HFSS. Right: Near-field radiation pattern for the AUT measured by HFSS.

The final aspect of the simulation involves analyzing the E-field distribution emanating from the AUT structure, conducted using HFSS. Theoretical insights reveal that the phase delay in the TFLN waveguide, caused by the EO effect, is closely related to the intensity of the induced E-field. Consequently, to maximize the EO effect, the TFLN waveguide must be strategically positioned to intersect the areas of highest electromagnetic (EM) field intensity emitted by the AUT. Beyond merely the intensity of the E-field, the length of the TFLN waveguide that traverses through the E-field plays a important role in influencing the EO effect. Therefore, the results depicting the E-field distribution from the AUT hold paramount importance for the project, as they provide critical data for optimizing the

placement and design of the TFLN waveguide to enhance the EO effect's efficiency. This detailed understanding of the E-field distribution is essential for tailoring the waveguide's characteristics to the specific EM environment generated by the AUT; as a result, ensuring the optimal interaction necessary for the intended sensing applications.

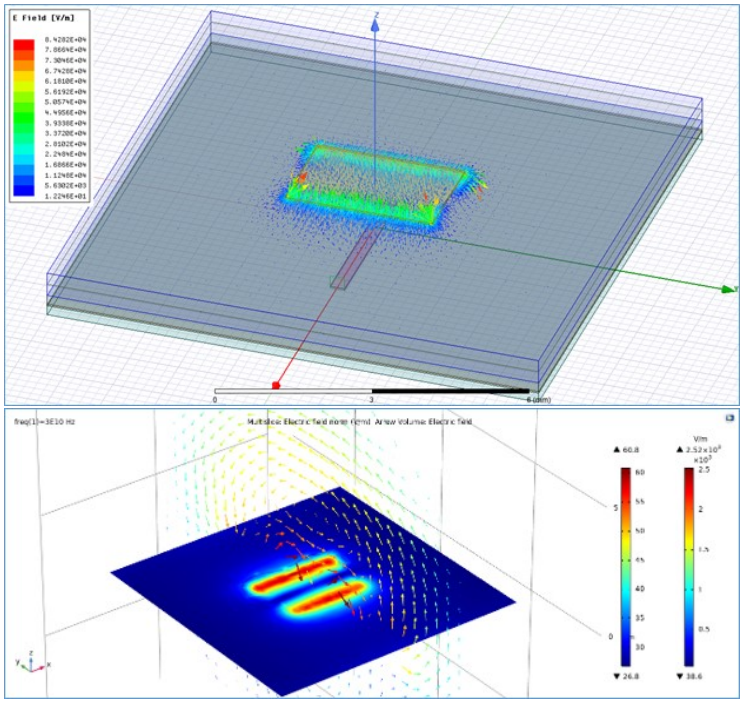

Figure 3.4: E-Field Distribution Simulation. Left: 45-degree top view HFSS simulation of E-field distribution for the AUT patch. Right: Top view of the E-field distribution from the AUT patch.

Figure 3.4 (left) demonstrates the E-field distribution surrounding the AUT patch and atop the AUT substrate, depicted through vibrant arrows. This illustration is derived from a simulation snapshot taken in HFSS from a 45-degree angular perspective. The AUT patch is centrally located at the origin of the XYZ-coordinate system, which also marks the top of the AUT substrate. The colourful arrows within the figure not only indicate the direction of field propagation but also visually represent the field intensity.

The AUT's radiated E-field originates from the patch's edges, extending into the free space beyond the patch. For simulation purposes, the antenna source voltage of the AUT has been set to 1 volt (V), equating to an input power of 100 milliwatts (mW). The intensity of the E-field is denoted by the colour of the arrows, with the colour bar positioned at the

top-left corner of the figure serving as a guide. The maximum E-field intensity, reaching 84200 V/m, is illustrated in red and is found at the corner of the AUT patch. Conversely, the minimum E-field intensity, measured at 14.2 V/m, is located in the middle of the patch's short edge, parallel to the y-axis. This observation suggests that the short edge of the patch is less significant for the EO effect due to its minimal E-field presence.

To improve the EO effect, the EO material waveguide should be positioned adjacent to the patch's longer edge, where the highest E-field intensity is recorded. However, as indicated in Figure 3.4 (right), there is a noticeable rapid decrease in E-field intensity from the patch's edge to the free space. This gradient of E-field intensity features the importance of the distance between the waveguide core and the patch edge, a critical parameter that necessitates careful consideration in the design of the Mach-Zehnder Interferometer (MZI). This detailed analysis of the E-field distribution is crucial for ensuring that the EO waveguide is optimally placed to harness the maximum EO effect, thereby enhancing the overall performance of the sensing application.

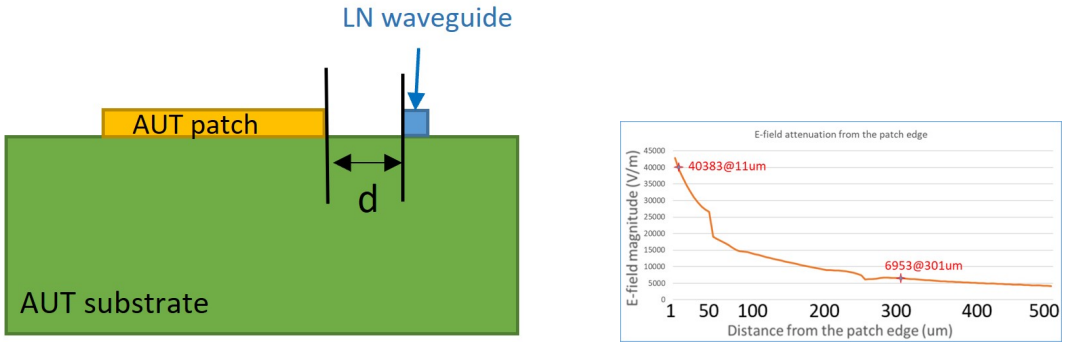

Figure 3.5: LN Waveguide Proximity Effect. Left: Schematic of the TFLN waveguide positioned on the AUT substrate with distance d. Right: Plot of E-field intensity versus distance d to the patch edge.

In Figure 3.5, the left panel represents a schematic depiction of the TFLN waveguide positioned atop the antenna's substrate, adjacent to the patch, with a specified distance, d, separating them. On the right panel, a simulation plot demonstrates the attenuation of the E-field intensity emanating from the edge of the AUT patch when the surrounding environment is air. This plot reveals that the E-field intensity diminishes with increasing distance from the patch edge, exhibiting three distinct phases in the rate of decrease.

During the initial phase, there is a sharp decline in E-field intensity, dropping from 45,000 V/m to 15,000 V/m as the distance extends from 0 µm to 75 µm. Subsequently, in

the second phase, the E-field intensity further decreases from 15,000 V/m down to 7,000 V/m, with the distance from the patch edge ranging from 80 µm to 250 µm. The rate of decrease in this phase is significantly slower compared to the initial phase. Finally, beyond 250 µm, the E-field intensity curve stabilizes, showing minimal variation across the distance span from 250 µm to 500 µm.

Based on these observations, it is imperative for the TFLN waveguide, intended for sensing the E-field emanating from the antenna patch, to be positioned as proximally as possible to the patch edge to capitalize on the higher E-field intensity. Moreover, the reference waveguide, part of the TFLN MZI structure, should ideally be situated at a distance of 250 µm or less from the patch edge. This placement strategy aims to minimize the influence of the diminishing E-field, ensuring the waveguide's effective operation in sensing applications. This attentive consideration of distance and positioning highlights the critical interplay between the physical configuration of the waveguide and its functional efficacy in capturing the E-field dynamics for optimal sensor performance.

3.3 Optical Simulation

In this section, a detailed review and analysis of the physical parameters of TFLN material will be undertaken. Key properties such as the refractive index variation with frequency, propagation loss, and temperature sensitivity are of paramount importance. Understanding these characteristics is crucial for accurately simulating the TFLN waveguide across different simulation platforms, with the ultimate goal of aligning simulation outcomes as closely as possible with real-world behaviour. The optical simulation of the TFLN waveguide will be executed using the Lumerical simulation package, and the specific parameters utilized within the simulation will be delineated for comprehensive understanding.

The project leverages two primary simulation software packages: the Lumerical Finite-Difference Time-Domain (FDTD) simulation package for optical field simulations and the COMSOL Finite Element Method (FEM) Multiphysics simulation package for hybrid simulations. Lumerical stands out as a versatile simulation suite tailored for the modelling and analysis of light interactions within photonic structures. It employs FDTD among other sophisticated methodologies such as Mode Solutions and DEVICE for conducting EO simulations. The FDTD method is particularly beneficial for its time-domain approach to Maxwell's equations in three dimensions, facilitating the precise modelling of intricate photonic interactions within waveguides and other photonic devices. This approach is instrumental in capturing a comprehensive array of optical phenomena that are

characteristic of waveguide structures, including dispersion, nonlinear effects, and mode propagation.

Moreover, Lumerical's capacity to accommodate a wide range of wavelengths and material properties renders it an indispensable tool in the design, optimization, and elucidation of waveguide behaviours across various photonic applications. The integration of these advanced simulation tools enables a deep dive into the nuanced performance of TFLN waveguides, ensuring that the simulated models reflect the complexities and intricacies of real-world photonic systems. Through meticulous parameter selection and simulation, this section aims to bridge the gap between theoretical predictions and practical outcomes, laying a solid foundation for the subsequent phases of the project.

On the other hand, COMSOL Multiphysics emerges as a highly adaptable simulation platform that excels in the numerical resolution of a diverse array of physics-based challenges. It utilizes the FEM for solving partial differential equations across various physical domains. This methodological foundation enables COMSOL to adeptly handle complex multiphysics scenarios, where the interplay among different physical processes—such as thermal dynamics, mechanical stresses, electrical fields, and fluid flows—is intricately interconnected and requires simultaneous consideration. A notable strength of COMSOL, particularly relevant for the simulation of EO effects, lies in its comprehensive multiphysics capability. This feature allows for the seamless integration of electrical and optical simulations, thereby offering a complete analysis of EO devices, including modulators and switches. The design achieves this by precisely modelling the impact of electrical fields on optical properties and their mutual interactions.

In comparison to Lumerical, which is finely tuned for photonic and waveguide simulations, COMSOL adopts a more expansive approach. This breadth makes it exceptionally suited for projects that demand a detailed examination of the interactions between electrical and optical phenomena within a unified simulation framework.

For the scope of this project, the simulation tasks pertaining to the optical domain devices will predominantly utilize the Lumerical simulation package. Therefore, this section will elucidate the variables relevant to the simulation, which include the source power and the source frequency spectrum. Given that FDTD operates within the time domain, the electromagnetic fields in Lumerical are calculated over time. Accordingly, the system under simulation is stimulated by an imported source, and the time signal of this source, s(t), is typically a pulse. The calculation of this pulse can be represented by the following equation:

$$s(t) = \sin(\omega_0(t - t_0)) \exp(-\frac{(t - t_0)^2}{2(\Delta t)^2} t) \tag{3.1}$$

This equation highlights the temporal dynamics of the electromagnetic fields, capturing the essence of the simulation's initial conditions and the source's characteristics. Through the meticulous application of these simulation tools—Lumerical for focused photonic simulations and COMSOL for integrated multiphysics analyses—the project aims to achieve a comprehensive understanding and accurate modelling of the EO effects within the designed devices. This dual-simulation strategy ensures that both the detailed photonic interactions and the broader EO phenomena are thoroughly explored, paving the way for innovative solutions in the realm of EO devices.

The transformation of the time-domain signal s(t) into the frequency domain is achieved through the Fourier transform, represented by the equation:

$$s(\omega) = \int exp(i\omega t) s(t) dt \tag{3.2}$$

Ideally, if s(t) were a Dirac delta function, then s(ω) would equal 1. This idealization permits Lumerical to deduce the system's response across all frequencies from a singular simulation run. Furthermore, the frequency domain field monitors within Lumerical's FDTD solvers capture the electric and magnetic fields at frequencies specified by the user and report the simulation outcomes in the continuous wave normalization state (cwnorm). As detailed in Lumerical's documentation, the simulation results returned in the cwnorm state are normalized by the Fourier transform of the source pulse. This normalization effectively provides the impulse response of the system within Lumerical [43]. Subsequently the impulse response of the electric field, $\vec{E}_{imp}(\omega)$, is given by:

$$\vec{E}_{imp}(\omega) = \frac{\int exp(i\omega t) \vec{E}(t) dt}{s(\omega)} \tag{3.3}$$

This formulation implies that the field reported in the cwnorm state corresponds to the field that would be present if a continuous wave (CW) source with amplitude E_0 had been utilized at the angular frequency ω. This adjustment eliminates any frequency dependency arising from the finite pulse length of the source, ensuring that the units of the returned fields align with those of the time-domain fields.

In Lumerical, the power of the source is represented as a ratio number, but it can be quantified through the Poynting vector, derived from the electric (E) and magnetic (H)

fields introduced by the source. This integral is calculated over the source's injection plane, and the power injected into the simulation in the cwnorm scenario is expressed as:

$$P_{cwnorm}(f) = \frac{\frac{1}{2}\int Re(P(f)^{source}) \cdot dS}{|sourcenorm|^2} \tag{3.4}$$

Here, P(f) source represents the Poynting vector, with the source power measured in Watts. The waveguide input source in the Lumerical simulation is a Gaussian Beam source, peaking at a 1550 nm wavelength. Figure 3.6 illustrates the plot for the source power in the frequency domain. Additionally, as a reference, the source mode time spectrum in the simulation is also presented in Figure 3.6 (right). With this comprehensive understanding of the simulation setup in Lumerical, the TFLN waveguide situated on the SiO_2 layer with a silicon substrate will be simulated using this detailed configuration.

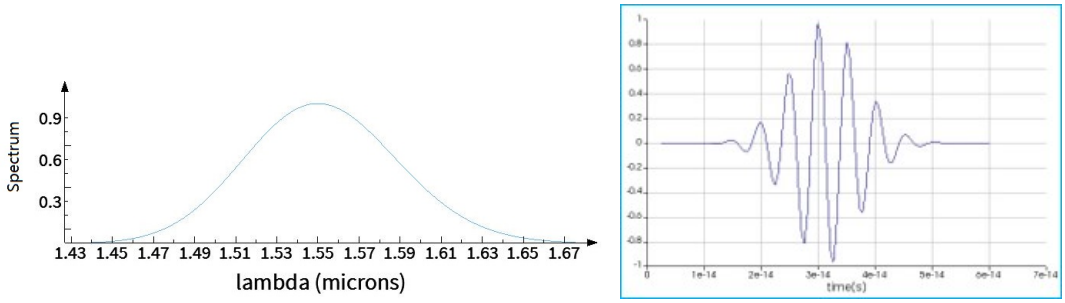

Figure 3.6: Simulation of Source Dynamics. Left: Source power simulation in the frequency domain. Right: Source mode time spectrum from Lumerical.

Following the detailed elucidation of the equations and simulation plots related to the source power within the simulation environment, attention now shifts to the optical properties of the TFLN waveguide, specifically focusing on its effective index and the propagation constant, denoted as beta (β). These optical properties are critical for understanding the waveguide's behaviour in guiding light and are directly influenced by the waveguide's geometry, material composition, and the operating wavelength of the light.

The effective index of a waveguide is a fundamental parameter that describes how the speed of light in the waveguide compares to the speed of light in vacuum. It is a dimensionless number that provides insight into the mode confinement and dispersion characteristics of the waveguide. The effective index is particularly important in the design and analysis of photonic integrated circuits, as it affects the phase velocity of light within

the waveguide and plays a crucial role in phase matching conditions in nonlinear optical processes.

The propagation constant, β, is another essential parameter that quantifies the phase change per unit length along the waveguide. It is directly related to the effective index by the equation:

$$\beta = \frac{2 * \pi}{\lambda} n_{eff} \tag{3.5}$$

where λ is the wavelength of light in vacuum and n_{eff} is the effective index of the waveguide mode. The propagation constant is instrumental in determining the phase and group velocities of light within the waveguide, as well as in the analysis of waveguide dispersion and coupling phenomena.

Figure 3.7 presents the simulation results for the effective index and the propagation constant of the TFLN waveguide. These results are obtained from the simulation environment, utilizing the previously discussed parameters and setup. The figure likely includes plots that depict how the effective index and β vary with wavelength or other relevant parameters, providing valuable insights into the waveguide's optical properties and its suitability for various photonic applications.

Understanding the effective index and propagation constant is crucial for the design and optimization of TFLN waveguides, especially in applications requiring precise control over light propagation, such as in optical communications, sensors, and integrated photonic circuits. The simulation data presented in Figure 3.7 thus serves as a key foundation for further analysis and design considerations in the development of LN-based photonic devices.

The effective index is a critical parameter in waveguide simulations, serving to specify the value around which the modes of the waveguide are solved. According to the simulation outcomes, a waveguide with a width of 0.75 µm is capable of supporting the transverse electric (TE) mode, which has been utilized to calculate both the effective index and the propagation constant. The imaginary part of the effective index, which arises due to the propagation loss inherent in the TFLN material, reflects the attenuation of the mode as it propagates through the waveguide. This attenuation is directly linked to the propagation loss values defined by the TFLN material properties, as discussed in the preceding section.

In the forthcoming section, the focus will shift towards the design and optimization of various segments within the TFLN waveguide structure—namely, the straight waveguide, the bending waveguide, and the Y-branch. The primary objective of this phase is to

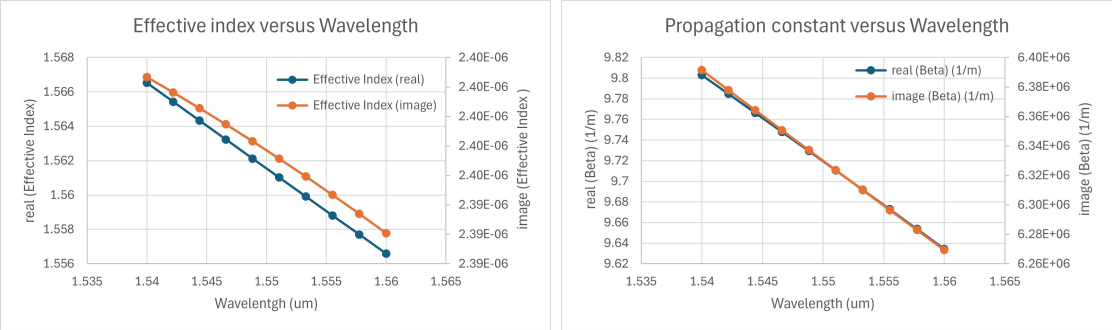

Figure 3.7: LN Waveguide Frequency Sweep. Simulated parameters for an TFLN waveguide (0.75 µm width), including left: effective index (real and imaginary) versus wavelength, and right: propagation constant (real and imaginary) versus wavelength.

minimize propagation loss, thereby enhancing the overall performance of the waveguide for its intended applications. To achieve this, Lumerical will be employed to meticulously design each segment, taking into account the unique challenges and requirements posed by their respective geometries and functionalities.

The choice of TFLN as the core material for the waveguide has been made after thorough consideration of its optical properties and suitability for the intended applications. The simulation environment has been carefully constructed to mirror real-world conditions as closely as possible, ensuring that the simulated behaviour of the waveguide segments accurately reflects their expected performance in practical scenarios. This approach not only facilitates a more reliable prediction of waveguide behaviour but also enables the identification and resolution of potential design issues before physical fabrication, saving both time and resources.

By systematically analyzing and optimizing each segment of the TFLN waveguide structure, the project aims to develop a highly efficient waveguide system with minimized propagation losses. This attempt is crucial for the successful implementation of TFLN waveguides in a variety of photonic applications, ranging from telecommunications to sensing and beyond, where precise control and manipulation of light are paramount.

3.4 Lithium Niobate

LN has emerged as a important material in the field of EO applications, distinguished by its unique physical properties in comparison to other EO materials. Among these properties,

the refractive index of TFLN is particularly noteworthy due to its significant frequency dependence, a characteristic that plays a crucial role in nonlinear optical processes. This frequency-dependent behaviour of the refractive index is instrumental in enabling a wide range of applications, from modulators and switches to frequency converters.

When compared to materials such as gallium arsenide (GaAs), TFLN demonstrates several advantages that underline its prominence in the field. One of the most significant advantages is its broader transparency range, which extends its usability across a wider spectrum of wavelengths. This characteristic is particularly beneficial in telecommunications and other applications that operate within the near-infrared spectrum, including the telecom wavelengths around 1550 nm. The transparency range of TFLN not only facilitates its application across various domains but also contributes to its versatility as a foundational material in photonic devices.

Furthermore, LN's superior phase matching capabilities are attributed to its unique dispersion properties. Dispersion, which describes how the refractive index of a material varies with frequency or wavelength, is a critical factor in many optical applications, especially those involving nonlinear optical processes. LN's dispersion properties allow for efficient phase matching, a condition where the phase velocity of different waves interacting within a medium is synchronized, thereby maximizing the efficiency of nonlinear optical interactions.

The refractive indices of LN, which range from approximately 2.2 to 2.3 at telecom wavelengths, are slightly lower than those observed in GaAs. This difference highlights LN's efficiency in optical waveguiding, as a lower refractive index contrast between the core and cladding materials can still facilitate effective light confinement with less material absorption. Reduced absorption is a key factor in enhancing the performance of optical waveguides by minimizing signal attenuation and preserving the integrity of the transmitted information.

In summary, the unique optical properties of lithium niobate, including its frequency-dependent refractive index, broad transparency range, and exceptional phase matching capabilities, make it an indispensable material in the development of advanced photonic devices. Its application in TFLN waveguides exemplifies the material's potential in harnessing and manipulating light for a multitude of cutting-edge EO applications.

Regarding propagation loss, TFLN presents a nuanced profile that merits close examination. Figure 3.8 illustrates the complex refractive index of TFLN at a 1550 nm wavelength, showcasing both the real part (n) and the imaginary part (k), according to the literature [44]. The plot reveals how the k value, which represents the material's absorption coefficient and is indicative of propagation loss, diminishes significantly as the

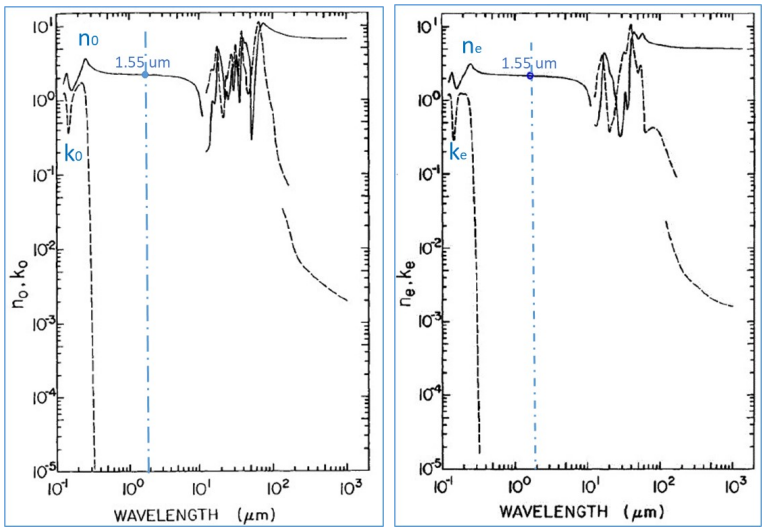

Figure 3.8: Wavelength Dependency of TFLN Indices. Log-log plot showing the variation of refractive indices n and k versus wavelength for LN, with left focusing on n_o and k_o, and right on n_e and k_e.

optical signal wavelength increases. Specifically, at a wavelength of 1550 nm, the ordinary refractive index (n_o) is recorded at 2.3007, and the extraordinary refractive index (n_e) at 2.2116. While LN's intrinsic losses are relatively low, the actual loss figures can vary notably depending on the crystal's quality and the specifics of the fabrication process.

In comparison, materials such as silicon nitride (Si_3N_4) are known for their lower propagation losses, often falling below 0.1 dB/cm. This is largely attributed to their superior material homogeneity and the refinement of fabrication techniques[44]. Nonetheless, advancements in TFLN fabrication technologies, including methods like proton exchange or ridge waveguide formation, have led to significant reductions in propagation loss. Recent achievements have seen propagation losses in TFLN ridge waveguides being lowered to as much as 0.2 dB/m[45]. Such advancements are important for the progress of high-performance optical communication systems and the broader field of integrated photonic circuits.

In the simulations conducted for this project, the TFLN material characterized by a propagation loss of 0.2 dB/m has been incorporated into the Lumerical simulation material library. This specific material profile is utilized as the waveguide material in all simulations, ensuring a realistic representation of LN's performance in photonic applications. This careful consideration of LN's propagation loss characteristics, coupled with

the latest improvements in fabrication technology, highlights the material's potential and adaptability in the evolving landscape of optical communications and integrated photonics.

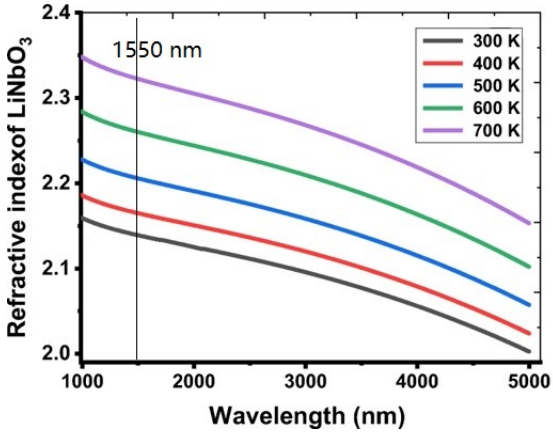

Figure 3.9: Temperature Dependence of TFLN Refractive Index. Variation of the refractive index of TFLN at different temperatures and wavelengths.

Temperature sensitivity is a crucial factor affecting the performance of LN, particularly impacting its refractive index and EO coefficients. Figure 3.9 illustrates the variation of LN's refractive index in response to temperature changes across different wavelengths, as documented in [45]. Specifically, at a wavelength of 1550 nm, an increase in temperature from room temperature 300 K to 400 K results in the refractive index of TFLN shifting from 2.14 to 2.18. This change highlights LN's thermo-optic coefficient, which is approximately 2×10^{-5} /^{o}C, positioning TFLN in a unique spot in terms of temperature sensitivity compared to other materials widely used in photonics and optoelectronics.

Silicon (Si), for instance, has a significantly higher thermo-optic coefficient, about 1.86×10^{-4} /^{o}C, which leads to a more substantial change in its refractive index with temperature variations. This characteristic of silicon offers greater tunability for devices, allowing for precise control over their optical properties. However, this also necessitates rigorous thermal management to ensure device stability and performance over varying operational conditions.

On the other hand, silicon dioxide (SiO_2) with a lower thermo-optic coefficient around 1×10^{-5} /^{o}C, provides a contrasting approach. Its relatively stable thermal response makes SiO_2 an excellent material for ensuring thermal stability within optical devices, making it a preferred choice in applications where minimal thermal dependence is desired.

The distinct thermal properties of lithium niobate, silicon, and silicon dioxide highlight

the critical role of material selection in the design and development of photonic devices. By understanding and leveraging these properties, engineers and designers can tailor devices to achieve an optimal balance between tunability and thermal stability. This balance is essential for the creation of high-performance photonic devices that can operate efficiently across a wide range of temperatures, ensuring reliability and effectiveness in various applications, from telecommunications to advanced sensing systems.

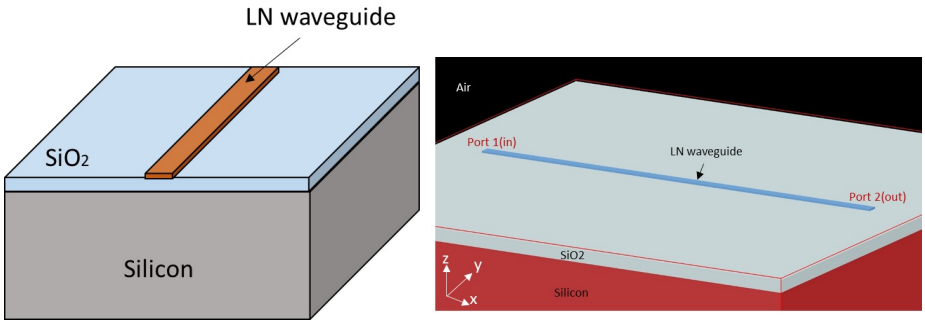

Figure 3.10: TFLN Ridge Waveguide for Simulation. Left: Schematic image of the TFLN ridge waveguide used in Lumerical simulations. Right: Simulation image of the TFLN waveguide in Lumerical.

After determining the physical parameters of LN, these variables are imported into Lumerical to facilitate the generation of the TFLN waveguide in the simulation. For this project, the focus is on the ridge waveguide configuration. Figure 3.10 (left) illustrates the TFLN ridge waveguide, complete with the isolation layer and the substrate as generated in the simulation environment, while the right side of Figure 3.10 showcases the TFLN ridge waveguide as created within Lumerical. Various types of waveguides have been employed in TFLN optical devices, including diffused waveguides for photo-exchanged TFLN devices and rib waveguides for TFLN devices. The choice of waveguide type for this project is significantly influenced by budgetary constraints and the available techniques for fabricating the TFLN waveguide.

During the pandemic, a TFLN wafer was acquired from a manufacturer. The cost of the TFLN wafer was contingent upon the thickness of the TFLN layer, with thicker layers incurring higher costs. For this project, a TFLN wafer featuring a 300 nm thick TFLN layer was procured, setting the waveguide's thickness at 300 nm. Additionally, the thickness of the SiO_2 isolation layer is set at 1 µm, and the thickness of the Si substrate is determined to be 500 µm. These parameters are meticulously incorporated into the simulation to ensure accuracy and relevance.

The refractive index of SiO_2 at a wavelength of 1550 nm is noted to be 1.444, and the refractive index of TFLN at the same wavelength is 2.21. The refractive index contrast, Δ, between TFLN and SiO_2 is a crucial parameter for waveguide design, affecting mode confinement and propagation. The refractive index contrast can be calculated using the equation below:

$$\Delta = \frac{{n_1}^2 - {n_2}^2}{2{n_1}^2} \tag{3.6}$$

where n_1 represents the refractive index of the core material (in this case, lithium niobate, LN) and n_2 means the refractive index of the cladding material (silicon dioxide, SiO_2, for the bottom cladding and air for the other three sides of the waveguide). Applying this equation to the TFLN waveguide design, where TFLN serves as the waveguide core material surrounded by SiO_2 and air as cladding, yields a refractive index contrast of 0.29. This significant contrast indicates that the TFLN waveguide exhibits strong guidance properties. Strongly-guiding waveguides confine the cross-sectional E-field profile predominantly within the core, as opposed to weakly-guiding waveguides where the E-field extends more into the cladding layer.

The width of the TFLN waveguide is another critical design variable in this project. The EO effect, induced by the E-field emanating from the antenna, contributes to the change in optical power at the output of the MZI waveguide. Given that the E-field intensity decreases with increasing distance from the antenna patch edge—specifically, it rapidly drops from 45,000 V/m to 15,000 V/m as the distance increases from 0 µm to 75 µm—minimizing the waveguide width can be advantageous. A narrower waveguide facilitates a more uniform distribution of refractive index changes within the TFLN waveguide, which is beneficial for the EO effect's efficiency.

However, reducing the width of the TFLN waveguide introduces certain challenges. Specifically, it complicates the fabrication process and may decrease the coupling efficiency for both GC and end-fire coupling methods. Considering the optical signal's wavelength of 1550 nm used in this project, two waveguide widths have been selected for investigation: half-wavelength (0.75 µm) and one wavelength (2 µm). These dimensions are chosen to explore the balance between effective EO modulation and practical considerations such as fabrication feasibility and coupling efficiency. Consequently, this approach aims to maximize the waveguide design for enhanced performance in EO applications, taking into account the intricate interplay between physical dimensions, optical properties, and fabrication constraints.

3.5 Lithium Niobate Based Optical Device

This section delves into the simulation results for a straight TFLN waveguide, aiming to elucidate the design and optical properties of the TFLN waveguide employed in this project. The straight TFLN waveguide serves as a foundational component of the LN-based E-field sensing structure, providing key insights into the behaviour and performance of the overall device.

The TFLN waveguide, chosen for its promising EO properties and compatibility with integrated photonic circuits, is initially simulated in its straight form. This preliminary step is essential for analyzing the optical characteristics intrinsic to the waveguide, which, in turn, influences the effectiveness and sensitivity of the E-field sensing mechanism.

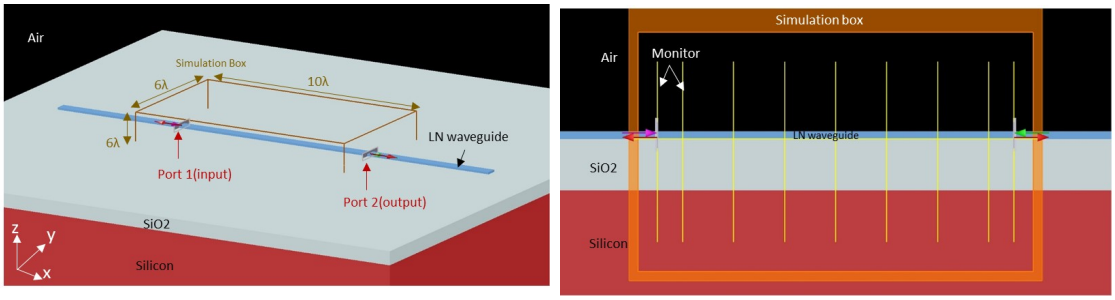

Figure 3.11: TFLN Waveguide Simulation Setup. Images of a straight TFLN waveguide on SiO_2 with simulation area setup. Left: 45-degree top view. Right: Cross-section view.

A detailed simulation of a straight TFLN waveguide, featuring dimensions of 750 nm in width and 300 nm in height, is depicted in Figure 3.11. The TFLN waveguide, highlighted in blue, is strategically positioned atop a silicon dioxide (SiO_2) layer, illustrating its integration within the waveguide structure. The simulation area, delineated by an original colour box, extends to 10 wavelengths in length along the x-axis and 6 wavelengths in height along the z-axis, with its width measured along the y-axis. The orientation of the simulation is clearly marked by the XYZ coordinate system, located at the left corner of the simulation image.

On the right side of Figure 3.11, the simulation image showcases yellow-coloured lines representing yz-plane field monitors. These monitors are strategically placed at various locations along the TFLN waveguide to detect the E-field distribution within the waveguide structure. This setup is crucial for analyzing the propagation characteristics of the optical signal through the TFLN waveguide and understanding how the waveguide's dimensions and material properties influence the E-field distribution.

It is noted that the simulation images for an TFLN waveguide with a width of 2 µm have not been included in this project, as they bear a strong resemblance to the simulation results for the 750 nm width TFLN waveguide. This decision stresses the focus on waveguide dimensions that are expected to significantly influence the EO effect and the overall performance of the TFLN waveguide in E-field sensing applications.

In addition, Figure 3.12 is dedicated to presenting the field profile of the optical signal as it propagates through the straight waveguide. This figure aims to elucidate the optical mode behaviour within the TFLN waveguide across different waveguide widths. By examining the field profile, insights into mode confinement, effective index, and propagation losses can be gleaned, which are critical for optimizing the waveguide design. This analysis is instrumental in tailoring the waveguide's dimensions and material composition to enhance its performance for specific applications, particularly in the realm of integrated photonics and EO devices. Through such detailed simulations, the project advances the understanding and application of TFLN waveguides in cutting-edge optical technologies.

The E-field distribution illustrated in Figure 3.12 was captured by the field monitor positioned on the lithium niobate waveguide. From the analysis of the electric field distribution for mode analysis, it is evident that the TE mode is the predominant mode for the optical signal propagating within the lithium niobate waveguide. This TE mode signal is effectively confined within the waveguide structure for both the 2 µm width waveguide and the 0.75 µm width waveguide. However, the transverse magnetic (TM) mode signal was observed to propagate through the silicon dioxide layer beneath the lithium niobate waveguide in both instances.

The propagation loss of the lithium niobate waveguide was not calculated in these simulation steps due to the waveguide's length being too short to clearly detect any significant propagation loss. The length of the TFLN waveguide in this simulation is 15 wavelengths (approximately 23 µm), and considering the imported propagation loss for lithium niobate material from the literature review is 0.2 dB/m, the propagation loss on a micrometre scale is minimal and can be disregarded.

In the lithium niobate-based electric field sensing device, the TFLN MZI waveguide structure plays a crucial role as it is utilized to convert phase differences into power differences at the MZI output. Nevertheless, the presence of many curved waveguides within the MZI structure could potentially introduce significant propagation loss for the optical signal transmitted through the structure. In Lumerical, the transmission parameter is employed to calculate the propagation loss of the waveguide structure. This normalized transmission parameter, denoted as T(f), is calculated based on the following equation:

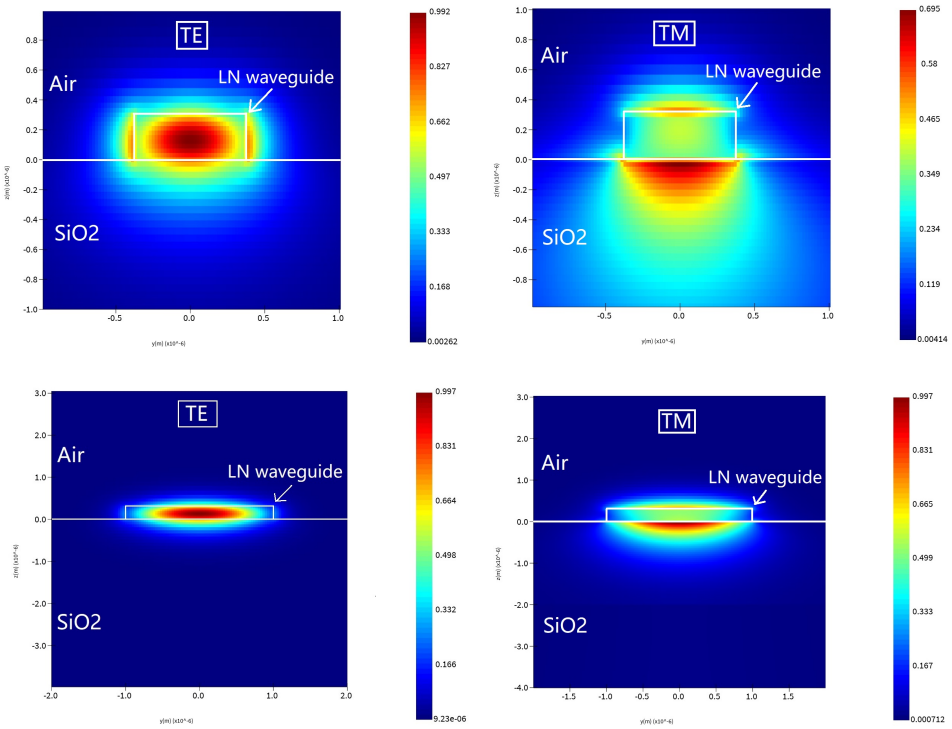

Figure 3.12: E-Field Distribution in TFLN Waveguide. Simulated E-field distribution for different modes and waveguide widths. Top left: TE mode in 0.75 µm width. Top right: TM mode in 0.75 µm width. Bottom left: TE mode in 2 µm width. Bottom right: TM mode in 2 µm width.

$$T(f) = \frac{1}{2}\frac{\int_{monitor} Re(p(f)) \cdot dS}{P_{source}(f)} \tag{3.7}$$

In the context, T represents the transmission as a function of frequency, where P(f) denotes the Poynting vector, illustrating the flow of electromagnetic power through a given area. The term dS refers to an infinitesimal element of the surface over which the Poynting vector is integrated, and it is oriented according to the surface normal. P_{source} is the normalized source power, serving as a reference for calculating the transmission. This normalization process allows for the comparison of transmitted power through the waveguide relative to the power initially introduced by the source.

The transmission value calculated provides insight into the efficiency of the waveguide

structure in guiding the optical signal. For example, a transmission value of 0.3 indicates that 30% of the optical power injected by the source has successfully passed through the waveguide structure and has been detected by the monitor. This metric is crucial for evaluating the performance of the waveguide, particularly in terms of its ability to minimize losses and maintain signal integrity over its length and through bends or other structural features.

Figure 3.13 displays simulation images for a bending TFLN waveguide situated on a silicon dioxide (SiO_2) layer, with the simulation area setup included. The left image provides a 45-degree top view of the bending waveguide, offering a perspective that highlights the curvature and the spatial relationship between the waveguide and its surrounding environment. The right image presents a direct top view within the simulation box, giving a clear depiction of the waveguide's path and the extent of the simulation area.

These simulation images are instrumental in understanding the behaviour of optical signals as they navigate through curved sections of the waveguide. Bending waveguides are particularly challenging due to the potential for increased propagation losses and mode distortion, which can significantly impact the device's overall performance. By analyzing these simulations, insights can be gained into optimizing waveguide design and layout to mitigate such issues, ensuring efficient signal transmission even through complex waveguide geometries.

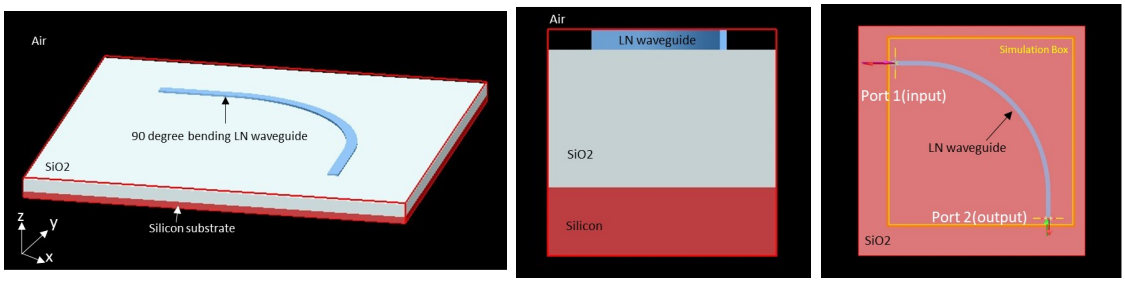

Figure 3.13: Bending TFLN Waveguide Simulation. Simulation images for the bending TFLN waveguide on SiO_2. Left: 45-degree top view. Middle: Cross-section view. Right: Top view with simulation box.

In the simulation, a bent TFLN waveguide with a 90-degree bending angle was constructed, featuring widths of 0.75 µm and 2 µm. A critical design parameter for this bent waveguide is the radius of curvature. A radius that is too small can lead to undesirable effects, such as optical signals reflecting back towards the input port or leaking into the cladding layer, which would significantly impair the waveguide's efficiency and signal integrity.

To mitigate propagation loss associated with the bend, it is essential to select a radius large enough to maximize signal transmission through the curved section of the waveguide. However, increasing the radius to enhance transmission introduces a trade-off with fabrication complexity. A longer bending waveguide, while potentially offering better performance in terms of minimizing loss and maintaining signal fidelity, complicates the manufacturing process and may introduce challenges in managing other optical signal modes.

To explore the relationship between the radius of the bent waveguide and its transmission efficiency, two power monitors are strategically placed along the TFLN waveguide: one at the input and another at the output of the bent section. This setup enables the capture and analysis of changes in optical signal mode as the light traverses the bend, facilitating the calculation of transmission through this critical part of the waveguide.

This investigation into the transmission characteristics of bent waveguides is crucial for optimizing waveguide design. By understanding how different radii affect signal loss and mode integrity, designers can make informed decisions to balance the competing demands of fabrication feasibility and optical performance. Such optimizations are essential for the development of high-efficiency, low-loss photonic devices that rely on precisely engineered waveguide geometries to achieve desired operational outcomes.

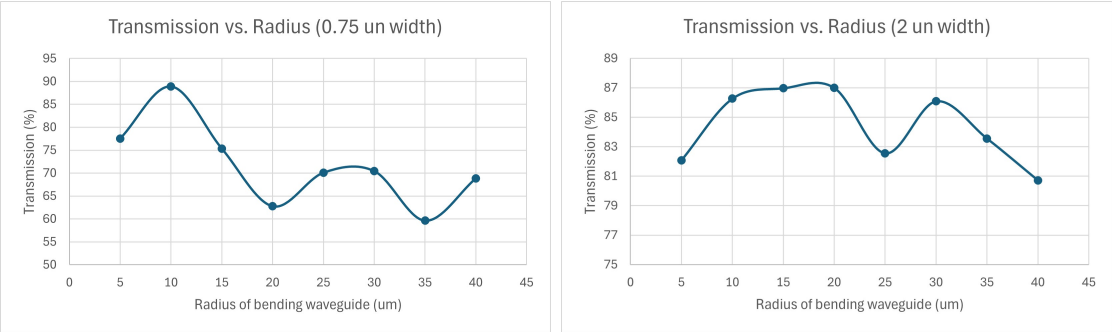

Figure 3.14: Transmission Versus Bending Radius. Simulated transmission at the output monitor for bending waveguides of different widths. Left: 0.75 µm width waveguide. Right: 2 µm width waveguide.

Figure 3.14 displays the simulation outcomes for the transmission values at the output of the bending waveguide. The left plot illustrates the transmission for a waveguide width of 0.75 µm and the right plot for a waveguide width of 2 µm. These transmission values are determined by the optical signal power measured at the waveguide's output power monitor, offering a quantitative evaluation of the waveguide's capability to guide light through the bend.

For the waveguide with a width of 0.75 µm, the simulation findings indicate that the maximum transmission of 90% is achieved at a bending radius of 10 µm. As the bending radius increases, the transmission decreases. Similarly, the waveguide with a width of 2 µm follows a comparable pattern in transmission relative to the waveguide radius as its narrower counterpart. The peak transmission of 90% for the wider waveguide is reached at a bending radius of 20 µm. The reduction in transmission rate observed beyond the peak point may be due to nonlinear reflections caused by the waveguide's inner sidewall at the bending area.

Additionally, the bending angle utilized in these simulations is 90 degrees. Such a significant bending angle in the waveguide could also lead to increased signal reflection within the waveguide, potentially impacting the transmission efficiency. This effect emphasizes the necessity of meticulously selecting the bending angle and radius in the waveguide design to minimize losses. The S-bending configuration in the MZI structure might adopt the same radius as identified in these simulation sections but with a reduced bending angle. This adjustment could help in decreasing reflection losses while preserving the required optical path length.

Subsequently, the simulation results concerning the electric field distribution and the mode profile of the bending waveguide with the highest transmission rate are detailed. This analysis is intended to shed light on the optical signal's behaviour as it navigates through the waveguide. Special attention is given to how the waveguide's geometry affects mode confinement and signal integrity, which is essential for refining the waveguide design to ensure effective light propagation, especially in intricate photonic circuits where precise optical signal control is critical.

Figure 3.15 demonstrates the simulation results for the bending TFLN waveguide that achieved the highest transmission, as identified in the previous plots. The top two images present the electric field distribution for a waveguide with a width of 0.75 µm and the mode profile at the waveguide's output. The bottom two images offer a top view of the waveguide with a width of 2 µm and the mode profile at its output. From the first pair of images, it is observed that the optical signal within the TFLN waveguide is predominantly confined within the core area, with a minimal amount of light leaking into the cladding layer. A clear TE mode is visible in the waveguide with a width of 0.75 µm and at the waveguide's output.

On the controversy, the scenario is markedly different for the waveguide with a width of 2 µm. Given that the width of this waveguide exceeds the wavelength of the optical signal, it is capable of supporting multimode optical signal propagation. As a result, the optical signal within this wider waveguide is not as well confined, and the mode profile observed

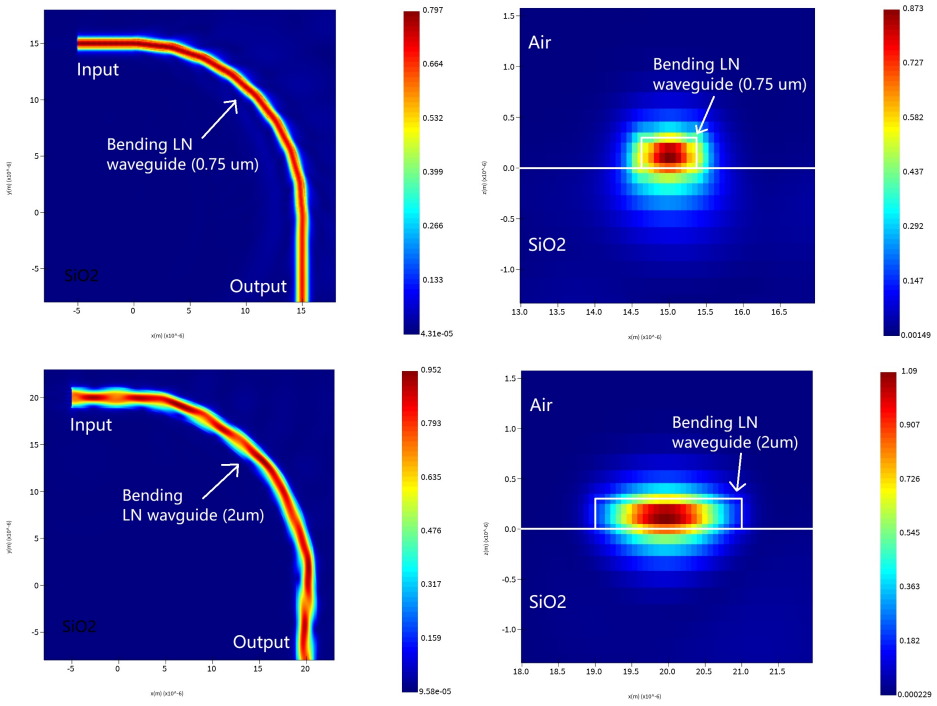

Figure 3.15: E-Field Distribution in Bending TFLN Waveguide. Top left: Top view for 0.75 µm width waveguide. Top right: Output for 0.75 µm width waveguide. Bottom left: Top view for 2 µm width waveguide. Bottom right: Output for 2 µm width waveguide.

at the waveguide's output exhibits differences. The waveguide with a width of 0.75 µm is suitable for implementing a 90-degree bending angle in the thin-film lithium niobate Mach-Zehnder Interferometer (TFLN-MZI) waveguide device, owing to its high transmission and effective signal confinement within the core area. Conversely, the waveguide with a width of 2 µm should avoid using a 90-degree bending angle in the device, opting instead for a lesser bending angle to enhance the transmission rate.

In the following section, the TFLN MZI waveguide utilizing both the directional coupler and the Y-branch will be simulated and analyzed for optimization purposes. This analysis aims to refine the design and functionality of the TFLN MZI waveguide, ensuring optimal performance and efficiency in light propagation and signal processing within the device. The goal is to achieve precise control over the optical signals, enhancing the device's overall effectiveness in applications requiring high precision and reliability.

3.6 MZI with Directional Coupler

The foundation of the TFLN waveguide E-field sensing device is undeniably the MZI waveguide structure. In this subsection, as a result, the essential component of designing the MZI will be discussed. A conventional MZI structure incorporates two passive mechanisms: the power divider and the power combiner. The propagation loss associated with the MZI waveguide is closely tied to the design of these components. Power dividers are ingeniously crafted to split an incoming optical signal into multiple outputs, allowing for precise control over the distribution of power among these outputs. This capability is vital for distributing signals within photonic integrated circuits. Conversely, power combiners consolidate multiple optical signals into a single output, therefore optimizing the utilization of light sources by amalgamating different wavelengths or signals from various origins. This dual functionality plays a crucial role in augmenting the efficiency and performance of optical communication systems, facilitating the sophisticated manipulation of light across a spectrum of applications, from telecommunications to sensing technologies.

Optical components such as the Y-junction, the directional coupler, and multimode interference (MMI) devices are instrumental both as power dividers and combiners within photonic circuits, each bringing unique advantages to the table. The Y-junction, with its versatility, can effectively split an incoming optical signal into two outputs or merge two signals into one, serving as a fundamental tool for both dividing and combining tasks. As a result, the simplicity and bidirectional functionality make it a favoured choice in optical networks. Directional couplers offer fine-tuned control over signal splitting and combining through evanescent wave coupling, making them suitable for applications that demand specific coupling ratios. MMI devices leverage self-imaging effects to distribute optical power across multiple ports, offering an alternative approach for signal division that can accommodate equal or variable splitting ratios.

In this project, the precision in controlling optical signals positions directional couplers as the preferred choice for the power divider/combiner within the lithium niobate MZI waveguide. A schematic diagram of a typical waveguide directional coupler, featuring a distance n_0 between the two waveguides, is illustrated in Figure 3.16 [46]. This selection features the importance of precise signal manipulation within the MZI structure, aiming to enhance the device's overall functionality and efficiency in E-field sensing applications.

In the directional coupler (DC), the optical signal intricately transfers between two waveguides, facilitated by the overlapping evanescent modes of light from one waveguide to the other. This mechanism allows for a portion of the optical signal to be precisely coupled from one waveguide to another, contingent upon the meticulously designed length

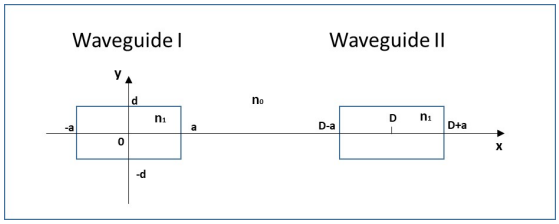

Figure 3.16: Directional Coupler Schematic. Schematic diagram of a directional coupler with two waveguides.

of the coupling region. The design and operational principle of the DC hinge on the ability to control the extent of this coupling through adjustments to the physical dimensions of the waveguide structure, particularly the length of the region where the waveguides are in close proximity, known as the coupling length (L_c).

For the DC waveguide configuration illustrated in Figure 3.16, the dimensions and spatial arrangement are specified as follows: the first waveguide possesses a width of 2a along the x-axis and a height of 2d along the y-axis. The separation between the first and the second waveguide is defined as D-a, where D represents the center-to-center distance to the second waveguide. Mirroring the first, the second waveguide also has a width of 2a and a height of 2d, with both waveguides characterized by a uniform refractive index (n_1).

The coupling length (L_c), or the length over which effective optical coupling occurs between the two waveguides, is a critical parameter in the design and functionality of the DC. It can be determined by the following equation:

$$L_c = \frac{\pi}{2\sqrt{\kappa^2 \beta^2}} \tag{3.8}$$

Where κ represents the mode coupling coefficient, and the exact equation of κ is:

$$\kappa = \frac{\sqrt{2\Delta}}{\alpha} \frac{(k_x \alpha)^2 (\gamma_\alpha)^2}{(1 + \gamma_\chi \alpha)\nu^3} \exp[-\nu_\chi (D - 2\alpha)] \tag{3.9}$$

In the context of designing and optimizing a DC, understanding the mode coupling coefficient is crucial. This coefficient, denoted as k, is a fundamental parameter that influences the efficiency of power transfer between the two waveguides in the DC. Moreover, the mode coupling coefficient is determined by several factors, including the dispersion characteristics of the DC, the asymmetry between the waveguides, and the operating frequency

of the optical signal. Understanding these components is essential for achieving efficient coupling:

1. Dispersion Equation ($k_x\alpha$): This equation describes how the propagation constant varies with frequency within the waveguide. Dispersion impacts the propagation of different wavelengths of light through the waveguide, which in turn affects the coupling efficiency between the waveguides. The dispersion equation is vital for ensuring proper phase matching conditions that are necessary for efficient coupling.

2. Asymmetrical Parameter (γ_χ): This parameter measures the asymmetry between the two waveguides in the DC. Differences in waveguide dimensions, refractive indices, or both can introduce asymmetry. This parameter is significant because it influences the mode overlap and, consequently, the coupling efficiency. Greater asymmetry may lead to reduced coupling efficiency due to a decrease in the overlap between the evanescent fields of the waveguides

3. Normalized Frequency (ν): Representing the frequency of the optical signal relative to the characteristic dimensions and refractive indices of the waveguide, the normalized frequency is a dimensionless quantity crucial for analyzing waveguide modes and their propagation characteristics. It aids in determining which modes are supported by the waveguide at a given frequency and how these modes interact during the coupling process.

The dispersion equation is shown in equation 3.10, the asymmetrical parameter can be calculated using equation 3.11. Additionally, the equation for calculating the normalized frequency is as follows:

$$k_x\alpha = (\rho - 1)\frac{\pi}{2} + \tan^{-1}\left(\frac{n_1^2\gamma_\chi}{n_o^2\gamma_\chi}\right) \tag{3.10}$$

$$\gamma_\chi{}^2 = \kappa^2(n_1^2 - n_1^2) - \kappa_\chi^2 \tag{3.11}$$

$$\nu = \kappa n_1 \alpha\sqrt{2\Delta} \tag{3.12}$$

Where n_1 and n_o represent the refractive indices of the waveguide core and the cladding material, respectively, surrounding the waveguide, Δ refractive index difference, and ρ denotes the eigenmode in the waveguide (ρ=1,2). In this context, the TFLN waveguide has a width of 0.75 µm, and the separation between the two waveguides is established at 0.3 µm. Based on these parameters, when the DC functions as a 3dB power splitter, the

coupling length of the DC waveguide is determined to be 3.86 µm. This specific coupling length serves as a valuable reference for subsequent simulations of the DC.

Following the determination of the coupling length for the lithium niobate directional coupler power splitter, the next step involves simulating the designed DC within the Lumerical 3-D simulation environment for further optimization. This simulation process aims to refine the DC's design, ensuring that it meets the desired specifications for efficient power splitting. Optimization in the simulation environment allows for adjustments to be made to the waveguide dimensions, coupling length, and other critical parameters, enhancing the DC's performance for its intended application in photonic integrated circuits and other optical systems. Through iterative simulation and optimization, the goal is to achieve a directional coupler design that optimally balances efficiency, fabrication feasibility, and operational requirements.

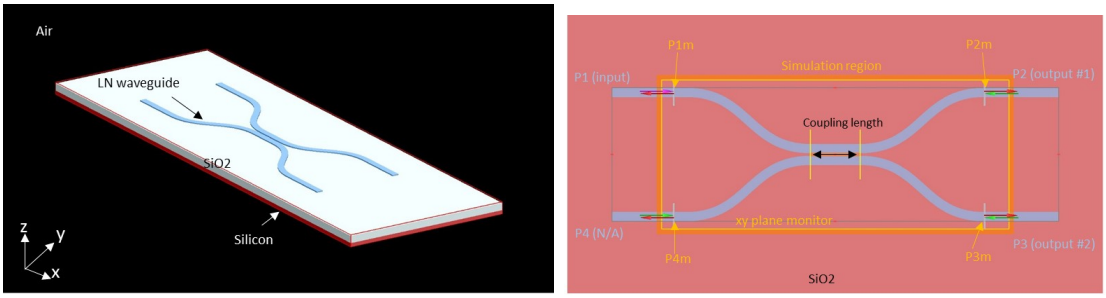

Figure 3.17: LN MZI Waveguide DC Simulation. Left: 45-degree top view. Right: Top view with labels for each component and port.

Figure 3.17 illustrates the TFLN waveguide DC situated on a silicon dioxide (SiO_2) insulating layer as modelled in Lumerical. The left image provides a perspective view of the DC, while the right side offers a top view, highlighting the coupling region located centrally between the waveguides. This configuration features four ports: Port 1 (P1) serves as the waveguide input, Ports 2 (P2) and 3 (P3) function as the outputs of the waveguide, and Port 4 (P4) is not utilized in the DC operation.

The separation between the waveguide at Port 1 and the waveguide corresponding to P4 is set at 300 µm. This distance was selected based on the analysis of the E-field intensity decrease observed in the previous section, ensuring that the design accommodates the effective range of E-field interaction for optimal signal transfer. The waveguide itself maintains a width of 0.75 µm, consistent with the dimensions conducive to efficient light propagation and coupling in the DC structure.

A subsequent simulation will investigate the relationship between the transmission at the waveguide output ports (p2 and p3) and the coupling length. This examination is essential for determining how changes in the coupling length—the distance over which the waveguides are closely aligned and interact—impact the efficiency of optical signal transfer between them. By analyzing the transmission data in relation to the coupling length, valuable insights can be obtained on how to optimize the DC design for improved signal distribution, reduced loss, and enhanced control over the signal pathways within the device.

Such simulations are instrumental in refining the DC's parameters to enhance its performance for applications in photonic integrated circuits, where precise manipulation of optical signals is vital. The goal is to achieve a directional coupler that not only meets the specific requirements of the application but also demonstrates high efficiency and reliability in its operation.

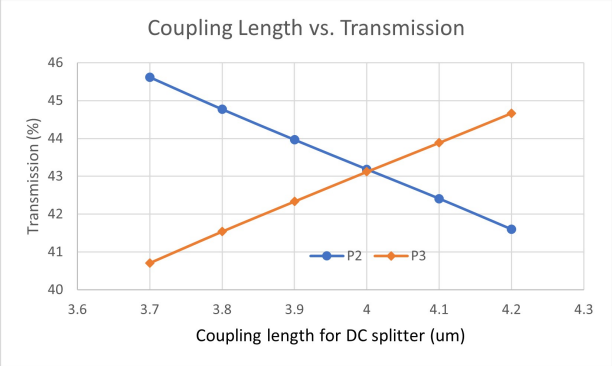

Figure 3.18: Coupling Length for 3 dB Power Splitter. Simulation results for the coupling length of the 3 dB power splitter DC.

Figure 3.18 displays the simulation results for the transmission at the output ports (P2 and P3) as a function of the coupling length. In the plot, the circle dots represent the transmission at P2, while the orange rhombus symbols indicate the transmission at P3. The data reveals that both P2 and P3 exhibit a similar transmission ratio of 43% when the coupling length is set to 4 µm. These simulation outcomes are in close agreement with the coupling length of 3.86 µm, as calculated from the theoretical equations discussed in the previous section. The slight discrepancy between the simulation results and the theoretical predictions may be attributed to the assumptions made during the equation calculations and the specifics of the mesh setup used in the simulation.

Following the determination of the optimal coupling length for the DC waveguide, simulations to map the E-field distribution were conducted. These simulations aim to

visualize and understand the behaviour of the optical signal within the waveguide structure. By examining the E-field distribution, insights into how the optical signal propagates through the DC, including how it splits between the coupled waveguides, can be gained. This analysis is crucial for further refining the DC design, ensuring efficient signal transfer, and minimizing losses within the device.

Such a detailed understanding of the E-field distribution within the DC is essential for optimizing the device's performance in photonic integrated circuits and other optical systems. It enables the identification of potential areas for improvement, such as adjustments to waveguide geometry or the coupling region, to enhance the overall efficiency and reliability of the optical signal routing and manipulation.

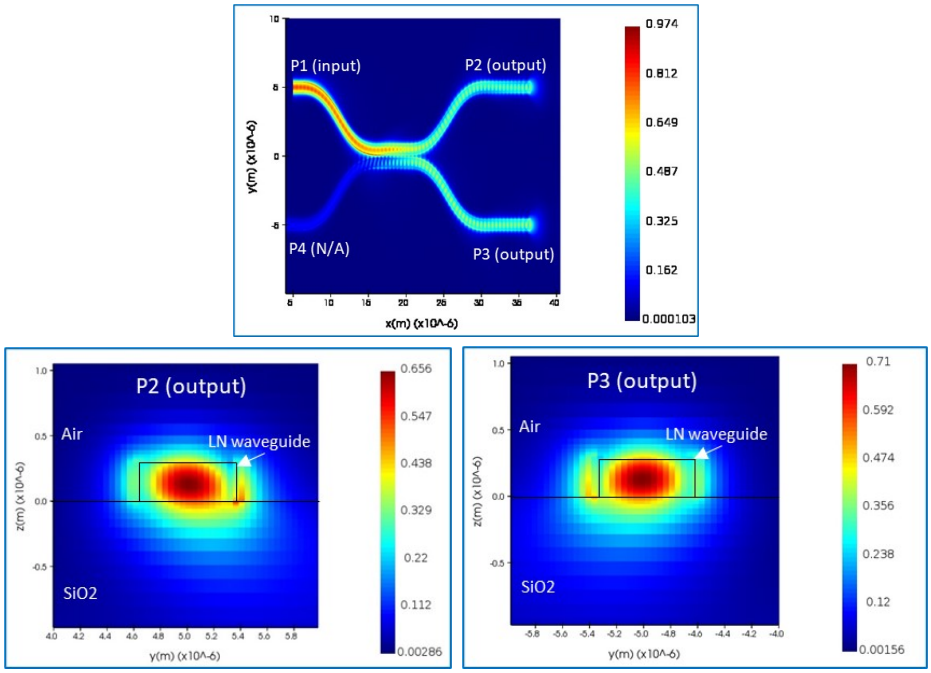

Figure 3.19: E-Field Distribution in 3 dB Splitter DC. Top: E-field profile at the XY plane. Bottom Left: E-field profile at Port 2. Bottom Right: E-field profile at Port 3.

Figure 3.19 represents the E-field distribution images from the simulated DC waveguide. At the top, the E-field profile is shown at the xy-plane for the entire DC waveguide. The bottom left image captures the E-field profile at the waveguide output Port 2, and the bottom right image displays the E-field profile at Port 3. Observations from the E-field distribution across the entire DC waveguide reveal a minor amount of light present at the waveguide leading to Port 4. However, Port 4 is designated as an isolated port and is not

utilized in this project, meaning any optical signal entering this port is considered part of the propagation loss.

From the coupling length plot, it is determined that the two output ports together account for 86% of the transmission, indicating that 14% of the input optical signal is lost during transmission through the DC waveguide. Minimizing the signal directed to Port 4 poses a challenge due to constraints on the waveguide geometry. Consequently, the minimum propagation loss for the TFLN DC waveguide is established at 14%, with each waveguide output port receiving 43% of the source power.

Additionally, common attributes sought in all DC designs include high directivity, effective impedance matching, and low insertion loss. The calculation of some of these parameters, such as the coupling factor, loss, isolation, and directivity, is crucial for optimizing the DC's performance. The equations for calculating these parameters are as follows:

1. Coupling Factor: This parameter quantifies the efficiency of power transfer between the coupled waveguides, essential for achieving balanced signal distribution.

2. Loss: Represents the total power reduction as the signal propagates through the DC, including both coupling loss and material absorption.

3. Isolation: Measures the degree to which the signal is prevented from leaking into unintended ports or pathways within the DC.

4. Directivity: Indicates the ability of the DC to preferentially direct the signal into the desired output port with minimal leakage to other ports.

By analyzing these parameters, further insights can be gained into the DC's operational efficiency and areas for improvement. Optimizing these aspects is key to enhancing the DC's functionality, ensuring it meets the stringent requirements of advanced photonic integrated circuits and optical systems where precise control over signal routing and minimization of losses are paramount.

The DC splitter utilized in this project is a conventional four-port device. Port 1 serves as the input port, where the power source is introduced. Port 2 is designated as the transmitted port, outputting half of the power received from Port 1. Port 3 functions as the coupled port, where the remaining half of the power applied to Port 1 is directed. Port 4 is identified as the isolate port and does not play a role in the operational design of the DC splitter.

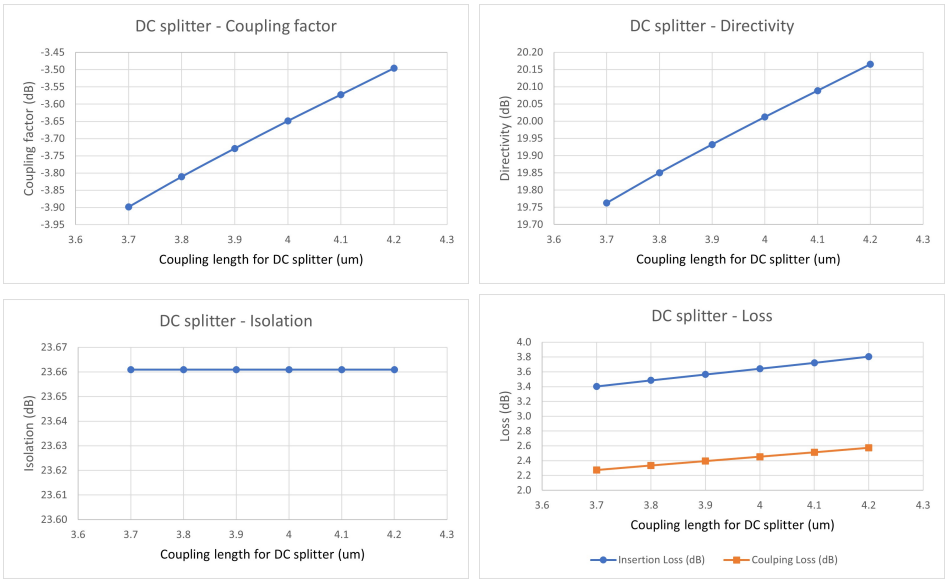

Figure 3.20: DC Splitter Performance Metrics. Simulation result plots showing various properties of the DC splitter. Top left: Coupling factor. Top right: Directivity. Bottom left: Isolation. Bottom right: Loss.

Based on the coupling factor of the DC splitter illustrated in Figure 3.20, the power coupled to Port 3 is approximately 3.6 dB when the coupling length is set to 4 µm. Additionally, the insertion loss at this coupling length is also 3.6 dB, with the coupling loss at this specific point being 2.2 dB. The isolation remains consistent at 23.6 dB across all coupling lengths, demonstrating effective isolation for the DC splitter at various coupling lengths. This level of isolation is crucial for ensuring that the DC splitter can effectively separate the optical signal into distinct pathways without significant leakage or cross-talk between the ports.

Given the requirement for a power splitter to divide an incoming optical signal into multiple outputs with precise control over power distribution and signal isolation among these outputs, a symmetric analysis of the designed DC waveguide was conducted. This analysis aimed to simulate the power transfer between the waveguides, providing insights into the efficiency and effectiveness of the power splitting mechanism.

This symmetric analysis is instrumental in understanding how the DC splitter manages the distribution of optical power between the transmitted and coupled ports. By carefully examining the power transfer dynamics and the associated parameters such as coupling factor, insertion loss, coupling loss, and isolation, the design of the DC splitter can be

advanced. The goal is to achieve a balanced distribution of optical power that meets the specific requirements of photonic integrated circuits and other optical systems, where precise signal routing and minimal loss are paramount for optimal performance.

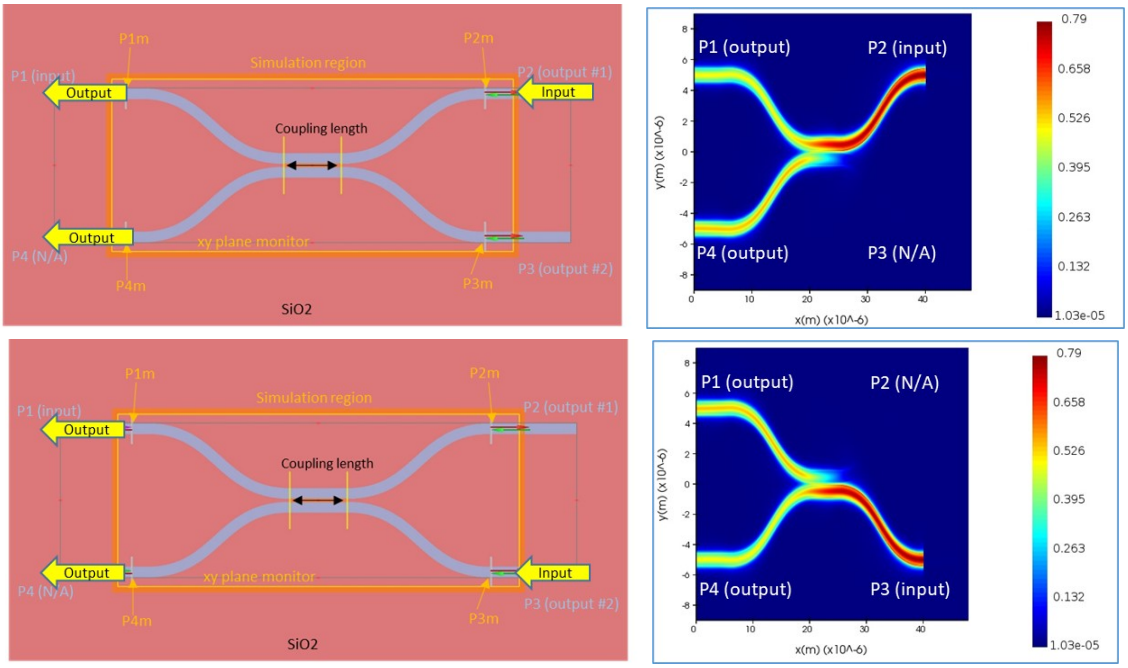

Figure 3.21: DC Waveguide E-Field Distribution. Simulation image and E-field distribution for the grating coupler waveguide in symmetric analysis. Top: Port 2 as the input waveguide. Bottom: Port 3 as the input waveguide.

The symmetric analysis method is a comprehensive approach used to evaluate and enhance the performance of DC by examining the propagation modes within the waveguides. This method involves identifying these modes and distinguishing between even and odd modes based on their symmetrical or anti-symmetrical field distributions. The analysis then proceeds to calculate coupling coefficients, which are essential for quantifying the power transfer between waveguides. Coupled mode theory, which focuses on the overlap of mode field distributions, is a cornerstone of this analysis, facilitating the optimization of the coupler design to meet specific performance criteria such as desired coupling ratios or minimal insertion loss.

In the context of the designed DC waveguide, Port 1 serves as the input waveguide, while Ports 2 and 3 are designated as the output waveguides. For the purposes of symmetric analysis, the roles are reversed, with either Port 2 or Port 3 acting as the input, and Ports 1

and 4 as the outputs. This reversal is crucial for understanding the bidirectional capabilities of the DC and for ensuring that the design is tailored for power transfer in both directions. A simulation image, Figure 3.21, along with the E-field distribution for the DC waveguide, illustrates the outcomes when Port 2 and Port 3 are used as the input source, respectively. When Port 2 serves as the input, the transmission measured at output Port 1 is 43%, and at Port 4, it is 46%. Conversely, when Port 3 is the input port, the transmission at Port 1 is observed to be 46%, and the transmission at Port 4 is 43%. These results from the simulation of the DC waveguide with a 4 µm coupling length indicate that the 3 dB power splitter component of the MZI waveguide is effectively realized.

Following the successful implementation of the 3 dB power splitter in the MZI waveguide, the next step involves simulating the complete TFLN MZI waveguide that incorporates two DC structures. This subsequent simulation is essential for evaluating the overall performance of the MZI waveguide in terms of power distribution, insertion loss, and signal integrity. By meticulously analyzing the complete MZI structure, further optimizations can be made to enhance the device's functionality, ensuring it meets the stringent requirements of advanced photonic applications.

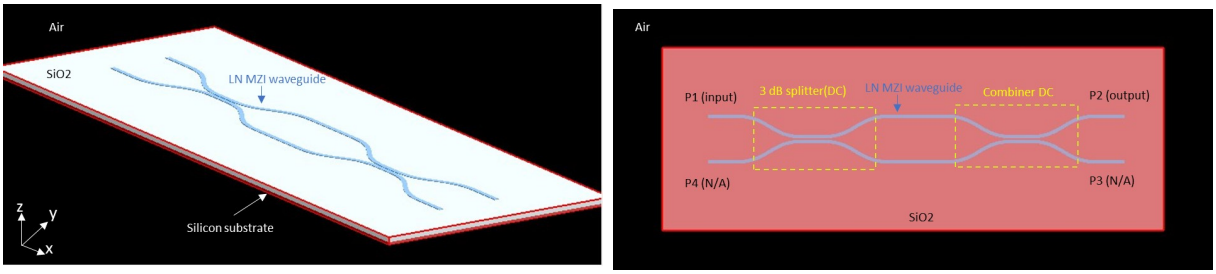

Figure 3.22: LN MZI Waveguide with DCs. Simulation images for the TFLN MZI waveguide with two grating couplers. Top: 45-degree top view. Bottom: Top view with labels on the directional coupler and waveguide ports.

Figure 3.22 displays the images of the TFLN MZI waveguide featuring two DC segments, as modelled in Lumerical. It is essential to note that the simulation process for the DC power combiner differs from that of the DC power splitter. The DC combiner is designed and simulated as an integral component of the MZI waveguide, with its performance and effects analyzed through the simulation results of the entire MZI structure.

Given that the output of the DC combiner coincides with the output of the MZI waveguide, adjustments to the coupling length of the DC combiner directly influence the MZI waveguide's output characteristics. This interdependence emphasizes the need for precise

design and optimization of the DC combiner to ensure that the overall MZI waveguide performs as intended, particularly in terms of power distribution and signal integrity.

The entire MZI waveguide, incorporating two DCs, can be conceptualized as a larger DC unit with four ports: the input port (P1), the transmitted port (P2), the coupled port (P3), and the isolated port (P4), as indicated in the bottom image of Figure 3.22. A critical aspect to remember is that the output of the MZI waveguide is through port 2, making the insertion loss a significant factor in the design of this DC configuration.

The emphasis on minimizing insertion loss is crucial because it directly affects the efficiency and effectiveness of the MZI waveguide in applications where signal fidelity and power conservation are paramount. Therefore, the design and simulation of the DC combiner within the MZI structure require careful consideration of how changes to its parameters, such as the coupling length, impact the overall performance of the MZI waveguide. This integral approach to simulation and analysis ensures that the MZI waveguide, with its integrated DC combiner, meets the stringent requirements of advanced photonic systems, optimizing signal routing and manipulation capabilities for a wide range of applications.

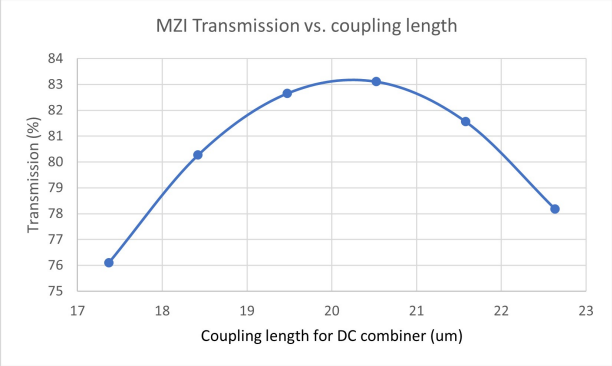

Figure 3.23: MZI Waveguide Transmission Analysis. Simulation results plot for MZI waveguide transmission versus the coupling length of the directional coupler combiner.

Figure 3.23 presents a simulation result plot illustrating the transmission through the MZI waveguide as a function of changes in the coupling length of the DC combiner. The plot reveals that the highest transmission, reaching 83%, occurs when the coupling length of the DC combiner is set to 20.5 µm. Comparatively, the total transmission achieved by the DC splitter across its two output ports is 86%, which is 3% higher than the transmission observed from the DC combiner. This discrepancy of 3% in source power represents the loss attributed to the design of the DC combiner, with a portion of this lost power potentially being directed to Port 4, which is not considered an output of the MZI waveguide.

Following this analysis, the discussion now turns to the four desired properties of directional couplers, examined in the context of the coupling length determined for the DC combiner:

1. Good Impedance Match: Achieving a good impedance match across the DC ensures that reflections within the waveguide are minimized, which is essential for preserving signal quality and reducing losses. An optimal impedance match contributes to the overall performance of the MZI waveguide by ensuring smooth signal propagation.

2. Low Insertion Loss: Insertion loss refers to the loss of signal power resulting from the insertion of the DC in the optical path. Minimizing insertion loss is vital for maintaining high transmission efficiency through the MZI waveguide, ensuring that a maximum amount of the input signal reaches the intended output.

3. Low Insertion Loss: Insertion loss refers to the loss of signal power resulting from the insertion of the DC in the optical path. Minimizing insertion loss is vital for maintaining high transmission efficiency through the MZI waveguide, ensuring that a maximum amount of the input signal reaches the intended output.

4. High Directivity: Directivity measures the ability of the DC to preferentially direct the signal into the desired output port with minimal leakage to other ports. High directivity is crucial for ensuring that the signal is efficiently routed through the MZI waveguide, maximizing the signal's integrity and minimizing undesired crosstalk.

By focusing on these properties and optimizing the coupling length of the DC combiner, the design of the MZI waveguide can be refined to enhance its performance. This involves balancing the trade-offs between directivity, impedance matching, insertion loss, and isolation to achieve a highly efficient and effective photonic device suitable for a wide range of applications.

In the analysis of the four plots concerning the DC within the MZI waveguide, insertion loss emerges as a paramount parameter. This emphasis is due to the MZI waveguide having a singular output port, which is the transmitted Port 2. The minimal insertion loss recorded at 0.8 dB coincides with a coupling length of 20.5 µm, as indicated in the insertion loss plot in Figure 3.24. This specific coupling length aligns with the findings from the MZI transmission plot, where the peak transmission of 83% was observed at the same coupling length of 20.5 µm.

However, at this optimal coupling length of 20.5 µm, the coupling factor, isolation, and directivity all register their lowest values in their respective simulation plots as illustrated

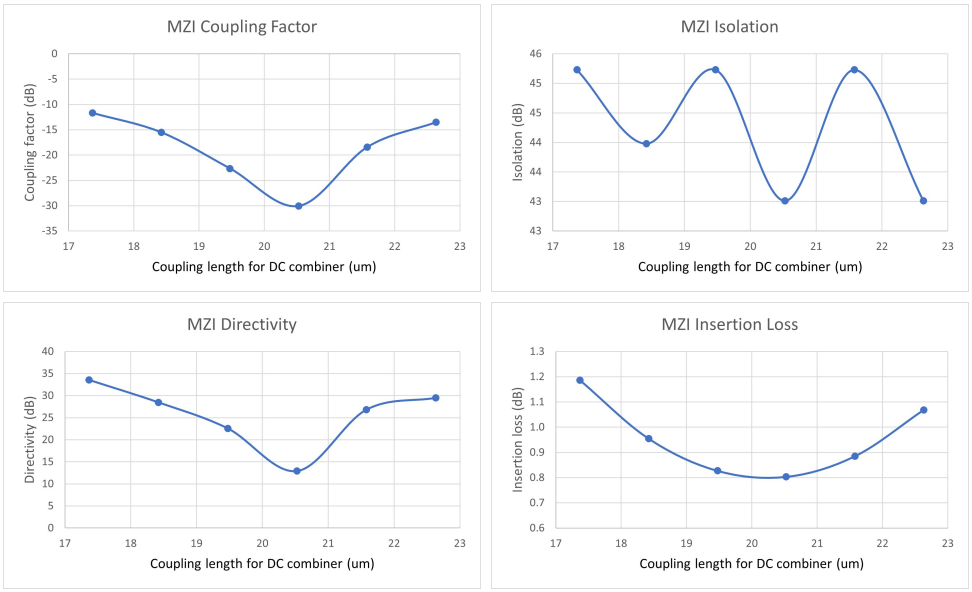

Figure 3.24: MZI Design Parameters Analysis. Simulation result plots for MZI design parameters versus the coupling length of the DC combiner. Top left: Coupling factor. Top right: Directivity. Bottom left: Isolation. Bottom right: Loss.

in Figure 3.24. Given that the MZI waveguide diverges from a conventional DC structure—primarily due to its single output port configuration—these three design parameters might not fully encapsulate the performance of the MZI waveguide under these conditions. The unique structure and operational requirements of the MZI waveguide necessitate a tailored approach to evaluating its performance, where the conventional metrics applied to typical DCs may not be entirely applicable or indicative of optimal functionality.

Following the determination of the optimal coupling length for the DC combiner, attention shifts to the E-field distribution within the MZI waveguide. Analyzing the E-field distribution is crucial for understanding how the optical signal propagates through the MZI structure, including how it interacts with the waveguide's components and interfaces. This analysis not only provides insights into the waveguide's efficiency and signal integrity but also identifies potential areas for further optimization. By examining the E-field distribution, especially in relation to the identified optimal coupling length, the design of the MZI waveguide can be refined to enhance its performance, ensuring efficient signal routing and minimizing losses for improved overall functionality in photonic applications.

The left side of Figure 3.25 demonstrates the simulation setup for the MZI waveguide, incorporating both the DC splitter and the DC combiner, with the input signal introduced

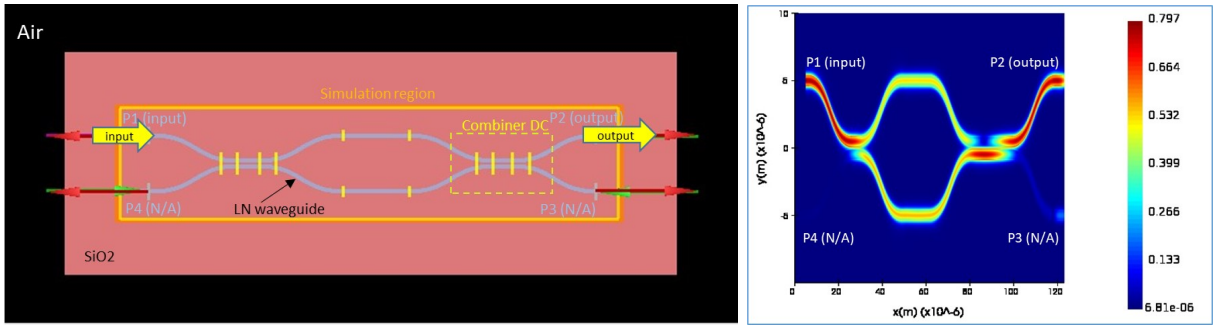

Figure 3.25: LN MZI Waveguide with DCs. Left: Simulation image of the TFLN MZI waveguide with two DCs and port labels. Right: E-field distribution in the TFLN MZI waveguide with two DCs.

at Port 1 and the output taken from Port 2. On the right side of the figure, the electric E-field profile of the MZI waveguide is illustrated, providing a visual representation of how the optical signal propagates within the structure.

From the E-field profile, it is observed that the optical signal entering through the input port is divided into two separate signals at the DC splitter. These signals are then reconverged at the DC combiner, directing the combined signal towards the MZI output at Port 2. However, it is noted that not all the light from the DC splitter is successfully combined into Port 2; a fraction of the light remains within the waveguide, continuing its propagation towards Port 3. This residual light, which does not contribute to the output at Port 2, is considered part of the propagation loss of the MZI waveguide.

Following this observation, a symmetric analysis, similar to that conducted for the DC splitter, is utilized to further improve the design of the DC waveguide. This analysis aims to refine the coupler design to meet specific performance criteria, such as achieving desired coupling ratios or minimizing insertion loss. The symmetric analysis method involves a detailed examination of the propagation modes within the waveguide, identifying even and odd modes based on their symmetrical or anti-symmetrical field distributions. By calculating coupling coefficients and employing coupled mode theory, which considers the overlap of mode field distributions, the analysis aids in fine-tuning the coupler design for optimal performance.

This optimization process is crucial for enhancing the efficiency and effectiveness of the MZI waveguide in photonic applications. By carefully adjusting the design parameters of the DC components within the MZI structure, the goal is to reduce propagation losses, improve signal integrity, and ensure that the maximum amount of light is directed towards

the intended output port. Through this meticulous design and optimization approach, the MZI waveguide can be tailored to meet the stringent requirements of advanced optical systems, facilitating precise control over signal routing and manipulation.

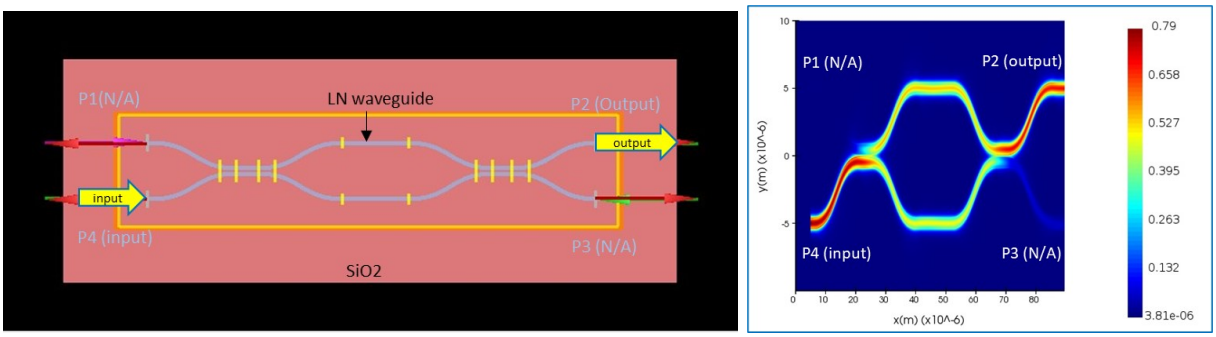

Figure 3.26: Symmetrical Analysis of TFLN MZI Waveguide. Left: Simulation image of the TFLN MZI waveguide in symmetrical analysis. Right: E-field distribution in the TFLN MZI waveguide under symmetrical analysis.

The simulation image of the TFLN MZI waveguide, as utilized in the symmetrical analysis, is displayed in Figure 3.26. The left side of the figure displays the simulation setup, while the right side presents the E-field distribution within the MZI waveguide during the symmetrical analysis. In this analysis, the optical signal enters the MZI waveguide through Port 4 and then encounters the DC splitter. The two optical signals emanating from the splitter are subsequently merged into a single signal by the DC combiner and directed towards the output at Port 2.

According to the simulation results, the transmission rate at Port 2 is 81%, which closely aligns with the 83% transmission previously measured in the designed MZI waveguide, albeit with a slight difference. This discrepancy may be attributed to the coupling dynamics occurring within the DC combiner. When Port 4 serves as the input port, Port 2 effectively becomes the coupled port, introducing coupling loss in this configuration.

This analysis concludes the simulation of the TFLN MZI waveguide that incorporates one DC splitter and one DC combiner. The subsequent section will delve into the design and simulation of the TFLN MZI waveguide that includes a Y-junction. The aim is to further boost the optical performance of the MZI waveguide by exploring alternative configurations and components. The inclusion of a Y-junction in the MZI waveguide design presents an opportunity to examine its impact on signal routing, distribution, and overall efficiency. By meticulously designing and simulating the MZI waveguide with a Y-junction, enhancements in optical performance can be achieved, potentially leading to improved signal integrity,

reduced losses, and more precise control over the optical signals within photonic integrated circuits and other advanced optical systems.

3.7 MZI with Y-junction

The Y-junction is recognized for its simplicity, cost-effectiveness, and ease of fabrication, distinguishing itself among various waveguide coupling methods. Its dual functionality as both a combiner and divider, without necessitating complex structures or precise coupling conditions, presents a straightforward approach to optical signal processing. This characteristic is particularly beneficial in scenarios where space conservation and simplicity are paramount. In light of the pandemic and associated limitations on fabrication techniques, this project has focused on designing and optimizing a TFLN MZI waveguide that incorporates two Y-branch waveguides—one serving as a 3dB power splitter and the other as a power combiner. The aim is to minimize propagation loss while ensuring efficient signal routing and distribution.

The design of the Y-junction structure within the MZI waveguide will be informed by the analysis of the E-field distribution as the optical signal traverses the MZI structure, alongside the transmission rate data. To explore a broader range of design possibilities and accommodate various fabrication options, two waveguide widths—0.75 µm and 2 µm—will be considered in the Y-junction simulations. This approach allows for a comprehensive examination of how different waveguide dimensions impact the performance and fabrication feasibility of the Y-junction within the MZI waveguide.

Initially, the Y-junction TFLN waveguide is created within the simulation environment, with clear labelling of the ports to facilitate a detailed analysis of signal flow and distribution within the structure. This step is crucial for understanding how the optical signal is divided and combined within the MZI waveguide, providing insights into the efficiency of the Y-junction design and its impact on the overall performance of the MZI structure.

By meticulously simulating and analyzing the Y-junction TFLN waveguide, the project aims to maximize the MZI waveguide's design for enhanced optical performance. This includes achieving balanced signal distribution, minimizing insertion and propagation losses, and ensuring that the MZI waveguide can meet the stringent requirements of advanced photonic applications. Through this process, the project seeks to demonstrate the viability and advantages of incorporating Y-junctions into MZI waveguides, highlighting their potential for simplifying optical signal processing in compact and cost-effective photonic integrated circuits.

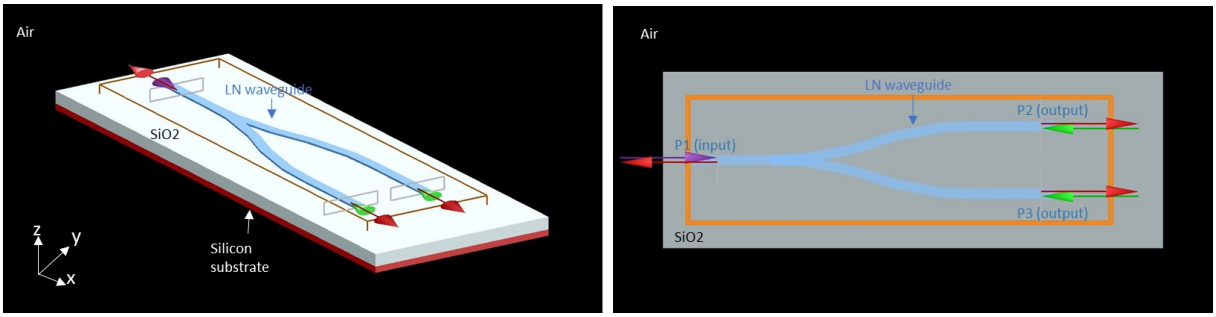

Figure 3.27: Y-Junction TFLN Waveguide Visualization. Left: 45-degree top view of the Y-junction TFLN waveguide. Right: Top view with labels for each port.

Figure 3.27 illustrates the simulation images for a Y-junction TFLN waveguide constructed within the simulation environment. On the right side of the figure, a top view of the Y-junction is provided, complete with labels for each port. Port 1 serves as the input port, while Ports 2 and 3 function as the output ports. Unlike the directional coupler waveguide, the Y-branch waveguide lacks a design variable analogous to the coupling length, which in directional couplers is directly related to the distribution of input power to the output ports. However, the Y-branch waveguide features an x/y ratio, which influences the output signal's characteristics.

The x/y ratio quantifies the difference between the Y-branch's span in the x-direction and its span in the y-direction. For example, if the Y-branch extends 30 µm in the x-direction and 10 µm in the y-direction, the x/y ratio would be 3. An increase in the x/y span ratio reduces the bending angle at the midpoint of the Y-branch structure, which, in turn, can decrease waveguide bending loss. Nonetheless, considering that the separation between the MZI sensing waveguide and the reference waveguide must exceed 300 µm, a higher x/y ratio implies an increase in the total length of the MZI structure. A larger waveguide structure and a higher aspect ratio may introduce challenges and increase the likelihood of fabrication defects during the manufacturing process.

Therefore, conducting simulations on the Y-junction waveguide with varying x/y ratios is crucial for the design and optimization process. These simulations aim to identify an optimal x/y ratio that balances the need for minimal bending loss with the practical considerations of waveguide fabrication and structural integrity. By carefully adjusting the x/y ratio, the goal is to enhance the performance of the Y-junction within the MZI waveguide, ensuring efficient signal routing and distribution while maintaining a manageable complexity and size of the overall photonic integrated circuit. This balance is essential for achieving a high-performance, reliable MZI waveguide suitable for advanced optical

applications.

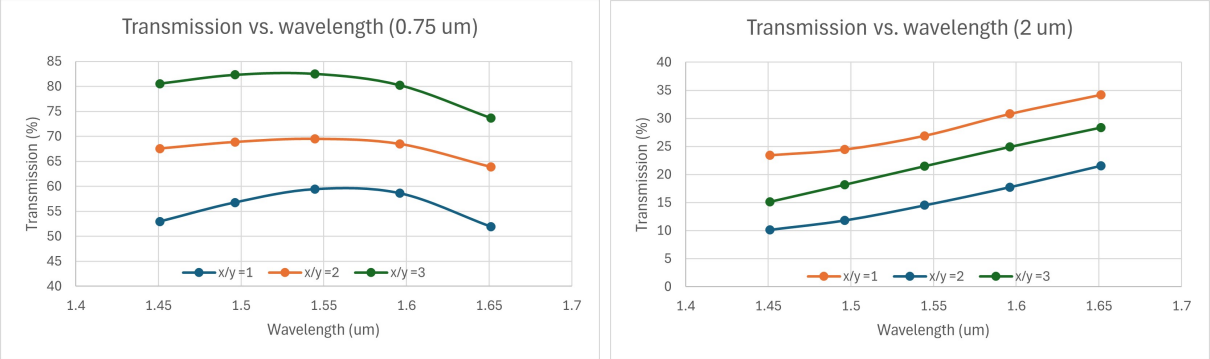

Figure 3.28: Normalized Transmission Analysis. Simulation result plot for normalized transmission versus wavelength with different x/y ratios for two waveguides. Left: 0.75 µm width waveguide. Right: 2 µm width waveguide.

Based on the simulation results illustrated in the left part of Figure 3.28, it has been observed that increasing the x/y ratio enhances the total transmission of the TFLN-MZI waveguide with a width of 0.75 µm at the output ports (Port 2 and Port 3 combined) in the Y-junction waveguide. For a waveguide with a width of 0.75 µm, the peak transmission of 82.3% occurs at a wavelength of 1.55 µm. In contrast, for a waveguide with a width of 2 µm, the maximum transmission observed is 34% at a wavelength of 1.65 µm. Interestingly, the optimal transmission for the Y-junction waveguide with a width of 2 µm is achieved with an x/y ratio of 1, diverging from the pattern observed in the waveguide with a width of 0.75 µm.

This discrepancy can be attributed to the differences in waveguide width relative to the signal wavelength. Specifically, the waveguide with a width of 2 µm exceeds the signal wavelength (1.55 µm), allowing the TFLN waveguide to support multiple modes. Y-junction waveguides with x/y ratios of 2 and 3, which feature less acute bending angles, may experience increased internal back-reflection from the waveguide sidewalls, contributing to the reduced transmission rates observed.

One method to verify this hypothesis is to examine the scattering parameters (S-parameters), particularly the S_{11} value, which reflects the amount of power reflected back towards the source. It is anticipated that the Y-junction waveguide with a width of 2 µm will exhibit higher S_{11} values for x/y ratios of 2 and 3 compared to an x/y ratio of 1, indicating greater reflection losses at these ratios.

Additionally, the S-parameters of the Y-junction waveguide for both waveguide widths

will be presented for a detailed analysis of the device's operational efficiency. The analysis will commence with the waveguide having a width of 0.75 µm, followed by the waveguide with a width of 2 µm. To simplify the discussion of the simulation results, the unit of S-parameters has been converted to normalized transmission, expressed as a percentage. This conversion facilitates a more straightforward comparison of transmission efficiencies across different waveguide configurations and x/y ratios, aiding in the optimization of the Y-junction waveguide design for improved performance in photonic applications.

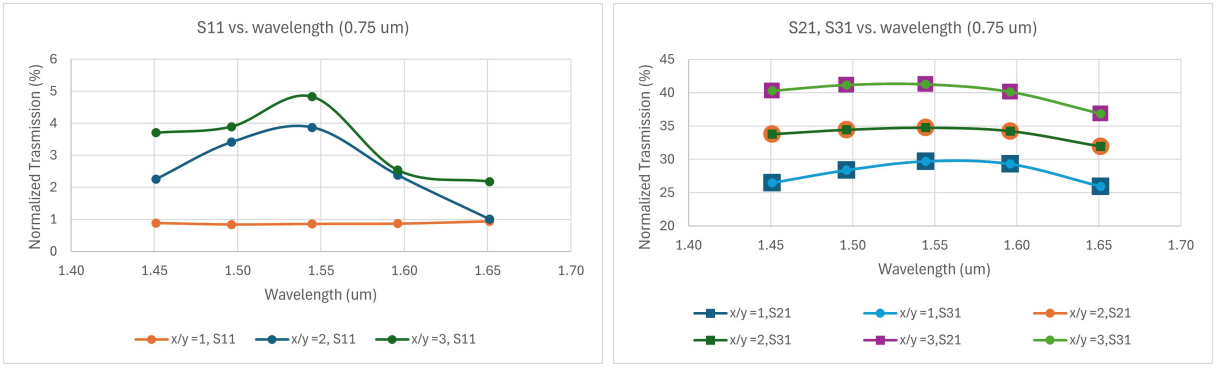

Figure 3.29: S-Parameter Analysis of TFLN Y-Junction. Simulated S-parameters for the TFLN Y-junction waveguide with 0.75 µm width and varying x/y ratios. Left: S_{11} versus wavelength. Right: S_{21}, S_{31} versus wavelength.

The simulation results for the S_{11} parameter, as depicted in Figure 3.29, reveal that the Y-junction waveguide with an x/y ratio of 3 not only exhibits the highest transmission rate but also the highest S_{11} value compared to the other configurations. The S_{11} parameter represents the reflection coefficient at the input port, indicating the portion of the optical signal that is reflected back towards the source rather than propagating to the output port. This reflected signal contributes to the propagation loss within the Y-junction, highlighting the need for further optimization efforts to minimize the S_{11} parameter in the design.

An additional notable observation from the simulation is the overlap between the S_{21} and S_{31} curves, indicating identical transmission values for these parameters across the simulations. This consistency in transmission values, regardless of changes in the x/y ratio, suggests that the Y-junction waveguide functions as an effective and stable power splitter, achieving a splitting ratio of 50/50 between the two output ports.

The stability and uniformity of the splitting ratio highlight the Y-junction's suitability for applications requiring precise power division between multiple pathways. However, the challenge posed by the S_{11} parameter and its contribution to propagation loss emphasizes

the importance of design adjustments aimed at reducing reflections and optimizing signal transmission through the waveguide.

Following this analysis, the S-parameter simulation results for the Y-junction waveguide with a width of 2 µm will be presented in Figure 3.30. This subsequent set of results will provide insights into how the waveguide's wider configuration impacts its performance, particularly in terms of reflection (S_{11}) and transmission (S_{21} and S_{31}) parameters. Understanding these dynamics is crucial for tailoring the Y-junction design to meet specific operational requirements, ensuring efficient signal routing and minimizing losses in photonic integrated circuits and other optical systems.

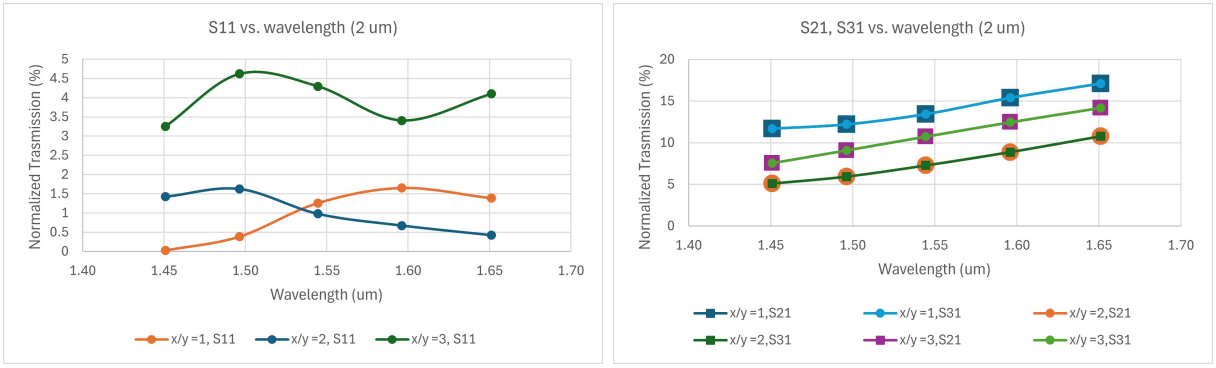

Figure 3.30: Broad Waveguide S-Parameter Analysis. Simulated S-parameters for the TFLN Y-junction waveguide with 2 µm width and different x/y ratios. Left: S_{11} versus wavelength. Right: S_{21}, S_{31} versus wavelength.

The simulated S-parameters for the TFLN Y-junction waveguide with a width of 2 µm and varying x/y ratios are showcased in Figure 3.30. The S_{11} plot within this figure indicates that the Y-junction with an x/y ratio of 3 exhibits the highest S_{11} value compared to the other configurations. Additionally, the Y-junction with an x/y ratio of 2 demonstrates a higher S_{11} value than that with an x/y ratio of 1, particularly before the 1.55 µm wavelength mark. This pattern in the S_{11} simulation plot lends substantial support to the hypothesis that back reflection is a primary factor contributing to the reduced transmission values observed in the Y-junction waveguide with a width of 2 µm, as opposed to the Y-junction with a width of 0.75 µm.

Furthermore, the simulation plots for S_{21} and S_{31} reveal that the Y-junction with an x/y ratio of 1 achieves the highest normalized transmission among the configurations tested. This outcome aligns with the insights derived from the S_{11} simulation results, reinforcing the notion that minimizing back reflection is crucial for enhancing transmission efficiency

in the Y-junction waveguide.

These findings emphasize the significant impact of waveguide geometry, particularly the x/y ratio, on the performance of Y-junction waveguides in terms of both reflection and transmission. The increased back reflection observed with higher x/y ratios, especially in waveguides with a width of 2 µm, highlights the need for careful design considerations to mitigate such effects. Optimizing the x/y ratio not only influences the waveguide's ability to efficiently split and combine optical signals but also plays a critical role in minimizing losses due to reflections.

As a result, the design and optimization of Y-junction waveguides must account for the intricate balance between geometric parameters and the waveguide's optical properties to achieve desired performance outcomes. This balance is essential for developing high-efficiency photonic devices capable of precise signal manipulation and routing, suitable for a wide range of applications in photonic integrated circuits and other advanced optical systems.

Figure 3.31 depicts the E-field distribution diagrams for the Y-junction TFLN waveguide, comparing configurations with widths of 0.75 µm and 2 µm, both set at the same x/y ratio of 3. The top two images illustrate the E-field distribution on the xy-plane and at the output port of the Y-junction with a 0.75 µm width waveguide. Conversely, the bottom two images present similar E-field distribution diagrams but for the waveguide with a 2 µm width.

In the case of the Y-junction waveguide with a width of 0.75 µm, the optical signal propagating through the waveguide exhibits a single-mode signal at the output port. This indicates effective signal confinement and mode propagation within the narrower waveguide structure. On the other hand, the E-field distribution at the output port of the Y-junction with a 2 µm width reveals the presence of multimode signals within the waveguide. This multimode signal propagation, coupled with significant signal reflection within the waveguide, are identified as primary factors contributing to the lower transmission observed in the Y-junction waveguide with a 2 µm width, compared to its 0.75 µm counterpart.

The waveguide with a width of 0.75 µm demonstrates a higher total transmission rate of 82% and superior optical signal confinement, highlighting the advantages of optimizing waveguide dimensions for specific operational requirements. The presence of multimode signals and increased reflections in the wider waveguide configuration stresses the need for careful design considerations to ensure efficient signal propagation and minimal loss.

Following this analysis, individual Y-junction waveguides will be integrated into the Mach-Zehnder Interferometer structure, and simulation results for the TFLN MZI waveguide incorporating two Y-junctions will be presented. This next step aims to advance the

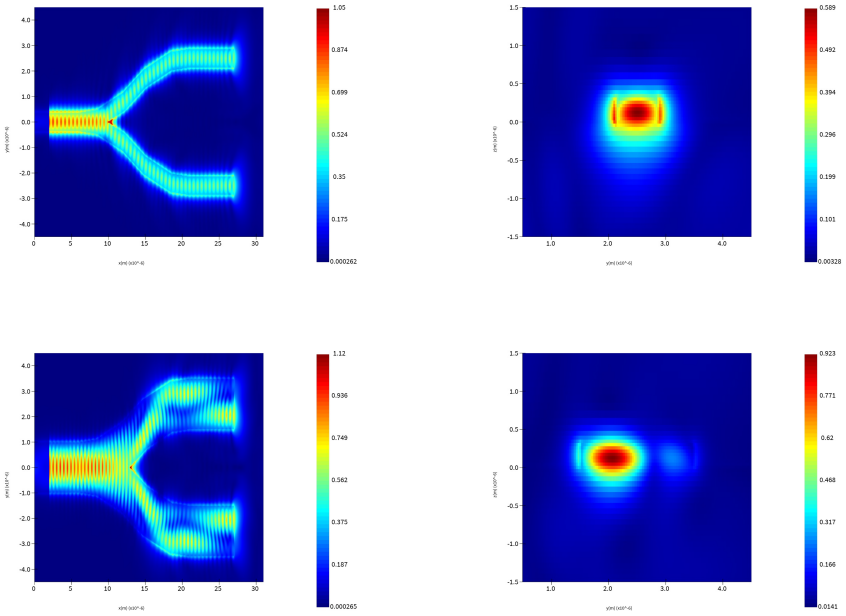

Figure 3.31: E-Field Distribution in Y-Junction TFLN Waveguide. E-field distribution of the Y-junction TFLN waveguide with an x/y ratio of 3. Top left: XY plane view of the 0.75 µm width waveguide. Top right: Output port 1. Bottom left: XY plane view of the 2 µm width waveguide. Bottom right: Output port 1.

designed structure by evaluating its performance with the inclusion of Y-junctions, focusing on enhancing signal routing, distribution, and overall efficiency of the MZI waveguide. Through meticulous simulation and optimization, the goal is to refine the MZI structure to achieve optimal performance, ensuring it meets the stringent requirements of advanced photonic applications and systems.

Figure 3.32 reveals the simulated TFLN MZI waveguide, which incorporates two Y-branch structures serving as the 3dB power splitter and combiner within a 3-D simulation environment. The Y-junction splitter is designed to evenly divide the incoming optical signal into two separate signals, each carrying 50% of the power and maintaining the same phase as the input signal.

In this MZI configuration, one arm of the waveguide, referred to as the sensing waveguide, is positioned close to an antenna patch. This proximity allows the optical signal travelling through this arm to be modulated by the E-field emanating from the antenna

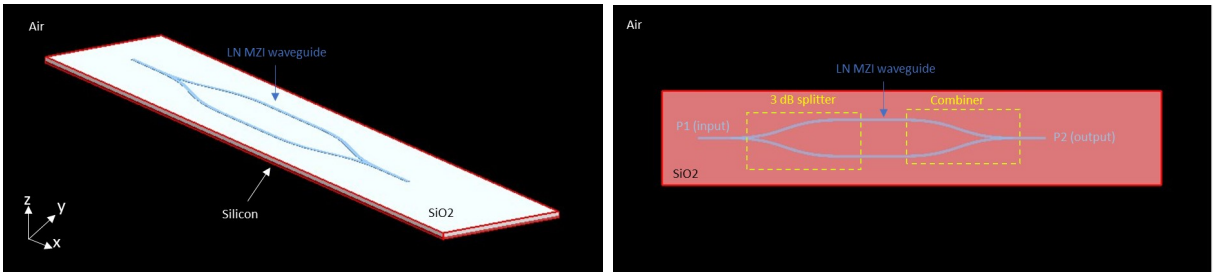

Figure 3.32: TFLN MZI Waveguide with Y-Branch. Simulation images for the TFLN MZI waveguide with a Y-branch. Left: 45-degree top view. Right: Top view with labels for each component.

patch, leveraging the EO effect. Conversely, the optical signal traversing the reference waveguide experiences a diminished EO effect, primarily due to the attenuation of the E-field intensity as the distance from the antenna patch increases. The two optical signals are then reconverged at the Y-junction combiner, resulting in a combined signal that is directed towards the output port. Drawing from the Y-junction simulation results discussed previously, the Y-junction waveguide with a width of 0.75 µm and an x/y ratio of 3 demonstrated a maximum transmission rate of 82%. Consequently, the MZI waveguide configuration, incorporating two such Y-junctions with these specific design parameters, is simulated to assess the S_{11} parameter and overall transmission efficiency.

This simulation aims to validate the effectiveness of using Y-junctions in the MZI waveguide design, particularly in terms of achieving optimal signal division and combination, minimizing propagation loss, and ensuring efficient signal modulation via the EO effect. By carefully analyzing the S_{11} parameter and transmission rates, insights can be gained into the performance of the MZI waveguide, guiding further optimizations to enhance its functionality for applications requiring precise optical signal processing and modulation. Through this meticulous approach, the project seeks to develop a high-performance MZI waveguide that meets the demanding requirements of advanced photonic systems and applications.

Figure 3.33 manifests the simulated scattering parameters (S_{11} and S_{21}) for the TFLN MZI waveguide, which incorporates two Y-junctions and features a waveguide width of 0.75 µm. In this simulation, the S_{11} parameter quantifies the portion of incident light that is reflected back to the waveguide's input port, a phenomenon attributed to structural imperfections within the Y-junctions. Notably, the S_{11} parameter reaches a peak value of 3.5% when the optical signal wavelength is 1.56 µm and stands at 2.5% for a wavelength of 1.55 µm.

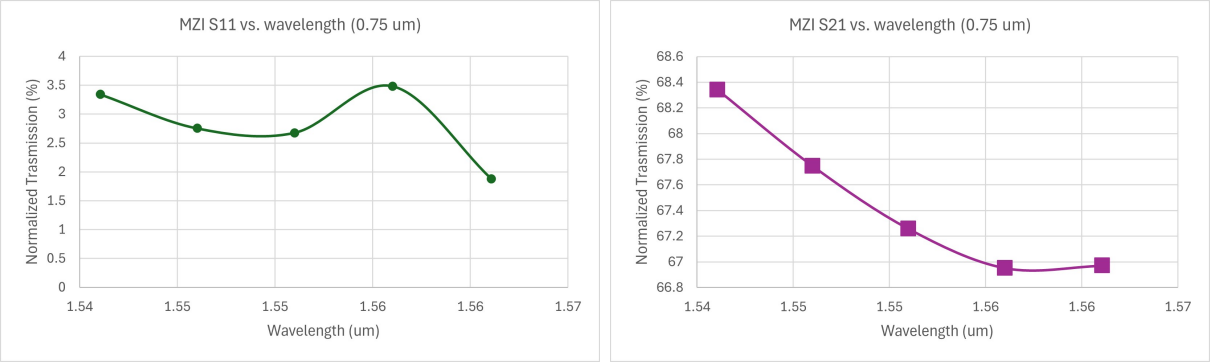

Figure 3.33: S-Parameters for TFLN MZI with Y-Junctions. Simulated S-parameters for the TFLN MZI waveguide with 2 Y-junctions and 0.75 µm waveguide width. Left: S_{11} versus wavelength. Right: S_{21} versus wavelength.

The S_{21} parameter, representing the transmission efficiency from port 1 (the input) to port 2 (the output) of the MZI waveguide, is observed to be 67.2% at a wavelength of 1.55 µm. This value effectively measures the optical signal transmission through the entire TFLN MZI waveguide structure. Therefore, with a waveguide width of 0.75 µm and incorporating two Y-junctions with an x/y ratio of 3, the TFLN MZI waveguide exhibits a propagation loss of 33.8%, resulting in a propagation efficiency of 67.2

This analysis highlights the impact of Y-junction design and waveguide dimensions on the overall performance of the MZI waveguide. The observed propagation loss features the subsequence of optimizing the Y-junction structure to minimize reflections and maximize signal transmission through the waveguide. Achieving a higher propagation efficiency is crucial for applications that require precise optical signal processing and modulation, as it directly affects the device's effectiveness in such roles.

The insights gained from the S_{11} and S_{21} parameters provide valuable guidance for further refining the MZI waveguide design. By addressing the factors contributing to signal reflection and loss, the goal is to enhance the MZI waveguide's performance, ensuring it meets the stringent requirements of advanced photonic systems and applications. This optimization process is essential for developing high-efficiency, low-loss photonic devices capable of reliable and precise optical signal manipulation.

Figure 3.34 features the scattering parameter (S-parameter) simulation results for the TFLN MZI waveguide, which incorporates two Y-junctions. This particular configuration has a waveguide width of 2 µm and an x/y ratio of 3 for the Y-junctions. On the left side of the figure, the plot illustrates the MZI's S_{11} parameter as a function of the signal

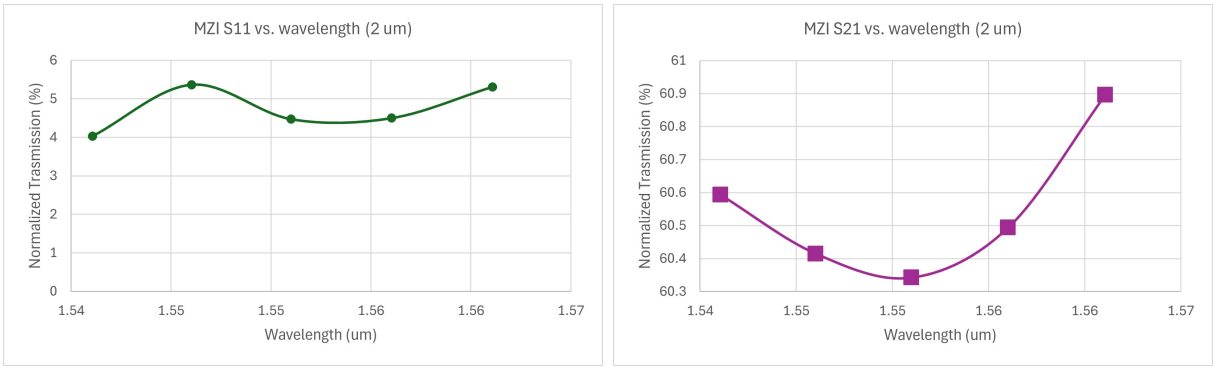

Figure 3.34: Detailed S-Parameter Simulation. Simulated S-parameters for the TFLN MZI waveguide with 2 Y-junctions and 2 µm waveguide width. Left: S_{11} versus wavelength. Right: S_{21} versus wavelength.

wavelength, revealing that the S_{11} reaches 5% when the wavelength is set to 1.55 µm. This S_{11} value of 5% is higher than that observed for the waveguide with a width of 0.75 µm, indicating that an increased waveguide width contributes to greater back reflection from the Y-junction, aligning with expectations based on individual Y-junction simulations conducted previously.

Furthermore, the S_{21} parameter, which represents the transmission efficiency from port 1 (input) to port 2 (output) of the MZI waveguide, is lower for the waveguide with a width of 2 µm compared to the waveguide with a width of 0.75 µm. Specifically, the normalized transmission for the waveguide with a width of 2 µm is recorded at 60.3%, whereas the waveguide with a width of 0.75 µm achieved a normalized transmission of 67.2%.

These findings highlight the impact of waveguide width on the performance characteristics of the MZI waveguide, particularly in terms of back reflection and transmission efficiency. The increased S_{11} value associated with the wider waveguide width (2 µm) suggests that structural and dimensional optimizations are necessary to reduce reflections and enhance signal propagation through the MZI structure. Additionally, the comparison of normalized transmission rates highlights the trade-offs involved in selecting waveguide dimensions, with narrower waveguides (0.75 µm) demonstrating superior transmission efficiency.

This analysis provides valuable insights for the design and optimization of TFLN MZI waveguides, emphasizing the need to carefully consider waveguide dimensions and structural configurations to achieve desired performance outcomes. By addressing the factors contributing to increased back reflection and optimizing for higher transmission rates, the

design of the MZI waveguide can be refined to meet the stringent requirements of advanced photonic applications, ensuring efficient and precise optical signal processing capabilities.

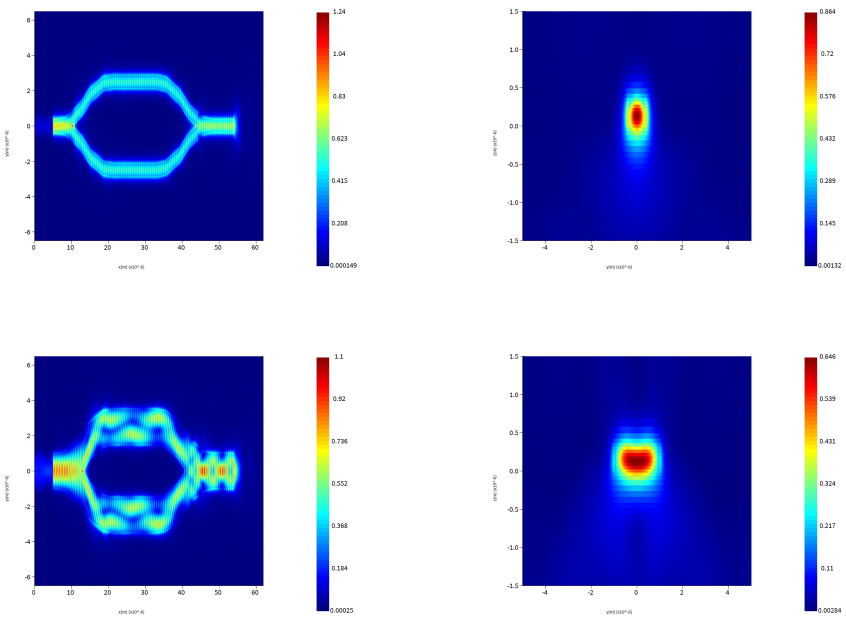

Figure 3.35: E-Field Distribution in TFLN MZI Waveguide. E-field distribution of the simulated TFLN MZI waveguide with an x/y ratio of 3. Top: Waveguide width of 0.75 µm. Bottom: Waveguide width of 2 µm.

Figure 3.35 examines the E-field distribution images for the TFLN MZI waveguide, comparing configurations with widths of 0.75 µm and 2 µm, both maintaining the same x/y ratio of 3. The top two images illustrate the E-field distribution on the xy-plane and at the output port of the MZI waveguide with a 0.75 µm width, while the bottom two images present similar E-field distribution diagrams for the waveguide with a 2 µm width.

In the configuration where the MZI waveguide has a width of 0.75 µm, the waveguide supports a single-mode optical signal, and a TE single mode signal is observable at the output port. This indicates effective mode confinement and propagation within the narrower waveguide structure. Conversely, the E-field distribution at the output port of the MZI waveguide with a 2 µm width reveals the presence of multimode signals within the waveguide. The mode profile of these signals differs significantly from that observed in the 0.75 µm waveguide, suggesting less effective mode confinement.The observation of lower

transmission values from the MZI waveguide with the larger waveguide width corroborates the findings from previous Y-junction simulations. This alignment of results underlines the impact of waveguide width on the performance characteristics of the MZI waveguide, particularly in terms of mode propagation and transmission efficiency.

Given these insights, the TFLN MZI waveguide configuration with a width of 0.75 µm and an x/y ratio of 3 is selected for further development and will be advanced to the device simulation phase. However, before proceeding with the device simulation, a detailed study of the GC is essential. This study will focus on designing and optimizing the coupling efficiency of the GC, a critical component for ensuring effective light coupling into and out of the photonic device.By thoroughly analyzing the GC's performance through simulation, the goal is to refine the overall design of the TFLN MZI waveguide, enhancing its functionality and efficiency for advanced photonic applications. This optimization process is crucial for developing high-performance photonic devices capable of precise optical signal manipulation and routing, meeting the stringent requirements of modern optical systems.

3.8 Grating Coupler

The GC is a fundamental component within the TFLN waveguide structure, serving as the primary means for coupling optical signals from external laser sources, such as laser fibres or free-air laser diodes, into the TFLN waveguide. The efficiency with which the GC performs this coupling task significantly influences the overall propagation loss of the TFLN waveguide structure, as well as the phase of the optical signal as it propagates through the waveguide. For this reason, a detailed analysis of the GC's optical performance is essential, utilizing Lumerical's 2-D simulation capabilities for this purpose.

Three critical parameters in the design of the GC directly impact its coupling efficiency: the position of the input laser source, the incident angle of the laser light, and the structural design of the GC itself. These parameters were thoroughly discussed in the Theory Chapter and are integral to the simulation process being described. Figure 3.36 provides a visual representation of the TFLN GC within Lumerical: the left image offers a perspective view, while the right image shows a cross-sectional view with a laser fibre positioned as the input laser source.

From previous theoretical explorations, it is understood that three main design parameters—grating period (Λ), etching length (w), and etching depth (d)—are crucial to the GC's coupling efficiency. The optimal range for Λ is estimated to be between 749 nm and 1122 nm, as derived from specific theoretical equations. These parameters are interdepen-

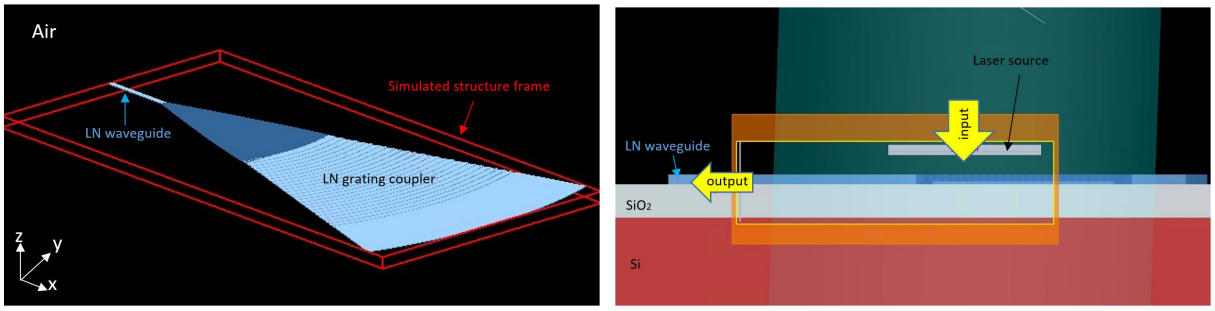

Figure 3.36: 3D and 2D GC Simulations. Left: Perspective view of the TFLN GC in 3D simulation. Right: Cross-section view of the TFLN GC with the input laser source on top in 2D simulation.

dent, contributing collectively to the GC's performance, and thus cannot be optimized in isolation.

To facilitate the design process, the duty cycle of the grating, denoted as W_{duty}, is used as a key design metric. The duty cycle represents the fraction of one period that is occupied by the grating's etched portion and is calculated using the equation:

$$W_{duty} = \frac{\Lambda - w}{\Lambda} \tag{3.13}$$

The duty cycle is a decisive parameter in the design of GC, representing the proportion of the grating period that is occupied by the grating tooth. This ratio significantly influences the central wavelength at which the GC operates most efficiently. In the context of TFLN waveguides, where the TE mode is predominantly utilized for signal propagation, understanding the relationship between the duty cycle and GC coupling efficiency is essential.

Simulation results, as depicted in Figure 3.37 (left), elucidate the correlation between the duty cycle and the GC's coupling efficiency in the TE mode. These results indicate that the optimal coupling efficiency, reaching 26%, is achieved when the duty cycle is set to 0.44. This finding suggests that for maximum coupling efficiency, the etching length should constitute 44% of the grating period.

Further exploration within the simulation extends to the etching depth, another essential factor affecting the GC's performance. Given that the height of the waveguide is constrained to 300 nm by the specifications of the TFLN wafer used in the experiment, understanding how the etching depth influences coupling efficiency is crucial. Notably, when

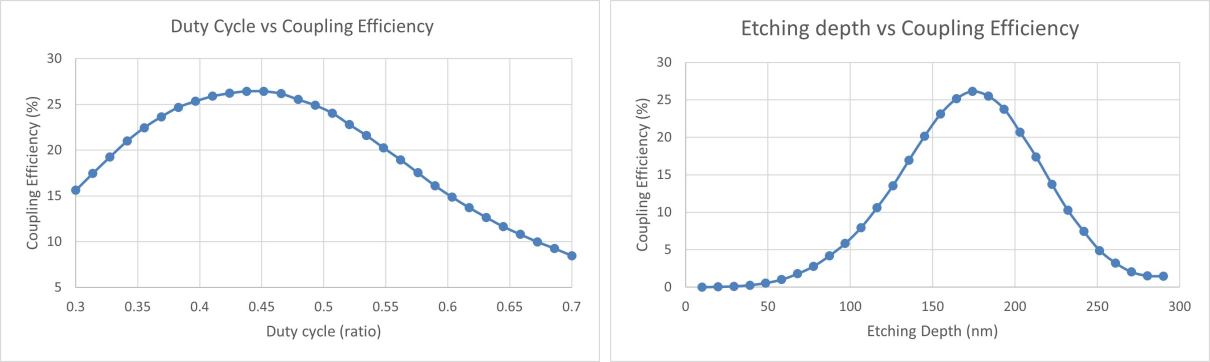

Figure 3.37: GC Coupling Efficiency Variables. Simulation results showing the effects on GC coupling efficiency. Left: Variation due to duty cycle differences. Right: Variation due to etching depth differences.

the etching depth reaches 300 nm, effectively fully etching the TFLN layer at the grating tooth area, the GC's coupling efficiency dramatically drops to 2%. This outcome is particularly relevant for fabrication processes where the grating tooth might be completely etched through, highlighting the importance of controlling the etching depth to avoid significant losses in coupling efficiency. These simulation results provide valuable insights into the design and optimization of GCs for TFLN waveguides. By carefully adjusting the duty cycle and etching depth, it is possible to enhance the GC's coupling efficiency, thereby improving the overall performance of photonic devices that rely on efficient light coupling for their operation. This optimization process is crucial for the development of high-performance photonic systems capable of precise optical signal manipulation and routing.

Figure 3.38 showcases the simulation results for the optimized GC waveguide structure, focusing on the E-field distribution during the coupling process. The top image provides a detailed view of the E-field distribution plot, highlighting the interaction between the incoming optical signal and the TFLN waveguide. This simulation reveals that only a small portion of the signal is successfully coupled into the TFLN waveguide, with the majority of the signal penetrating the TFLN layer and being reflected off the silicon substrate beneath.

These reflected signals are then recaptured by the TFLN waveguide, leading to the generation of back-transmitted optical signals that propagate in the direction opposite to that of the initially coupled optical signal. The bottom left image of Figure 3.38 illustrates the TE mode optical signal within the TFLN waveguide post-coupling. In this visualization, the coupled optical signal moving to the left is depicted in bright red, indicating its propagation path. Conversely, a cluster of optical signals is observed moving in the opposite

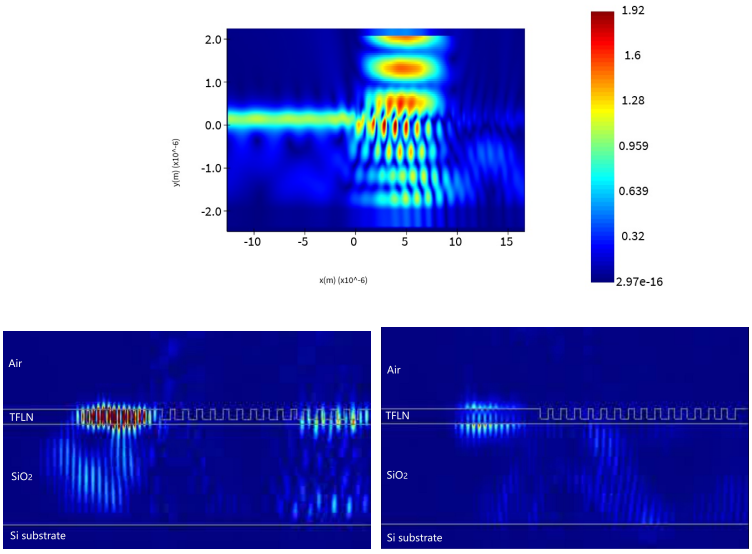

Figure 3.38: E-Field Profiles in GC Coupling. Top: E-field profile for GC coupling of the input optical signal in TE mode. Bottom Left: TE mode signal in the TFLN waveguide. Bottom Right: TM mode signal in the TFLN waveguide.

direction, a result of the input optical signal's back reflection from the silicon substrate. Additionally, a small amount of optical signal is seen propagating in both directions within the silicon dioxide (SiO_2) layer.

The bottom right image of Figure 3.38 focuses on the TM mode optical signal within the TFLN waveguide following the coupling from the input source. According to these simulation results, a minimal amount of TM mode optical signal is observed propagating within the TFLN waveguide, with most of the optical signal traversing through the TFLN layer after emanating from the input source. These findings stress the challenges associated with efficiently coupling optical signals into TFLN waveguides using GC structures. The significant reflection from the silicon substrate and the subsequent generation of back-transmitted signals highlight the need for further optimization of the GC design. This includes potentially adjusting the grating parameters, the waveguide's material composition, or the overall structure to enhance coupling efficiency and minimize losses due to reflection and signal dispersion.

Improving the GC's design to ensure more efficient signal coupling and reduce back reflections is crucial for the development of high-performance photonic devices. Such opti-

mizations are essential for leveraging the full capabilities of TFLN waveguides in advanced optical systems, where precise control and efficient propagation of optical signals are vital. After finalizing the design and optimization of the GC structure through 2-D simulations, the next step involves conducting Lumerical 3-D simulations to evaluate the optical performance of the designed GC in a more comprehensive manner. This phase is crucial for understanding how the GC functions within a three-dimensional context, which can provide insights that are not apparent in 2-D simulations. However, it's important to note that 3-D simulations are significantly more resource-intensive, requiring extended periods to complete and potentially leading to conflicts over software license usage among group members.

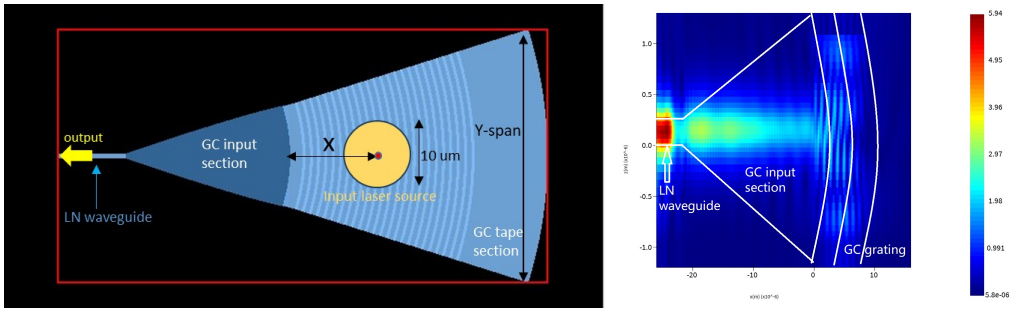

Figure 3.39: 3D GC Simulation and E-Field Profile. Left: 3-D simulation images of the GC top view with the laser source and labels for each section. Right: E-field profile for incident light coupling into the TFLN waveguide through the GC.

In the 3-D simulation, two key variables are closely monitored to refine the GC design for enhanced coupling efficiency: the location of the incident laser focus point on the GC and the radius of the GC tape section, also referred to as the Y-span. Figure 3.39 (left) illustrates a schematic diagram showing the position of the incident laser source relative to the GC, with the distance X representing the gap between the laser focus point and the GC input section. The diagram features a yellow square marking the input laser source, with a diameter of the laser spot set at 10 µm. It is highlighted that the size of the laser source, chosen specifically for simulation purposes, has minimal impact on the GC's coupling efficiency, provided that the laser source remains smaller than the grating area of the GC.

Several design variables determined during the 2-D simulation phase, such as a duty cycle of 0.44 and an etching depth of 170 nanometers, are carried forward into the 3-D simulation. Figure 3.39 (right) displays the E-field profile as incident light is coupled into the TFLN waveguide through the GC. The red coloration within the image signifies the

optical signal within the TFLN waveguide, while lighter colours in the GC input section and grating area indicate that the optical signal is being directed into the TFLN waveguide via the tapered waveguide and grating.

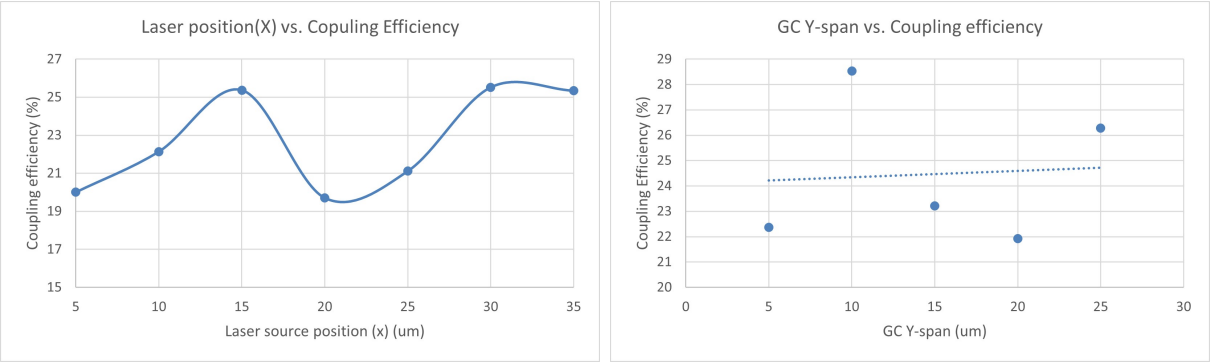

Figure 3.40: Coupling Efficiency Analysis. Simulation results plots for GC coupling efficiency. Left: Input laser source position versus coupling efficiency. Right: GC Y-span versus coupling efficiency.

Figure 3.40 (left) features the simulation result plots that correlate the position of the input laser beam with the GC coupling efficiency. The plots reveal a significant finding: the peak coupling efficiency of 26% is attainable when the input laser source is positioned at two distinct points—15 µm and 30 µm away from the GC input section. This insight is particularly valuable for the experimental setup phase, offering guidance on optimally positioning the input laser source during the fibre coupling process.

The simulation results indicate that the coupling efficiency exhibits a degree of tolerance to variations in the input source's location, with efficiency values fluctuating between 19% and 25% across different positions. This characteristic suggests that the coupling process is relatively insensitive to minor shifts in the positioning of the input source. Consequently, this tolerance could simplify the experimental measurement process by alleviating the need for ultra-precise fine-tuning of the input source's position at the micrometre scale. Such a finding has practical implications for the setup and execution of experiments involving GCs and fibre coupling. It implies that while optimal positions for the input laser source exist (at 15 um and 30 um from the GC input section), there is flexibility in the system that accommodates slight deviations from these points without drastically compromising the coupling efficiency. This flexibility can be particularly advantageous in laboratory settings where precise positioning equipment may be limited or where slight misalignments may occur due to environmental factors or equipment limitations.

Aligning the input laser source from an optical fibre with the GC is a precise task, complicated by the GC's micrometre-scale dimensions (60 µm) and the fact that the 1550 nm laser operates outside the visible light spectrum. One proposed solution to this alignment challenge is to increase the radius of the GC tape section, thereby enlarging the entire GC and making alignment more manageable. However, expanding the GC's Y-span introduces additional fabrication complexities, including a potential imbalance between the tape section and the grating teeth, which could complicate the etching process. To strike a balance between coupling efficiency, fabrication feasibility, and experimental alignment requirements, a Y-span of 25 µm has been selected. This choice results in a GC coupling efficiency of approximately 25%, which corresponds to an excess insertion loss of 6 dB. This efficiency level represents a compromise that considers the practical aspects of GC fabrication and usage within experimental setups.

In conclusion, the optimized GC design parameters, based on comprehensive 2-D and 3-D simulations, include a total GC radius of 60 µm, a duty cycle of 0.44, an etching depth of 170 nm, a Y-span of 25 µm, and an optimal placement of the input optical source 15 µm from the GC input section. While additional techniques exist for enhancing GC coupling efficiency—such as employing non-uniform grating patterns or varying grating tooth heights—such optimizations were deemed unsuitable for this project due to material preparation and fabrication facility constraints. Thus, the GC design achieving a coupling efficiency of 25% will advance to subsequent compact model device simulation stages and the forthcoming fabrication chapter. This approach ensures that the GC design is not only theoretically sound but also practical for real-world application and experimentation within the constraints of available resources and facilities.

3.9 Device and EO Effect

Following the detailed simulation of individual optical components within the Lumerical framework, including the TFLN waveguide, the MZI waveguide, directional couplers, and GC, the subsequent phase involves the integration of these components. This integration aims to construct a cohesive optical device, wherein the components function in concert to achieve the desired optical performance. However, the amalgamation of multiple components into a singular simulation framework presents significant challenges. Specifically, the complexity introduced by the addition of numerous elements can compromise the stability of the simulation setup, potentially leading to errors and substantial delays in simulation time. Addressing this issue does not merely involve adjustments to the simulation setup but necessitates a comprehensive approach to simulate the collective behaviour of the optical

components.

To surmount the challenges posed by the integration of multiple components, device-level simulations are conducted utilizing Lumerical INTERCONNECT. This simulation program is distinctively designed for the analysis of photonic integrated circuits, enabling the evaluation of complex systems through key performance metrics derived from individual components. Unlike field-based simulation methods, such as FDTD or FEM, which discretize the structure for electromagnetic analysis, device-level simulations abstract the performance of the entire optical device through essential parameters. These parameters include scattering parameters (S-parameters) from directional couplers, coupling efficiency from grating couplers, propagation loss from TFLN waveguides, and EO coefficients within TFLN waveguides. By leveraging these significant parameters, device-level simulations facilitate the inclusion and simultaneous analysis of numerous components, offering a holistic view of the device's functionality. This approach is instrumental in identifying the interdependencies between components and assessing their cumulative impact on the device's optical performance.

The integration process is informed by previous simulations, which identified the TFLN MZI waveguide configuration with directional couplers as yielding superior power transmission compared to configurations utilizing Y-junctions. The selected parameters for the MZI waveguide include a width of 0.75 µm and an x/y ratio of 3 for the directional couplers. The grating coupler, tasked with coupling incident light from the fibre into the MZI waveguide, exhibited a coupling efficiency of 25% in simulations. Furthermore, the EO effect, important for signal modulation within the TFLN waveguide, is quantified through the relationship between optical signal phase changes and the E-field intensity, with an E-field intensity set at 30,000 V/m based on antenna simulations. These parameters serve as the foundation for the device-level simulation, aiming to accurately model the performance of the integrated optical device. Through this comprehensive simulation approach, the project enhances the design and functionality of the photonic device, ensuring its efficacy in advanced optical systems and applications.

Figure 3.41 illustrates the simulation setup for the TFLN MZI waveguide within the device simulation framework. In this configuration, the primary power source for the entire waveguide structure is an Optical Network Analyzer (ONA), positioned at the top left of the depicted image. The ONA generates a continuous wave signal mode laser source at a wavelength of 1550 nm, which is subsequently transmitted to the input GC via the ONA's output port. This input GC, labelled "in GC," serves the critical function of coupling the optical signal from free space or other optical devices into the TFLN waveguide. The efficiency of this coupling process, and consequently the coupling loss, is directly influenced by the GC's coupling efficiency.

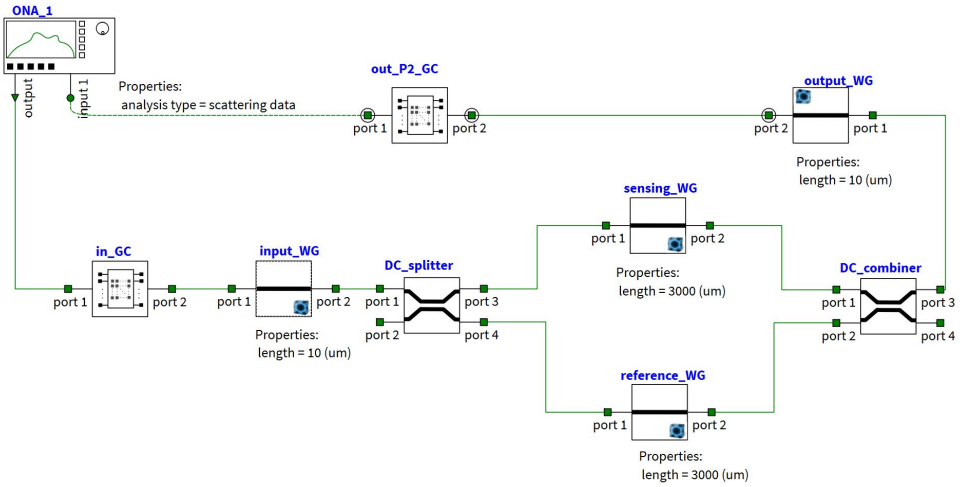

Figure 3.41: TFLN MZI Waveguide Device Simulation. Device simulation image for the TFLN MZI waveguide with two DCs and two GCs.

Following the initial coupling, the incident optical light traverses a short segment of the TFLN waveguide before reaching the DC splitter. This segment of the TFLN waveguide, while not possessing unique properties, is strategically placed to facilitate the connection between the GC and the DC. Upon entering the DC splitter, the signal is evenly divided into two paths: one leading to the sensing waveguide within the MZI structure, and the other directed towards the reference waveguide. The optical signal passing through the sensing waveguide is subject to modulation by the EO effect, a phenomenon that has been simplified in this device simulation for practicality. In reality, the EO effect exhibited by the TFLN waveguide involves complex second-order nonlinear behaviour. However, for the purposes of this simulation, a simplified model is employed, incorporating an EO effect equation into the sensing waveguide's parameters. Activation of the antenna and the resultant E-field from the antenna modulate the signal within the sensing waveguide. This modulated signal is then merged with the reference signal at the DC combiner. Due to phase differences between the signal from the sensing waveguide and that from the reference waveguide, the combined optical signal exhibits a reduction in optical power when the antenna is enabled, compared to scenarios where the antenna is inactive.

Both the sensing and reference waveguides are designed with a length of 3000 µm, mirroring the length of the antenna patch to ensure that the waveguide fully benefits from the antenna's E-field. Ultimately, the modulated optical signal is conveyed to the output GC, where it undergoes reverse coupling back to the ONA's input port. In this simulation,

the ONA functions both as the laser source and as a power meter, analyzing the optical signal received at its input port. This comprehensive device simulation encapsulates the integration of key optical components within the TFLN MZI waveguide structure, providing valuable insights into the device's overall optical performance and the impact of the EO effect on signal modulation. Through this simulation, the interplay between component efficiencies, signal modulation, and phase differences is elucidated, offering a foundation for further optimization and development of advanced photonic devices.

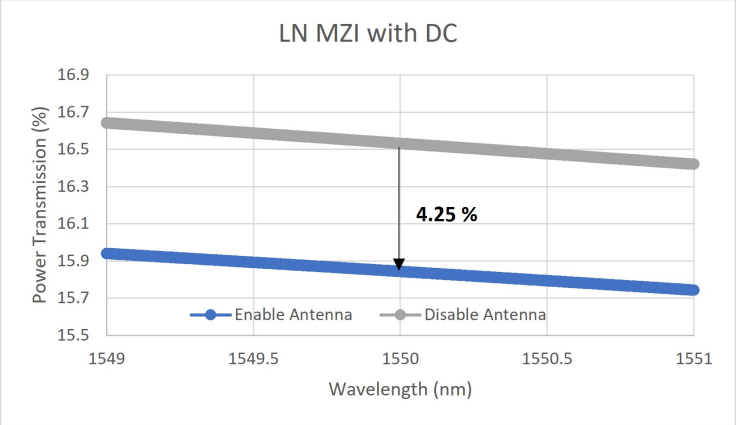

Figure 3.42: TFLN MZI Waveguide Power Transmission. Device simulation results plot for power transmission in the TFLN MZI waveguide with DCs and GCs, and the E-field from the antenna.

Figure 3.42 manifests the power transmission characteristics of the TFLN MZI waveguide, equipped with GC for both input and output, across various wavelengths of the optical signal. Notably, the power transmission of the TFLN MZI waveguide, in the absence of an antenna, registers at 16% for a wavelength of 1550 nm. When the antenna is activated, introducing the EO effect, the power transmission slightly decreases to 15%. This activation of the antenna and the resultant EO effect lead to a reduction in power transmission by approximately 4.25% compared to the scenario without the antenna. These simulation outcomes are in alignment with theoretical calculations predicting a 6% reduction in optical signal intensity under the influence of an E-field emanating from the antenna. Although the power transmission rates for the TFLN MZI waveguide are relatively low, with values below 20%, the optical detector designed for E-field intensity sensing applications demonstrates its responsiveness to changes in the surrounding E-field. This capability emphasizes the potential utility of the TFLN MZI waveguide in applications requiring sensitive detection of environmental E-field variations.

In addition to the DC based configurations, the Y-junction waveguide has also been explored within the simulation chapter. The TFLN MZI waveguide incorporating Y-junctions as both the splitter and combiner exhibited inferior power transmission compared to configurations utilizing DCs. Despite this drawback, Y-junction waveguides offer significant advantages in terms of fabrication ease due to their simpler structure. Moreover, they exhibit a higher tolerance for fabrication defects, making them a viable option for certain applications.

Next, the device-level simulation of the TFLN MZI waveguide, featuring two Y-junction structures, has been conducted to further discuss and evaluate its performance. This analysis aims to balance the trade-offs between ease of fabrication, tolerance to defects, and operational efficiency. By examining different waveguide coupling components and their impact on power transmission and device functionality, this comprehensive simulation work contributes valuable insights for the development and optimization of photonic devices tailored for specific applications, including E-field sensing and beyond.

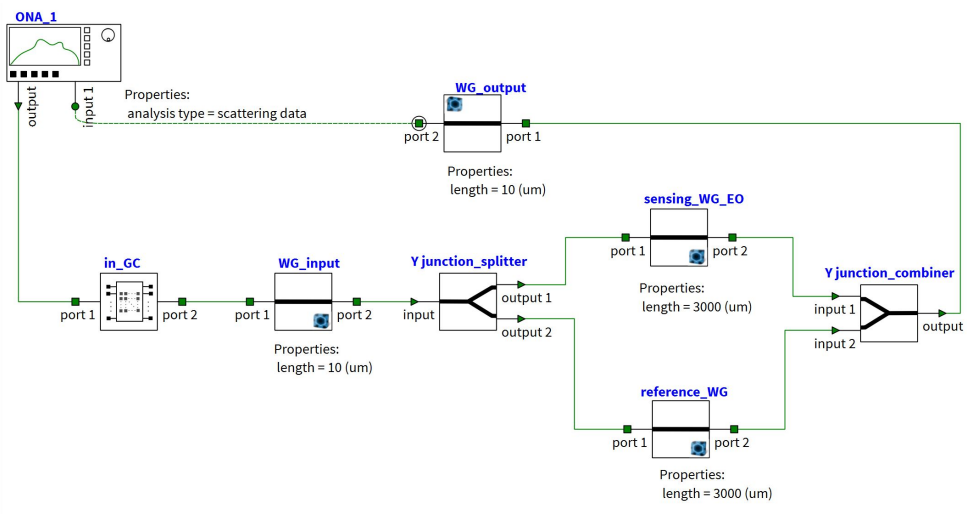

Figure 3.43: TFLN MZI Waveguide with Y-Junctions Simulation. Device simulation image for the TFLN MZI waveguide with two Y-junctions and GC.

Figure 3.43 explores the device-level simulation setup for the TFLN MZI waveguide, which incorporates Y-junctions as both the power divider and combiner. This simulation introduces three significant modifications compared to the previous TFLN MZI waveguide configuration that utilized DC: the width of the TFLN waveguide, the adoption of Y-junctions, and the method of waveguide output.

1. Waveguide Width Adjustment: In this iteration of the simulation, the waveguide width has been increased to 2 µm, as opposed to the 0.75 µm used in the MZI waveguide configuration with DCs. This adjustment aims to simplify the fabrication requirements while retaining the waveguide's capability to sense the E-field radiated from an antenna. The broader waveguide width is anticipated to reduce fabrication complexity and increase the robustness of the waveguide's structure.

2. Implementation of Y-Junctions: Y-junctions have been selected for this version of the TFLN MZI waveguide to facilitate the coupling process. An x/y ratio of 3 is maintained for both the power divider and combiner components within the Y-junctions. This choice reflects a strategic design consideration to balance the waveguide's E-field sensing capabilities with the practicalities of its fabrication and assembly.

3. Modification of the Output Method: A notable change in this simulation is the selection of the output method for the waveguide. Unlike the previous configuration, where GC were employed to couple the optical signal from the waveguide to the ONA power meter, this setup utilizes the end-fire coupling method. Grating couplers, while effective in light coupling, demand high precision in fabrication and experimental setup, with their performance being highly sensitive to structural accuracy and susceptible to fabrication defects. Additionally, measuring GCs experimentally requires sophisticated equipment for precise positional control during the coupling process.

The end-fire coupling method, by contrast, involves edge coupling, where the optical signal is directly emitted from the waveguide's end and captured by the power meter in free space. This method simplifies the experimental setup by eliminating the need for intricate alignment mechanisms and reduces the dependency on high-precision fabrication techniques for coupling efficiency. By adopting these modifications—the increased waveguide width, the use of Y-junctions, and the end-fire coupling method—the simulation aims to develop an TFLN MZI waveguide that balances minimal fabrication requirements with effective E-field sensing capabilities. This approach stresses the project's commitment to optimizing the design and functionality of photonic devices, ensuring they meet the demands of practical applications while accommodating fabrication and measurement constraints.

Figure 3.44 reviews the power transmission plot derived from the device simulation of the TFLN MZI waveguide, which incorporates Y-junctions as both the power splitter and combiner. The dashed lines within the plot serve as trend lines, illustrating the general behaviour of power transmission across the simulated conditions. The simulation results reveal a power transmission of 2.78% when the antenna is inactive, and a slightly reduced

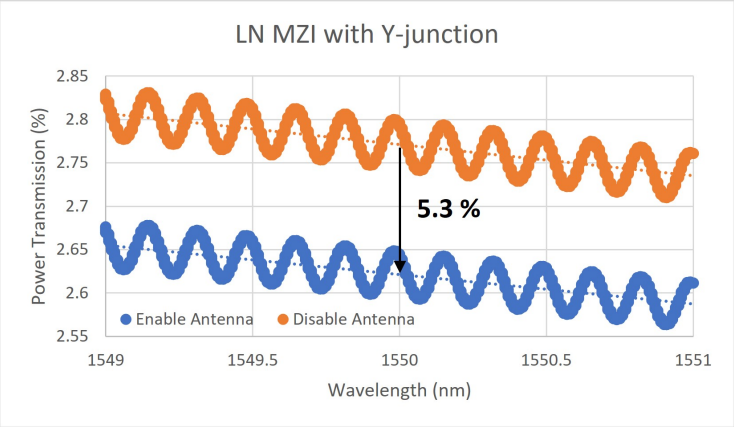

Figure 3.44: Power Transmission and E-Field Simulation. Device simulation results plot for the power transmission in the TFLN MZI waveguide with Y-junctions and the E-field from the antenna.

transmission of 2.63% upon activation of the antenna. The activation of the antenna, thereby inducing the EO effect within the TFLN waveguide due to the E-field emanating from the antenna, results in a 5.3% decrease in the output optical signal power from the MZI waveguide compared to the scenario where the antenna is disabled. This reduction in power transmission attributable to the EO effect aligns with observations from simulations involving GC for input and output, albeit with minor discrepancies that could stem from differences in the simulation environment setup and optical component parameters.

The comparison of power transmission between waveguide configurations utilizing Y-junctions and edge coupling methods versus those employing GCs is stark, with transmission rates dropping from 16% to approximately 2.6%. This significant decrease in power transmission can be attributed to several factors, including the lower coupling efficiency associated with Y-junctions and edge coupling methods, as well as the transition to a wider waveguide width of 2 µm. The ability of the 2 µm wide TFLN waveguide to support multiple mode signals contributes to the observed variability in power transmission, as indicated in the plot.

The findings from this simulation highlight the impact of waveguide design choices on the overall performance of the TFLN MZI waveguide, particularly in terms of power transmission efficiency. The selection of Y-junctions and edge coupling methods, while simplifying the fabrication process and potentially increasing the robustness of the waveguide structure, presents challenges in maintaining high levels of power transmission. Additionally, the increase in waveguide width to 2 µm, although beneficial for supporting multiple

mode signals, further complicates the efficient transmission of optical power through the waveguide.

3.10 Summary

Simulation serves as a fundamental bridge from theoretical design to practical experimentation, facilitating the transition of conceptual designs into tangible, optimized structures within a simulated physical environment. This chapter has meticulously detailed the simulation processes undertaken for both the radio device, represented by the aperture-coupled patch antenna, and the optical device, embodied by the TFLN waveguide, utilizing distinct simulation packages tailored to their respective domains.

The aperture-coupled patch antenna, designed for operation at 30 GHz, underwent extensive simulation within the HFSS package to refine its S-parameters. Key outcomes include the identification of the antenna's lowest S_{11} at -28.5 dB occurring at 28.5 GHz, with a bandwidth spanning from 27 GHz to 31 GHz. The analysis of the near-field E-field emanating from the antenna patch emphasized its critical role in this project, given the linear relationship between the phase difference induced by the EO effect and the intensity of the E-field. The simulation revealed the highest E-field intensity at 45,000 V/m near the interface between the patch and the silicon substrate, demonstrating a rapid decrease in intensity with increasing distance from the patch edge.

The simulation of optical devices commenced with the generation of TFLN material parameters, incorporating these into the Lumerical simulation package alongside the EO effect simulation, which integrates E-field data from the antenna simulation with optical parameters. Individual optical components, including TFLN waveguides, bending waveguides, directional couplers, Y-junction couplers, and grating couplers, were simulated for optimization. This comprehensive approach facilitated the design of an TFLN MZI waveguide employing directional couplers for power splitting and combining, achieving a maximum power transmission of 16%.

The introduction of the EO effect, stimulated by the antenna's E-field, resulted in a 5.3% reduction in power transmission, highlighting the sensitivity of the TFLN waveguide to environmental E-field changes. An alternative TFLN MZI waveguide configuration utilizing a Y-junction for splitting and combining, and edge coupling for output, demonstrated a significantly lower power transmission rate, attributed to the Y-junction's lower efficiency and the challenges associated with broader waveguide widths supporting multiple mode signals. The device-level simulations underline the trade-offs between component

efficiency, fabrication complexity, and experimental measurement requirements. The forthcoming chapter will transition from simulation to the nanoscale fabrication of LN-based optical components, adhering to the design parameters established through simulation. This progression marks a critical step towards realizing practical photonic devices capable of precise E-field sensing and modulation, guided by the foundational insights garnered from the simulation studies detailed in this chapter.

Chapter 4

Fabrication of Antenna and TFLN Waveguide Device

Upon the successful completion of simulation processes for both the Antenna Under Test (AUT) and the meticulously designed Thin Film Lithium Niobate (TFLN) Mach-Zehnder Interferometer (MZI) waveguide structures, employing a diverse array of simulation tools, the subsequent significant phase involves the precise fabrication of these entities within highly specialized facilities. This phase is embarked upon with the overarching objective of minimizing potential fabrication anomalies that could detrimentally affect the performance and dependability of the engineered components. In the framework of this research project, the comprehensive fabrication procedure is delineated into two distinct, yet inherently intertwined components: the construction of the AUT and the creation of the TFLN-MZI waveguide.

4.1 Antenna: Design and Overview

This section is dedicated to presenting an exhaustive depiction of the manufacturing itinerary for a state-of-the-art, wide-band, aperture-coupled patch antenna, which is adroitly affixed atop a multilayer printed circuit board (PCB). This antenna is elaborately designed to cater to the operational demands of Ka-band frequencies, specifically within the ambit of 26.5-40 GHz. It is pertinent to note that the Ka-band spectrum is of paramount importance in a myriad of advanced technological arenas, including but not limited to satellite communications, sophisticated radar system deployments, and the rapidly evolving domain of wireless communication technologies.

The production process of the AUT is a meticulously choreographed sequence of critical steps, initiating with the judicious selection of materials that meet the stringent requirements for high-frequency operation. This is followed by the deployment of precision machining techniques, aimed at sculpting the materials into their desired geometries with utmost accuracy. The culmination of this process is the assembly of the components into a multilayer PCB configuration, engineered to harness the full potential of the antenna's design specifications.

4.1.1 Fabrication Process

A sophisticated, multilayer standard PCB process is employed to fabricate the proposed aperture-coupled patch antenna on a conventional Rogers substrate. This manufacturing process was carried out by the highly regarded Poly-Grames Research Center in Montreal. Owing to the facility's ability to handle mass production and its exceptional product management, the resulting AUT benefits from reduced costs, shortened fabrication times, and minimal fabrication defects. Additionally, the level of precision required for AUT equipment is not as demanding as that needed for TFLN waveguide fabrication due to the higher frequency involved.

Since the AUT is relatively large and can be manufactured using well-established antenna production techniques, the focus is placed on minimizing the cost of the structure rather than maximizing fabrication accuracy. Bearing this in mind, the following section delves into the intricacies of the AUT geometry and the materials used in the fabrication process, providing insights into the design considerations and trade-offs involved in achieving a cost-effective and reliable antenna solution for K-band applications.

Figure 4.1 provides a comprehensive view of the antenna's diameter from multiple perspectives in the HFSS simulation images. The materials designated for each layer of the antenna are meticulously outlined in the explanatory diagram presented in Figure 4.2. According to the diagram, the AUT boasts a sophisticated six-layer structure, consisting of a patch, three substrates, a ground layer, and a feeding network. For both the feeding network, positioned at the bottom, and the patch, situated at the top, copper serves as the material of choice due to its excellent electrical conductivity and reliability.

For the substrates, ROGERS series materials with varying dielectric constants are employed to suit the requirements of the different layers. The RO4450F material, strategically inserted between the top substrate and the copper ground plane, functions as an adhesive to create a robust bond between the two materials. A high dielectric constant is essential

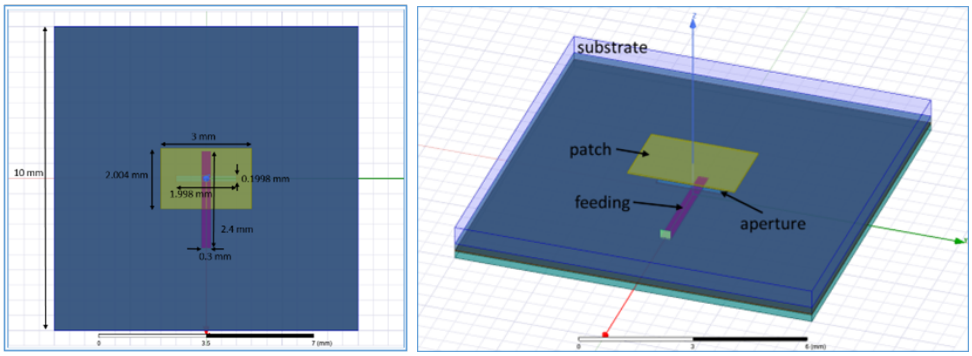

Figure 4.1: AUT Detailed Simulation. Simulation picture of the AUT with size labels for each part. Left: 45-degree top view of the AUT. Right: Top view of the AUT in HFSS.

for the substrate situated between the feeding and ground layers, as it contributes to the enhancement of the bandwidth, thereby improving the antenna's overall performance.

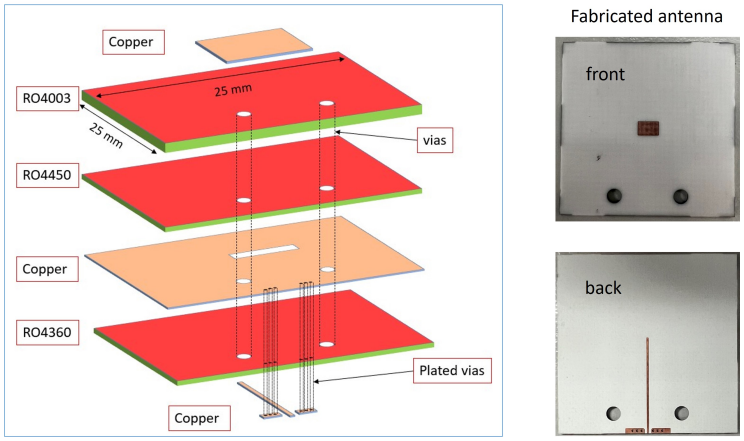

Figure 4.2: AUT Multilayer Design for Manufacturing. Diagram explaining the multilayer structure of the AUT for industry manufacturers.

As detailed in Figure 4.2, the AUT substrate measures 25 mm by 25 mm, which is larger than the dimensions of the simulated AUT in the HFSS. Moreover, the final AUT design incorporates two larger plated vias spanning six layers and six smaller plated vias connecting the copper layer to the ground. By expanding the AUT substrate geometry, sufficient fabrication tolerance is achieved, and additional space is created for extra components, such as plated vias and the coaxial cable connector. It is crucial to consider the proximity of these conductive components to the patch, as their presence may impact the radiation

pattern and induce electromagnetic (EM) reflection. As a result, two larger copper pillars serve as mounting structures between distinct layers, while six smaller copper pillars facilitate a connection between the copper layer and the ground, represented by the coaxial cable connector. This meticulous design approach ensures optimal antenna performance while accounting for fabrication tolerances and the seamless integration of supplementary components.

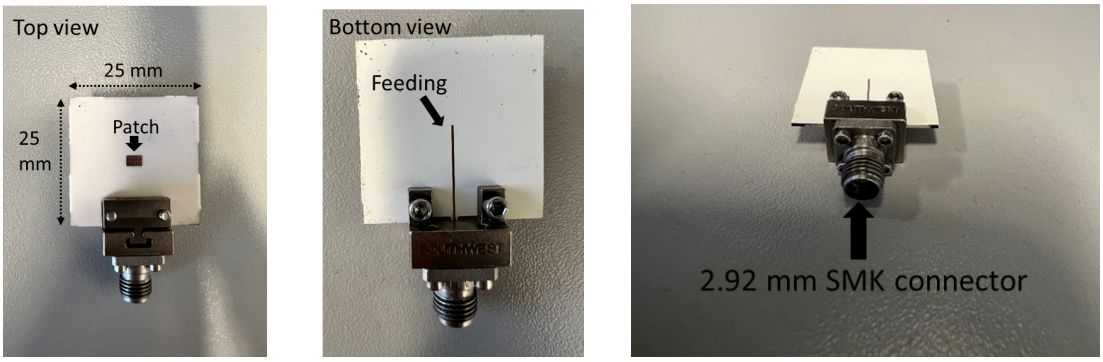

Figure 4.3: AUT Measurement Setup. Left: AUT on a 3D printed stand. Middle: AUT and the horn antenna from the near-field measurement setup. Right: Keysight PNA-X network analyzer and the robot motion controller.

Figure 4.3 (above) displays images of the fabricated AUT, which incorporates an SMA connector. The AUT is designed as an aperture-coupled patch antenna that operates at 30 GHz and exhibits circular polarization. The top surface of the antenna hosts a copper patch, while a copper feeding line is located at the bottom. This complicated six-layered structure is assembled using ROGERS materials and copper. The antenna's dimensions are 2.5 cm by 2.5 cm, in accordance with the AUT schematic diagram, and it has a total thickness of 1 mm. Additional images of the antenna are available in the supplementary materials.

The AUT feeding line at the bottom is connected to an SMA coaxial cable connector supplied by SOUTHWEST, enabling seamless interfacing with various external devices. The subminiature version A (SMA) connector is a widely employed coaxial cable connection method, utilized in numerous antenna and communication devices, including Keysight PNA-X network (VNA) analyzers and THORLABS optical devices. The SMA connector features a 50 Ω impedance and is compatible with the K-connector, which can operate up to 40 GHz [47].

In a strategic effort to pave the way for forthcoming combined experimental pursuits, a via was ingeniously incorporated into the AUT's design, enabling the seamless transit of

the tapered fiber across the AUT during experimental procedures. This via was fabricated subsequent to the initial AUT construction phase to ensure an optimal fit with the dimensions of the tapered fiber and the optical experimental apparatus. Figure 4.4 showcases the AUT post-fabrication, complete with the via. Given the AUT's complex multilayered constitution, involving laminates and metallic constituents, the laser cutting apparatus and methodologies accessible on the campus premises were adjudged incompatible for this task. Additionally, the expenditure associated with commercial laser cutting services surpassed the financial allocations of the project.

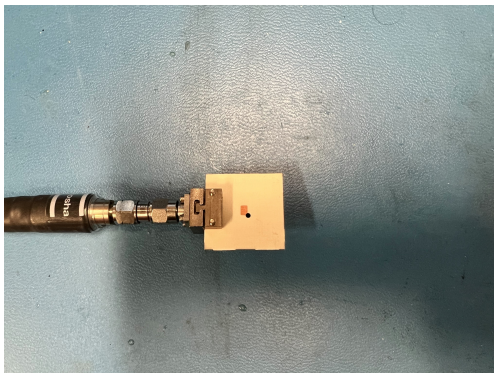

Figure 4.4: Antenna with Drilled Via. Image of the antenna featuring drilled vias.

The drilling operation was ultimately undertaken at the Machine Shop situated within the Engineering 5 building. A high-speed drill, outfitted with a 1.6 mm drill bit, was deployed for the creation of the via as shown in Figure 4.4. This drill was securely affixed to a drill press rotary tool workstation stand, significantly enhancing the precision of the hole while concurrently minimizing breakout occurrences. A subsequent polishing procedure was applied to rectify laminate imperfections and smoothen the via's sidewall. Following the fabrication, the via's dimensions exhibited a slight expansion beyond the diameter of the drill bit, by a margin of less than 0.2 mm, a variance attributable to the precision constraints inherent to the utilized equipment. This variance assumes critical significance, particularly when the via is situated in proximity to the antenna patch, presenting a potential risk of inflicting damage upon the patch.

Once the fabrication process is complete, the AUT undergoes comprehensive assessment at the CIARS (Centre for Intelligent Antenna and Radio Systems) microwave laboratory to verify its performance and ascertain whether it meets the desired specifications. Both near-field and far-field radiation characteristics of the AUT are scrutinized in the antenna laboratory, leveraging the advanced NSI-MI near-field system. In contrast, the AUT's

S-parameter is evaluated in the microwave laboratory, utilizing a VNA in tandem with a standard calibration toolbox. The following section elaborates on the near-field experiment setup, discussing the measurement results for the AUT and providing an in-depth analysis of its performance characteristics, as well as any observed deviations from the simulation data.

4.2 TFLN-MZI Waveguide Fabrication

The primary aim of this project is to conceptualize and manifest the innovative application of optical devices for the sensing of the electric field emanating from antennas. By scrutinizing the outputs derived from these optical devices, the operational state of the transmitting antenna can be analyzed with precision, without necessitating any modifications to the antenna itself. Furthermore, the integration of optical devices, characterized by their compact size and construction from non-conductive materials, into the antenna unit within an array, heralds a new era of sophisticated antenna system design. A TFLN MZI waveguide structure has been meticulously devised and modeled through simulations for this purpose.

Lithium Niobate (LN) is distinguished by its exceptional electro-optic and nonlinear-optical properties, securing its status as a material of choice for contemporary optical modulators over several decades. TFLN distinguishes itself from conventional Thin Film (TF) materials by its capacity for significant reduction in thickness—from several centimeters to less than a half-micrometer. This attribute is crucial for the integration of optical devices, as it directly impacts the minimization of device footprint, a critical consideration in the realm of integrated optical technologies [48]. The development and refinement of TFLN fabrication techniques have seen rapid advancements in recent years, influenced by the geometrical and structural demands of TFLN devices. Predominantly, there are two main fabrication methodologies for TFLN waveguides: lithography combined with etching [49], and ion-slicing followed by wafer bonding [50].

The lithography and etching technique stands as a fundamental method for delineating ridge/wire and rib waveguide patterns. This process commences with the application of either photolithography or electron beam (e-beam) lithography to define the waveguide pattern on a layer of photoresist or e-beam resist coated on the substrate. Subsequent to the resist patterning, an etching procedure, employing methods such as reactive ion etching (dry etching) or wet chemical etching, is utilized to transfer the pattern onto the TFLN [51].

Photolithography occupies an important role in the semiconductor and microfabrication industries, facilitating the transfer of complex patterns onto substrates through the selective exposure of a light-sensitive material, photoresist, to ultraviolet (UV) light via a photomask. The development process that follows, contingent on the type of photoresist utilized (positive or negative), creates the pattern on the substrate. Despite its widespread application, owing to a balance of resolution, processing simplicity, and cost-effectiveness, photolithography's resolution limitations become apparent when juxtaposed with e-beam lithography, particularly for nanoscale feature requirements [52].

E-beam lithography, in contrast, emerges as a superior technique for high-resolution and precision applications. This method eschews light in favor of a focused electron beam to inscribe patterns directly onto a substrate coated with e-beam sensitive material [53]. Achieving resolutions at the nanometer level, e-beam lithography excels in fields requiring detailed feature definition such as quantum computing, nanophotonics, and advanced semiconductor research.

In nanofabrication, e-beam lithography's utility is accentuated through the use of positive and negative e-beam resists. Positive resists, becoming soluble upon electron beam exposure, allow for the removal of exposed areas, facilitating high precision in feature creation. Negative resists, conversely, harden upon exposure, remaining intact on the substrate [54]. Each type of resist presents unique advantages and challenges, with positive resists offering finer resolution but susceptible to edge blurring due to electron scattering, and negative resists providing sharper edges but at the expense of resolution.

A critical objective in this project's fabrication phase is the exploration and evaluation of using e-beam resist as a hard mask in the TFLN fabrication process. Traditional direct etching of lithium niobate typically relies on physical etching processes, such as argon ion bombardment [28]. While common mask materials like silicon dioxide (SiO_2) and amorphous silicon (a-Si) are effective, they introduce additional fabrication steps and potential defects. Employing e-beam resist as a hard mask proposes a streamlined approach, potentially reducing the number of fabrication steps and minimizing defects, thereby enhancing the overall quality and integrity of the fabricated TFLN devices.

4.2.1 Design Considerations

The fabrication journey of the TFLN-MZI waveguide is conducted distinctly from that of the AUT, with operations set to unfold within the advanced confines of the Quantum-Nano Centre (QNC) nanofabrication facility at the University of Waterloo. This subsection is dedicated to elucidating the fabrication design, testing methodologies, resultant outcomes,

and the optimization strategies employed for the TFLN MZI waveguide structure, including the Grating Coupler (GC).

A 4-inch TFLN wafer, backed by a silicon substrate, has been selected as the foundational material for the TFLN devices (comprising the waveguide and GC). The initial preparation phase involves segmenting this wafer into multiple smaller TFLN samples, each measuring 20 by 20 mm, to facilitate subsequent fabrication steps. Given the diminutive scale of the TFLN waveguide structure relative to the sample size, it is feasible to fabricate multiple waveguide devices on a single sample, optimizing material use and experimental efficiency.

Within the QNC laboratory, three distinct fabrication methodologies have been deployed to construct TFLN MZI samples: one utilizing PMMA, another employing ZEP, and a third combining SiO_2 with ZEP. Furthermore, three variations of TFLN waveguide devices were realized: the straightforward TFLN waveguide, the TFLN-MZI waveguide, and the TFLN GC structure. The intricacies of e-beam lithography necessitate separate design files for positive and negative resists, hence, the waveguide pattern design file will be discussed in tandem with its specific fabrication protocol.

In summarizing the fabrication outcomes, it was observed that the samples utilizing ZEP as the hard mask yielded superior quality in terms of GC formation, reduction of fabrication defects, and minimization of waveguide surface roughness, in comparison to the other two methods. Samples prepared with PMMA exhibited the smoothest waveguide surfaces but fell short in GC quality. Conversely, samples that incorporated SiO_2 and ZEP displayed suboptimal results post the e-beam lithography phase, particularly in waveguide and GC formation. A notable issue with the SiO_2 mask was its failure to tolerate the reactive ion etching (RIE) process, attributed to the high aspect ratio between the GC pitch and GC gap, leading to its degradation.

This meticulous exploration and evaluation of different fabrication techniques underline the complexities and nuanced considerations inherent in the manufacturing of TFLN-MZI waveguide structures. The findings not only highlight the critical role of material selection and process optimization but also pave the way for future enhancements in the fabrication of TFLN devices, aiming for improved efficiency and quality in optical waveguide and grating coupler construction.

4.2.2 Material Selection and Preparation

For the fabrication of TFLN-MZI waveguide devices within this project, a Z-cut 4 inch TFLN wafer was meticulously selected. This particular wafer boasts a 300 nm thick TFLN

layer atop and is supported by a silicon substrate with a thickness of 0.5 mm. The thickness of the TFLN layer is variable, ranging from 300 nm to 700 nm; however, it is noteworthy that an increase in thickness correlates with a proportional increase in the material's cost. This TFLN layer, a single crystal form, is adhesively bonded to a SiO_2 layer, which measures 2 µm in thickness, facilitating a robust and integrated structure.

The production of this TFLN layer employs the ion implantation method, a technique renowned for its widespread application in the manufacture of TFLN. This method involves the strategic bombardment of helium ions into a bulk TFLN crystal, facilitating the formation of a thin TFLN layer that can subsequently be delineated from the bulk material. Following the ion implantation, the nascent TFLN layer undergoes a bonding process with the SiO_2 layer, succeeded by a regimen of thermal treatment and mechanical stress application. This process culminates in the TFLN layer's separation from the bulk TFLN crystal, resulting in its fusion with the SiO_2 and Si substrate, thus achieving the desired TFLN structure.

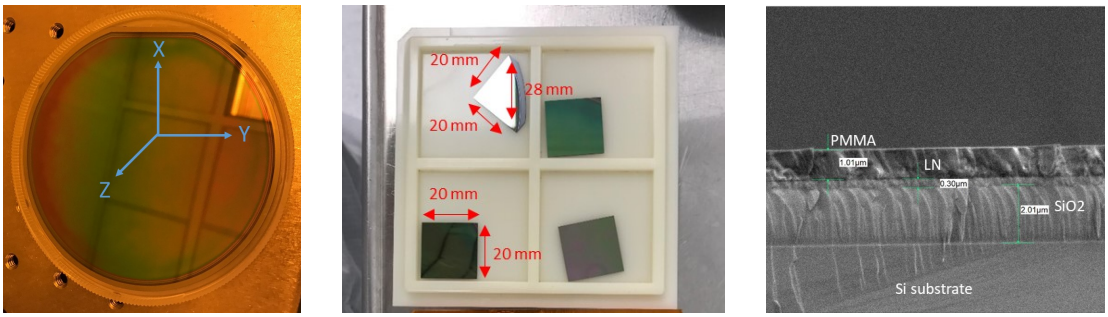

Figure 4.5: TFLN Wafer Processing. Left: XYZ coordinate system on TFLN wafer. Middle: Diced TFLN sample in the container. Right: SEM image of the TFLN sample after the dicing process.

The 4 inch wafer, precisely oriented with its long cut aligned along the crystal's Y-axis, is segmented into 20 mm by 20 mm squares utilizing a silicon dicing saw. This saw boasts a remarkable accuracy of 2-3 µm, with the dice width approximately measuring 225 µm. To safeguard the TFLN layer throughout the dicing operation, a PMMA photoresist layer is uniformly spin-coated onto the TFLN wafer. Post-dicing, each TFLN square is meticulously marked at a corner on the reverse side to denote the crystal's Y-axis orientation. This marking is instrumental in identifying the optimal direction for optical signal propagation within the waveguide during the e-beam lithography phase. Figure 4.5, sequentially arranged from left to right, presents a visual narrative of the TFLN wafer marked with the XYZ coordinate system, the TFLN squares post-dicing, and a Scanning

Electron Microscope (SEM) cross-sectional portrayal of a TFLN square subsequent to the dicing process.

4.2.3 Fabrication Process: HSQ

Three fabrication processes have been developed and implemented in this project's fabrication phase. The inaugural method utilizes hydrogen silsesquioxane (HSQ) as a negative e-beam resist, serving as the hard mask throughout the etching procedure. Figure 4.6, presented below, delineates the step-by-step fabrication process employing the HSQ methodology.

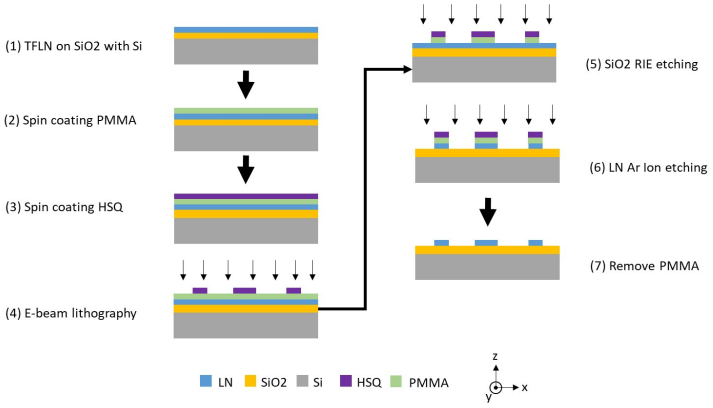

Figure 4.6: Fabrication Process for HSQ E-Beam Resist. Process diagram for using HSQ as an e-beam resist and the hard mask in fabrication.

The HSQ-based fabrication process for the TFLN sample unfolds through the following steps:

1. A Z-cut TFLN wafer is segmented into 20 mm by 20 mm squares, with each piece's crystal Y-axis distinctly marked on one corner at the back. These samples are then subjected to cleaning with Piranha solution to remove any organic residues and to prepare the surface for further processing.

2. A 450 nm thick layer of PMMA is applied through spin coating, utilizing both spin coater and baking apparatus. This PMMA layer serves as the foundation of a bilayer structure in conjunction with HSQ.

3. Subsequently, a 166 nm thick layer of HSQ negative resist is uniformly spin-coated onto the prepared substrate.

4. The HSQ resist is patterned using e-beam lithography, followed by a development process and a post-baking session to finalize the pattern.

5. Utilizing RIE, the pattern established in the HSQ is precisely transferred to the underlying PMMA layer. During this step, the 450 nm PMMA layer is etched away, with the HSQ resist functioning effectively as a hard mask.

6. Following the etching of the PMMA, argon ion milling is employed to etch a 300 nm deep TFLN ridge waveguide. In this phase, both HSQ and PMMA layers serve as hard masks, safeguarding the integrity of the underlying structures.

7. The process concludes with the removal of the PMMA resist using Remover PG solution. This step also ensures the elimination of any residual HSQ resist, leaving a clean and precisely patterned TFLN sample ready for subsequent processing or analysis.

The Piranha solution, a potent mixture of sulfuric acid (H_2SO_4) and hydrogen peroxide (H_2O_2), acts as a robust oxidizing agent. This concoction is widely employed within the microelectronics realm for the purpose of purging photoresist or organic residues from silicon wafers. It effectively decomposes most organic substances and modifies most surfaces to become highly hydrophilic. This increased hydrophilicity enhances the capillary flow of photoresist across surfaces, facilitating a uniform distribution on the TFLN surface, thereby establishing a level spin-coating layer.

Subsequently, the process involves the application of a polymethyl methacrylate (PMMA) positive photoresist layer onto the substrate through spin coating. In this context, the PMMA layer serves not as a mask for photolithography but rather as a medium for facilitating the removal of the HSQ layer. Conventionally, the removal of HSQ resist employs the buffered oxide etch (BOE) technique, comprising a blend of ammonium fluoride (NH_4F) and hydrofluoric acid (HF) [55]. BOE's utility extends to etching SiO_2 and stripping photoresist in photolithography, yet its application in this project could potentially undermine the SiO_2 layer integrity, leading to structural collapse of the waveguide and damage to device architecture.

Conversely, the selected solvent for PMMA resist removal, Remover PG, a proprietary N-methyl-2-pyrrolidone (NMP) based solution, is specifically formulated for the efficient extraction of PMMA and its copolymers without inflicting harm on the project's materials.

The strategic placement of the HSQ layer atop the PMMA layer means that the removal of PMMA concurrently facilitates the extraction of the HSQ layer.

The ensuing step entails the spin coating of HSQ resist atop the PMMA layer. Following this application, the TFLN sample, now bearing the HSQ layer, is subjected to e-beam lithography for precise patterning. Immediate transfer of the sample to the e-beam development bench ensures the development of the HSQ, removing unexposed areas. This meticulously crafted HSQ pattern, destined for silicon etching, embodies the detailed design outlined in the project's GDS file for the TFLN-MZI waveguide, inclusive of Y-junctions and grating couplers.

The comprehensive HSQ fabrication procedure culminates in the creation of a TFLN-MZI waveguide structure, detailed in Figure 4.7's GDS design file. This file visually encapsulates the waveguide's design, facilitating an understanding of the structure in its entirety before proceeding to characterization. Given the waveguide's dimensional disparities along the y-axis and x-axis, optical microscopy predominantly concentrates on specific segments of the structure for detailed analysis. This preemptive overview of the waveguide structure significantly enhances the comprehension of the fabrication process in its totality.

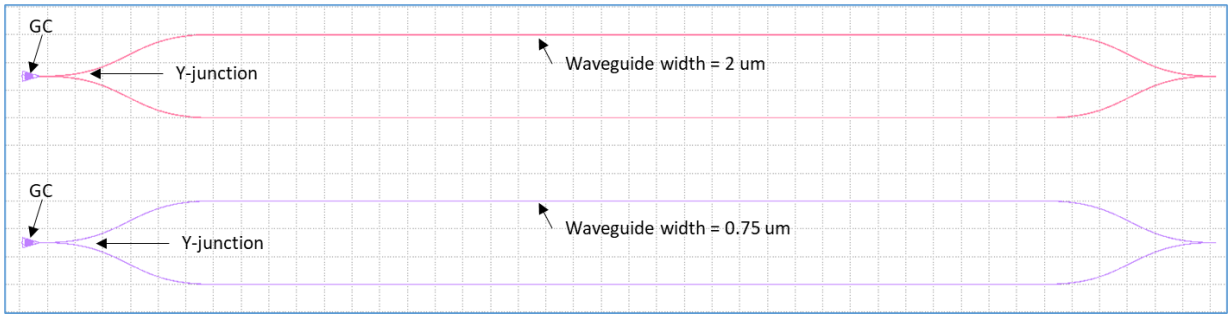

Figure 4.7: GDS Design for TFLN-MZI Waveguide. Image of the GDS design file for TFLN-MZI waveguide with Y-junction and GC structure.

The fifth step involves transferring the HSQ pattern onto the PMMA layer using the RIE process. RIE, a sophisticated physical dry etching technique, utilizes chemically reactive plasma to selectively remove material from the target sample. This method is known for producing anisotropic etch profiles, offering a significant advantage over the isotropic profiles characteristic of wet chemical etching. However, the inclusion of oxygen gas in the RIE process can lead to the oxidation of materials on the etching target, affecting the etch quality and material properties.

Subsequently, the sixth step in the fabrication sequence is the etching of TFLN using

the argon (Ar) ion milling process. This process is a form of physical sputtering where argon ions are accelerated towards the lithium niobate surface, effectively removing material. Given the crystal structure of LN, traditional etching methods, including wet etching or RIE, may induce significant sidewall roughness, which could detrimentally affect waveguide propagation loss. Argon ion milling, in contrast, achieves highly anisotropic etching, and the direct impact of Ar ions aids in smoothing any pre-existing surface irregularities, thus yielding a more uniform etch surface. Additionally, the TFLN sample is etched at a tilt angle of 30 degrees to the ion beam, optimizing the etch rate and minimizing substrate damage and heating, a technique validated by prior experiments and literature to be effective especially at angles between 30 to 60 degrees.

Finally, the photoresist layers are removed using Remover PG solution. Since the HSQ resist was applied over the PMMA layer, stripping the PMMA also effectively removes the HSQ layer from the TFLN sample. The sample is then meticulously cleaned with acetone and isopropanol to eliminate any residual contaminants. The prepared TFLN sample is forwarded for characterization, employing both optical microscopy and Scanning Electron Microscopy (SEM). The SEM technique, in particular, offers high magnification capabilities, with resolutions achievable down to the 10 µm scale, allowing for detailed examination of the fabricated structures.

4.2.4 Characterization: HSQ

Based on the observations from Figure 4.8, the TFLN MZI waveguide, featuring dimensions of 2 µm and 0.75 µm in width, was successfully fabricated utilizing HSQ negative resist through electron beam lithography. The sample clearly exhibits the Y-junction and the GC connected waveguide, with no residual resist observed under bright field microscopy. However, an issue was identified with the GC's fabrication, as depicted in the microscope image situated in the top right corner. The grating's maximum span in the x-direction measures 36 µm, while its span along the y-axis is 26 µm. Notably, the grating lines nearest to the GC's edge exhibit suboptimal adherence to the PMMA layer, leading to a grating appearance that deviates from the intended uniform design. This inconsistency represents a significant fabrication defect, given that the HSQ pattern is intended to serve as a hard mask in subsequent fabrication steps.

The dark field images further detail the TFLN-MZI waveguide and the GC, allowing for the identification of smaller structures not directly related to the waveguide. Specifically, the dark field imaging of the GC reveals that the grating pitch failed to form as expected post-lithography, with the grating lines and pitches indistinguishable within the central

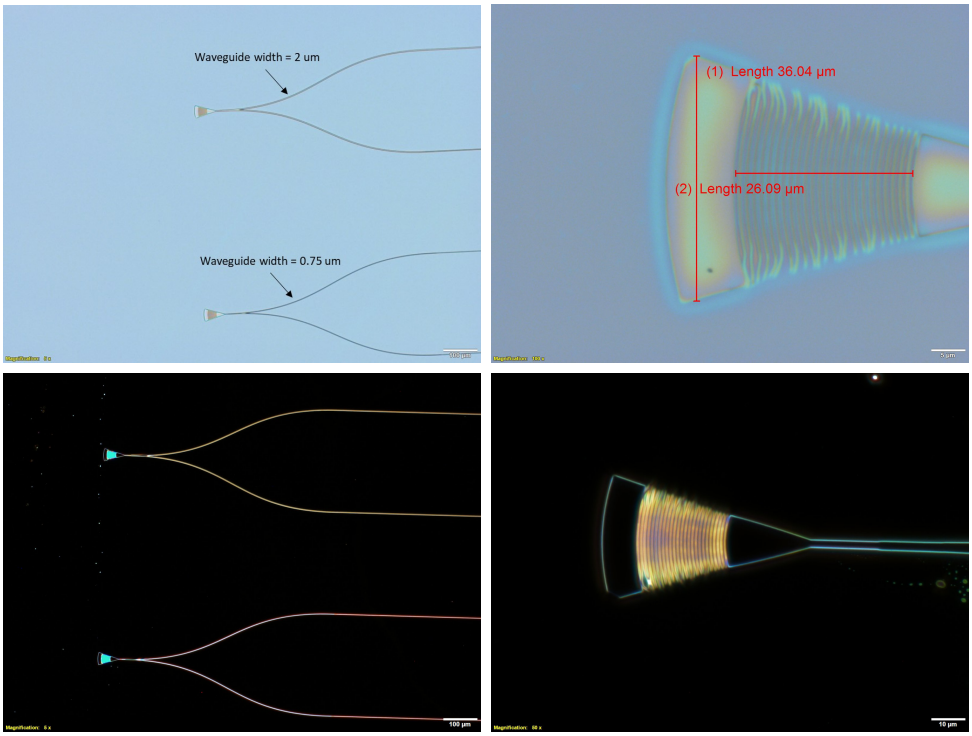

Figure 4.8: TFLN Waveguide Post-Lithography. Microscope images of TFLN sample after e-beam lithography. Top left: TFLN waveguide with 2 µm and 0.75 µm width under bright field. Top right: GC under bright field. Bottom left: TFLN MZI waveguide with 2 µm and 0.75 µm width under dark field. Bottom right: GC under dark field.

area of the GC. Despite attempts to rectify this issue through adjustments to lithography parameters and the adhesive qualities of the HSQ resist, no successful resolution was achieved. The weak bond between the HSQ negative resist and the PMMA positive resist is particularly problematic for the fabrication of fine grating lines and pitches, as it leads to displacement of the pattern.

Bright field and dark field microscopy are essential optical microscopy techniques that enhance specimen contrast and visibility. Bright field microscopy, the more conventional approach, allows light to transmit directly through the specimen, with light-absorbing areas appearing darker and light-transmitting areas lighter. Conversely, dark field microscopy employs angled illumination to prevent direct light entry into the objective lens, causing the specimen to scatter light into the lens while keeping the background dark. This technique is especially valuable for highlighting structural edges and small components, offering a

distinct advantage in visualizing the fine details of waveguide structures and identifying fabrication anomalies.

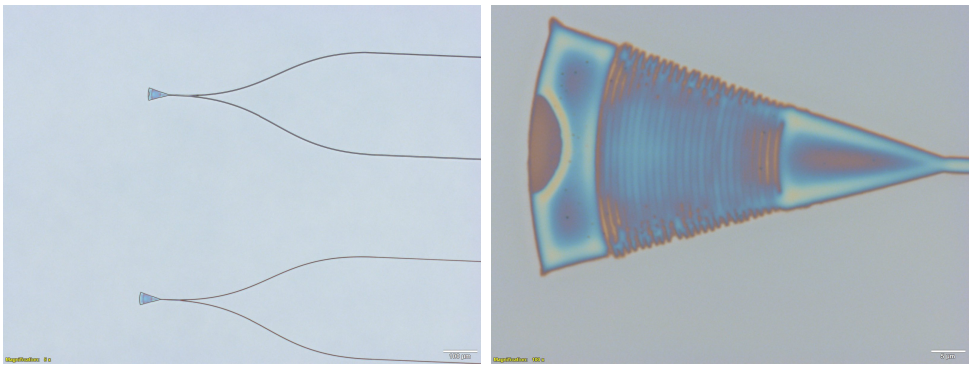

Figure 4.9: TFLN-MZI Post-Ion Milling Microscopy. Left: MZI waveguide. Right: GC structure. Images showcasing the TFLN-MZI sample after ion milling etching.

Figure 4.9 presents a bright field microscope image of the TFLN-MZI waveguide and GC following the ion milling etching procedure. This image reveals that the ion milling process, utilizing HSQ resist as the hard mask, has effectively fabricated the TFLN MZI waveguide structure. A notable change in color observed on the GC suggests the presence of residual HSQ resist on the sample, indicating incomplete removal during the process. Additionally, it is evident that the grating pitch was not etched as intended, with the grating lines remaining interconnected rather than being distinctly separated as per the design. This outcome points to a developmental issue in the electron beam lithography stage, where the HSQ, serving as the hard mask, did not facilitate the precise etching required for the grating lines and pitches. This scenario underlines the critical importance of accurate development in e-beam lithography to ensure the successful execution of subsequent etching steps and the overall fidelity of the fabricated waveguide structures.

Figure 4.10 displays SEM images of the TFLN sample following the ion milling etching process and the subsequent removal of PMMA, revealing varied outcomes in the fabrication process. The top left image indicates a failure in generating the intended grating pitch and lines within the GC, attributing this to inaccuracies in the HSQ pattern formed during the E-beam lithography stage. Contrarily, the top right image showcases the sensing and reference waveguides of the MZI structure, where the spacing closely aligns with the 300 µm specification from the design, suggesting a high degree of fabrication accuracy in this aspect. A closer examination of the Y-junction in the bottom left image reveals a waveguide width of 2.002 µm, matching the design width of 2 µm, yet it also uncovers TFLN dots and fabrication defects likely caused by redeposited TFLN particles during the

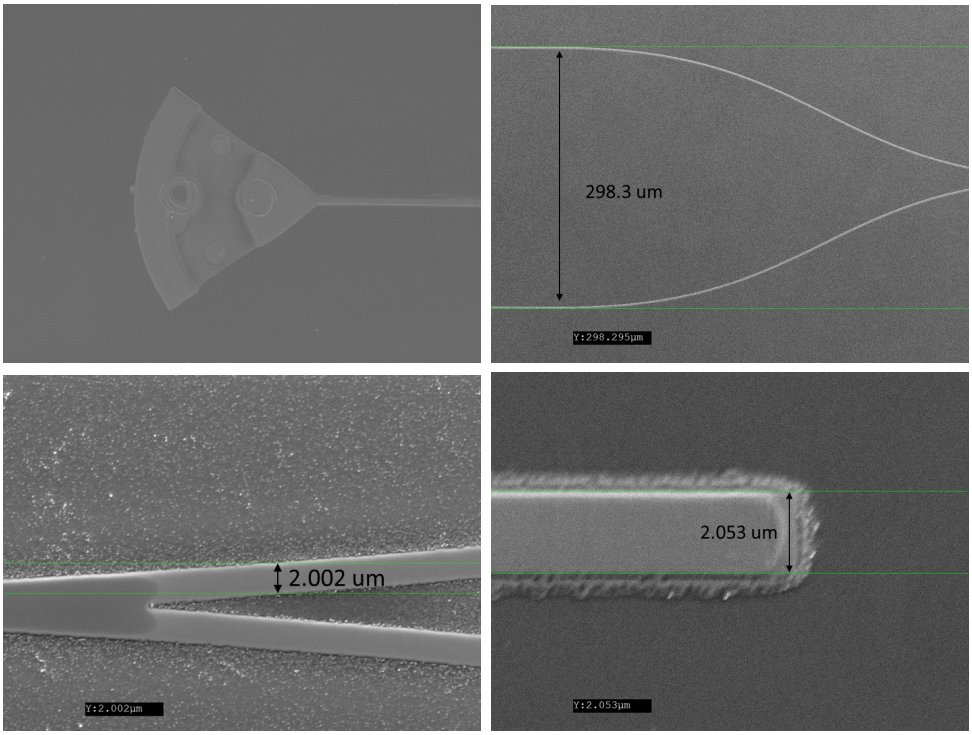

Figure 4.10: SEM Images of Fabricated TFLN-MZI Waveguide. Top left: GC structure. Top right: Sensing and reference waveguides. Bottom left: Y-junction. Bottom right: Waveguide edge.

ion milling. The bottom right image, focusing on the waveguide endpoint with a width of 2.053 µm, consistent with the Y-junction measurements, exposes remaining TFLN material around the waveguide suggesting potential high propagation loss and a curved waveguide edge, indicating its unsuitability for edge coupling methods due to inefficient light coupling. Collectively, these images provide a nuanced view of the fabrication process's achievements and challenges, highlighting the precision in waveguide spacing and the critical areas needing refinement for future iterations.

4.2.5 Fabrication Process: ZEP

The fabrication of the TFLN MZI sample utilizing ZEP, designated as a positive e-beam resist for electron beam lithography, is discussed in this section. Following the e-beam lithography, the ZEP layer serves as a hard mask essential for the formation of the TFLN waveguide. Addressing the non-conductivity of the ZEP layer, which may lead to charging artifacts during lithography, an Electra 92 conductive layer is applied subsequent to the ZEP resist's spin coating. Electra 92, a conductive polymer, is specifically chosen to counteract the potential charging effects on the non-conductive resist, ensuring smoother lithographic outcomes. This layer can be conveniently removed using a water (H_2O) solution, and it is cleansed away post the e-beam exposure and during the development phase of the ZEP layer. The removability of ZEP with Remover PG solution additionally allows for the exclusion of the PMMA layer from the process, streamlining the fabrication steps. Figure 4.11 illustrates the detailed fabrication procedure employing the ZEP method, showcasing how the integration of ZEP and Electra 92 enhances the fabrication process by mitigating charging issues and simplifying the resist removal process.

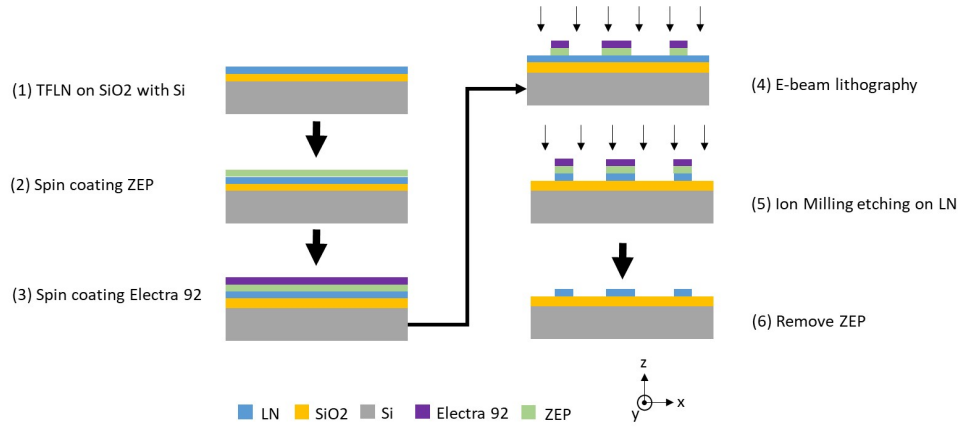

Figure 4.11: Fabrication Process Visualization for TFLN-MZI with ZEP Resist. Illustrates the use of ZEP positive resist in the E-beam lithography process for TFLN-MZI waveguide fabrication.

The fabrication process for the TFLN sample using ZEP involves the following steps:

1. Clean the TFLN sample with Piranha solution to remove organic residues and prepare the surface.

2. Spin coat 350 nm of ZEP, a positive e-beam resist, onto the TFLN sample.

3. Apply an 80 nm layer of Electra 92, a conductive polymer, on top of the ZEP to add conductivity to the non-conductive ZEP layer.

4. Pattern the ZEP resist using e-beam lithography, followed by development of the resist and a post-baking process.

5. Utilize argon ion milling to etch 300 nm of the TFLN material, forming the TFLN ridge waveguide, with the ZEP layer serving as a hard mask.

6. Remove the ZEP resist using Remover PG solution, then clean the sample with acetone and isopropanol to ensure a clean and precisely defined TFLN ridge waveguide.

The fabrication process for the ZEP method shares similarities with the HSQ resist approach, with a notable modification where the PMMA layer is substituted by the Electra 92 layer, leading to a streamlined process. The primary distinction between these two methodologies lies in the type of e-beam resist utilized during lithography. Specifically, HSQ, a negative e-beam resist, eliminates areas not exposed to the e-beam, resulting in a TFLN-MZI sample where only the TFLN devices persist post-lithography and ion milling etching. Conversely, positive resist e-beam lithography, employed with ZEP, delineates the waveguide pattern by exposing resist areas around the waveguide structure during the e-beam exposure step, which are then removed during development. This technique, although advantageous for creating complicated patterns like fine grating lines in grating couplers—circumventing the weak bonding issue observed with HSQ lithography—significantly increases e-beam exposure time due to the expanded exposure area from the waveguide to its surroundings. Figure 4.12 illustrates the GDS design file for the TFLN-MZI waveguide structure tailored for the ZEP method, highlighting the design considerations and adaptations made to accommodate the specifics of positive resist e-beam lithography.

According to the diagram, regions delineated by dashed lines represent areas where the ZEP resist has been exposed during the lithography process. Specifically, the width of the ZEP exposed area along the x-axis totals 100 µm, with a 50 µm distance from the waveguide to the edge of this exposed region. Transitioning to the ZEP method introduced a new complication, particularly evident when attempting edge coupling at the waveguide's endpoint. This issue arises because the lithography process removes only the material surrounding the waveguide, leaving the waveguide endpoint obscured when viewed from the negative y-axis direction. Consequently, the TFLN structure that persists between the waveguide endpoint and the sample's edge not only obstructs the detector's ability to capture the waveguide's output signal but also significantly contributes to light diffusion, complicating the detection and analysis of the signal.

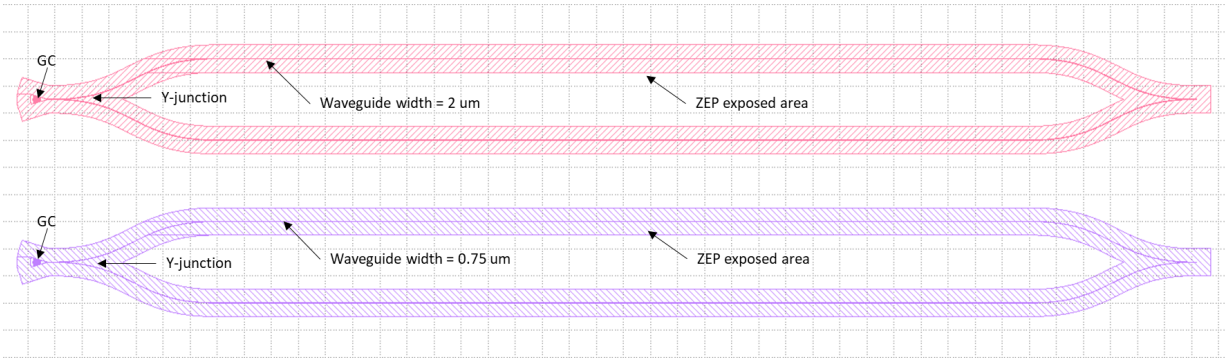

Figure 4.12: GDS Design for ZEP Positive E-Beam Lithography. Image of the GDS design file tailored for ZEP positive resist e-beam lithography process.

To facilitate edge coupling, a post-fabrication dicing procedure was implemented, targeting the area adjacent to the waveguide endpoint that had been exposed during lithography. This dicing operation utilized the same dicing saw equipment previously employed for slicing the TFLN samples, which, as mentioned in an earlier section, boasts an accuracy of 2 µm—sufficient precision for this particular task. The dicing process effectively removes the TFLN material located between the waveguide and the sample's edge, thereby rendering the waveguide endpoint visible from the sample's cross-section. This strategic removal ensures unobstructed access to the waveguide's output for edge coupling applications. Figure 4.13 provides a visual depiction of the post-fabrication dicing strategy employed to prepare the TFLN sample for edge coupling, following the etching process, highlighting the meticulous approach to overcoming obstacles associated with the ZEP method and enhancing the sample's compatibility with desired optical testing and application techniques.

4.2.6 Characterization: ZEP

Figure 4.14 presents microscope images of the TFLN sample following ZEP e-beam lithography, where the dark green hue in the light field microscope image signifies the regions covered by ZEP resist, contrasting with the lighter green areas where the TFLN layer is exposed to air. This distinction is crucial as the ZEP layer serves as a hard mask for subsequent etching processes, aligning with the patterns of the TFLN-MZI waveguide and the GC. The images confirm successful patterning of the waveguide and GC structures with a 2 µm width post-lithography. However, the formation of the 0.75 µm width waveguide encountered issues, evidenced by a twisted crack across the exposed area, suggesting that the suboptimal fabrication resulted primarily from the dose level utilized during e-beam

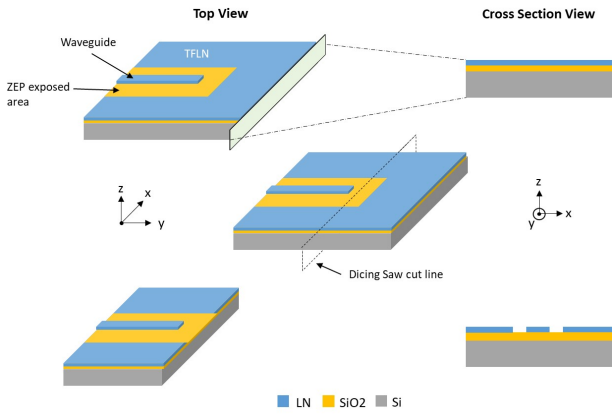

Figure 4.13: Post-Dicing Waveguide Endpoint Visualization. Image showcasing the clearer waveguide endpoint cross-section after the dicing process.

lithography. With a dose level of 20 µC/cm^2 at 20 kV and an exposure time of approximately three hours per TFLN-MZI waveguide device, this falls short of the manufacturer's recommended range of 30 to 35 µC/cm^2 for ZEP resist. While a reduced dose level might enhance the precision of fine structures during exposure, it significantly extends the exposure duration. Further experimentation with a dose level of 15 µC/cm^2 at 20 kV did not yield improvements in forming the 0.75 µm width waveguide, pointing to additional contributing factors such as the intrinsic properties of ZEP resist, development process timing, and more.

The top right bright field image illustrates the GC post-lithography, showing generally clean and organized grating pitches with separated lines, albeit with non-uniform spacing—some lines are notably closer together. This variance in grating line spacing might stem from lithography parameter adjustments specifically made for the GC area, which has distinct structural geometry and size requirements. An optimized lithography setup was therefore applied to the GC area, as evidenced by both bright field and dark field imaging confirming successful development of the grating pitches. The concluding light field image reveals the TFLN-MZI waveguide endpoint and the Y-junction connected to it, with no observable fabrication defects in these areas, indicating a successful application of optimized lithography parameters to these critical components of the waveguide structure.

Figure 4.15 showcases a light field microscope image of the TFLN-MZI waveguide and the GC following the removal of the ZEP resist, with Remover PG solution marking the final step in the ZEP resist fabrication process. According to the microscope image analysis, the TFLN-MZI waveguide, featuring a 2 µm width, along with the GC, has been success-

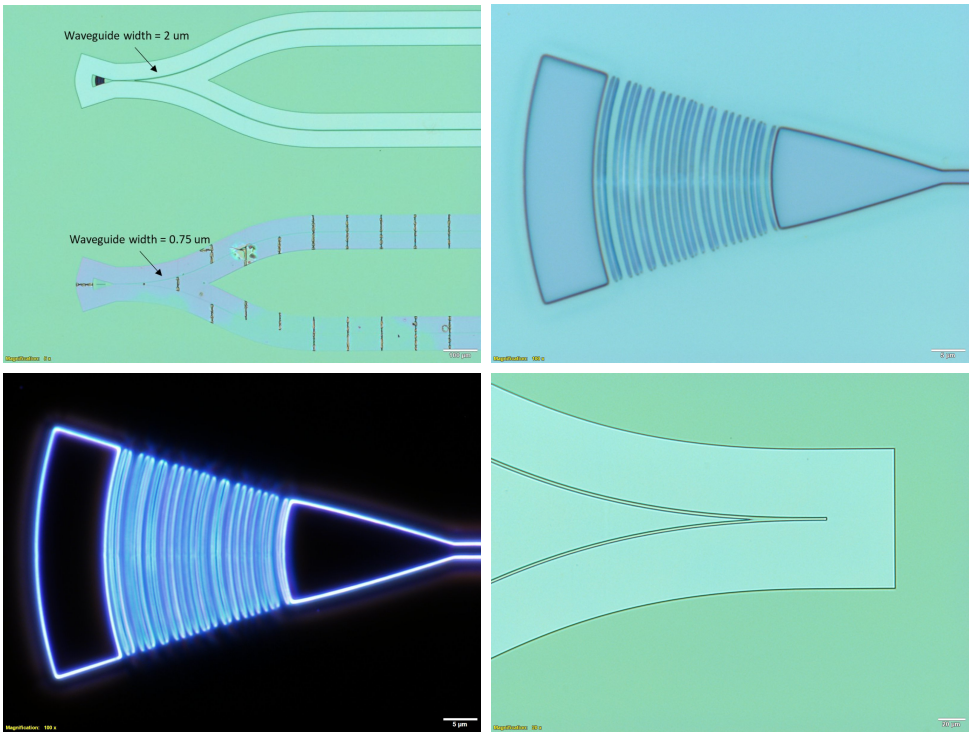

Figure 4.14: TFLN Sample Post-E-Beam Lithography with ZEP. Microscope images showing the TFLN sample with ZEP resist. Top left: GC and waveguide under light field. Top right: Waveguide under light field. Bottom left: GC under dark field. Bottom right: Waveguide endpoint under light field.

fully fabricated using the ion milling etching process. The observed spacing between the two waveguides (sensing and reference) measures 296 µm, slightly less than the 298 µm spacing documented from the HSQ resist fabrication process and the anticipated 300 µm spacing derived from simulations. This minor discrepancy may stem from measurement inaccuracies during the microscopic examination. The radius of the grating lines within the GC is noted to be 26.58 µm, and the width of the waveguide proximal to the GC is 1.94 µm, while the width at the waveguide endpoint reaches 2.11 µm, marginally exceeding the 2 µm width outlined in the design specifications. Despite these slight variations, the geometry of the fabricated TFLN-MZI waveguide and GC aligns closely with the design parameters set forth in the simulations, demonstrating a successful fabrication outcome with minor deviations. However, the attempt to fabricate the TFLN-MZI waveguide with a 0.75 µm width, alongside the GC, was unsuccessful in this process, leading to surface defects ob-

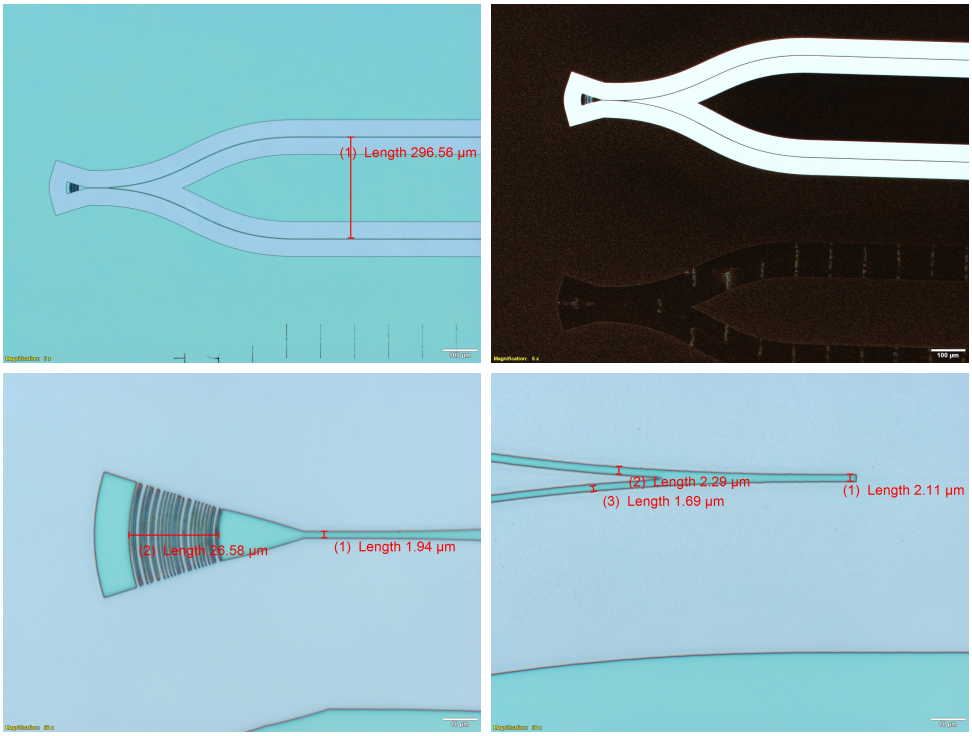

Figure 4.15: TFLN Sample After ZEP Removal. Microscope images displaying the TFLN sample after ZEP layer removal. Top left: GC and waveguide under light field. Top right: GC under light field. Bottom left: Waveguide endpoint under light field.

servable in both light field and dark field microscopy images, emphasizing the challenges faced in achieving fidelity with finer structural features in the fabrication process.

Figure 4.16 displays an SEM image that encapsulates the entirety of a TFLN-MZI waveguide along with the GC, presenting a comprehensive view of the device from left to right. This image includes the GC, a Y-junction designed to function as a 50/50 splitter, the 3 mm long sensing and reference waveguides, and the endpoint of the waveguide. The areas depicted in darker shades represent regions where the TFLN layer has been meticulously etched away, while the lighter structures encircled by these darker areas correspond to the waveguide and the GC structure. Due to the significantly larger scale of the etched areas compared to the waveguide itself, there's a notable potential for confusion when distinguishing between the waveguide and the surrounding etched regions. This visual ambiguity demonstrates the precision and scale of the etching process, highlighting the sophisticated balance between removing material to define the waveguide's path and

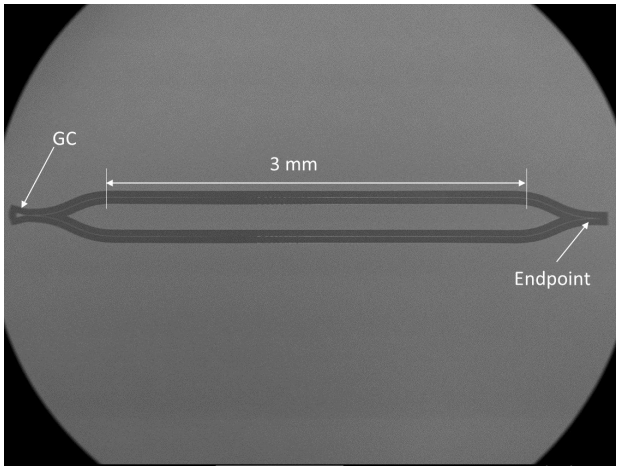

Figure 4.16: Complete TFLN-MZI Waveguide and GC with ZEP. SEM image showing the entire TFLN-MZI waveguide and GC structures post-ion milling and ZEP removal.

preserving the structural integrity of the waveguide and GC themselves.

Figure 4.17 presents SEM images that offer detailed views of various sections of the TFLN-MZI waveguide and the GC, highlighting the SEM's capability to provide high magnification images essential for characterizing and examining nanoscale structures. The first image, positioned at the top left with a magnification of x270, showcases the TFLN waveguide and GC without any noticeable fabrication defects or surface roughness. The adjacent image to the right offers a magnified view (x1800) of the GC, where the grating pitch and lines are clearly discernible. This closer examination confirms the successful fabrication of the grating pitch and lines, albeit with some lines closer together than others, and the spherical shape at the ends of the grating lines diverging from the square shape depicted in simulations. This spherical shape, consistent with the appearance post-E-beam lithography, suggests nonisotropic and precise etching achieved through ion milling, indicating high-quality fabrication. Nevertheless, bright dots observed on the surface point to the presence of redeposited TFLN and other minor surface defects.

The bottom left image, with a magnification of x500, focuses on the waveguide endpoint, where surface defects, though expected, are not visible at this scale. The final SEM image, offering a higher magnification of x15000, meticulously measures the waveguide's width at 1.719 µm and reveals a rough sidewall alongside randomly distributed fabrication defect dots. These findings demonstrate the potential benefits of implementing a smoothing process post-etching to mitigate surface roughness and, consequently, reduce propagation loss. However, due to budget constraints and other insurmountable factors,

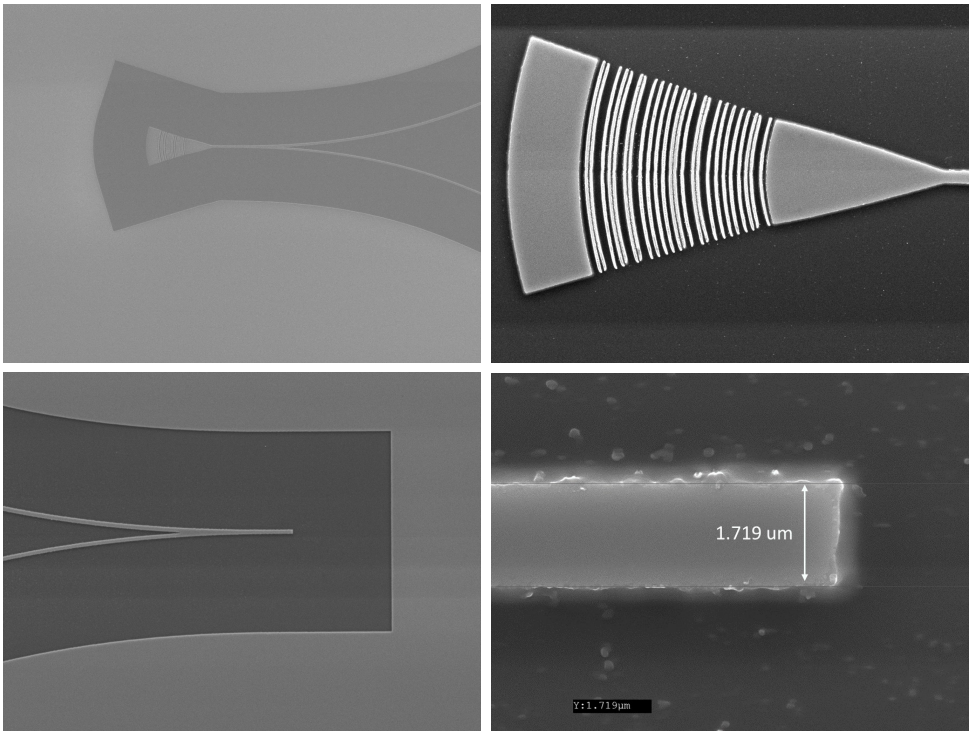

Figure 4.17: SEM Imaging of TFLN-MZI Waveguide Post-ZEP Fabrication. Images showing the waveguide structure after ZEP resist fabrication process. Top left: GC and connected Y-junction waveguide. Top right: GC. Bottom left: Waveguide endpoint. Bottom right: Endpoint at higher magnification.

further optimization processes were not pursued within this project's scope, leaving room for potential improvements in future iterations.

A U-shaped dual TFLN-MZI waveguide configuration incorporating GC was realized through the ZEP resist fabrication process. The initial figure 4.18, positioned in the upper left quadrant, delineates the GDS file design of the U-shaped dual TFLN-MZI waveguide structure. This design features two interconnected MZI waveguides linked by a 90-degree bending waveguide. Importantly, both the ingress and egress points of the waveguide employ GC structures to facilitate the coupling of optical signals into and out of the waveguide. The SEM image, displayed in the upper right, reveals the successfully fabricated U-shaped structure. In this image, the focus is on the MZI waveguides and the GC, as the comprehensive structure's dimensions exceed the SEM's imaging capabilities. From this visualization, it is evident that two MZI waveguides were simultaneously fabricated within

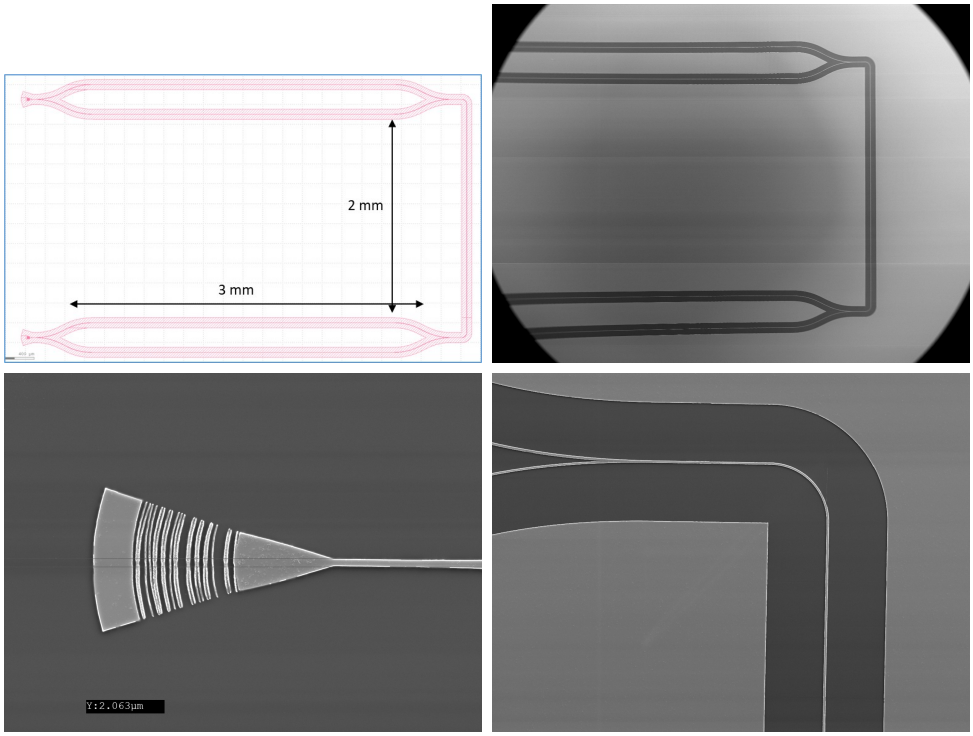

Figure 4.18: GDS Design and SEM Images of TFLN-MZI Waveguides. Top left: GDS design file for two TFLN-MZI waveguides. Top right: SEM image of fabricated waveguides. Bottom left: SEM image of the GC. Bottom right: SEM image of a 90-degree bending waveguide.

a single fabrication cycle, with no discernible defects. The lower left SEM image, offering a 1500x magnification view of the GC, highlights the grating pitch creation. However, it also reveals a critical fabrication anomaly: the fusion of two grating lines into a singular, broader line—a prevalent issue accompanied by irregular line edges and a rough surface texture. Such imperfections in the grating lines, which are integral to the GC's functionality, invariably diminish its coupling efficiency. Consequently, it is recommended that the GC within the U-shaped TFLN-MZI structure undergo a distinct fabrication process, segregated from other waveguide structures. Additionally, the SEM depiction of the 90-degree bending waveguide, located in the figure's bottom right, showcases its pristine and sharply defined sidewalls, devoid of any significant fabrication flaws.

This U-shaped waveguide's successful fabrication demonstrates the ZEP process's capability to create large-scale TFLN waveguides with bending structures and GCs. The

dimensions of the y-axis and x-axis are 2.6 mm and 3.4 mm, respectively, markedly exceeding the waveguide's width of 2 µm. The strategic incorporation of two MZI waveguides in this design is advantageous, enhancing the antenna's transmission of a stronger E-field along the two extended edges, thereby amplifying the electro-optic (EO) effect through the TFLN-MZI waveguides' dual E-field sensing capability. Nevertheless, the measurement of this fabricated U-shaped dual TFLN-MZI waveguide structure in the Advanced Optical Laboratory has not been conducted, attributed to the limitations in optical instrumentation and the temporal constraints of the project.

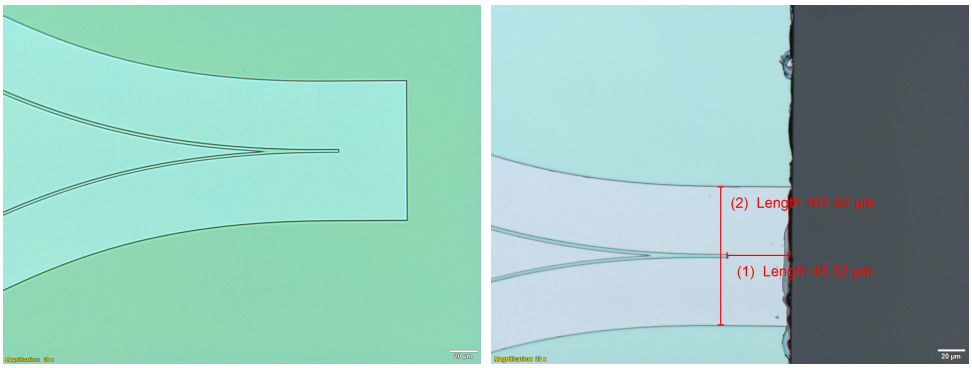

Figure 4.19: TFLN Waveguide Endpoint Pre and Post-Dicing. Microscope images showing the TFLN waveguide with ZEP endpoint before and after the dicing process.

Lastly, but of significant importance, the TFLN waveguide, realized through the ZEP fabrication technique, necessitates a post-fabrication step aimed at eliminating the superfluous TFLN layer interspersed between the waveguide's termination point and the sample's perimeter. Figure 4.19, as referenced above, showcases light field microscopy images of the TFLN sample both prior to and subsequent to the dicing procedure. From the design specifications, the exposure area extending from the endpoint to the edge of the TFLN layer was intended to span 50 µm. The image on the right illustrates that, following the dicing process, the measured distance from the endpoint to the edge of the TFLN sample is approximately 45.32 µm, with the absence of any residual TFLN layer or other structures in the intervening space. It should be noted that the observable crack along the sample's edge is a direct consequence of the dicing operation and is beyond rectification.

This detail demonstrates the criticality of precision in the post-fabrication phase to ensure the integrity and functional reliability of the TFLN waveguide. The meticulous removal of excess TFLN material is important in achieving the desired waveguide characteristics and operational performance. Furthermore, the acknowledgment of unavoidable

damage, such as edge cracking due to dicing, highlights the inherent challenges and limitations within the fabrication process. These insights are essential for refining fabrication techniques and improving the overall quality and effectiveness of TFLN waveguides in future iterations.

4.2.7 Fabrication Process: SiO_2 and ZEP

In the concluding phase of the TFLN MZI waveguide fabrication, the employment of SiO_2 as a robust hard mask combined with ZEP resist tailored for electron beam lithography stands out for its precision in defining the waveguide's sophisticated architecture. The SiO_2 hard mask provides exceptional resistance to etching processes, ensuring the integrity of the micro scale patterns essential for optimal waveguide performance. Concurrently, the ZEP resist, distinguished by its high resolution, facilitates the accurate etching of complex geometries onto the TFLN substrate, ensuring fidelity to the original design specifications.

Post-fabrication, the waveguide structures are meticulously analyzed through advanced microscopy and SEM, enabling a comprehensive evaluation of their structural integrity, geometric precision, and surface quality. This rigorous characterization process demonstrates the effectiveness of the SiO_2 and ZEP resist in producing waveguides that meet stringent quality standards, thereby contributing significantly to advancements in optical engineering and photonics research.

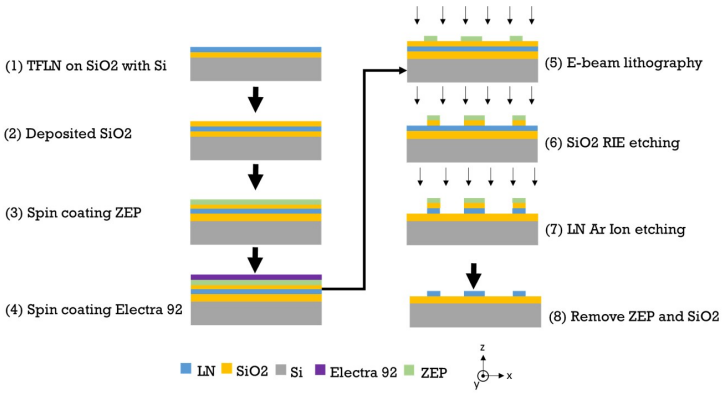

Figure 4.20: TFLN-MZI Fabrication Process Visualization with SiO_2 and ZEP. Detailed visual representation of the TFLN-MZI waveguide fabrication process using SiO_2 and ZEP positive resist for E-beam lithography.

The TFLN sample fabrication with SiO_2 encompasses the following steps:

1. Cleaning of the TFLN sample using Piranha solution to ensure a contaminant-free surface.

2. Deposition of 460 nm SiO_2 on the TFLN sample via Plasma Enhanced Chemical Vapor Deposition (PECVD) for the hard mask layer.

3. Application of 350 nm ZEP positive e-beam resist on the TFLN sample through spin coating, preparing it for electron beam lithography.

4. Addition of 80 nm Electra 92 negative resist on top of ZEP via spin coating, serving as a conductive layer to facilitate electron beam lithography.

5. Patterning of ZEP resist using electron beam lithography, followed by development and post-baking to finalize the resist pattern.

6. Transfer of the ZEP pattern to the SiO_2 layer using Reactive Ion Etching (RIE), where the 460 nm SiO_2 layer is etched away, with ZEP resist functioning as the etching mask.

7. Utilization of argon ion milling to etch 300 nm of the TFLN ridge waveguide, with both ZEP resist and SiO_2 layer serving as hard masks.

8. Removal of ZEP resist using Remover PG solution, followed by SiO_2 layer etching via RIE. The sample is then cleaned with acetone and isopropanol to remove any residues.

The fabrication of the TFLN-MZI waveguide, employing SiO_2 as a hard mask in conjunction with ZEP resist for lithography, mirrors the process used exclusively with ZEP resist. Initially, a layer of SiO_2 is deposited onto the sample, followed by the sequential spin coating of ZEP resist and Electra 92 conductive layer. Post electron beam lithography, the ZEP pattern is created, after which the sample undergoes a RIE process to transfer this pattern onto the SiO_2 layer through etching, with the ZEP resist serving as the hard mask.

Subsequently, ion milling etching targets the lithium niobate layer, where both the remaining ZEP and SiO_2 layers act as hard masks. The nature of ion bombardment, coupled with the high energy of Ar ions, results in an equal etching rate for both the ZEP layer and the lithium niobate, meaning 300 nm of lithium niobate and ZEP are etched simultaneously. This necessitates a resist removal step, where the remaining ZEP resist is dissolved using Remover PG solution, followed by a cleaning process using acetone and isopropanol. Finally, the SiO_2 layer undergoes etching via the RIE process.

From previous fabrication attempts, it's noted that the residual SiO_2 layer measures approximately 50 nm in thickness. Adjustments to the RIE process are made to target this 50 nm of SiO_2, based on lab-collected etching rate data. However, this RIE etching does not exclusively affect the SiO_2 layer but also the underlying TFLN layer. Prolonged etching not only fully removes the SiO_2 but also begins to etch into the TFLN layer. Complications arise with the hard mask coverage, especially around the TFLN-MZI waveguide and GC, which post-ion milling, are not entirely shielded by the SiO_2 layer. Introducing an additional RIE process risks damaging the waveguide's sidewalls and the SiO_2 layer between the TFLN and the silicon substrate. The project's resolution to this challenge involves optimizing the SiO_2 layer thickness on the TFLN such that a thin SiO_2 layer remains post-ion milling etching, allowing for a brief final RIE process to minimize damage. The detailed GDS design file for the TFLN-MZI waveguide structure, incorporating SiO_2 and ZEP resist, is depicted in Figure 4.21 below.

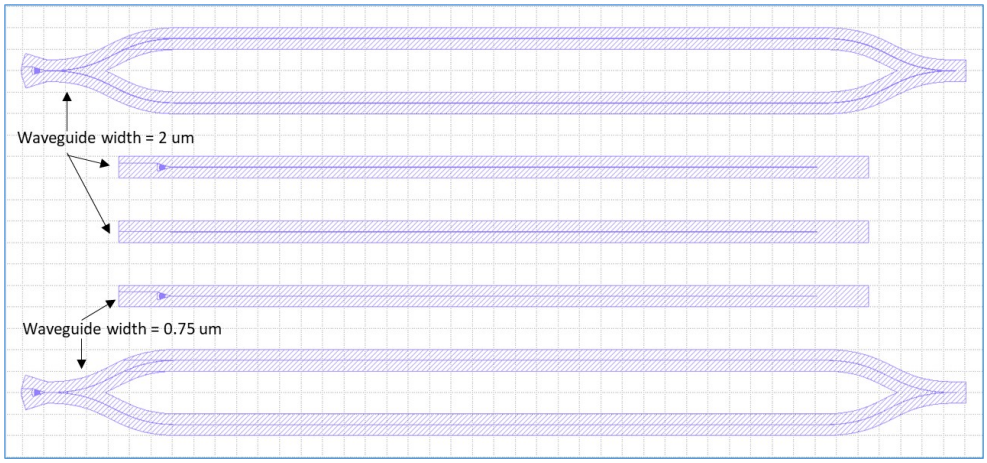

Figure 4.21: GDS Design for TFLN-MZI with SiO_2 and ZEP. Image of the GDS design file for TFLN-MZI waveguide fabrication using SiO_2 and ZEP.

In the refined fabrication process, additional devices were incorporated, including two straight waveguides each 2 µm in width—one equipped with a GC and the other without—and a narrower straight waveguide measuring 0.75 µm in width, also featuring a GC. This expansion builds upon the previous methodology that utilized HSQ and ZEP for fabricating multiple MZI waveguide structures along with GCs on a single TFLN sample. Initially, these waveguide structures were replicas from a single GDS file containing only one MZI waveguide design.

As the process for fabricating TFLN-MZI waveguides has matured, becoming more

reliable, and given the diminishing availability of lithium niobate samples in the laboratory due to numerous rounds of fabrication iterations, there was a strategic decision to diversify the waveguide structures fabricated in each cycle. This approach aims to enhance the experimental setup, providing a broader array of waveguide structures for comprehensive testing and measurement. The addition of these waveguides is a direct response to the evolving needs of the research, aiming to maximize the utility of each fabrication run by including diverse waveguide configurations for subsequent experimental investigations.

4.2.8 Characterization: SiO_2 and ZEP

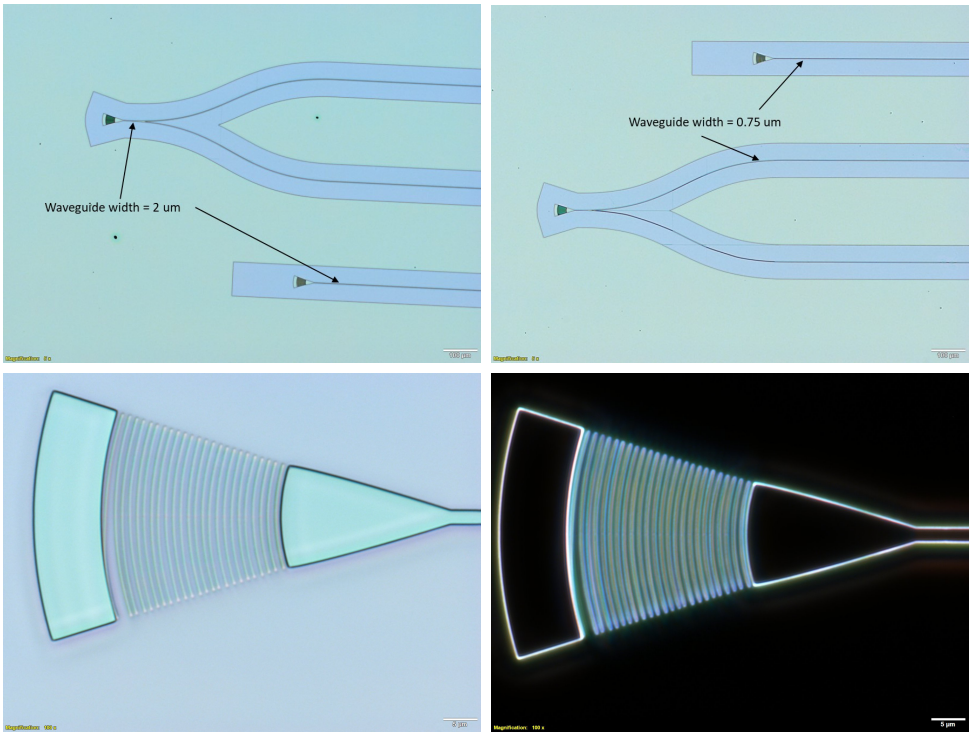

Figure 4.22: TFLN-MZI Waveguide Post-ZEP Lithography Microscopy. Top left: MZI and straight waveguide with 2 µm width. Top right: MZI and straight waveguide with 0.75 µm width. Bottom left: GC under light field illumination. Bottom right: GC under dark field illumination.

Microscopic imaging was employed for the analysis of the TFLN-MZI waveguide and the GC, with Figure 4.22 showcasing these images. The top left image presents the TFLN-

MZI waveguide alongside a straight waveguide of 2 µm width under light field microscopy, while the top right image displays both the MZI waveguide and a straight waveguide of 0.75 µm width, also in light field. These images confirm the successful creation of MZI and straight waveguides of both 2 µm and 0.75 µm widths through the ZEP resist electron beam lithography process. However, due to the low magnification (x5), the GC structures are not discernible in these images. Notably, fabrication defects in the form of dark dots are observable on the sample surface, particularly in the image featuring the 2 µm width waveguide.

The bottom left image, taken with a light field microscope at x100 magnification, focuses on the GC structure. This image reveals a failure in the electron beam lithography process to accurately form the grating lines and pitches. While the tapered area connecting to the waveguide is well-formed, the grating lines are absent, leaving only the ZEP resist markers visible on the surface. Conversely, the bottom right image, captured using dark field microscopy, shows the grating lines appearing brightly against a dark background, indicating the presence of resist markers. In dark field imaging, a solid structure of certain thickness typically exhibits brightness only at its edges, confirming that the observed brightness is due to the resist markers left on the surface rather than the intended grating lines.

Microscopic evaluations of the TFLN sample subsequent to the final RIE process are illustrated in Figure 4.23. The upper portion showcases two light field microscopy images: one of the MZI waveguide and another of the straight waveguide, with widths of 2 µm and 0.75 µm, respectively. The dark dots, previously noted in SEM imagery, are also visible here, having increased in size and clarity as a result of additional etching steps. These images further reveal the disappearance of grating lines within the GC, leaving behind only faint marks. This observation corroborates the earlier hypothesis that the grating lines failed to materialize from the electron beam lithography process, suggesting that the visible structures were indeed resist markers, not the intended grating features.

The lower section of Figure 4.23 contains two more microscope images focusing on the GC, captured in both light field and dark field modalities. These images confirm the absence of grating lines at the center of the GC, while the tapered structures leading into the GC are accurately crafted. This absence of grating lines underlines the challenges faced in the lithography and etching processes, highlighting the importance of refining these techniques to ensure the successful fabrication of complicated waveguide components. The detailed observation of these microscopic images provides crucial insights into the fabrication process's efficacy and areas requiring optimization to achieve the desired structural integrity and functionality of the waveguide and GC features.

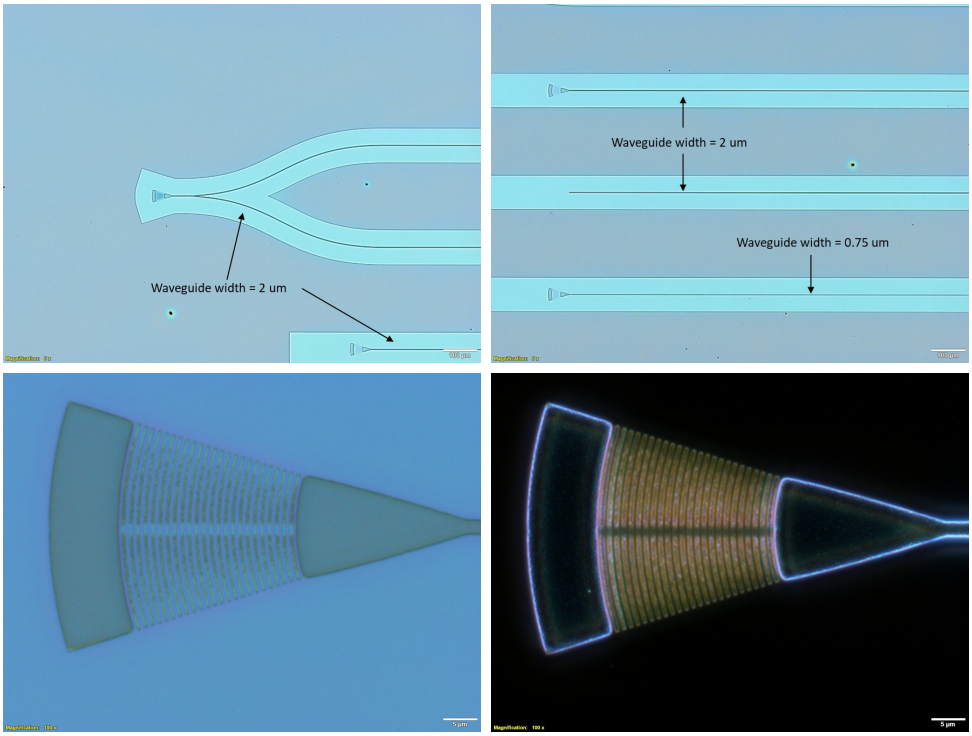

Figure 4.23: Post-RIE Process TFLN-MZI Waveguide Microscopy. After the final RIE process for SiO_2 removal, images show: top left: MZI and straight waveguide with 2 µm width; top right: Straight waveguides with both 2 µm and 0.75 µm widths; bottom left: GC in light field; bottom right: GC in dark field.

Scanning Electron Microscope (SEM) imagery of TFLN waveguide devices following the ultimate RIE process is detailed in Figure 4.24, offering a comprehensive view at various magnifications. The top left SEM image, captured at a lower magnification, displays a set comprising an MZI waveguide alongside straight waveguides of varying widths, 2 µm and 0.75 µm. Due to the selected magnification, the waveguide structures themselves are indiscernible, merging into the background as their dimensions fall below the threshold for clear visualization at this scale. The lighter areas depicted are indicative of the TFLN layer subjected to etching, a consequence of using ZEP positive resist.

The top right image, with a 250x magnification, delineates the GC and an adjacent waveguide of 2 µm width, where the features are readily distinguishable. Notably, the grating lines anticipated within the GC are absent, having been obliterated during the etching process, leaving the GC structure devoid of its critical light-coupling geometry.

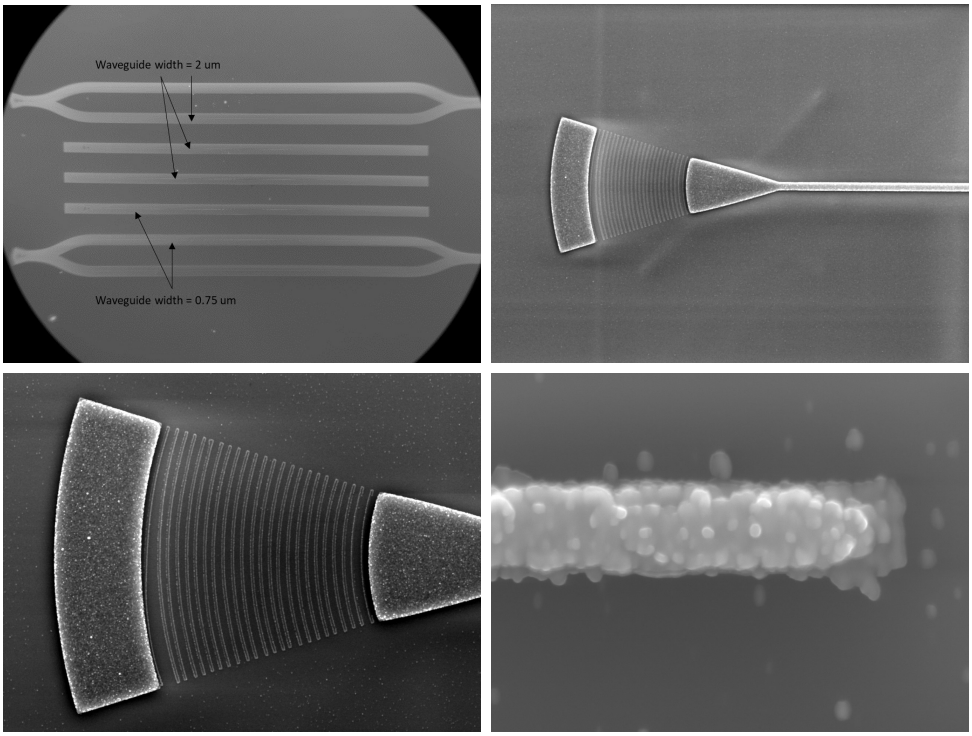

Figure 4.24: SEM Imaging Post-SiO_2 and ZEP Fabrication. SEM images of the TFLN waveguide structure after SiO_2 layer involved ZEP resist fabrication process. Top left: Overview of all devices including the MZI waveguide, straight waveguide, and GC. Top right: Close-up of GC and waveguide. Bottom left: GC at high magnification. Bottom right: Waveguide endpoint at high magnification.

A more detailed examination of the GC structure is presented in the bottom left image, captured at a magnification of 960x. Here, light markers are observable at locations originally designated for grating lines. These markers are remnants of the etching process targeted at the resist markers identified in prior imaging, suggesting a misalignment between the intended and actual outcomes of the lithography and etching processes.

The bottom right SEM image, taken at an extraordinary magnification of 25,000x, reveals the endpoint of a waveguide, showcasing over-etching and consequential morphological alterations. The waveguide's edge is eroded, deviating from its intended flat terminal surface to one characterized by protrusions and depressions, significantly compromising the structure's integrity. The vicinity of the waveguide is littered with particles of varying sizes, indicative of a rough etching aftermath.

This detailed visualization implies a pervasive issue of surface roughness across the fabricated waveguide structures, likely extending beyond merely the endpoints. Such textural irregularities are predictive of elevated propagation losses within the waveguide, as the rough surfaces introduce scattering losses that degrade the waveguide's optical performance. The SEM analysis underlines the critical need for optimization in the fabrication process to minimize surface roughness and ensure the structural fidelity and functional efficacy of TFLN waveguide devices.

4.3 Summary

In this chapter, the fabrication processes of TFLN waveguide devices were meticulously executed through three distinct methodologies: the HSQ process, the ZEP process, and the SiO_2 process. Among these, the ZEP process, which employs ZEP positive resist for electron beam lithography and serves as a hard mask, demonstrated superior performance in comparison to the other two techniques. It involved six principal fabrication steps and yielded devices with a minimal level of surface roughness. The ZEP process successfully fabricated the GC and the waveguide endpoints with only minor defects, such as deviations in grating line positioning and sidewall roughness of the waveguides. However, it encountered difficulties in fabricating waveguides with a width of 0.75 µm, necessitating additional post-processing to facilitate edge coupling.

The HSQ method, utilizing HSQ negative resist for electron beam lithography and as a hard mask for the etching process, offered the advantage of producing waveguides of various widths without the need for post-processing. Nonetheless, this method fell short in effectively fabricating GC due to insufficient adhesion between the PMMA and HSQ layers.

Conversely, the SiO_2 method, which leverages a SiO_2 layer as the hard mask combined with ZEP positive resist for electron beam lithography, is a commonly preferred technique for its protective and structural formation capabilities during the etching process. Despite its widespread use, the necessity to remove the SiO_2 layer at the conclusion of the fabrication introduces complexity, rendering this method the most challenging and yielding less satisfactory outcomes compared to the ZEP process in this specific project.

In the forthcoming chapter, the focus will shift towards the optical characterization of the fabricated samples on the optical table, examining their coupling efficiency and, critically, the electro-optical (EO) effect induced by the E-field from the antenna. Notably, three TFLN samples fabricated using the ZEP process are designated as the primary

subjects for the subsequent measurement phase. Samples produced through the HSQ and SiO_2 processes lack the GC structure for optical coupling, limiting their compatibility with the optical setup required for these measurements, thereby excluding them from this phase of the project evaluation.

Table 4.1: Performance Comparison of the Three fabrication Processes

	HSQ	ZEP	SiO2 and ZEP
Hard Mask	HSQ	ZEP	SiO2
E-beam Resist	HSQ	ZEP	ZEP
Number of Process	7	6	8
Surface Roughness	minor	minor	major
Grating Coupler	Fair	Success	Fair
Waveguide Endpoint	Success with defects	Success	Fair
Waveguide Width	0.75 um, 2 um	2 um	0.75 um, 2 um
Post Process	None	Dicing sample	Dicing sample

Chapter 5

Experimental Setup and Measurement Results for TFLN Waveguide and Antenna

5.1 Introduction of Experiment

Recent advancements in thin film lithium niobate (TFLN) have garnered significant attention, particularly due to the material's enhanced electro-optical (EO) properties and reduced dimensions compared to conventional lithium niobate (LN) wafers. The ability to limit the thickness of TFLN to sub-micrometer levels marks a notable evolution from traditional bulk LN structures. This development positions TFLN as a versatile material with potential applications extending from optical to radio frequency (RF) technologies. In particular, TFLN waveguides with integrated grating couplers have shown promise as dielectric optical devices capable of sensing electrical fields (E-fields) emanating from antenna systems.

The preceding sections have detailed the conceptualization, design, and simulation processes undertaken for TFLN waveguide and grating coupler (GC) structures. Following these initial stages, the design implementations were realized through meticulous fabrication processes in the Quantum Nano Centre (QNC) laboratory at the University of Waterloo. These processes employed a diverse array of fabrication methodologies. Subsequent to fabrication, the focus shifted to the development of a comprehensive measurement apparatus. This apparatus encompassed both an optical setup, tailored for the assessment of TFLN devices, and an antenna setup, designed for the evaluation of patch antennas. Given

the disparate operational frequencies and equipment requirements of optical and antenna measurements, the initial setup stages necessitated separate configurations within different laboratory environments. These configurations were eventually integrated, culminating in a multifaceted measurement system. The integration and resultant data from this system are anticipated to form a cornerstone of this research, offering empirical validation for the project's theoretical underpinnings.

The EO effect intrinsic to LN induces a modulation in the refractive index of LN waveguides when subjected to an external E-field, such as that from an antenna. This phenomenon is particularly pronounced in the context of a Mach-Zehnder interferometer (MZI) configured within the LN structure. The MZI effectively converts phase discrepancies between a sensing waveguide and a reference waveguide into measurable power differentials at the MZI's output. A primary aim of the optical measurement phase is to ascertain the total power efficiency of the entire TFLN MZI structure, achieved by quantifying the optical signal output from the TFLN MZI waveguide. In parallel, the antenna-centric experimentation focuses on delineating the near-field radiation pattern and evaluating the S_{11} parameters, with the near-field radiation defining the E-field proximal to the antenna patch—a crucial E-field source in this study. The overarching objective of the integrative experimental approach is to quantify the optical signal power variations in the TFLN MZI waveguide consequent to the activation of the antenna and the subsequent E-field induction on the sensing waveguide. Additionally, this research seeks to elucidate the relationship between the intensity of the induced E-field and the observed power differentials, both with the antenna operational and non-operational, by comparing these empirical findings against the predictions made in the simulation phase.

5.2 Antenna Measurement Setup

The antenna measurement procedures were conducted in two distinct laboratory environments: the Advanced Antenna Laboratory for near-field measurements and the Microwave Lab, adjacent to the Advanced Optical lab, for assessing the S_{11} parameters. Figure 5.1 illustrates the near-field experimental setup within the antenna laboratory. The AUT is placed on a 3D-printed stand, constructed from a material chosen for its low electromagnetic (EM) reflection properties. Connectivity between the AUT and the Vector Network Analyzer (VNA) is facilitated using an SMA cable, with the metallic SMA connector and cable enveloped in an E-field absorber to minimize EM reflections. Positioned opposite the AUT is a 30 GHz horn antenna mounted on a robotic arm, capable of bidirectional movement in the x and y axes with a minimum step size of 5 mm. A blue structure behind

Figure 5.1: AUT Measurement Setup Reiteration. Left: AUT positioned on a 3D printed stand. Middle: AUT and horn antenna in the near-field measurement setup. Right: The Keysight PNA-X network analyzer and robot motion controller.

the horn antenna serves as the E-field absorber for the robotic arm.

The right-side image in Figure 5.1 displays the control station for the antenna experiment system. Here, a VNA links to both the AUT and the horn antenna through SMA cables. This station also houses devices for controlling and calibrating the robotic arm's motion. The AUT and horn antenna alternate roles between transmitting and receiving antennas based on VNA instructions. During measurements, the AUT remains stationary while the horn antenna, guided by the robotic arm, traverses the XY plane. Data captured by the horn antenna is analyzed and post-processed using the network analyzer.

The E-field amplitude is ascertained using the inverse Fourier transform method, an indirect measurement technique for calculating far-field properties. Initially, the AUT's radiation pattern is measured with the near-field setup, with the horn antenna acting as the receiving probe placed 20 mm from the AUT. The measured near-field radiation pattern is then converted to a far-field radiation pattern using Fourier transform functions on a computer. Subsequently, the far-field radiation pattern is translated into E-field intensity through inverse Fourier transform functions, enabling E-field intensity calculation via a post-processing technique. This post-processing method offers the advantage of reducing interference between the receiving antenna and the AUT, as physical proximity is not required.

The S_{11} parameter measurements occur in the Microwave Lab adjacent to the Advanced

Optical lab. Figure 5.1 right shows the Keysight PNA-X network analyzer (PNA), utilized for measuring the AUT's S_{11} parameter. Accurate measurement necessitates calibration of the VNA using a standard coaxial cable calibration box connected via two coaxial cables. The network analyzer's maximum output power is set to 20 dBm at a 30 GHz frequency, corresponding to an input power of 100 mW for the antenna. This input power level is crucial as it determines the electric field intensity generated by the antenna for subsequent measurements.

Post-calibration, the AUT is connected to the VNA using a single coaxial cable, focusing primarily on the S_{11} parameters. For S_{21} and S_{12} parameter measurements, an additional receiving antenna would be required, mirroring the setup used in the near-field distribution measurements in the antenna lab.

5.3 Antenna Data Collection and Analysis

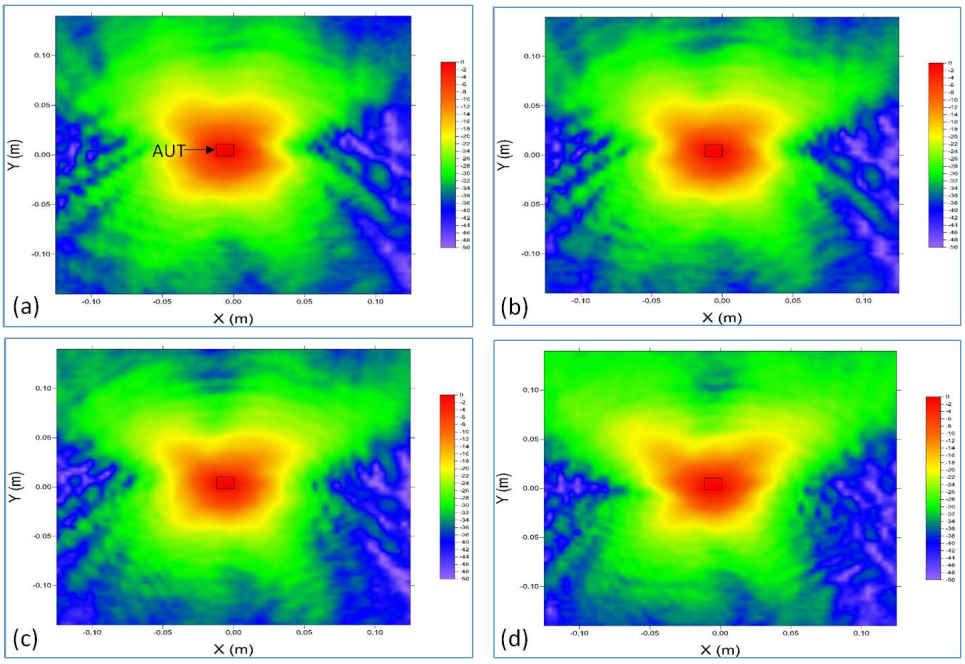

Figure 5.2: Near-Field Radiation Pattern Measurements. Presenting measured near-field radiation patterns at frequencies: (a) 30.5 GHz, (b) 31 GHz, (c) 31.5 GHz, and (d) 32 GHz, showcasing variations in radiation pattern with frequency.

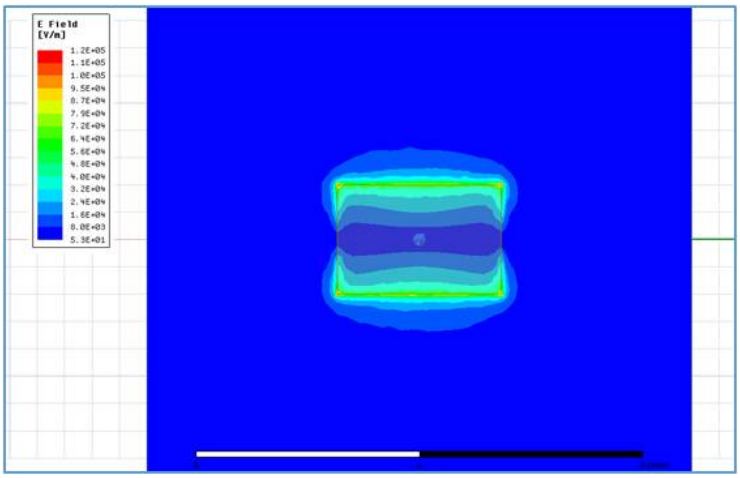

Figure 5.3: E-Field Distribution of AUT Patch. Top view of the E-field distribution from the simulated AUT patch in HFSS.

In Figure 5.2, the near-field amplitude measurement results at various frequencies between 30.5 GHz and 32 GHz are presented. The black squares in each image demarcate the location of the AUT. These near-field plots, obtained through post-processing of the radiation pattern data, visually depict the E-field distribution across different frequencies. Notably, the experimental near-field amplitude closely mirrors the E-field distribution observed in the HFSS simulation, as shown in Figure 5.3. The most intense fields emanating from the active edge of the AUT indicate effective antenna radiation, aligning well with the design expectations. Such consistency between the experimental outcomes and the simulations instills confidence in both the precision of the simulation methodologies and the robustness of the fabrication process.

A point of interest is observed in the near-field amplitude distribution, particularly between 30.5 GHz and 31 GHz, and then at 31.5 GHz. At the higher frequency of 32 GHz, the field distribution along the bottom active edge of the AUT appears reduced in comparison to the distributions at lower frequencies. This observation hints at a possible deviation in antenna performance at the upper end of the frequency spectrum, potentially attributable to factors like fabrication tolerances or other influences that might affect the antenna's behavior.

Transitioning to far-field amplitude distribution analysis, the AUT's measured near-field radiation pattern is transformed into far-field properties via Fourier transform functions. This conversion facilitates a holistic understanding of the antenna's performance, enabling an evaluation of key characteristics such as antenna gain and the radiation pattern

under diverse operational conditions.

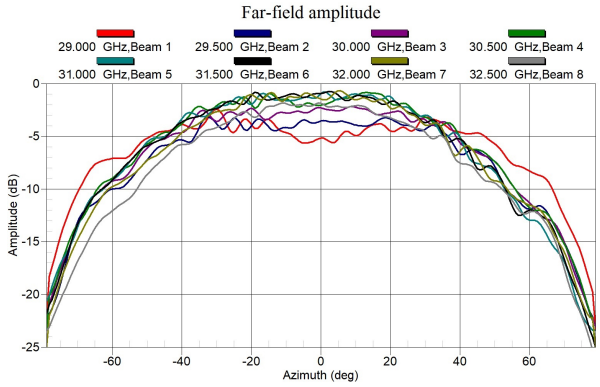

Figure 5.4: Far-Field Amplitude Variation. Illustrates the far-field amplitude at different frequencies ranging from -60 degrees to 60 degrees, across the frequency spectrum from 29 GHz to 32 GHz.

Figure 5.4 illustrates the far-field amplitude distribution over a range of -60 degrees to 60 degrees at various frequencies, specifically from 29 GHz to 32 GHz. The far-field plots exhibit close similarity and even distribution within the -20-degree to 20-degree region, with amplitudes above -5 dB. This far-field distribution also aligns with the radiation pattern obtained from the HFSS simulation, further validating the accuracy of the simulation and the effectiveness of the fabrication process.

Subsequently, the S_{11} parameter analysis of the AUT is conducted in the microwave laboratory, utilizing a network analyzer and the standard calibration toolbox. The S_{11} parameter is an important factor in characterizing the antenna's performance, as it provides insight into the reflection coefficient and the impedance matching of the AUT. By examining the S_{11} parameter, researchers can evaluate the efficiency of the antenna's power transmission, which directly impacts the overall performance of the antenna in real-world applications.

The combination of near-field and far-field amplitude distributions, along with the S_{11} parameter analysis, provides a comprehensive assessment of the AUT's performance across various frequencies. The data obtained from these measurements can inform future iterations of the antenna design, ultimately leading to improved efficiency and suitability for specific applications.

In contrast, Figure 5.5 presents a comparison between the measured S_{11} parameter obtained from the AUT using the PNA and the simulated S_{11} results derived from HFSS.

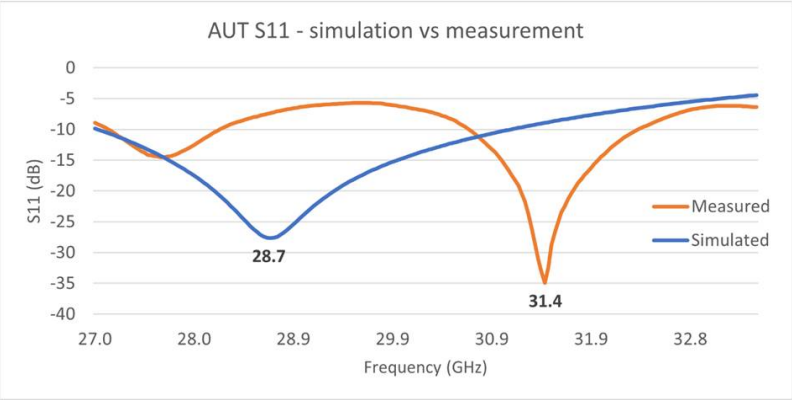

Figure 5.5: S_{11} Parameter Simulation vs. Measurement. Comparison of simulated and measured S_{11} parameters for the AUT, showcasing the accuracy of simulations against real-world measurements.

As illustrated in Figure 5.5, the peak of the measured S_{11} plot is observed at 31.4 GHz, deviating from the simulated S_{11} peak at 28.7 GHz. The measured S_{11} value at 31.4 GHz is less than -30 dB, showcasing a narrow bandwidth. The simulated AUT center frequency, as determined by HFSS, is at 28.7 GHz, with an operating frequency range spanning 26 GHz to 31 GHz. The shift in the center frequency of the AUT may be attributed to fabrication defects and E-field reflection caused by surrounding structures in close proximity to the AUT. These factors can influence the antenna's performance, leading to discrepancies between the simulated and measured results.

In Figure 5.6, the impact of incorporating vias into the antenna is studied, showcasing both simulated and measured S_{11} parameters for the antenna with and without vias. In simulations, adding vias to the antenna design caused a slight shift in the S_{11} pattern to higher frequencies and a reduction in the S_{11} peak. The experimental results mirrored this pattern, with the S_{11} shifting to higher frequencies and a decrease in bandwidth. This correlation between the simulation and experimental findings highlights the significant impact of vias on the antenna's structural integrity and performance. The measurement results align with the initial design and simulation predictions, indicating that introducing vias into the antenna permanently alters its structure, thereby significantly influencing its performance. The size and placement of these vias emerge as critical factors that require meticulous consideration in future experiments.

Finally, the E-field intensity radiated from the antenna is estimated based on experimental results obtained from vector analysis. The vector analysis within the antenna measurement setup is capable of adjusting the power to the antenna between -10 dBm and

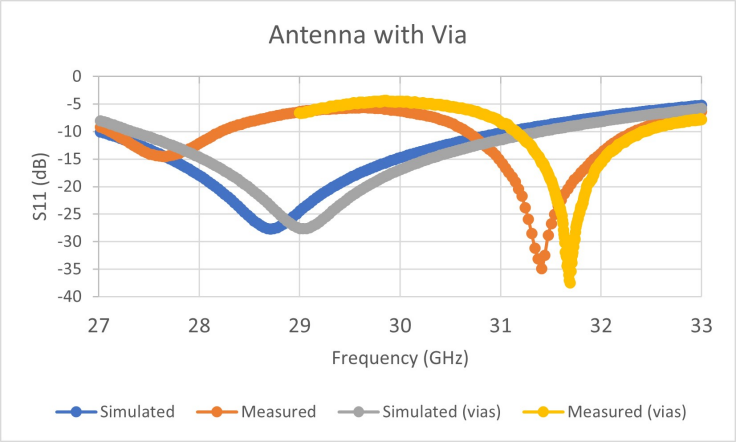

Figure 5.6: Antenna S_{11} Parameters: With and Without Via. Comparative analysis of simulated and measured antenna S_{11} parameters, illustrating the effect of implementing a via in the design.

20 dBm at a frequency of 30 GHz. According to the vector analysis user manual, a power level of 10 dBm corresponds to an output of 100 mW, while 20 dBm equates to 100 mW. Consequently, the E-field intensity emanating from the antenna in the near-field region can be calculated from the vector analysis output power.

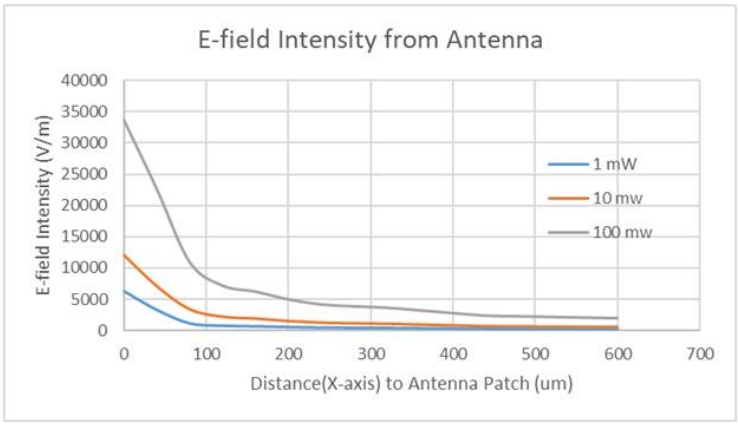

Figure 5.7: E-Field Intensity Variation by Input Power. Shows how the E-field intensity from the antenna patch varies with different levels of input power.

Figure 5.7 illustrates the E-field intensity as the distance from the antenna patch increases, measured at different vector analysis output power levels of 1 mW (0 dBm), 10

mW (10 dBm), and 100 mW (20 dBm). The E-field intensity experiences a rapid decline from zero to 100 microns, then transitions to a more gradual decrease beyond 100 microns. Based on these E-field intensity plots, it is discerned that the TFLN-MZI waveguide should be positioned as close to the antenna patch as possible to maximize E-field intensity, thereby enhancing the effectiveness of the overall setup.

5.4 Design and Development of Optical Measurement Setup

The design and development of the optical measurement table are instrumental to the success of the experimental initiatives, serving as the foundational element for the series of combined experiments that ensue. Central to this apparatus is a laser emitting at a 1550 nm wavelength, which is channeled through a single-mode fiber. This fiber interfaces with a tapered fiber, a critical component for achieving efficient coupling into the TFLN GC. The design of the tapered fiber, with a spot diameter smaller than that of the TFLN GC, is instrumental in enhancing the coupling efficiency. The laser subsequently traverses the entire MZI structure, culminating in detection by a power meter at the output of the TFLN MZI, where an edge coupling methodology is employed to ensure optimal signal transmission. A detailed schematic representation of this setup is delineated in Figure 5.8.

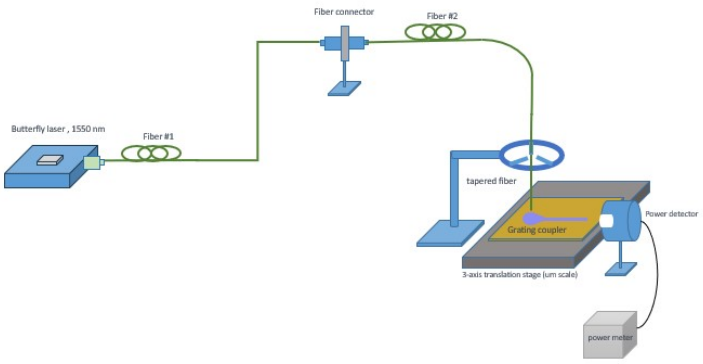

Figure 5.8: Schematic of Optical Measurement Setup. Diagram showcasing the optical measurement setup with a 1550 nm laser source.

The developmental phase encountered several challenges necessitating innovative solutions. The primary challenge was the alignment of the tapered fiber with the GC, compounded by the non-visible nature of the 1550 nm wavelength laser. To circumvent this, a

laser operating at a visible wavelength of 633 nm was integrated for alignment purposes. The alignment mechanism required the fiber and sample stage to possess micrometer-scale adjustment capabilities for precise calibration. Furthermore, a 3-axis sample stage was deemed essential to facilitate precise multi-directional positioning of the TFLN MZI sample. A critical design consideration was to minimize the spatial separation between the sample and the power meter, ensuring maximal capture of the laser output emanating from the waveguide.

To address these challenges, the experimental setup incorporated a 633 nm wavelength laser, specifically for the alignment phase. Figure 5.9 illustrates the configuration employed during this phase. Post alignment with the TFLN GC structure using the 633 nm laser, the system transitions to the 1550 nm laser to resume the experiment as initially planned. To augment the accuracy of the measurements, the fundamental components of the setup, including the fiber holder, sample stage, and microscope, were outfitted with three degrees of freedom. Additionally, to bolster the stability of the measurement process, the entire assembly was constructed atop a vibration isolation table.

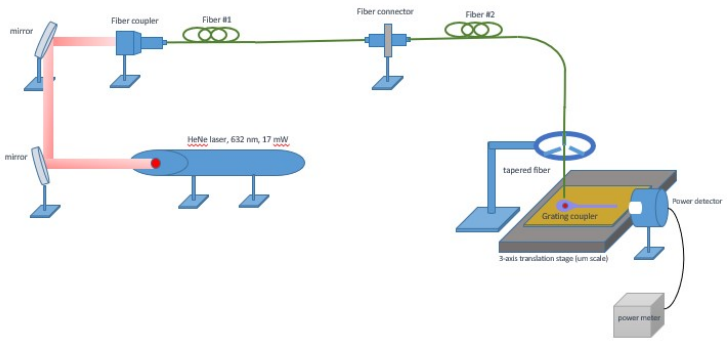

Figure 5.9: GC Alignment Optical Setup Schematic. Diagram of the optical measurement setup utilizing a 633 nm laser source specifically for GC alignment.

5.5 Experimental Setup in Advanced Optical Lab

The experimental setup in the Advanced Optical lab begins with the selection of the laser sources: a THORLABS 633 nm HeNe laser and a THORLABS 1550 nm Fabry-Perot Laser Diode. The 633 nm laser utilizes an air-space collimator for coupling the laser from free space into the optical fiber, while the 1550 nm laser is housed in a 14-pin butterfly package,

connected to a polarization-maintaining fiber. Once connected to the single-mode fiber using FC/APC connectors, these lasers can be easily interchanged during the experiment.

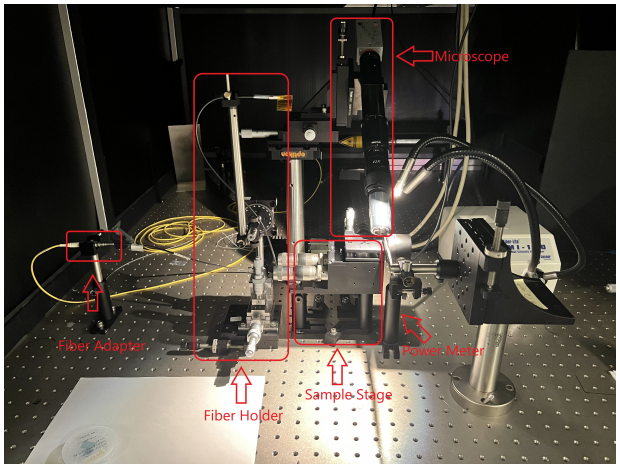

Figure 5.10: Optical Measurement Setup Photography. Photo depicting the entire optical measurement setup arranged on the optical table.

Following this, a single-mode tapered fiber designed for 1550 nm wavelength with an FC/APC connector is connected to the laser fiber using fiber optic connector adapters. This tapered fiber, boasting a spot diameter of 2.5 microns and a working distance of 14 microns, is mounted on the optical table using optical posts and post holders to reduce the influence of fiber switching on the adapter.

Adjacent to this setup is the fiber holder, which includes a small kinematic V-clamp mount for the tapered side of the fiber, crucial for grating coupler alignment. This mount is connected to a manual rotation stage, which allows adjustment of the incident angle of the tapered fiber to the TFLN GC. Furthermore, the rotation stage is mounted on a 3-Axis stage, providing three degrees of freedom. This assembly, comprising the 3-Axis stages, rotation stage, and V-clamp, constitutes the fiber holder, as illustrated in Figure 5.11.

The next critical instrument in this optical experiment is the TFLN MZI waveguide sample stages. A THORLABS pitch and yaw stage, mounted on a 3-axis flexure stage, replaces the regular top plate, enabling fine control in five axes at the micron scale. This pitch and yaw stage, serving as the sample stage, holds the sample attached to its right front corner to minimize the distance to the following instruments. A photodetector covering a 500 nm – 1700 nm wavelength range is mounted on the optical table adjacent to the sample stage and connected to a high-sensitivity NEWPORT 2936-C power meter. This setup

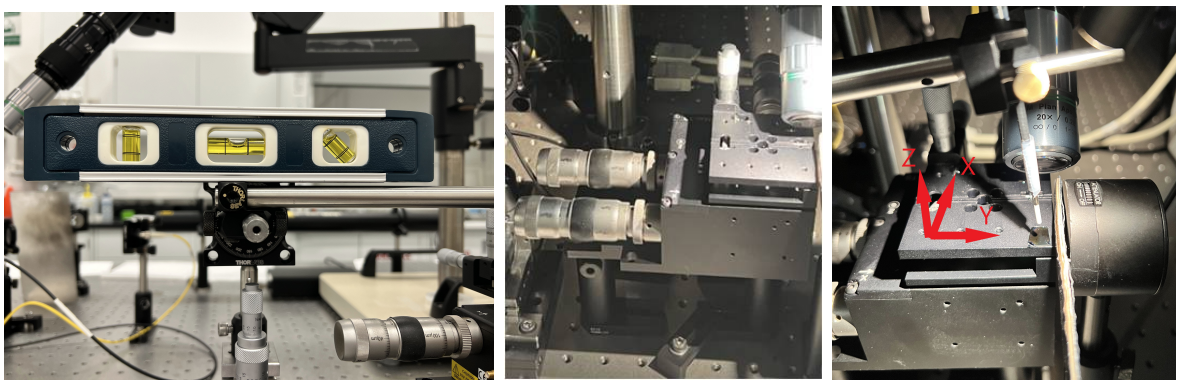

Figure 5.11: Optical Measurement Equipment. Photos showing key components of the optical measurement setup. Left: fiber holder. Middle: Sample stage. Right: Full optical measurement setup with an XYZ-coordinate system.

ensures the laser signal, after coupling through the TFLN-GC structure and transmitting through the waveguide, is efficiently captured by the power meter after traveling less than 10 millimeters through air via edge coupling.

The NEWPORT 918D Indium Gallium Arsenide (InGaAs) photodetector is engineered for the measurement of low optical power within the 800-1650 nm wavelength range. According to the manufacturer's datasheet, the noise-equivalent power (NEP) of this photodetector spans $4 \times 10^{-14}\,\mathrm{W}/\sqrt{\mathrm{Hz}}$ for wavelengths ranging from 901 to 1650 nm. NEP is delineated as the incident power that yields a signal-to-noise (S/N) ratio of one within a 1 Hz bandwidth [56]. In the context of this project, when an optical signal at a wavelength of 1550 nm is detected using this photodetector, the requisite optical power for achieving an S/N ratio of one is calculated to be 0.5 µW, as per the following equation 5.1:

$$P_{S/N=1} = NEP \times \sqrt{\frac{C}{\lambda}} \tag{5.1}$$

Here, C represents the speed of light, and λ denotes the wavelength of the optical signal. The datasheet for this photodetector, in conjunction with a power meter, indicates that sufficient resolution for measuring the power output of the TFLN waveguide can be achieved, provided that the output power exceeds one microwatt.

A NAVITAR 12X Zoom system coupled with a 20X Mitutoyo infinity-corrected objective forms a high-resolution microscope capable of detailed micrometer-scale observations. This microscope system, interfaced with the lab computer, enables control of parameters

and displays images. The resolution of the microscope images, however, is affected by the absence of a dedicated light source for the NAVITAR lens system, necessitating the use of an external light source.

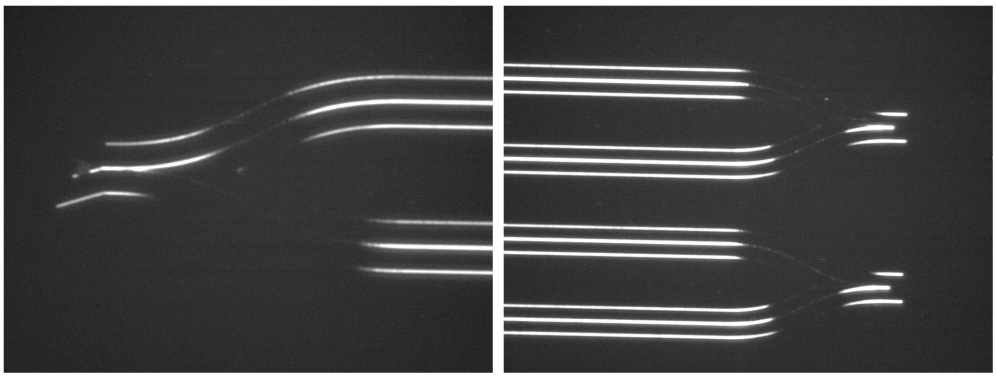

Figure 5.12: TFLN-MZI Waveguide Microscopic Imaging. Left: TFLN-MZI waveguide and GC. Right: Output end of the TFLN-MZI waveguide, captured through the microscope system.

The experimental process initiates with placing the TFLN-MZI waveguide sample at the right bottom corner of the sample plate on the stage, ensuring the sample's edges are close to the plate's sides. The fiber holder arm is then lowered, positioning the tapered fiber above the sample. The rotation stage is unlocked, and the arm is rotated to achieve the desired incident angle for the laser, which is then locked in place.

After connecting the 633 nm laser to the fiber adapter and activating it, a bright spot from the laser is visible on the sample under the microscope. The XY position of the tapered fiber is manually adjusted while frequently monitoring the microscope until the laser spot aligns with the TFLN-GC structure.

Once the fiber's height is optimized so that the entire laser spot is within the TFLN-GC structure, the alignment process is deemed complete, and the 633 nm laser is replaced with the 1550 nm laser. Care is taken to maintain the fiber holder and the sample stage at the same Z-height to prevent any damage to the closely positioned tapered fiber.

During the experiment, several modifications and optimizations were implemented. The most notable is the introduction of a baffle between the sample and the power meter, made from non-reflective material and featuring three degrees of freedom. This baffle helps reduce environmental noise like scattered light, which can interfere with optical signal measurements.

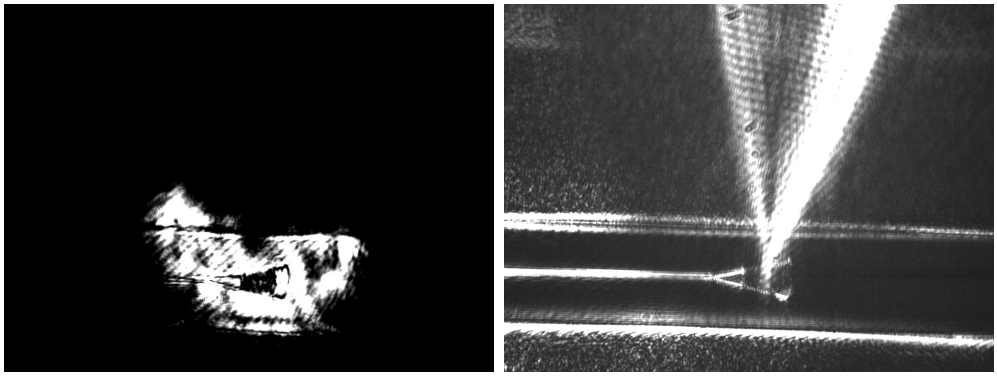

Figure 5.13: GC and Laser Spot Visualization. Image capturing the GC and the laser spot under the microscope using a 633 nm laser.

Figure 5.14 demonstrate the setup, highlighting the baffle's role in mitigating environmental light noise. However, some scattering light from the waveguide is observed, indicating the need for further data analysis to enhance noise reduction.

5.6 Optical Data Collection and Analysis

The initial phase of optical data collection involved determining the methodology for data acquisition, given the complexity of the optical experiment setup with its myriad of optical equipment, rotation stages, and other optomechanical components. To ensure accuracy, it was decided that each measurement would consist of six readings taken over an hour, with a 10-minute interval between each reading. To ensure consistency, when measuring two different setups, they were evaluated concurrently without any modifications to the measurement setup.

The first optical measurement undertaken was the assessment of the laser signal input power from the tapered fiber to the TFLN-MAI waveguide at a 1550 nm wavelength over a one-hour period. This also corresponded to the output power from the tapered fiber, which was measured using a power meter. Figure 5.15 illustrates the output power from the tapered fiber within this timeframe. The data reveals an increase in power from 2.48 mW to 2.51 mW in the initial 10 minutes, stabilizing in the subsequent 50 minutes with an average of 2.51 mW. The dashed line in the figure represents the trendline for the input power results. These findings indicate that the optical experiment setup initially experienced instability, likely due to movement of optical components and vibrations caused

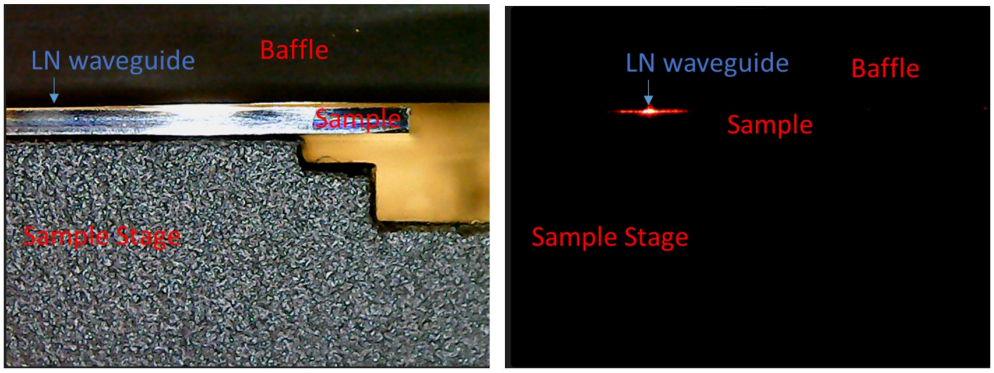

Figure 5.14: TFLN Sample Illumination Comparison. Left: Camera image of the TFLN sample and baffle under flashlight illumination. Right: Image with the 633 nm laser enabled and no flashlight, highlighting the laser interaction.

by other activities in the lab. However, the setup stabilized after the first 10 minutes, yielding accurate and reliable results thereafter. This pattern of stabilization was observed consistently in subsequent optical measurements.

Subsequent measurements focused on the output power of the laser signal from the TFLN-MZI waveguide, using the same data collection methodology. Figure 5.16 displays the output power measured at the waveguide's end by the power meter. Two scenarios are depicted: one where the incident laser is not aligned with the GC (diamond shape plot) and the other where it is aligned (square shape plot). The average power received when misaligned was 11.46 uW, which increased to 18.50 uW when aligned. This demonstrates a 7.04 uW increased power which is 61.5% more output power when the tapered fiber proper alignment with the GC.

A critical parameter for evaluating the precision of power detection is the S/N ratio. In this experiment, the power detection was facilitated by a NEWPORT InGaAs photodetector, which exhibits a NEP of $4 \times 10^{-14}\,\mathrm{W}/\sqrt{\mathrm{Hz}}$ over a wavelength range from 901 to 1650 nm. According to detailed specifications provided by the manufacturer, achieving an S/N ratio of 1, particularly at the 1550 nm wavelength, necessitates a minimum optical power of 0.5 µW. Based on these stringent criteria, the S/N ratios for the optical powers captured by the power meter under conditions of misalignment and precise alignment were calculated to be 13 dB and 15 dB, respectively.

The recorded power when the incident laser is off alignment is attributed to environmental background noise and scattered light leakage from the baffle, as corroborated by camera images in Figure 5.14 showing detected scattering light at the sample site. The

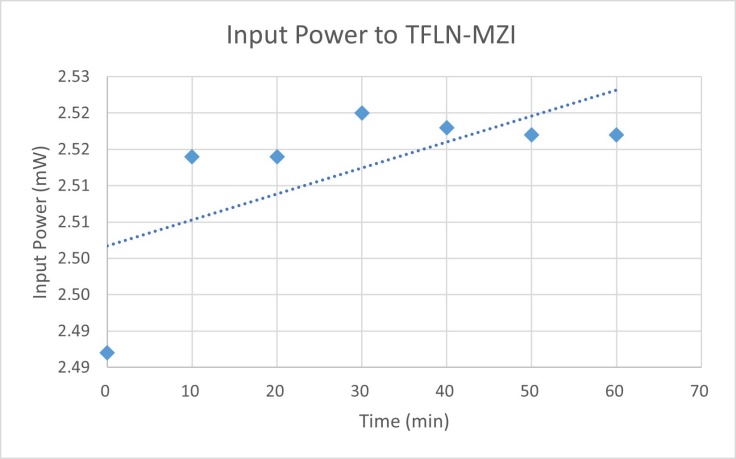

Figure 5.15: Input Power Stability Over Time. Graph depicting the stability of input power from the tapered fiber into the TFLN-MZI waveguide over a duration of one hour.

power efficiency of the entire TFLN-MZI waveguide structure, calculated from the input and output powers and depicted in Figure 5.17, was found to average 0.74%, lower than the simulated efficiency. This discrepancy can be ascribed to factors such as fabrication defects (surface roughness, grating pitch damage, etc.) and experimental setup errors.

Further in the study, the influence of the tapered fiber's tilting angle relative to the GC was scrutinized. Figure 5.18 displays the variation in output power from the TFLN-MZI waveguide at different tilting angles, both with and without the GC alignment. The figure also includes a comparative plot showing the percentage increase in power due to alignment. Notably, when the tilting angle of the fiber was set to 0 degrees, implying a perpendicular orientation above the sample, the increase in power was significant. However, it was observed that at a 5-degree tilting angle, the output power surged, indicating an approximate 61% increase compared to the non-aligned scenario. In cases of misalignment, the output power across various tilting angles remained within the 10 uW to 11 uW range, suggesting that changes in tilting angle had a minimal impact on output due to the predominant contribution of scattered light and environmental noise, rather than the waveguide's involvement in light propagation.

Conversely, with the fiber aligned to the GC, the tilting angle became a critical factor influencing output power. The results demonstrated that at a 5-degree angle, the output power not only increased by about 61% in comparison to the non-aligned case but also nearly doubled the power increase achieved at a 0-degree angle. This outcome emphatically confirmed the critical roles of both the GC and the waveguide in the optical experiment,

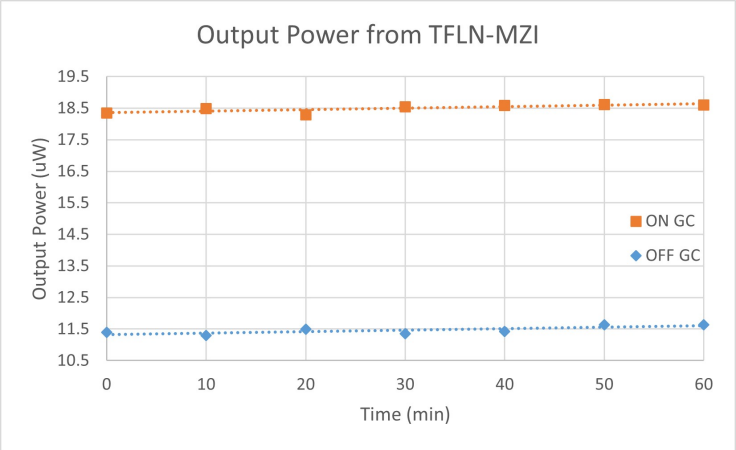

Figure 5.16: Alignment Impact on Output Laser Power. Output laser power from the TFLN-MZI waveguide with and without alignment (ON and OFF) with the GC.

aligning with the design objectives. The measurement results thus provided crucial insights into the optimal alignment and angulation for efficient light coupling into the waveguide.

In conclusion, the experimental results established the operational efficacy of the optical setup. The overall power efficiency of the TFLN-MZI waveguide structure was determined to be 0.76%, based on the collected measurements. When the input laser fiber was not aligned with the GC, the output power from the waveguide structures averaged at 11.46 uW. However, this output power experienced a significant increase to 18.5 uW upon meticulous alignment of the laser fiber with the GC, translating to a 63% enhancement in comparison to the non-aligned output. These findings not only validated the functionality of the optical measurement setup but also underlined its readiness for subsequent phases, specifically the combined measurement stage.

5.7 Combined Experience Data Collection and Analysis

In the crucial phase of the combined measurement experience, the antenna measurement setup, originally situated in the Microwave lab, was methodically relocated to the Advanced Optical lab for integration with the existing optical measurement table. This strategic move, leveraging the proximity of the Microwave lab to the Advanced Optical

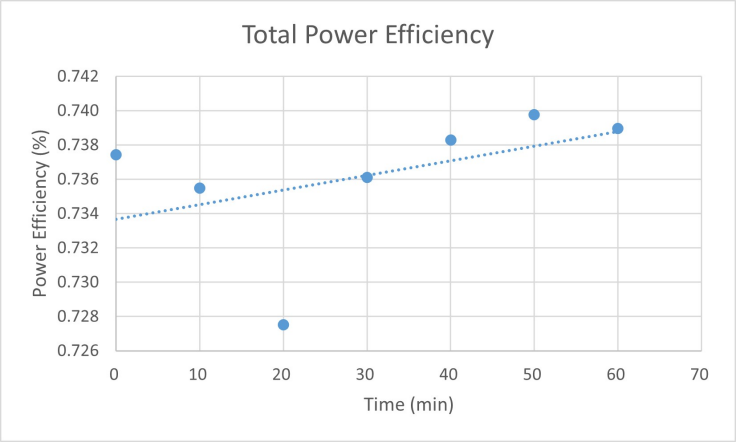

Figure 5.17: Output Power Efficiency of TFLN-MZI Waveguide. Calculated output power efficiency from the entire TFLN-MZI waveguide structure.

lab, was meticulously planned to minimize any potential disruption or damage to the sensitive antenna measurement apparatus. Figure 5.19 provides a visual representation of this enhanced setup, showcasing the seamless incorporation of the antenna holder and network analyzer into the optical measurement framework.

Building upon the foundational elements of the optical measurement setup, the enhanced measurement configuration introduced a three-degree-of-freedom antenna holder onto the optical table. This innovative holder was meticulously designed to securely position the antenna directly above the TFLN-MZI sample throughout the measurement process. In a carefully orchestrated arrangement, the antenna was inverted and mounted onto the holder, with its cable connection situated at the rear, thereby facing the TFLN-MZI waveguide. The substrate was oriented upwards, a configuration vividly illustrated in Figure 5.20. Furthermore, an optical lens was integrated into the setup, positioned adjacent to the photodetector, to augment the collection efficiency of light emanating from the waveguide's output. This critical enhancement, essential in the end-fire coupling method, demonstrated a significant improvement in the optical signal received from the waveguide.

Moreover, the strategic coupling of the lens with the photodetector served a dual purpose: it not only mitigated the influence of ambient light, thereby enhancing the fidelity of the measurements, but also significantly improved the precision control capabilities of the apparatus. This was achieved through the utilization of 3-axis stages, which facilitated meticulous alignment and positioning, ensuring optimal interaction between the optical components. Such advancements demonstrate the importance of precision in the

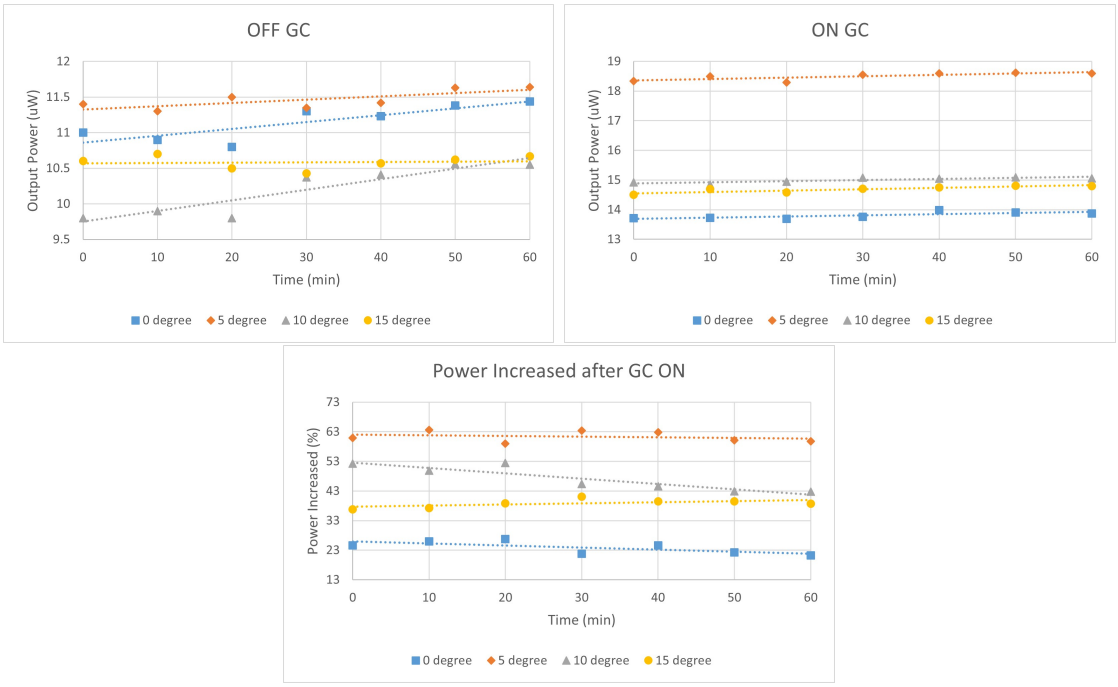

Figure 5.18: Laser Fiber Alignment Power Increase. Top: Output power measured with laser fiber alignment, showing the state without (OFF) and with (ON) the GC. Bottom: Percentage increase in power due to alignment.

alignment and integration of optical components, highlighting the critical role of innovative mechanical designs in augmenting the efficiency and accuracy of optical measurement systems.

The methodology for the combined measurements differed from that used in the optical-only setup. Since the antenna positioned above the sample limited the use of the microscope for fiber alignment, alignment had to be completed before positioning the antenna. Additionally, the fiber running through the antenna vias was delicate and prone to bending, which could alter the tilting angle and affect power transmission within the waveguide. Consequently, after passing the fiber through the antenna, adjustments in the XY plane were prohibited. Figure 5.21 illustrates the alignment process designed for the combined measurements.

Initially, alignment of the tapered fiber with the GC was achieved using a 633 nm wavelength laser, observed under a microscope. After switching to the 1550 nm laser, the antenna vias alignment process commenced. The fiber's height was recorded using the

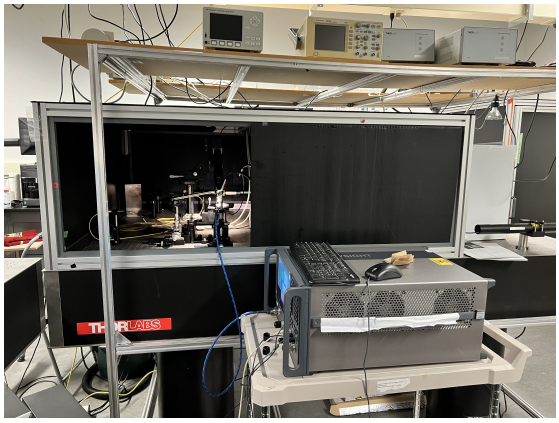

Figure 5.19: Combined Measurement Setup. Photo showcasing the combined measurement setup, including network analysis equipment and the black room covering the optical table for controlled conditions.

stage micrometer on the fiber holder and then raised by 20 mm. The antenna, mounted on its holder, was then carefully placed atop the TFLN-MZI sample. Meticulous alignment of the antenna vias with the fiber was conducted using a combination of microscope and external camera observations. The antenna was incrementally lowered towards the sample, continually checking and adjusting the XY position to ensure precise alignment of the vias with the fiber. This process was repeated until the antenna neared the sample, and the fiber was positioned at the recorded height, ensuring no XY movement post-alignment. Figure 5.22 displays camera images of the vias alignment process.

For the combined measurements, an increased data set was collected to enhance accuracy for subsequent analysis. Three sets of experimental data were recorded for the TFLN-MZI output power, each comprising seven measurements spread over an hour. All measurements were conducted with the fiber aligned with the GC, focusing on the effects of the antenna's E-field on the optical signal within the TFLN-MZI waveguide. Variations in output power between the data sets were observed due to the independent nature of each measurement set. Each set was recorded following fiber and vias alignment processes, with the network analyzer output power set to 100 mW (20 dBm).

Figure 5.23 and Figure 5.24 presents the experimental results for the waveguide output power, comparing scenarios with and without the antenna. The data indicates a clear influence of enabling the antenna on the TFLN-MZI waveguide's output power, showing a 2% decrease when the antenna is active, compared to a 5% power difference anticipated from LUMERICAL Simulation Package predictions. The discrepancy is attributed to experi-

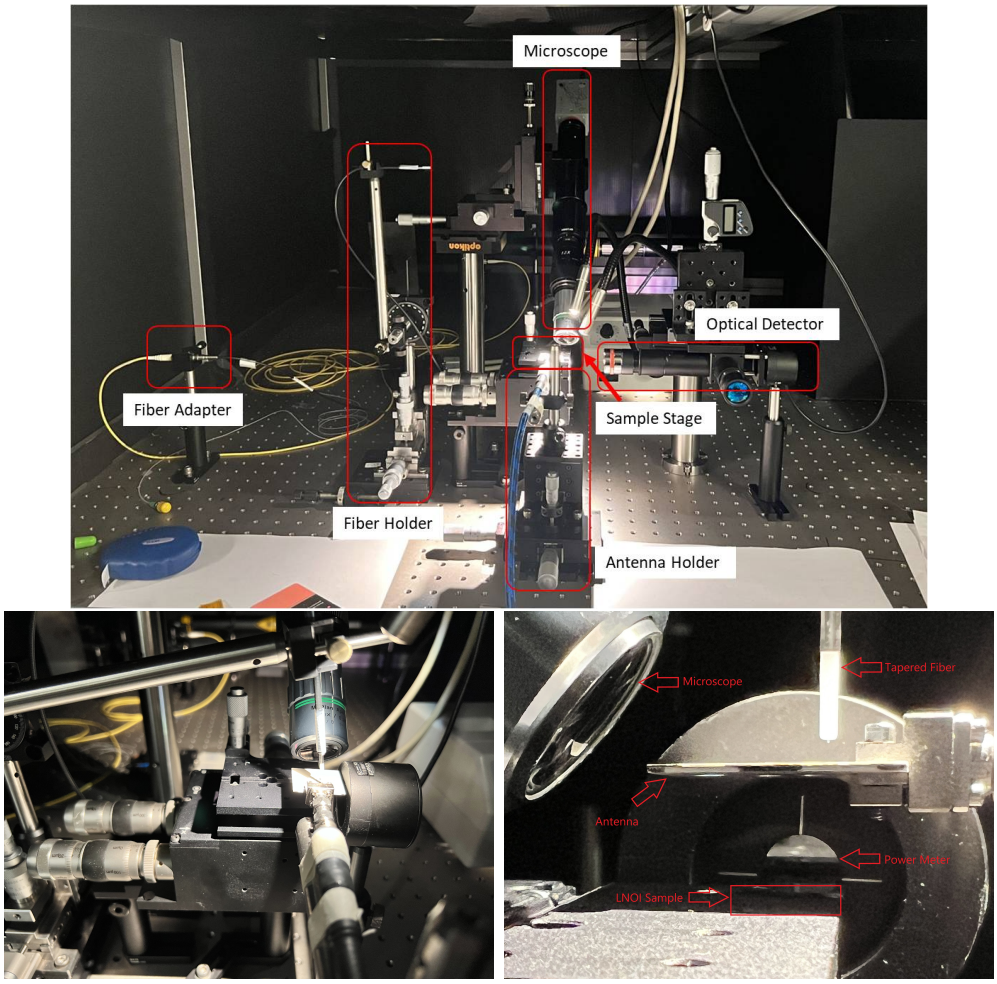

Figure 5.20: Combined Measurement Setup Overview. Top left: General view of the optical table in the combined measurement setup. Top right: Close-up of the antenna and the sample stage. Bottom: 45-degree view of the antenna and the TFLN-MZI sample.

mental inaccuracies, including a larger-than-simulated distance (approximately 200 um) between the sensing waveguide and the antenna patch, and a reduced E-field intensity at this distance. Additionally, lower power efficiency resulting from coupling methods and fabrication defects on the TFLN-MZI waveguide sample also contributed to this variance.

The experimental results illustrated in Figure 5.25 indicate that the most significant power difference occurs at an antenna input power of 100 mW. At lower input powers (1 mW and 10 mW), the E-field generated by the antenna is weaker, exerting negligible

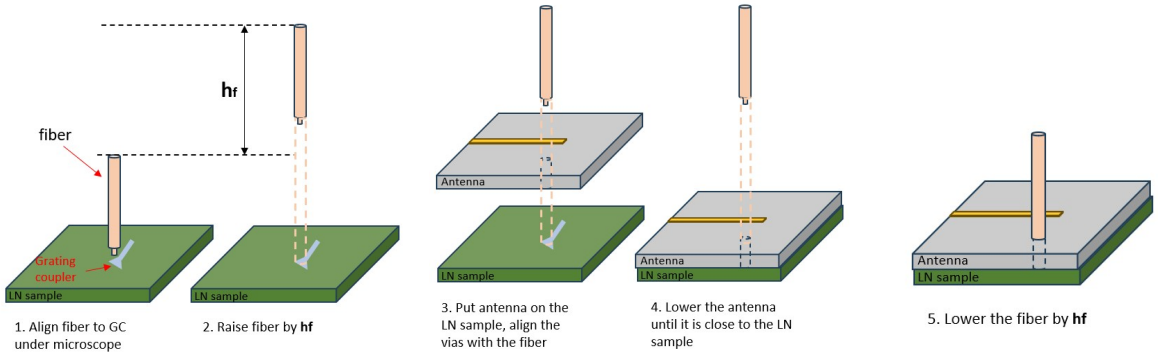

Figure 5.21: Vias Alignment Process Schematic. Diagram illustrating the schematic process for aligning vias in the combined measurement setup.

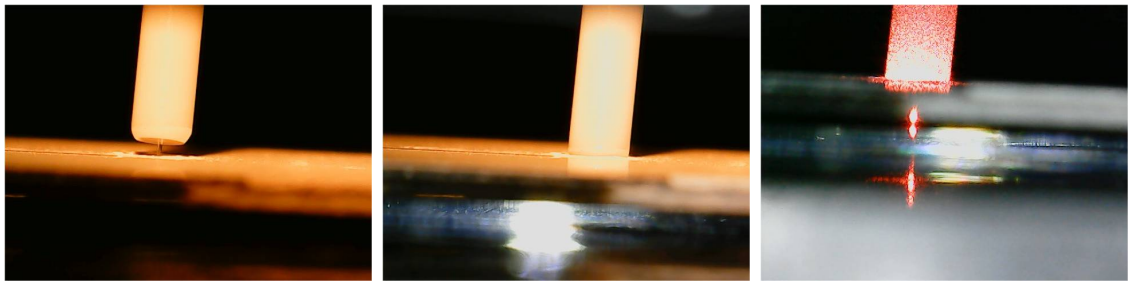

Figure 5.22: Vias Alignment Process Camera Images. Showing the stages of vias alignment: Left: Vias aligned with the fiber. Middle: Fiber passing through the vias. Right: Tapered fiber illuminated by a 633 nm laser.

influence on the waveguide output. An average of 0.3% power difference was recorded when the antenna was activated with 10 mW and 1 mW input power. However, with the antenna power at 100 mW, the power difference caused by antenna activation was around 2%. This aligns with simulation predictions, where a reduction in antenna power from 100 mW to 10 mW results in a significant drop in E-field intensity.

Theoretical studies suggest that the change in output power upon antenna activation correlates with the E-field intensity on the sensing waveguide. To explore the impact of varying network analyzer output power on the TFLN-MZI waveguide output power difference, further combined measurements were conducted and analyzed in Figure 5.26.

In summary, the combined measurement results demonstrated that with an antenna power of 100 mW from the network analyzer, enabling the antenna near the waveguide

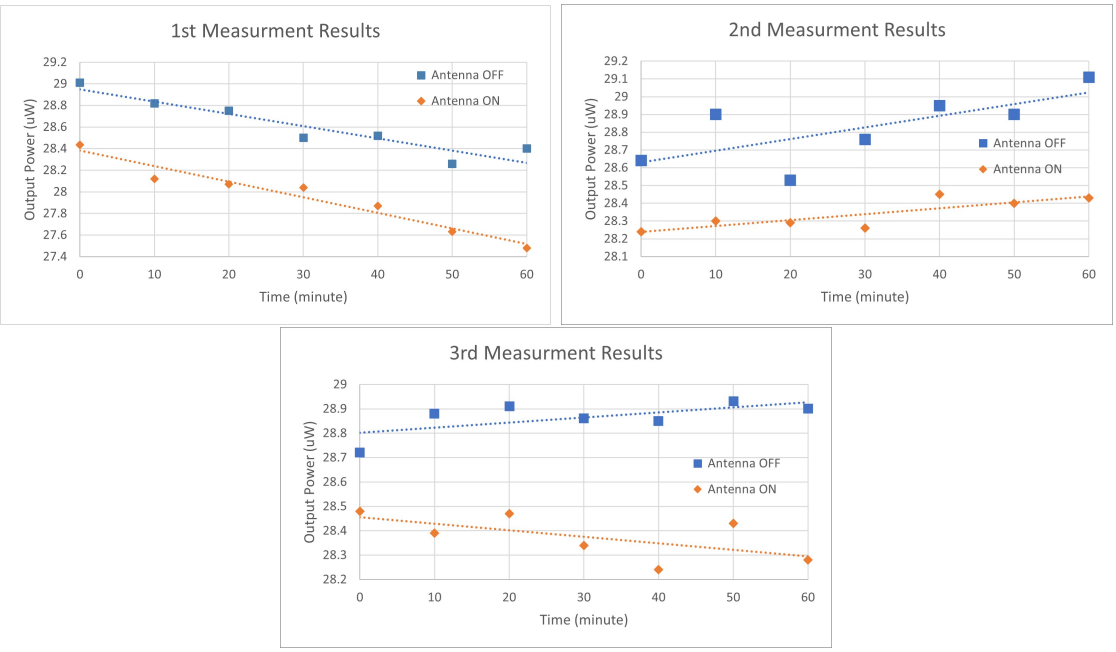

Figure 5.23: TFLN-MZI Waveguide Output Power: Antenna E-field Effect. Shows three individual measurement results for the TFLN-MZI waveguide output power with the antenna enabled (ON) and disabled (OFF).

edge altered the TFLN-MZI waveguide output power from 28.77 uW to 28.22 uW, a 2% difference. This change, induced by the electro-optical effect on the sensing arm, confirms that the TFLN-MZI waveguide structure can effectively sense the near-field generated around the patch antenna.

5.8 Challenges and Solutions

The integration of the antenna measurement setup with the optical table presented a unique set of challenges due to the disparate scales and operational frequencies of the antenna and waveguide components. The antenna, designed for a 30 GHz frequency, had a larger physical footprint, measuring 20 mm by 20 mm. In contrast, the dimensions of the TFLN-MZI waveguide were significantly smaller, around 500 um by 3000 um. A critical aspect of this setup was the precise positioning of the antenna patch, situated at the center of the antenna, in close proximity to the waveguide. The juxtaposition of these

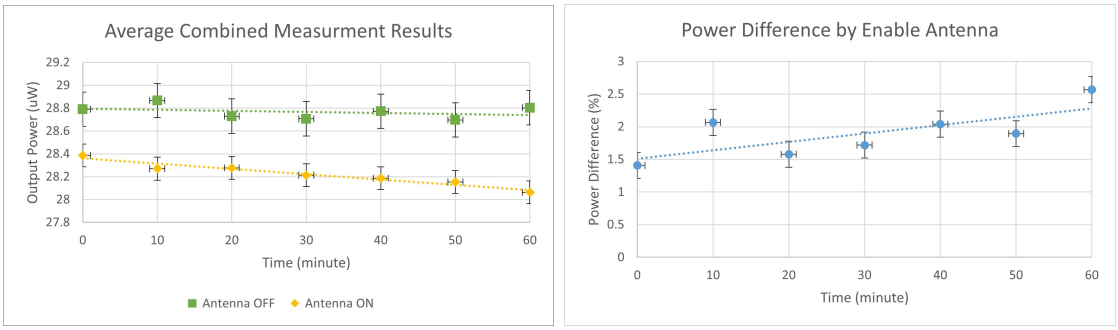

Figure 5.24: Averaged Output Power Measurements. Left: Averaged measurement results for output power. Right: Power difference post-antenna activation, based on averaged results.

different-sized components necessitated a careful rethinking of the spatial arrangement and alignment strategies within the experimental setup.

Figure 5.27 showcases the post-integration antenna measurement setup on the optical table. The left side of the figure illustrates the antenna holder, which was equipped with a three-degree freedom adjustment capability, an essential feature for fine-tuning the antenna's position relative to the TFLN-MZI sample. The right side of the figure displays the complete antenna measurement setup, now including the network analyzer and calibration box, alongside the optical table. To ensure compatibility and functionality, all mounting components used for the antenna were adapted to fit the specifications of the optical instruments. This adaptability was vital for the precise placement and stability of the antenna during measurements. Additionally, the network analyzer calibration was meticulously conducted before each combined measurement session. This calibration process was critical to confirm the accuracy and reliability of the antenna's output power, a key parameter in the combined experimental setup.

The physical disparity between the antenna and the TFLN-MZI sample posed a significant challenge. The antenna's larger size, coupled with the front-facing orientation of the patch, made it impractical to move the TFLN-MZI sample closer to the antenna using the existing equipment in the Advanced Optical lab. To circumvent this limitation, the antenna was inverted and carefully positioned above the sample. This orientation change facilitated a more effective alignment of the antenna patch with the waveguide. The solution involved creating vias in the antenna, allowing the optical fiber to pass through directly to the GC on the TFLN-MZI sample, thereby bridging the gap imposed by the differing sizes of the components.

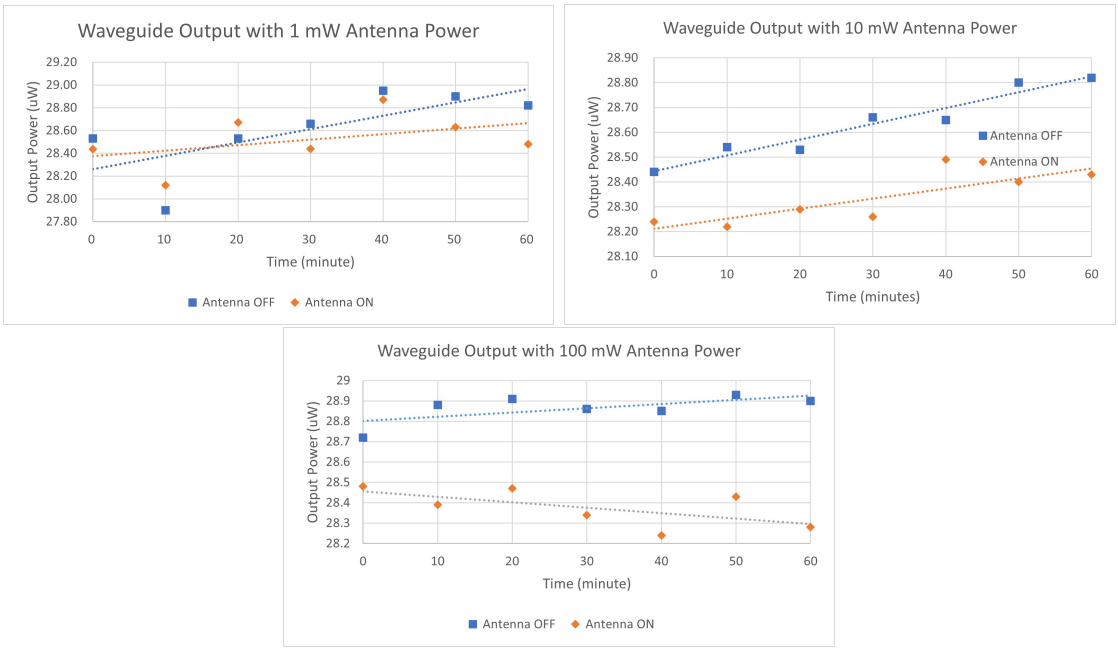

Figure 5.25: TFLN Waveguide Output Power vs. Antenna Power Settings. Demonstrates the TFLN-MZI waveguide output power changed with different antenna power settings: Top Left: 1 mW, Top Right: 10 mW, Bottom: 100 mW.

Figure 5.28 displays the simulation image and an actual photo of the antenna with the newly fabricated vias. The diameter of these vias was set at 1.6 mm, slightly larger than the diameter of the fiber's protective layer, to ensure a snug fit without causing damage or undue pressure on the fiber. The strategic placement of the vias next to the antenna patch, with their centers positioned 800 um (half the diameter of a via) from the patch's edge, was crucial. This positioning ensured that when the fiber was threaded through the vias and aligned with the GC, the TFLN-MZI waveguide would be optimally situated beside the antenna patch. In this configuration, one of the waveguides in the TFLN-MZI structure would function as the sensing waveguide, positioned closer to the patch, while the other served as the reference waveguide.

Another significant challenge was minimizing environmental influences on the measurement results, such as equipment vibration and background light noise. To mitigate equipment vibration, the entire setup, including the combined optical measurement, was built on THORLABS passive isolation optical tables. Initial experiments showed large variances in measurement results over time, attributed to fiber instability due to gravity.

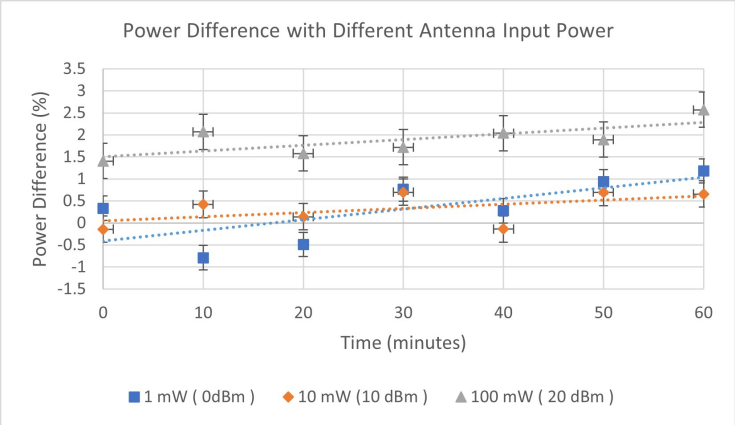

Figure 5.26: Output Power Difference After Antenna Activation. This figure presents the difference in TFLN waveguide output power post-antenna activation, showcasing variations across different antenna power levels.

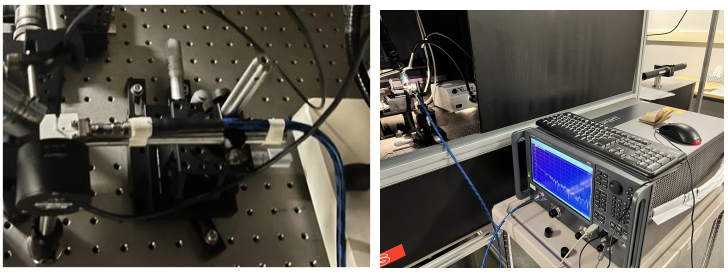

Figure 5.27: Antenna Setup on Optical Table. Left: A close-up of the antenna holder situated on the optical table. Right: The comprehensive antenna measurement setup, integrated with the optical setup, highlighting the synergy between the antenna and optical components.

Implementing a support structure for the fiber on the holder significantly reduced these variances, stabilizing output power differences to under 10% after an hour.

For optical measurements, the challenges posed by background light noise and scattering light from the source were particularly pronounced, especially in experiments involving visible-range lasers. To mitigate the effects of scattering light, a light baffle was utilized. However, this measure alone was insufficient to fully address the issue of ambient light interference. Consequently, a more comprehensive solution was implemented: the entire optical measurement setup was encased within a black box. This enclosure, constructed

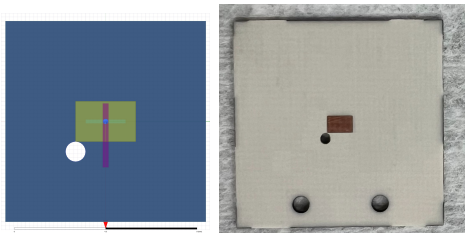

Figure 5.28: Vias Visualization in Antenna. Left: A simulation image depicting the vias on the antenna, providing a theoretical insight into their configuration. Right: A real photo of the antenna showcasing the actual vias, serving as a practical counterpart to the simulation.

from dark, non-reflective material, proved highly effective in significantly reducing the impact of background light.

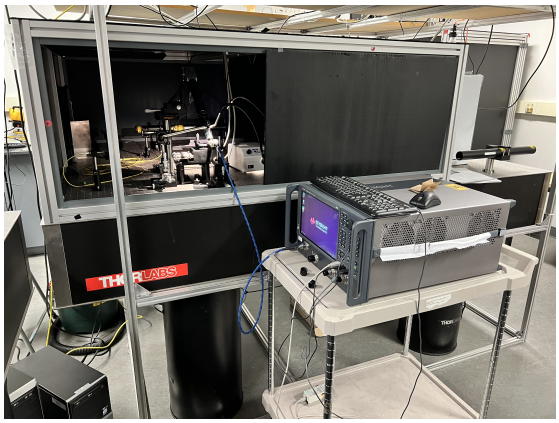

Figure 5.29: Optical Measurement in Controlled Environment. Displays the optical measurement setup positioned on a vibration-isolated table, meticulously covered with a black box to ensure controlled lighting conditions and minimize external disturbances.

Figure 5.29 depicts the optical measurement setup, securely positioned on a vibration-isolated table and encompassed by the black box. This strategic enclosure was instrumental in enhancing the overall quality of the optical measurements. By effectively minimizing extraneous light influences, the black box enclosure ensured a more controlled and stable environment for the sensitive optical experiments, leading to more accurate and reliable data collection.

5.9 Conclusion and Implications

The primary objective of this experiment was to conduct individual and combined measurements of the fabricated TFLN-MZI waveguide structure and the antenna to validate the design and simulation results. The TFLN-MZI waveguide was meticulously measured using an optical setup equipped with a high-resolution microscope and precision positioning mechanisms for fiber alignment. The antenna measurements, on the other hand, were conducted in two separate locations: near-field pattern measurements in the antenna chamber lab with a reference antenna and S_{11} parameter measurements in the Microwave lab adjacent to the optical setup.

The results from the antenna measurements revealed key insights. The near-field pattern measurements illustrated the E-field distribution around the antenna patch, while the S_{11} parameter measurements indicated a shift in the peak from -28 dB at 28.5 GHz in the simulation to -35 dB at 31.5 GHz in the fabricated antenna. Additionally, the bandwidth of the fabricated antenna was narrower compared to the simulation. The introduction of vias into the antenna design led to subtle changes in the S_{11} parameter, underscoring the impact of structural modifications on antenna performance.

In the realm of optical measurements, foundational to the combined measurement phase, meticulous fiber alignment with the GC in the TFLN-MZI waveguide was verified under a microscope. The output power from the waveguide was measured using a time-averaging method, capturing seven data points over an hour. The calculated total power efficiency of the TFLN-MZI waveguide stood at 0.74%, lower than the simulated efficiency of 2.78%, primarily due to edge coupling power loss at the waveguide output. Analysis of the tapered fiber's tilting angle revealed that maximum coupling efficiency occurred at a 5-degree angle, with the output power increasing by 73% when the fiber was aligned with the GC.

The culmination of the experiment was the combined measurement in the Advanced Optical lab, integrating both optical and antenna setups. For accuracy, fiber alignment was diligently conducted for all measurements, maintaining a 5-degree tilting angle. The output power from the TFLN-MZI waveguide was recorded with the antenna both enabled and disabled to assess the impact of the antenna's E-field. The findings indicated a 2% decrease in waveguide output power when the antenna was enabled with 100 mW input power, suggesting that the E-field altered the refractive index of the sensing waveguide in the MZI structure. This outcome was slightly lower than the 5% decrease predicted in simulations, attributable to experimental inaccuracies and fabrication flaws. Furthermore, the influence of varying antenna input powers on the waveguide output power and

efficiency was analyzed. It was observed that at lower antenna powers (1 mW and 10 mW), enabling the antenna had a negligible impact on waveguide output, aligning with simulation predictions of reduced E-field intensity at these power levels.

These results affirm that the TFLN-MZI waveguide structure can effectively sense the E-field emitted from a nearby antenna. This capability to detect changes in waveguide output power based on antenna operation presents practical applications, particularly in antenna array diagnostics. For instance, a 2% drop in waveguide output power could indicate suboptimal functioning of an adjacent antenna, a crucial insight for systems with large antenna arrays.

Chapter 6

Conclusion and Outlook

In conclusion, this research has developed and validated an innovative approach utilizing LN-based optical devices for sensing the E-field emitted from antenna elements within a phased-array antenna system. In contrast to traditional methods that employ horn antennas or other metallic counterparts, the proposed LN-based optical devices are entirely dielectric, which is solely composed of LN material. The LN MZI waveguide device has demonstrated the capability to detect the E-field radiated by nearby antennas, altering the power of the optical signal traversing the device in response to variations in the E-field. These LN-based devices are promising as integral components of the antenna calibration process, providing valuable insights into the antenna's operational status, transmitting power, and phase patterns.

Furthermore, the device's compact geometry, with a length of under 10 mm and a height of less than 1 mm, along with low power consumption, facilitates integration into antenna packages, representing a significant advancement in the field. The primary contribution of this research is its demonstration of a passive, completely dielectric LN-based optical device for sensing near-field transmissions from antennas. This innovation allows for the optical conduct of the antenna calibration process, which can proceed during antenna operation, thus ensuring zero electromagnetic interference with the antenna's radiation pattern.

The thesis embarks on a comprehensive investigation into optical strategies for E-field sensing, beginning with a design and theoretical examination that establishes the groundwork for this inquiry. It extensively explained the fundamental theories central to this research, particularly the EO effect and various EO modulators. Subsequently, an in-depth discussion on optical waveguide theory, with a special focus on the MZI waveguide structure, is provided. The design process of the TFLN waveguide is carefully outlined, aiming

for optimal positioning near a patch antenna's radiation edge to capture a more potent E-field. Through the deployment of MZI structures, which translate phase variations into detectable differences in optical signal power, the thesis achieves significant advancements in measurement precision. The theoretical models suggest that the optimized TFLN-MZI E-field sensing waveguide structure is projected to exhibit a 6.2% decrease in optical signal intensity in response to an E-field intensity of 30,000 V/m emanating from the antenna patch.

The optimization of optical parameters for the TFLN MZI waveguide, including the DC, the Y-junction waveguide, and the GC, was intensively pursued through computer mathematical simulations. These simulations were essential for refining the design and were performed using two specialized software packages: the HFSS FEM simulation package for antenna and RF aspects; meanwhile, the Lumerical FDTD simulation package for optical components. These tools provided detailed insights into the EO effect and its optimization within the TFLN waveguide and other associated TFLN-based optical components. As a result, TFLN-based optical devices that incorporate the GC for waveguide input, edge coupling method for output, and Y-junction for power splitting and combining, achieved a power transmission efficiency of 2.55% at a 1.55 µm wavelength. Furthermore, a TFLN waveguide with a width of 2 µm exhibited a 5.8% decrease in power transmission due to the EO effect.

The fabrication of the TFLN waveguide devices, guided by these simulations, was implemented using three distinct methodologies: the HSQ process, the ZEP process, and the SiO_2 process. The ZEP process, which utilizes ZEP positive resist for electron beam lithography and serves as a hard mask, was identified as the most effective, characterized by six principal fabrication steps and resulting in devices with minimal surface roughness. This method adeptly fabricated the GC and waveguide endpoints with merely minor defects, such as grating line positioning deviations and sidewall roughness. Challenges were observed in fabricating waveguides with widths as narrow as 0.75 µm, necessitating further post-processing for edge coupling. Conversely, the HSQ method, employing HSQ negative resist for electron beam lithography and as a hard mask for etching, facilitated the creation of waveguides of varying widths without additional post-processing. However, it encountered challenges with the effective fabricating of GC due to poor adhesion between PMMA and HSQ layers. Finally, the SiO_2 process, which utilizes a SiO_2 layer as the hard mask in conjunction with ZEP positive resist for electron beam lithography, is favoured for its protective qualities and structural integrity during the etching process.

The culmination of experimental efforts in antenna and optical measurements yielded significant insights, particularly regarding the influence of the EO effect on optical signal power. Antenna measurements revealed a deviation in the peak S_{11} parameter from its sim-

ulated counterpart and a narrower bandwidth in the fabricated antenna, highlighting the sensitivity of the antenna's performance to structural modifications. Optical assessments concentrated on the power efficiency of the TFLN-MZI waveguide, which registered lower than anticipated, primarily attributed to losses incurred through edge coupling. A crucial observation emerged during combined measurements in the Advanced Optical Laboratory, where activating the antenna with 100 mW of input power resulted in a 2% reduction in waveguide output power. This decrease, attributed to the EO effect's modulation of the waveguide's refractive index, although slightly below simulation forecasts, emphasizes the pronounced impact of the EO effect in diminishing optical signal power. This finding highlights the critical importance of experimental precision and the calibration of antenna power levels in optimizing waveguide efficiency.

This research establishes a solid foundation for future explorations, particularly in the integration of optical devices into antenna calibration processes. A primary avenue for subsequent investigation is the incorporation of the TFLN MZI waveguide E-field sensing device within phased-array antennas. With the trend towards smaller geometries, compact sizes, and higher operating frequencies in modern phased-array antenna systems, the continuous monitoring of antenna unit status becomes increasingly essential. The TFLN-based E-field optical sensor, which is capable of being integrated onto the antenna array's top layer during fabrication, offers a fully dielectric and passive solution, powered by the antenna's emitted E-field energy. Additionally, the application scope of the TFLN E-field optical sensor extends beyond phased-array antennas, potentially benefiting other high E-field emitting devices, such as cellular site equipment located in hard-to-reach areas, hence enabling real-time operational monitoring.

Future studies could focus on enhancing signal coupling efficiency and minimizing propagation loss in the MZI waveguide, potentially unveiling more detailed information, such as the phase of the emitted electromagnetic field from the antenna system. Additionally, advancements in the LN waveguide fabrication process, including the adoption of dual lithography techniques for patterning both the waveguide and the grating, could achieve greater precision in grating tooth formation. This approach aligns with findings from the simulation chapter, which highlighted the GC's coupling efficiency sensitivity to structural exactitude. Further enhancements might include an annealing process for fabricated TFLN waveguides to eradicate surface defects and improve edge coupling efficiency.

In summary, this thesis not only advances the understanding of TFLN-based optical devices for E-field sensing in complex antenna systems but also sets a promising direction for future research. The integration of such devices into real-world applications represents a significant step toward the development of more efficient, compact, and precise sensing technologies. Standing at the forefront of these technological advancements, the potential

for innovation in the field of optical sensing and antenna design is substantial and ripe for exploration. The work presented herein contributes valuable knowledge to the scientific community and paves the way for future innovations that could redefine the boundaries of what is technologically feasible.

References

[1] John L. Volakis, *Antenna Engineering Handbook, Fourth Edition*. New York: McGraw-Hill Education, fourth edition ed., 2007.

[2] X. Gu, D. Liu, C. W. Baks, O. Tageman, B. Sadhu, J. Hallin, L. Rexberg, and A. Valdes-Garcia, "A multilayer organic package with 64 dual-polarized antennas for 28ghz 5g communication," *2017 IEEE MTT-S International Microwave Symposium (IMS)*, pp. 1899–1901, 2017.

[3] Warren L. Stutzman, Gary A. Thiele, *Antenna Theory and Design, Third Edition*. Wiley, 2012.

[4] F. Cecelja and W. Balachandran, "Electrooptic sensor for near-field measurement," *IEEE Transactions on Instrumentation and Measurement*, vol. 48, no. 2, pp. 650–653, 1999.

[5] L. Chen and R. M. Reano, "Compact electric field sensors based on indirect bonding of lithium niobate to silicon microrings," *Opt. Express*, vol. 20, pp. 4032–4038, Feb 2012.

[6] Y. Salamin, W. Heni, C. Haffner, Y. Fedoryshyn, C. Hoessbacher, R. Bonjour, M. Zahner, D. Hillerkuss, P. Leuchtmann, D. L. Elder, L. R. Dalton, C. Hafner, and J. Leuthold, "Direct conversion of free space millimeter waves to optical domain by plasmonic modulator antenna," *Nano Letters*, vol. 15, no. 12, pp. 8342–8346, 2015. PMID: 26570995.

[7] Y. Salamin, W. Heni, Y. Fedoryshyn, C. Haffner, C. Hoessbacher, P. V. Johnston, D. L. Elder, R. Bonjour, M. Zahner, R. Cottier, A. F. Tillack, L. R. Dalton, C. Hafner, and J. Leuthold, "Direct rf-to-optical detection by plasmonic modulator integrated into a four-leaf-clover antenna," in *2016 Conference on Lasers and Electro-Optics (CLEO)*, pp. 1–2, 2016.

[8] Signal Hound, "Rf probe – 12 ghz – p20b," 2024. [Online; accessed February 25, 2024].

[9] A. Yariv and P. Yeh, *Photonics : optical electronics in modern communications*. Oxford series in electrical and computer engineering, New York: Oxford University Press New York, sixth edition ed., 2007.

[10] J. Capmany and D. Novak, "Microwave photonics combines two worlds," *Nature Photonics*, vol. 1, pp. 319–330, June 2007.

[11] J. Wells, "Faster than fiber: The future of multi-g/s wireless," *IEEE Microwave Magazine*, vol. 10, no. 3, pp. 104–112, 2009.

[12] D. Marpaung, J. Yao, and J. Capmany, "Integrated microwave photonics," *Nature Photonics*, vol. 13, pp. 80–90, Feb. 2019.

[13] M. Bazzan and C. Sada, "Optical waveguides in lithium niobate: Recent developments and applications," *Applied Physics Reviews*, vol. 2, p. 040603, 10 2015.

[14] S. Saravi, T. Pertsch, and F. Setzpfandt, "Lithium niobate on insulator: An emerging platform for integrated quantum photonics," *Advanced Optical Materials*, vol. 9, no. 22, p. 2100789, 2021.

[15] C. T. Phare, Y.-H. Daniel Lee, J. Cardenas, and M. Lipson, "Graphene electro-optic modulator with 30 GHz bandwidth," *Nature Photonics*, vol. 9, pp. 511–514, Aug. 2015.

[16] Q. Wu and X.-C. Zhang, "Free-space electro-optics sampling of mid-infrared pulses," *Applied Physics Letters*, vol. 71, pp. 1285–1286, 09 1997.

[17] L. Xu, X. Zhang, and D. H. Auston, "Terahertz beam generation by femtosecond optical pulses in electro-optic materials," *Applied Physics Letters*, vol. 61, pp. 1784–1786, 10 1992.

[18] S. R. Marder, B. Kippelen, A. K.-Y. Jen, and N. Peyghambarian, "Design and synthesis of chromophores and polymers for electro-optic and photorefractive applications," *Nature*, vol. 388, pp. 845–851, Aug. 1997.

[19] Y. Salamin, B. Baeuerle, W. Heni, F. C. Abrecht, A. Josten, Y. Fedoryshyn, C. Haffner, R. Bonjour, T. Watanabe, M. Burla, D. L. Elder, L. R. Dalton, and J. Leuthold, "Microwave plasmonic mixer in a transparent fibre–wireless link," *Nature Photonics*, vol. 12, pp. 749–753, Dec. 2018.

[20] A. Sosunov, R. Ponomarev, A. Zhuravlev, S. Mushinsky, and M. Kuneva, "Reduction in dc-drift in linbo3-based electro-optical modulator," *Photonics*, vol. 8, no. 12, 2021.

[21] Y. Qi and Y. Li, "Integrated lithium niobate photonics," *Nanophotonics*, vol. 9, no. 6, pp. 1287–1320, 2020.

[22] S. Toroghi and P. Rabiei, "Thin film lithium niobate electric field sensors," *Review of Scientific Instruments*, vol. 93, p. 034702, 03 2022.

[23] S. S. Sriram and S. A. Kingsley, "Sensitivity enhancements to photonic electric field sensor," in *Enabling Photonic Technologies for Aerospace Applications VI* (A. R. Pirich, M. J. Hayduk, and E. Donkor, eds.), vol. 5435, pp. 143 – 152, International Society for Optics and Photonics, SPIE, 2004.

[24] Y. Sakashita and H. Segawa, "Preparation and characterization of LiNbO3 thin films produced by chemical-vapor deposition," *Journal of Applied Physics*, vol. 77, pp. 5995–5999, 06 1995.

[25] F. Gitmans, Z. Sitar, and P. Günter, "Growth of tantalum oxide and lithium tantalate thin films by molecular beam epitaxy," *Vacuum*, vol. 46, no. 8, pp. 939–942, 1995.

[26] M. Levy, J. Osgood, R. M., R. Liu, L. E. Cross, I. Cargill, G. S., A. Kumar, and H. Bakhru, "Fabrication of single-crystal lithium niobate films by crystal ion slicing," *Applied Physics Letters*, vol. 73, pp. 2293–2295, 10 1998.

[27] J. Miguel Levy, Richard M. Osgood, "Crystal ion-slicing of single-crystal films," U.S. Patent US6120597A, Feb. 1998.

[28] D. Zhu, L. Shao, M. Yu, R. Cheng, B. Desiatov, C. J. Xin, Y. Hu, J. Holzgrafe, S. Ghosh, A. Shams-Ansari, E. Puma, N. Sinclair, C. Reimer, M. Zhang, and M. Lončar, "Integrated photonics on thin-film lithium niobate," *Adv. Opt. Photon.*, vol. 13, pp. 242–352, Jun 2021.

[29] S. L. Chuang, *Physics of Photonic Devices*. Wiley Publishing, 2 ed., 2009.

[30] S. L. Chuang, *Physics of optoelectronic devices*. Wiley series in pure and applied optics, New York: Wiley New York, 1995.

[31] S. Adachi, *Physical properties of III-V semiconductor compounds : InP, InAs, GaAs, GaP, InGaAs, and InGaAsP*. New York: Wiley New York, 1992.

[32] A. Raeesi, *Phased-Array Antenna-in-Package Technology for Emerging Millimeter Wave Application*. PhD thesis, University of Waterloo, 2022.

[33] R. Ding, T. Baehr-Jones, Y. Liu, R. Bojko, J. Witzens, S. Huang, J. Luo, S. Benight, P. Sullivan, J.-M. Fedeli, M. Fournier, L. Dalton, A. Jen, and M. Hochberg, "Demonstration of a low vπl modulator with ghz bandwidth based on electro-optic polymer-clad silicon slot waveguides," *Opt. Express*, vol. 18, pp. 15618–15623, Jul 2010.

[34] S. Bhunia, *Microstrip Patch Antenna Design, A Novel Approach*. LAP LAMBERT Academic Publishing, 01 2014.

[35] B. E. A. Saleh and M. C. Teich, *Fundamentals of photonics*. New York: Wiley New York, 1991.

[36] R. G. Hunsperger, *Integrated optics: theory and technology*. Advanced texts in physics, Berlin: Springer Berlin, 5th ed ed., 2002.

[37] Z. Chen, R. Peng, Y. Wang, H. Zhu, and H. Hu, "Grating coupler on lithium niobate thin film waveguide with a metal bottom reflector," *Opt. Mater. Express*, vol. 7, pp. 4010–4017, Nov 2017.

[38] G. Chen, K. Chen, Z. Yu, and L. Liu, "Low-loss and broadband polarization-diversity edge coupler on a thin-film lithium niobate platform," *Opt. Lett.*, vol. 48, pp. 4145–4148, Aug 2023.

[39] L. Cheng, S. Mao, Z. Li, Y. Han, and H. Y. Fu, "Grating couplers on silicon photonics: Design principles, emerging trends and practical issues," *Micromachines*, vol. 11, no. 7, 2020.

[40] D. Taillaert, F. Laere, M. Ayre, W. Bogaerts, D. Thourhout, P. Bienstman, and R. Baets, "Grating couplers for coupling between optical fibers and nanophotonic waveguides," *Japanese Journal of Applied Physics*, vol. 45, pp. 6071–6077, 08 2006.

[41] U. R. Fawwaz Ulaby, *Fundamentals of Applied Electromagnetics, 7TH Edition*. Pearson, 08 2014.

[42] J.-M. Jin, *Theory and Computation of Electromagnetic Fields, Second Edition*. Wiley-IEEE Press, 09 2015.

[43] "Understanding frequency domain CW normalization, how-published = https://optics.ansys.com/hc/en-us/articles/360034394234-understanding-frequency-domain-cw-normalization, note = Accessed: 2024-03-24."

[44] E. D. Palik, *Handbook of Optical Constants of Solids*. Elsevier Inc., 1985.

[45] A. Ahmed, H. Elsayed, and A. Mehaney, "High-performance temperature sensor based on one-dimensional pyroelectric photonic crystals comprising tamm/fano resonances," *Plasmonics*, vol. 16, 04 2021.

[46] K. Okamoto, *Fundamentals of Optical Waveguides*. Academic Press, 01 2006.

[47] A. Company, *Anritsu Microwave K Connector™ and Extended-K Connector™*. Anritsu Company, 490 Jarvis Drive,Morgan Hill, CA 95037-2809, U.S.A., November 2020.

[48] L. Kovács and G. Corradi, "New trends in lithium niobate: From bulk to nanocrystals," *Crystals*, vol. 11, no. 11, 2021.

[49] C. Wang, M. Zhang, B. Stern, M. Lipson, and M. Lončar, "Nanophotonic lithium niobate electro-optic modulators," *Opt. Express*, vol. 26, pp. 1547–1555, Jan 2018.

[50] P. Rabiei and P. Gunter, "Optical and electro-optical properties of submicrometer lithium niobate slab waveguides prepared by crystal ion slicing and wafer bonding," *Applied Physics Letters*, vol. 85, pp. 4603–4605, 11 2004.

[51] N. Courjal, M.-P. Bernal, A. Caspar, G. Ulliac, F. Bassignot, L. Gauthier-Manuel, and M. Suarez, "Lithium niobate optical waveguides and microwaveguides," in *Emerging Waveguide Technology* (K. Y. You, ed.), ch. 8, Rijeka: IntechOpen, 2018.

[52] K. Buschow, *Encyclopedia of Materials: Science and Technology*. No. Volume 10 in Encyclopedia of Materials: Science and Technology, Elsevier, 2001.

[53] S. Talukder, P. Kumar, and R. Pratap, "Electrolithography- a new and versatile process for nano patterning," *Scientific Reports*, vol. 5, p. 17753, Dec. 2015.

[54] W.-M. Yeh, D. E. Noga, R. A. Lawson, L. M. Tolbert, and C. L. Henderson, "Comparison of positive tone versus negative tone resist pattern collapse behaviora," *Journal of Vacuum Science & Technology B*, vol. 28, pp. C6S6–C6S11, 11 2010.

[55] ALLRESIST, "Sxar n8200-1 english allresist product information," tech. rep., Allresist, 2020.

[56] S. L. Chuang, *Physics of Photonic Devices, 2nd Edition*. Wiley Series in Pure and Applied Optics, Wiley, 2009.

[57] L. R. Dalton, P. A. Sullivan, and D. H. Bale, "Electric field poled organic electro-optic materials: State of the art and future prospects," *Chemical Reviews*, vol. 110, no. 1, pp. 25–55, 2010. PMID: 19848381.

[58] W. L. Stutzman and G. A. Thiele, *Antenna theory and design*. Hoboken, NJ: Wiley Hoboken, NJ, 3rd ed ed., 2013.

[59] R. S. Weis and T. K. Gaylord, "Lithium niobate: Summary of physical properties and crystal structure," *Applied Physics A*, vol. 37, pp. 191–203, Aug. 1985.

[60] E. Wooten, K. Kissa, A. Yi-Yan, E. Murphy, D. Lafaw, P. Hallemeier, D. Maack, D. Attanasio, D. Fritz, G. McBrien, and D. Bossi, "A review of lithium niobate modulators for fiber-optic communications systems," *IEEE Journal of Selected Topics in Quantum Electronics*, vol. 6, no. 1, pp. 69–82, 2000.

[61] A. Shams-Ansari, G. Huang, L. He, Z. Li, J. Holzgrafe, M. Jankowski, M. Churaev, P. Kharel, R. Cheng, D. Zhu, N. Sinclair, B. Desiatov, M. Zhang, T. J. Kippenberg, and M. Lončar, "Reduced material loss in thin-film lithium niobate waveguides," *APL Photonics*, vol. 7, p. 081301, 08 2022.

[62] Y. Zhang, S. Yang, A. E.-J. Lim, G.-Q. Lo, C. Galland, T. Baehr-Jones, and M. Hochberg, "A compact and low loss y-junction for submicron silicon waveguide," *Opt. Express*, vol. 21, pp. 1310–1316, Jan 2013.

[63] H. Xu, D. Dai, L. Liu, and Y. Shi, "Proposal for an ultra-broadband polarization beam splitter using an anisotropy-engineered mach-zehnder interferometer on the x-cut lithium-niobate-on-insulator," *Opt. Express*, vol. 28, pp. 10899–10908, Apr 2020.

[64] M. Zhang, W. Ai, K. Chen, W. Jin, and K. S. Chiang, "A lithium-niobate waveguide directional coupler for switchable mode multiplexing," *IEEE Photonics Technology Letters*, vol. 30, no. 20, pp. 1764–1767, 2018.